Loughborough University

A Coupled CFD Approach for Combustor-Turbine Interaction

by

Paolo Legrenzi

Submitted in partial fulfillment of the requirements for the award of Doctor of Philosophy of Loughborough University

2017

Puisqu'on ne peut être universel et savoir tout ce qui se peut savoir sur tout, il faut savoir peu de tout. Car il est bien plus beau de savoir quelque chose de tout que de savoir tout d'une chose; cette universalité est la plus belle.

Blaise Pascal

Abstract

The current approach in the industry to numerically investigate the flow in a gas turbine considers each component, such as combustor and turbine, as a standalone part, involving no or very minor interactions with other parts, mainly applied through static boundary conditions. Efficient and very specialised CFD codes have been developed in the past to address the different flow characteristic occurring in the different regions of the engine. In order to meet the future requirements in terms of fuel consumption and pollutants emissions, an integrated approach capable of capturing all the possible interactions between different components is necessary. An efficient and accurate way to achieve integrated simulations is to couple already existing specialised codes in a zonal type of coupling. In this Thesis work a methodology to couple an incompressible/low-Mach number pressure-based combustion code with a compressible density-based turbomachinery code for industrial application has been developed. In particular two different couplings have been implemented: the first, based on the exchange of existing boundary conditions through files, comes as a completely separated tools from the original codes, of which no modifications are required, and it is applied to steady state simulations; the second instead, based on the exchange of boundary conditions and body forces through message passing, requires some modifications of the source codes and it is applied to both steady and unsteady cases. A simple analysis shows that not all the primitive variables can be made continuous at the coupling interface between the two codes and a compromise was found that allows minor discontinuity in some of the variables while achieving mass flow conservation and continuity of the temperature profiles. The coupling methodology has been applied to a simplified but realistic industrial case, consisting of a RQL (Rich Burn - Quick quench - Lean burn) combustor coupled with the first stage of the HP turbine. The analysis of the steady case has shown that the combustor field is affected as far as 150% axial chord lengths upstream of the blades leading edge, affecting RTDF and OTDF at the interfaces. In the turbine stage significant differences in both efficiency and degree of reaction were found in the coupled cases with respect to standard standalone simulations using radial inlet profiles. The analysis of the unsteady simulation has instead shown the hot streaks behaviour across the turbine, that are only partially mitigated by the stator blades and, due to segregation effect of hot and cold gases, migrate towards the pressure side of the rotor blades.

Acknowledgements

I would like to thank first of all my family for their constant, never missing support during these years. I thank my brother for always being ready to help and for our great trips across Europe, my parents for being on my side on every choice I made, my sister and my little sweet niece.

I thank my supervisor, Dr Gary Page, for his constant help and great advices. It was a pleasure to work with him. I thank Dr Andrew Garmory. I thank my colleagues, in the office and not: Dr Mehriar Dianat for our walks and our useful talks on wild fruits, Dr Parviz Beherouzi, always kind and ready to give advices on life, Dr Vipran Kannan, for our discussions on the coupling and our trips in the UK, Dr Richard Adoua, who sat next to me, for his very kind spirit and his tips on the English language and Dr Dalila Ammour, always there if I needed help. I thank Dr Indi Tristanto from Rolls-Royce Derby, for being always ready to help on the code development and to reply to my numerous emails. I thank Dr Cristian Nastase and Dr Anand from Rolls-Royce Indianapolis and Dr Max Staufer from Rolls-Royce Deutschland for our useful meetings and their technical support.

I thank all the people involved in the EU FP7 COPA-GT Project and the European Union for funding the project.

I thank all my friends and my housemates: my friend Simone for his constant presence and our Skype talks, Laurent and Emily for being great housemates before and friends after, my friend Javier and also Kim, Aw Yong and Matt. I thank Natasha for her precious support during the difficult time of finishing up this work. I thank all the other people I haven't cited in here, without whom I couldn't have made it!

Contents

List of Figures

List of Tables

List of Symbols

$\bar{\phi}$	Reynolds averaged quantity
$\boldsymbol{\tau}_{ij}$	viscous stress tensor
$\Delta h^0_{f,k}$	formation enthalpy of species k
δ_{ij}	Kronecker delta
$\dot{\omega_k}$	change in mass of species k due to reaction
$\dot{\omega}$	heat release due to the combustion process
$\dot{Q}$	heat due to external sources
$\dot{q}_k$	production rate of species k
ϵ	turbulent dissipation
γ	heat ratio
γ_{BF}	constant in the body force term
λ	thermal conductivity
μ	molecular viscosity
μ^v	bulk viscosity
ϕ''	Favre fluctuations of quantity ϕ
ϕ'	Reynolds fluctuations of quantity ϕ
ψ	fuel/air equivalence ratio
ρ	density

$\rho_{(0)}$, $\mathbf{u}_{(0)}$, $T_{(0)}$, $Q_{(0)}$ zeroth-order quantity in the Mach number expansion

$\tilde{\phi}$ Favre averaged quantity

ξ mixture fraction

AFR local air to fuel ratio

c speed of sound

C_p, C_v specific heats at constant pressure/volume

E specific energy

e specific sensible energy

E_0 total specific energy

e_0 total specific sensible energy

f volume force

FAR local fuel to air ratio

H specific enthalpy

h specific sensible enthalpy

H_0 total specific enthalpy

h_0 total specific sensible enthalpy

k turbulent kinetic energy

m_{AIR} mass from air stream

m_{FU} mass from fuel stream

N number of species

p pressure

$p_{(0)}, p_{(1)}, p_{(2)}$ non dimensional zeroth-order, first-order and second-order pressure in the Mach number expansion

$p_g = p_{(2)}^{ILM-PBS}$ gauge pressure in the ILM-PBS domain

p_{therm} reference thermodynamic pressure

Pr Prandtl number

q, Q heat flux

Sc Schmidt number

T temperature

u_j velocity components

V_k diffusion velocity of species k

var^C variable on a compressible assumption

var^{ILM} variable on an incompressible/low-Mach number assumption

var_B variable at the C-DBS boundary node

var_{ext} variable at the C-DBS external virtual node

var_R reference variable for non-dimensionalisation in the C-DBS code

x_j Chartesian coordinates

Y_k mass fraction of species k

Le Lewis number

R specific gas constant

Abbreviations

COPA-GT	**C**oupled **P**arallel **G**as **T**urbine
DNS	**C**omputational **F**luid **D**ynamics
DNS	**D**irect **N**umerical **S**imulation
LES	**L**arge **E**ddy **S**imulation
RANS	**R**eynolds **A**veraged **N**avier **S**tokes
URANS	**U**nsteady **R**eynolds **A**veraged **N**avier **S**tokes
EBU	**E**ddy **B**reak **U**p
FGM	**F**lamelet **G**enerated **M**anifold
PDF	**P**robability **D**ensity **F**unction
BML	**B**ray **M**oss **L**ibby
CSM	**C**onserved **S**calar **M**odel
TPDF	**T**ransport **P**robability **D**ensity **F**unction
CV	**C**ontrol **V**olume
CHIMPS	**C**oupler (for) **H**igh-performance **I**ntegrated **M**ulti (-) **P**hysics **S**imulations
OpenPALM	**O**pen **P**rojet (d)**A**ssimilation (par) **L**ogiciel **M**ulti-methode
UTC	**U**niversity **T**echnology **C**enter
ILM-PBS	**I**ncompressible **L**ow **M**ach (number) - **P**ressure **B**ased **S**olver
C-DBS	**C**ompressible - **D**ensity **B**ased **S**olver

Chapter 1

Introduction and Objectives

This Thesis develops in the context of coupled simulations for gas turbine aero-engines. In order to develop the future aeronautical propulsion systems, improved fuel efficiency and reduced emissions have to be achieved, as set by the ACARE 2020 and later ACARE 2050 [1] European objectives for air transport. A detailed and accurate prediction of the entire flow field inside the gas turbine is a key aspect to gain further improvements in the current engine performance and polluting characteristics.

The aim of this work is to develop a robust and reliable methodology to couple simulations of different components of a gas turbine, in particular combustor and turbine, in order to properly understand their interactions and to be able to predict multi-component effects, such as combustion instabilities or combustor-turbine hot-streak migration. In that way simulations will be able in future to substitute, at least partially, very expensive experimental rig tests.

1.1 Introduction

The design process of a gas turbine engine usually analyses each component as a separate part. Specific and very specialised tools have been developed, tuned and validated to properly capture all the information of interest for engineering development and design of a specific region of the engine, such as the combustor, compressor or turbine parts. These tools generally reflect the different flow conditions and physical phenomena occurring in different components. In a combustor high swirl, detached flows and high

turbulence levels are present and also the flow is mainly characterised by mixing processes. Multiphase flows may be present when dealing with liquid fuels, and in this case atomisation and evaporation processes are involved too. Finally the combustion of often complex hydrocarbons is occurring, with the consequent high temperatures and heat transfer to the containing structure. The flow is generally low speed, to allow for good combustion, and the pressure is almost constant. Low Mach number pressure based codes with combustion models have been successfully applied for the prediction of the flow in this component [2]. In contrast the flow is fully compressible in the turbomachinery as the Mach number can be high and shocks may occur. The flow is often assumed to have uniform constant physical properties or mixture of non reacting fluids with thermodynamic properties varying with temperature and composition (e.g. calorically perfect gas) [3]. The accurate description of thin boundary layers around blades and walls, tip gaps and leakage flows is required to correctly predict losses and performance. The rotating parts introduce a further complication, as regions with different relative rotational speed have to be accounted for, either by modelling or by introducing relative geometry movement. Density-based compressible flow solvers [4] capable of handling relative rotating zones and thin shear layers are commonly used in the industry.

The interactions between combustor and turbomachinery components are only partially taken into account through simplified models and parameters, generally applied as boundary conditions. An example of this are the temperature distribution functions which characterise the temperature profile at any combustor/turbine interface plane. The Overall Temperature Distribution Function (OTDF) and Radial Temperature Distribution Function (RTDF) are defined as

$$RTDF(r) = \frac{\overline{T}(r) - \overline{\overline{T}}}{\overline{\overline{T}} - T_\infty} \tag{1.1}$$

$$OTDF = \frac{T_{MAX}(r,\theta) - \overline{\overline{T}}}{\overline{\overline{T}} - T_\infty} \tag{1.2}$$

where $\overline{\overline{T}}$ is the temperature averaged in both circumferential and radial directions, while $\overline{T}(r)$ is the temperature averaged in the circumferential direction only. The OTDF is the ratio of the difference between the peak and mean temperature to the mean combustor temperature rise. The RTDF instead is the ratio of the difference between the

circumferentially averaged temperature and the mean temperature to the mean combustor temperature rise. The OTDF is important in the design of the NGVs, because the peak temperatures affect the stator blade life, while the RTDF is important for the rotor blades life expectancy which experience the average temperature during their rotation. Due to their impact on the turbine blades the temperature profiles at the combustor-turbine interface are a design criteria for the combustor as well as being used in the definition of inlet boundary conditions for the turbine design. However, an assumption of relatively smooth temperature field is made when adopting them. Thirty years of research experience [5] have shown instead how strong circumferential and radial temperature gradients, so called hot-streaks, may occur at the combustor exit, invalidating this assumption. Moreover experimental measurements of the temperature distribution functions are generally limited to non reacting cases and most frequently rely on simplified combustors. In real life engines the turbine entry temperatures have increased to obtain improved engine efficiency, and they typically are above the turbine melting temperature by some hundreds of degrees. Furthermore, as lean combustion is being introduced in aero-engines to meet the future requirements in terms of fuel consumption and pollutants emission, the interaction between combustor and turbine potentially increases. The high swirl generated to sustain the flame in a lean combustor is still generally present at the combustor exit and it may significantly lower the effectiveness of the turbine cooling system, stripping away the cooling flow from the surface or modifying its design path. The presence of the turbine blades might change the stability properties of the combustor itself, which is intrinsically much more unstable than in a standard RQL (Rich burn - Quick quench - Lean burn) configuration. On the other hand these instabilities can be responsible for the generation of hot spots which migrate into the turbine. Finally, requirement for compactness and lightness in aeronautical applications make all the components strongly interacting. It is then clear how only a fully coupled approach capable of taking into account the interactions between different components will allow a confident predictive simulation.

1.2 Motivations

The state-of-the-art in industry for the design of a Gas Turbine is to treat each component separately, as a standalone part of a bigger puzzle. This approach has been the only

one feasible for many years in the industry, for very practical reasons: computational cost and modelling.

Nowadays, in the era of massively parallel computers, this limitation can be partially overcome and new strategies developed to investigate the flow in a Gas Turbine. In fact the current approach, that has been proved to be very convenient, it is likely to be unable to capture all the extremely complex phenomena that can take place in the engine (that currently could be studied only after the assembly). The interaction between different components and different physical processes needs to be taken into account, if a confident high fidelity simulation has to be achieved.

Even though the increasing availability of computational resources and the improved efficiency of future flow solvers will allow the simulation of an entire engine, looking at the huge variety of flow phenomena that have to be simulated, it is clear that only the use of multiple specialized flow solvers can guarantee accuracy and efficiency. This is particularly true when coupling turbomachinery portions and combustor. Moreover, in order for such a simulation to be useful, it should deliver results sufficiently accurate within an acceptable timeframe (typically an overnight run). As an example, a full LES simulation of the whole engine could be computationally prohibitive, but since it will greatly improve the prediction of detached flows and free turbulence in the combustor, this type of simulation may be performed in this portion of the engine only. The combustor is also characterised by heat release and chemical reactions, and additional transport equations have to be solved to model the combustion process. Again the solution of these equations can be limited to the combustor. The reaction is generally assumed to occur at constant pressure and the flow Mach number is usually very low. Hence pressure-based low Mach number solvers can be used to model the flow in this part of the engine, avoiding the additional complication of compressibility which can make the computational time step small. In the turbomachinery parts, a precise description of the turbulent boundary layers around the blades, tip gaps and leakage flows, is required. High Mach and Reynolds numbers characterise the flow. Hence density-based compressible flow solvers capable of handling rotating components and thin shear layers are generally used. In the industry the flow solvers for this type of problems are based on RANS simulations, and years of experience led to a good degree of confidence on the various parameters needed to model the turbulence [6–8]. A RANS or URANS approach, that is computationally affordable, may then be used in the turbomachinery parts.

A complete simulation of a virtual gas turbine using a single flow solver resolving all the flow features can take many years for development and validation. The same knowledge can be achieved by coupling existing specialised flow solvers simulating each sub-system. This type of approach, in which each zone is treated separately, is called zonal coupling and has previously been applied to gas-turbine simulation by some research groups [9–11]. A zonal type of coupling in which each region in the engine is simulated using its own specialised flow solver is a very accurate way of investigating components interactions in gas turbines. Years of development and valuable experience in the industry in the prediction of each component will be exploited. The development of new tools capable of accurately describe the entire engine with a reasonable computational cost is yet to be achieved. Codes coupling currently represents a very convenient as well as very accurate approach.

This work concentrates on the hot HP (high pressure) section of an aeronautical gas turbine engine, namely the combustor and the first stage of the HP turbine. Different approaches have been presented in the past to study computationally this part of the engine, some relying on the inclusion of the stator blades in the combustor domain in a single comprehensive simulation [12–14], some others using a coupled approach of different codes [9, 11].

1.3 Code coupling

The expression "code coupling" refers to a simulation performed using two or more different modelling codes which communicate some data between each other to provide an integrated numerical solution of a specific physical problem. This is a very broad definition since any piece of simulation software can be part of a coupled simulation. We can try to distinguish between coupling:

[I] codes which are used to solve the same physics but with different methods that are more appropriate to a specific region of the computational domain (e.g. close to an aerofoil/in the farfield);

[II] codes which solve completely different physics in the same domain (e.g. radiative heat/fluid dynamics);

[III] codes which solve different physics in different parts of the domain (e.g. fluid dynamics/heat transfer in the solid);

[IV] codes which solve different approximations of the same physics (or slightly different physics) in different regions (e.g. Incompressible/Compressible)

[V] the same code with different degrees of modelled physics involved in different regions (e.g. reacting/non-reacting, LES/RANS);

[VI] the same code solving the same physics with the same numerical methods on different regions of the domain (e.g. sliding planes, chimera methods).

When dealing with two completely different physics solved in two different regions (point III), such as conjugate heat transfer calculations, the two domain regions (solid and fluid) are sharing a common interface through which some of the variables are exchanged and made continuous, such as temperature and heat flux. The interface acts as boundary conditions for the two regions, and many studies have been devoted to defining appropriate and stable coupling configurations for such variables. When two fluid regions instead are being coupled some different situations might occur. We shall recall that the splitting of the domain into smaller regions which are being coupled has been applied extensively in computational fluid dynamics for other practical reasons than multi-physics, such as to accelerate the solution of large linear systems or to help the grid generation process when dealing with complex geometries. The strategies to decompose the domain into smaller regions are generally divided into overlapping and non overlapping methods, and their coupling characteristics have been studied and analysed. For these types of applications the same set of equations is being solved using the same numerical methods in all the coupled regions (point VI). A different situation instead arises when different methods are used in different regions (point I). A further complication is added when different approximations of the fluid physics are being coupled (point IV). In this last case in fact the variables involved in the solution of each region might be the same (and having the same name), but their behaviour and consequently their physical meaning might not be fully consistent such that aiming at continuity of all variables across the regions' interfaces could eventually be incorrect.

An additional classification of the coupling methodologies could be done on the degree of intimacy that is established between the two coupled solvers, ranging from tight to

loose coupling. This classification is not easy to be done, but generally speaking a tight coupling can be established where the physics involved and numerical methods are similar between the codes (e.g. only one code is used VI), while some degree of relaxation is necessary to be introduced where the physics and numerical methods are not consistent. This work aims at coupling two different codes which solve two different approximations of the physics of the fluids (incompressible/low Mach number and compressible) using different solution techniques (pressure-based, density-based) and involving a different degree of modelled physics (reacting/non-reacting), in two different regions, but partially overlapping, of the computational domain. The differences between the codes are such that a loose type of coupling has been preferred and investigated.

1.4 Objectives

The objectives of this work are the following:

[I] Consider existing validated industrial CFD codes for combustion and turbomachinery, and exploit existing interpolation tools to develop a zonal type of coupling;

[II] develop a methodology to couple the existing unmodified codes, as a user friendly external coupling tool for coupled steady simulations

[III] develop a methodology to improve the coupling between the codes, both in terms of results accuracy and coupling time efficiency, with the freedom of introducing modifications to the original CFD source codes, for both steady and unsteady simulations;

[IV] assess the methodologies on simple test cases;

[V] apply the methodologies to a realistic industrial case to predict combustor-turbine interaction.

1.5 Contents of the Thesis

In this Chapter 1 the statement of the problem and the objectives of this work were declared. In Chapter 2 some background is given on the subject. In Chaper 3 the

original numerical tools used are detailed while in Chapter 4 the new developments of the coupling are explained. The assessment of the coupling methodology on various test cases is reported in Chapter 5. In Chapter 6 the application of the coupling on a realistic industrial test case is reported. In Chapter 7 some conclusions are drawn.

Chapter 2

Literature Review

The combustor is the region of the gas turbine where the combustion process occurs. There are many requirements in the design of an aero-engine combustor. It should realise a stable and efficient combustion, completely burning the fuel and holding the flame inside the chamber. It should be as light and short as possible and allow for a wide range of operating conditions. To obtain efficient combustion, a low flow speed, complete mixing and suitable equivalence ratios are required; while achieving these the combustor should introduce acceptable pressure losses. It should also generate a target exit temperature profile, as previously mentioned. Furthermore, it has to conform to the strict regulations in terms of polluting emissions, such as CO_2 and NO_x. Not last the containing metal structure has to withstand the extremely high temperatures occurring. Diffusion-flame combustors represent the technology traditionally used in the past and still the main one for current applications. They are stable and reliable but they produce high levels of thermal NO_x. This type of nitrogen oxide formation is due to dissociation of N_2 naturally present in the air at the very high flame temperatures reached in a traditional configuration. In order to reduce NO_x formation the typical configuration adopted nowadays in the industry is the one of an RQL (Rich burn - Quick quench - Lean burn) combustor [15]. Figure 2.1 shows a highly swirling region in the first part of the combustor where rich combustion occurs that stabilise the flame, a middle region where the injection of fresh air through primary and secondary dilution holes makes the combustion process much leaner and a third region towards the exit where the mixture is very lean and the combustion process is completed. The idea is to exploit the two regions of equivalence ratio in which NO_x is reduced, respectively at very rich and

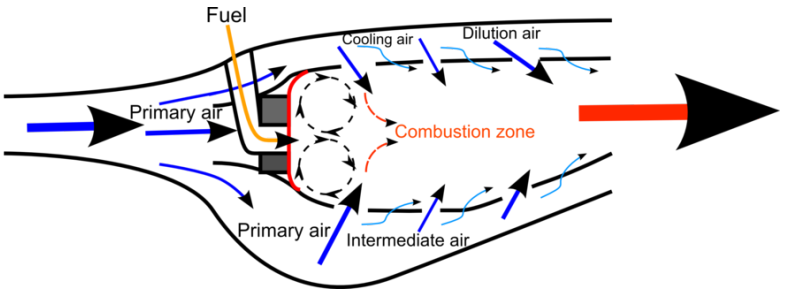

FIGURE 2.1: Configuration of an RQL combustor [18]

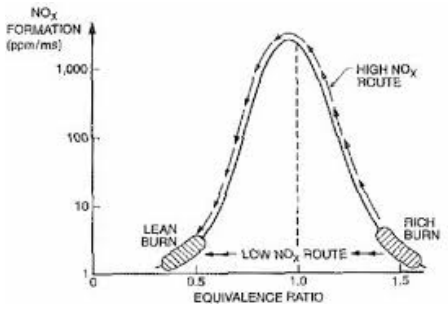

FIGURE 2.2: NO_x production in a RQL combustor

lean conditions (Fig. 2.2). The key region is the middle one in which quick dilution is obtained through injection of jets of fresh air bringing the mixture from rich to lean conditions: possible stoichiometric pockets may occur, with consequent NO_x generation. As anticipated, more recently a new configuration, fully lean, has been introduced in the industry to further reduce NO_x emissions. The combustion zone is operated with excess air to avoid the presence of stoichiometric regions and reduce the flame temperature. In Fig. 2.3 is shown a schematic of a lean combustor. The clear features of this engine is the completely closed chamber, with no dilution holes: the entire amount of air participating in the combustion is directly delivered through the injector, which results in it being much larger than in a standard RQL configuration, obtaining in such a way the desired low equivalence ratio combustion. The drawback of lean-combustion systems is the very common presence of combustion instabilities [16]. These are unsteady flow oscillations that can influence the engine operation or even lead to failure in some cases. The combustor may in fact be greatly damaged by excessive structural vibration and heat transfer. Moreover, as shown, the chambers are typically almost entirely closed, while the processes tending to attenuate these instabilities are very weak. While a proper design can eliminate instability problems in traditional diffusion-flame combustors, this is still an open field of research in a lean approach. Many factors influencing the development of instabilities have been analysed and reported in the literature [17], ranging from

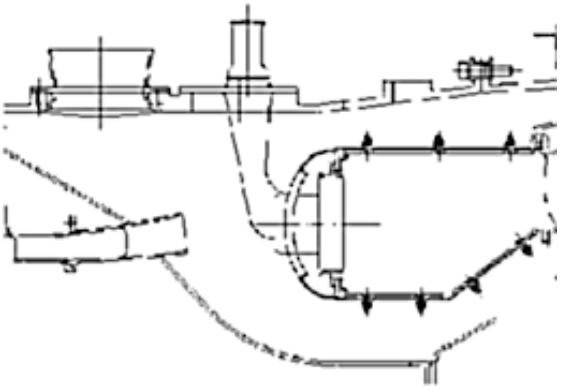

FIGURE 2.3: Schematics of a lean combustor [19]

experimental works to theoretical derivations or CFD computations. An up-to-date description of lean-premixed technology may be also found in [17]. It is clear that even a small change in operating parameters or in the geometry, including the presence of a downstream turbine, can be of great importance in generating or eliminating unstable combustion. By analysing a lean combustor using an incompressible assumption the thermo-acoustics effects, which are one of the main driving forces of instability, are not automatically captured by the simulation. The acoustics in the combustor have to be studied in a second step, which is a limiting assumption.

The turbine is the part of the aero engine in which the hot air exiting the combustor is expanded, cooled down and accelerated to high speed to generate the engine thrust while extracting from the fluid the energy needed to power the fan, the compressor and all the on-board devices. Typical configuration is of an axial turbine, in which the air flows through a series of subsequent axial stages, each comprising stator vanes (the stator) and rotating blades (the rotor). In a modern aero-engine multiple turbine stages are present, generally subdivided in high pressure (HP), intermediate pressure (IP) and low pressure (LP) sections, which are eventually mounted on different shafts and hence rotating at different speeds. In the design of an aeronautical turbine stage many considerations are made necessary. A good compromise between stage efficiency and number of stages has to be met. In general the higher pressure drop achieved the less efficient the stage is. The degree of reaction of the stage, defined as the fraction of the static enthalpy drop (and consequently the pressure drop) that is occurring in the rotor, is carefully chosen. An increase in the pressure drop per stage can be beneficial in one hand (increasing the temperature drop and possibly lowering the weight of the engine, if less stages are

required for the same cumulative pressure drop of the turbine), but on the other hand deteriorate the performances in terms of viscous losses and flow separation, and hence efficiency. In general few stages (less than 10) are enough to extract the required energy from the fluid in modern engines. Nowadays one of the major problems for turbine designer is to keep the turbine blades alive by constantly cooling them both internally and externally with relatively fresh cooling air. This is an important issue especially for the first stages of the HP turbine in which the extremely hot gases coming from the combustor directly impinge the blades. Another key issue is the very high rotational speed which generates enormous stresses on the blades. It is clear how material and stress engineering are of fundamental importance together with fluid dynamics.

In this Chapter 2 a comprehensive description of the numerical approaches in the study of combustor and turbomachinery components is reported in Sec. 2.1. A review on the history of CTI (combustor-turbine interaction) simulations and experiments can be found in Sec. 2.2, while in Sec. 2.3 a literature review of flow coupling for multi-components simulations is presented. Conclusions are drawn in Sec. 2.4.

2.1 CFD for gas turbine applications

Computational Fluid Dynamics has become one of of the major tools in solving practical problems in industry, and it is still the only available tool for certain applications where experimental results are impossible to be achieved (very high Mach number and temperatures). For an introduction on CFD methods refer to [20–22].

2.1.1 CFD for turbomachinery applications

Most probably CFD plays a more important role in the design of turbomachinery than it does in most of other engineering fields [23]. In turbomachinery, numerical methods have been developed since the 1940s [24, 25] even before the advent of the modern computers and they have been successfully used for decades by the turbomachinery designers. However most effects of 3D flow, such as effects of blade lean and sweep, of tip leakage and secondary flows [26–29] can only be captured by fully 3D simulations, firstly introduced in the late 1970s. Denton in 1979 performed a single blade row CFD simulation based on sheared H-meshes and finite volume time-marching scheme. In the

1980s these steady computations became more and more common. Steady simulations are based on RANS (Reynolds Averaged Navier-Stokes) approach, where the flow is time averaged and all the scales of turbulence need to be modelled. This approach nowadays is widely used and tested, and the numerous turbulence models proposed are all well-known in their capabilities and limits.

A limited number of numerical schemes have been applied to 3D turbomachinery flows. The most common are time marching solutions of the Navier-Stokes equations. A typical algorithm is a multi-step (4 or 5 step) Runge-Kutta temporal scheme with variable time step and multigrid acceleration. Implicit solutions are not typically used and these simpler explicit methods are largely preferred. A few pressure correction methods have been used for turbomachinery applications. A second order accurate spatial discretisation is often adopted, having demonstrated to be at the moment the best compromise between accuracy and level of complication. Generally speaking, explicit density-based flow solvers of the fully compressible Navier-Stokes equations have historically been used for simulations of the turbomachinery part of a gas turbine. The grid system for this type of applications was historically based on structured meshes. CFD solvers nowadays are mainly built upon an unstructured assumption, as it is a more general approach even though intrinsically more computationally expensive. Nevertheless for turbomachinery simulations it is still convenient and typical to work on multi-block hexahedral meshes. In fact the relatively simple shape of the blade geometry allows a relatively easy structured discretisation, at least for the main flow path, when complex features such as tip gap leakage, cooling holes, struts or fan assemblies are not modelled. Using tetrahedral unstructured grids in turbomachinery is only a very recent approach. It is in fact more requiring in terms of CPU effort and it is more difficult to obtain good quality tetrahedral meshes in the discretisation of the boundary layer (where far less points are necessary along the wall than in the direction normal to it), which is a fundamental requirement for turbomachinery applications.

In order to model the unsteady interaction between two adjacent blade rows which are in relative rotation some methods have been proposed and widely applied in the industry. An early method proposed by Denton is the “mixing plane” [30]. With the objective of averaging out the unsteady interactions and predicting the time average of the unsteady flow from a steady calculation, a mixing process is assumed to occur at this “mixing plane”. The flow leaving one blade is simply circumferentially averaged before feeding it

into the next row. The mixing is then instantaneous and does not occur gradually as it should be. The objective is to keep using the usual steady RANS equations, averaging the effect of the unsteadiness due to the mixing. This method produces errors and further developments have been proposed to improve it [31].

A very important role for the efficiency and aerodynamic performance of a turbomachinery is played by the interaction between primary and secondary flows. In the last decade CFD simulations have been able to partially simulate both primary and secondary gas path simultaneously. An overview of the current limitations of the application of CFD in turbomachinery in industry may be found in [32].

The intrinsic unsteadiness of a flow in a turbomachinery can lead to incorrect results or missed convergence of the steady simulation. Unsteadiness sources as well as the main unsteady modelling approaches are reviewed in [33] and [34]. In the 1990s unsteady multistage CFD simulations appeared on the scene thanks to the increased computational power available [35, 36]. Unsteady multi-blade row codes able to handle multiple rows had been in fact developed at the end of the 1980s [37]. Sliding planes appeared between blade rows to properly resolve stator-rotor interactions. The rotor mesh rotates (slide) relative to the stator, being incremented in the tangential direction every time step. Being an unsteady 360^o annulus calculation very computationally expensive, adjustments in modelled blade count and pitch on a particular blade row is often accepted to obtain a circumferentially periodic simulation. This unsteady approach is based on URANS (Unsteady RANS) simulations. Care has to be taken to ensure a spectral gap is present between the resolved and modelled scales. Between mixing planes and sliding planes a "frozen rotor" assumption allows us to increase the steady flow modelling fidelity at the price of no temporal (relative) wake movement. A mixture of sliding planes and mixing planes can be used to increase accuracy and reduce the computational cost in a multi-stage simulation, as proposed by Montomoli [38].

In the last decade the linear harmonic analysis [43, 44] was developed and applied in particular for flutter calculations. The usual RANS mean solution is calculated but an equation for a small linear perturbation about this mean is also solved, either in the time or frequency domains. Non-linear Harmonic methods, such as the Balance method, have also been proposed and tested [45, 46].

Large Eddy Simulations (LES) are the most accurate tool in the hands of the turbomachinery engineers (DNS are far too computationally expensive to be applicable for industrial applications). A filter in space is applied to the N-S equations and only the smallest eddy scales are modelled, while most of the turbulence energy is resolved. LES offer advantages when off-design conditions are considered and may help to understand the physics of generation of new vortices resolving transient turbulent structures unresolved in RANS [47]. The drawback with LES is the extreme increase in computational cost. Currently LES for complex systems tend to be under-resolved since the grids are insufficiently fine. The near-wall regions, where the dimension of the turbulent structures to be resolved becomes very small, pose a particular challenge. Moreover few simulations make use of properly defined boundary conditions for LES, and this is an open field of research. LES best practices are needed.

Hybrid LES-RANS methods have been recently developed, such as DES (Detached Eddy Simulation) and LNS (Limited Numerical Scales). They combines RANS and LES in a single flow solver, and this requires a sensor to determine when to switch from one approach to the other.

A detailed scheme of the unsteady methods currently available, ordered according to their level of fidelity, can be found in the red box of Fig. 2.4 from Tucker [33]. In the figure the dashed boxes represent respectively on the left of the red box the approaches where the unsteady flow is reduced to steady problem and on the further left the very early 1D and 2D (Quasi 3D) methods.

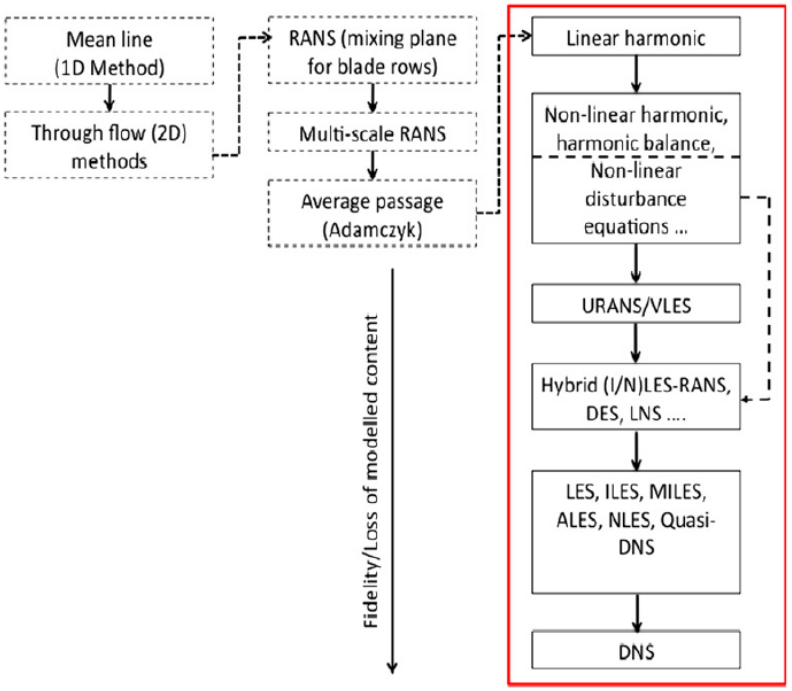

FIGURE 2.4: Schematic of unsteady modelling hierarchy, from [33]

2.1.2 CFD for combustion applications

Combustion is a very complex subject. It involves heat transfer, chemical reactions, turbulent fluid flows, and many type of combustion processes exist, such as gaseous fuel combustion, liquid fuel combustion, solid fuel combustion, pulverised fuel combustion and spray combustion. Even considering only gaseous combustion two different categories have to be distinguished: premixed and non-premixed combustion. At the same time it represents one of the most important processes in engineering: combustion occurs in aero-engines, in gas turbine combustors, internal combustion engines, furnaces, power station combustors, boilers, and home gas heaters etc. CFD methods have grown rapidly in the last years for combustion applications. Combustion processes are basically governed by the same transport equations for fluid flow and heat transfer but models for combustion chemistry and radiative heat transfer have to be added. A bigger number of equations has to be solved and this leads to an increased computational cost of the simulation. Detailed informations on CFD combustion modelling and implementations can be found in [48] and [49].

Most common combustion reactions involve oxidation of hydrocarbon fuels that have a high content of carbon and hydrogen. Combustion mechanisms even for very simple

fuels are very complicated and a large number of species are involved. Combustion of a fuel in fact does not occur in a single reaction but involve a number of different steps. Even the simplest reaction we can imagine, such as H_2 combustion in oxygen, involves in practice many intermediate steps. The number of these elementary reaction steps is often too large to be fully taken into account for an engineering computation.

We are not entering the details of the combustion theory, but we can spend a few words about how combustion is implemented in CFD modelling. As mentioned above transport equations for each species are solved along with continuity, momentum and energy equations (the latter may not be solved if the particular combustion model evaluates the temperature in different ways). New terms appear in the equations, related to the combustion process. One of the most important term to be evaluated is the source term in the species transport equations. It describes the rate of production/destruction of a particular species, that can be formed and consumed in a number of different reactions, and depends on species concentrations.

Detailed combustion mechanisms have been developed for common hydrocarbons and can be found in the literature. But since the computational cost of a simulation is directly related to the level of detail in the reaction mechanisms, many more practical reaction schemes involving fewer reactions to represent combustion of basic fuels have been proposed (i.e 2-steps mechanism) [50]. Often a non-dimensional variable called "mixture fraction" ξ is defined to further reduce the number of transport equations. In the most general way it can be seen as the mass percentage of fuel (both burned and unburned) in a gaseous mixture. It is directly related to the species mass fractions. ξ is a conserved scalar, neither created nor destroyed by chemical reactions and it obeys a transport equation. So a transport equation for the mixture fraction is often computed and mass fraction after combustion of fuel, products or inert species can be reconstructed once given the resulting mixture fraction.

One of the major problems encountered when modelling combustion is the interaction with turbulence. In fact in many combustion processes the rate of combustion depends on flow, turbulence and diffusion processes, which dominate the mixing. When modelling turbulence an average process is applied to the governing equations. The localised heat generation in reacting flow causes the density to vary. The presence of these density fluctuations gives rise to additional terms when traditional Reynolds averaging is used;

a density-weighted averaging procedure (Favre average) is more appropriate in such a case. The main problem arises when an average for the source term in the species transport equations has to be calculated, since it can not be expressed as a function of Favre-averaged variables. As a consequence an effort has been made to develop models which completely avoid solving the average species mass fraction equations. Also the Favre-averaged mixture fraction $\tilde{\xi}$ transport equation, once solved, it is not of immediate usage for the calculation of mean species. In fact the relationship between species mass fractions and mixture fraction relate to instantaneous mixture fraction ξ and not to Favre-averaged $\tilde{\xi}$.

One of the ideas is to introduce a statistical approach: the "Probability density function" (PDF) method is based on one-point statistics. The mean value of a variable can be determined from instantaneous values if the probability of finding this value at a certain location $P(\xi)$ is known. This idea has been used for the instantaneous mixture fraction scalar ξ and extended to the instantaneous reaction rate which is a function of the species mass fractions and temperature. Since the real PDF is difficult and expensive to be calculated, as a simplification a presumed PDF can be assumed. One of the most popular is the β-function. The presumed PDF $P(\xi)$ is defined by the mean value of the variable $\tilde{\xi}$ and by its variance $var(\tilde{\xi})$. With an integration process time-average variables can be recovered from Favre-averaged statistics. Instead of using a presumed PDF there are more elaborate methods which solve a transport equation to obtain a PDF (Transported PDF) [51].

Another very simple approach initially proposed by Spalding [52] is the eddy break-up model (EBU). It is based on the assumption that at high Damköhler numbers, chemical reactions are purely controlled by mixing processes. In context of RANS methods, the mixing time can be estimated from the turbulent mixing time k/ϵ represented by the turbulent kinetic energy k and the turbulent dissipation rate ϵ. The rate of reaction is expressed in terms of the turbulence time scale. The dissipation rates of fuel, oxygen and products are taken into account. Only the transport equation for the mass fraction of fuel is solved together with transport of mixture fraction, and the model takes the actual reaction rate of fuel to be equal to the slowest of these rates. If also the chemical reaction rate is considered because the combustion processes are kinetically influenced, the net fuel reaction rate is taken as the minimum of the chemical reaction rate and the mixing rate.

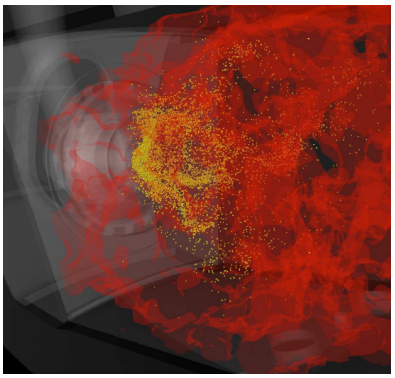

FIGURE 2.5: A state of the art LES simulation, snapshot of iso-surfaces of temperature and fuel sprays in a Pratt & Whitney gas turbine engine combustor, Stanford University [54]

A very common combustion model present in modern CFD solvers is a compromise between simplicity and need to account for a more detailed chemistry. It involves the definition of "laminar flamelets". These are structures assumed to resemble the flame sheets responsible for combustion in a laminar flame. They are considered to be stretched and strained by the flow and turbulence. So the flame is viewed as an ensemble of stretched moving laminar flamelets embedded within the turbulent flow. The heat release is considered to occur mainly in the vicinity of stoichiometric surfaces. This model is based on the assumption that the flame is very thin, so that flame curvature or turbulent eddies do not disturb the inner structure of the flame. Therefore, flames have a unique structure, and can be represented by 1-D laminar flames. The properties of the laminar flamelet (density, temperature, species mass fractions) as a function of mixture fraction are evaluated and stored in a database (Flamelet Generated Manifolds FGM [53]), that can subsequently be used to simulate multidimensional flames. Data for the laminar flamelets databases can be obtained from either 1D free propagating laminar premixed flames or from non-premixed counter flow diffusion flames. In the FGM approach the flame is completely determined by two parameters, the mixture fraction and a non-equilibrium parameter or a progress variable. Since these parameters are statistically distributed in a turbulent flow, a PDF approach can be applied with FGM to model turbulence-combustion interaction.

Many other models and more complicated (such as the conditional moment closure model, the Thickened flame model [55] etc.) for RANS or LES simulations, for premixed or non-premixed combustion have been proposed. The topic is very ample and various and we are not entering any more details.

The current situation sees most of the combustion solvers based on low Mach number approximations. These solvers were often developed for the industry of process engineering, chemical engineering etc. where slow flow conditions occur and compressibility effects could often be neglected. They are typically implicit (to avoid the stiffness of the problem) solvers using pressure-correction schemes (SIMPLE, SIMPLEC, PISO etc.) or the artificial compressibility method [56]. Since density variations are not linked to the pressure, the mass conservation is a constraint on the velocity field; in the most typical approach the continuity equation is combined with the momentum equation and the constraint on the velocity field becomes an elliptic equation for the pressure (Poisson equation). More recently new combustion solvers appeared, density-based, explicit and fully compressible (e.g. AVBP from CERFACS [57]). They generally require small time steps and they often need some preconditioning to be applied at the study of low Mach number flows. They naturally conserve the acoustics and they can be used to simulate high-speed regions of the turbomachine. The drawback is that they are computationally more expensive, and their low Mach number counterparts are still preferred in the industry.

As already mentioned above in a combustor the proper mixing of air and fuel is of primary importance, and its correct prediction is the main goal of combustion CFD. To properly capture the equivalence ratio the exact mass split between all the domain inlet has to be achieved, such that generally a mass flow imposition is used at boundary inlets. Simplified or more complicated geometries are considered, where geometrical features are either modelled through boundary conditions or resolved in the simulation. Due to the often complicated geometries involved, unstructured meshes are typically used to discretise the domain.

Grid resolution and modelling at the wall is still a challenge for good LES simulations. But flows where wall modelling is not critical, such as those in combustors, are notable areas of LES success. Since the combustor is characterised by detached flows, heat release and it is governed by mixing, and it is not necessary to obtain well resolved boundary layers, LES simulations can definitely greatly improve the predictions. An up-to-date review of the state of the art in LES simulations for gas turbine combustion can be found in [58], while a picture from a state of the art simulation is shown in Fig. 2.5.

2.2 CTI - Combustor/Turbine Interactions

"Combustor-Turbine Interaction" is a relatively recent field of study. Early experimental and numerical investigations of the influence of combustor exit conditions on the first stages of the turbine date back to the early 80s [59], while studies on the influence of the turbine blades on the combustor is a new research area, and limited to numerical computations. We shall here briefly resume the history of experiment and computations on the subject.

CTI in the literature

Some of the first experimental and numerical investigations on combustor-turbine interaction, and in particular on hot streak migration, are summarised in [5].

The Combustor Exit Radial Temperature Simulator (CERTS) was introduced at the NASA Lewis Research Center as early as 1980 to generate turbine inlet radial temperature profiles [59]. It was used to experimentally investigate the influence of hot streaks on the first stage of a turbine on a subsonic configuration [60]. Total pressure profiles were also introduced together with total temperature profiles using the CERTS. The case was also object of numerical investigations [61]. The study showed that the inlet temperature variation mixes out through the turbine stage and the performance of the turbine was found not to be affected by the inlet profiles.

A second test facility was set up at the United Technology Research Center [62]. The Large Scale Rotating Rig (LSRR) allowed the introduction of hot streaks while maintaining static and total pressure identical to the free stream values. The investigations were conducted at low speed. The experimental results showed that the hot streak does not affect the stator but it results in a segregation of hot and cold gases which migrate towards the pressure and suction surfaces of the rotor respectively. This was explained by a condition where pressure and absolute flow angle of the fluid inside and outside the hot fluid region are the same at the stator exit, but the temperature is different. This leads to a different absolute velocity in the cold and hot regions, which means a greater angle of attach and greater velocity relative to the rotor in the hot streak with respect to the cold area, generating the fluid segregation. The numerical investigations, both 2D [63] and 3D [64] confirmed the general findings that the hot streak is relatively

unaffected as it is convected through the NGV passage (the width decreases due to flow acceleration) but it strongly interacts with the rotating blades, migrating towards the pressure surface.

Hot streaks migration in a transonic turbine was studied by Shang [65] in a test rig developed at MIT. Blade surface temperature measurements were performed. Heat transfer on the pressure surface of the rotor was found to increase due to the hot/cold gas segregation. Moreover, the generation of secondary flows by temperature gradients was observed, transporting midspan hot fluid towards hub and tip regions along the rotor pressure surface.

Th effect of introducing both temperature and velocity profiles at the turbine inlet was studied on a single NGV blade by Thole [66]. In particular the effect of non uniform inlet profiles on the endwall secondary flows were investigated, showing that the stagnation pressure gradient is the key parameter driving the formation of secondary flows. The effect of high free-stream turbulence was also investigated by Thole [67]; typical levels of turbulence at the combustor exit are reported to be up to 40% and its influence has to be taken into account. The experimental measurements showed how the high turbulence in general increased the endwall heat transfer, but the smallest increase was observed in those regions most affected by the secondary vortices.

To obtain even more realistic conditions at the turbine inlet a representative combustor was developed by the group of Thole as a large scale wind tunnel section, including dilution jets and cooling holes [68]. The turbulence level at the combustor exit was found to be $15 - 18\%$. The stator vane used in previous studies [69] was then added to the experimental facility for an integrated analysis of combustor-turbine interactions [70, 71]. Numerical simulations of the test case, performed in incompressible assumption, was also performed [72]. Both experiments and simulation showed the importance of considering all the non-uniformities exiting the combustor to predict secondary flow patterns. The effectiveness of the cooling system for the junction region between combustor and NGV was also analysed.

One of the first CFD analysis including a real combustor and a NGV was presented in [13] by ANSYS. The configuration was a fully compressible reacting simulation of the entire domain. The presence of a vortex core affecting the turbine was predicted,

confirming the experimental findings. A similar approach was presented later by Klapdor [12], where the influence of the turbine blade on the combustor flow field is also shown.

Two other groups active on understanding in particular the influence of combustor exit conditions on the turbine characteristics are based in Oxford University and at the University of Florence. Both groups use as a testcase the MT1 turbine originally installed in the Turbine Test Facility at QinetiQ, Farnborough, UK. Although the MT1 turbine was designed for RQL combustors, both groups try to simulate the effect of highly swirling flow of a lean combustor on this turbine geometry. A combustor swirl simulator in the Oxford Turbine Test Facility is used to generate aggressive inlet swirl conditions [73]. Heat transfer and aerodynamics measurements are obtained on the turbine. Numerical investigations are also used and compared with experiments, and the effect of the inlet swirl in both the flow field and heat transfer is analysed in the turbine [74]. The group in Florence [75] concentrates instead on the numerical approach and uses the experimental results obtained by QinetiQ for comparison. In some of their publications a representative combustor designed ad-hoc is used together with the MT1 turbine for a steady simulation [76]. The novelty is the use of a coupling approach to simulate the two regions, namely combustor and NGV [11]. Both regions are simulated with the compressible assumption, but in the combustor the flow is reacting and the solution method is pressure-based, while in the NGV a density-based approach is used and the reaction is assumed to have ended. Either the same code or different codes are coupled. The same group, in collaboration with ONERA, presented [77] an unsteady simulation of the entire first stage NGV-rotor of the MT1 turbine with inlet temperature distortions and compared them with the experiments provided by QinetiQ in the frame of the TATEF and TATEF2 EU framework projects. A collaboration between the Oxford and Florence groups can also be found in the literature, where both experimental and numerical results are shown [78]. Again the MT1 turbine subject to nonuniform inlet temperature profile was used for this study. The temperature profile that was used in both experiments and CFD is representative of an engine-take-off condition combined with the full combustor cooling, hence an extreme cycle point. A study of the flow field influence on the blade thermal load showed that the hot streak migration mainly affects the rotor pressure side from 20% to 70% of the span, where the Nusselt number increases by a factor of 60% with respect to the uniform case. Furthermore it was found that a nonuniform temperature distribution may be beneficial for the rotor tip, contrary to the

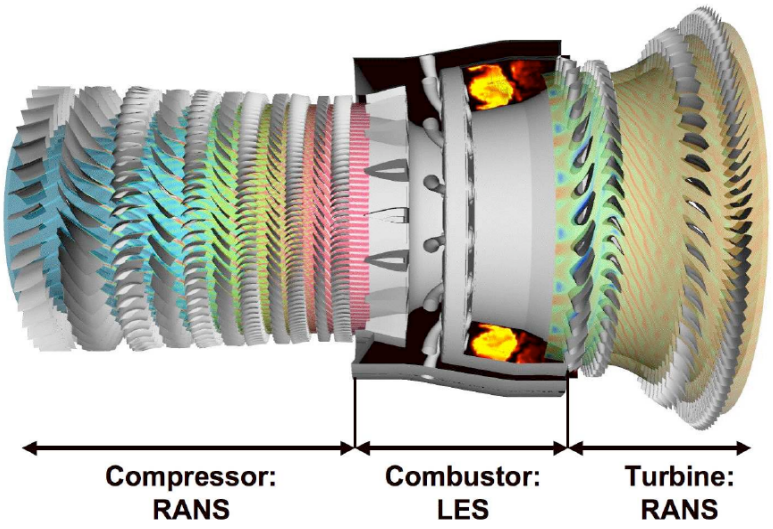

FIGURE 2.6: Full engine simulation, Stanford University [80]

results found in open literature. The radial profile contributed significantly to cooling the turbine casing.

Another recent experimental and numerical investigation is shown by Loughborough University [79]. The study is one of the first of its kind, since the whole engine hardware of a real combustor is used together with nozzle guide vanes. The turbine is here added solely to represent the influence on the combustor. The paper shows the influence of the potential field generated by the NGV blades on the upstream field, as well as the complexity and magnitude of the turbulence levels at the combustor/NGV interface. Comparison with the case without the inclusion of the NGV is reported.

Relatively very small attention was paid in past to the influence of the turbine on the combustor field. An integrated simulation with a detailed analysis of the effect of the inclusion of the NGV blades in the combustor domain is reported in [14].

2.3 Coupling Review

Very a few papers have been published on the topic of flow coupling for multi-component simulations. This demonstrates how open this problem still remains. Two major investigators can be found in the United States: the NASA Glenn Research Laboratory, under the National Propulsion System Simulation (NPSS) program, and Stanford University, as part of the DOE (Dept of Energy) ASC program. Under another earlier NASA

program, the AST program, a full engine simulation of a GE engine turbomachinery was performed by the Allison Engine Company, now Rolls-Royce, Indianapolis, using the ADPAC code [81]. A review of high-fidelity gas turbine engine simulations may be found in [82]. More recently new players started developing strategies to couple different components in a gas turbine, such as CERFACS and Turbomeca [83] and the University of Florence [11]. To the author's knowledge the most recent work on coupling applied to CTI problems is found in [84]. A commonality between most of the works in the literature is the presence of an overlapping region between coupled domains. We shall report in the following some of these works with few or more details based on the relevance they have with respect to the current work.

NPSS program

A NASA Technical Memorandum dated 2004 [10] reports the full-engine simulation of the three dimensional flow in the GE90-94B high bypass ratio turbofan engine. The authors' aim is to demonstrate a high-fidelity complete turbofan engine simulation using an advanced three dimensional Navier-Stokes turbomachinery solver (APNASA, that incorporates the average passage model [85]) coupled with the National Combustion Code (NCC). Coupling between the codes has been done across common interface planes. In particular each component had been previously run separately and later the simulation is run sequentially with the fan first, followed by the booster, HPC (High Pressure Compressor), combustor and turbine. Boundary conditions for the downstream components are set up only after the solution of the current domain has completed. The simulation of the downstream component is then submitted to the batch queue in an automatic process. A considerable discrepancy was found in mass flow at the interfaces. It must be specified that the coupling with the combustor was only done with radial profiles of quantities. In [86] Turner showed how the components could be "unzoomed" (a performance map is generated for each component) and rerun as a full engine, so that the engine can be rebalanced for any components discrepancy, and successively rerun. In more detail, a form of variable complexity analysis (labelled "zooming" and "unzooming") is used to reduce setup and simulation time for the 3D analysis by coupling a cycle model to the 3D model. The boundary conditions in the full-engine model, such as flows and wheel speed, are defined from the boundary conditions in the balanced, steady-state cycle.

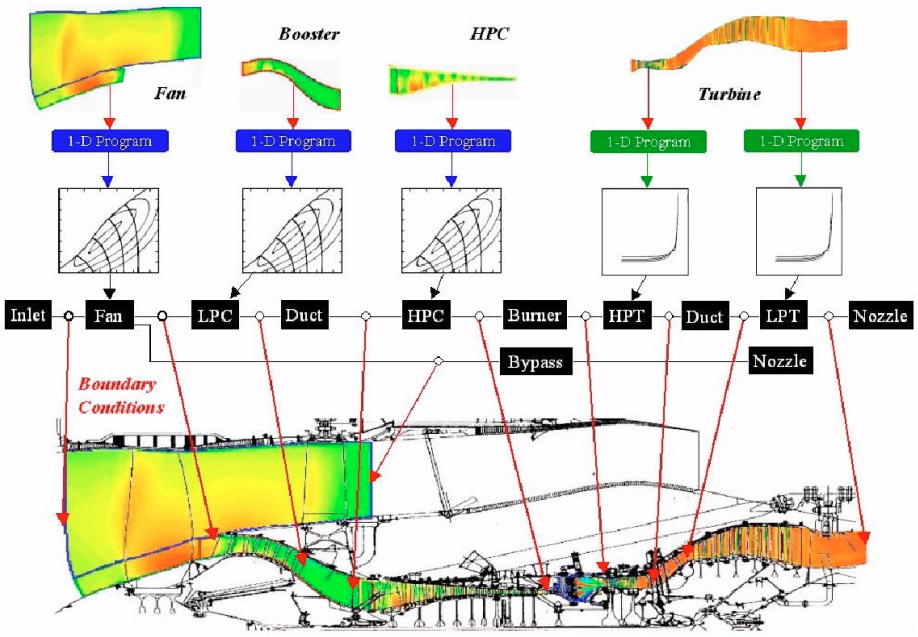

FIGURE 2.7: Coupling of 3D full engine model with Zero-D cycle model, Glenn Research Center [86]

Some issues were found [87], that are relevant to the current work. Even if the steady-state result was expected (APNASA is a steady-state code), the iterative approach adopted could lead to oscillatory solutions, especially in the HPC. This problem was attributed by the authors to the unsteadiness of the physical separate 3D flow. An iteration averaging process has been adopted to damp this behaviour. One of the major problems was to get consistency in the fluid properties between the Zero-D cycle and the 3D simulation. The cycle used a routine to evaluate the properties of air that could take into account also the humidity. In the turbomachinery code a linear variation of the heat ratio γ with temperature was modelled, but the specific gas constant R, that should not be constant (i.e. in a turbine with a profile of combustion products), was a fixed value for the Average Passage code. Moreover the turbomachinery was not able to track the products of combustion coming from the combustor. In the combustor instead the species are tracked and the effective properties were not consistent with the cycle calculation. Among the above cited works, this is the most industry oriented approach.

Stanford Center for Turbulence Research

The ASC program at Stanford was very ambitious and was set up to include the unsteady effects of the turbomachinery as well as LES modeling of the combustor. In many

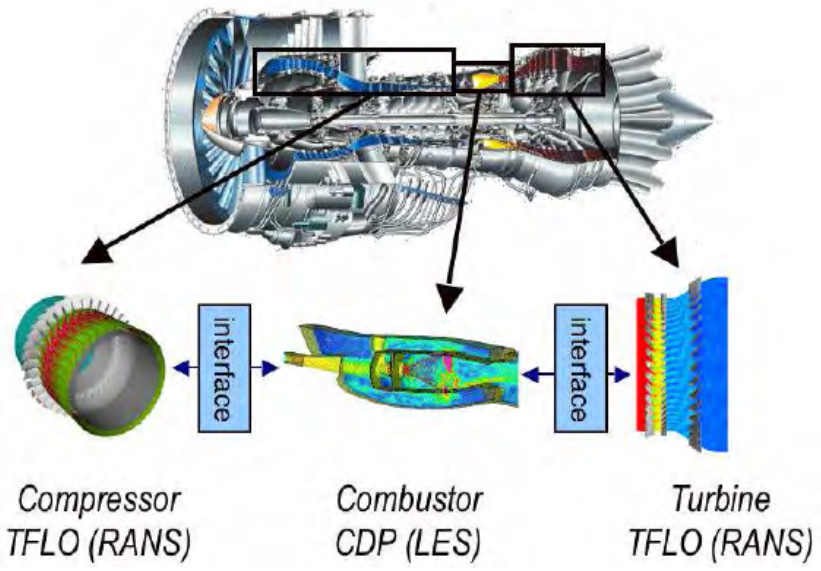

FIGURE 2.8: Decomposition of the engine for full engine simulation, Stanford University [9]

publications dated between 2001 and 2009 they presented the coupling of RANS simulations in the compressor and turbine with an LES simulation of the combustor [88–94]. The latest documents on RANS/LES integration for computations of flows in a gas turbine are the *Annual Research Brief 2006* [95] and the AIAA publication dated 2007 [96], where the group presents the new software module CHIMPS [80, 97, 98], while in previous papers a pure MPI approach was shown to couple solvers [9]. CHIMPS interpolation capabilities are exploited in a part of the current work. In one of the first papers [88] the unsteady turbomachinery code TFLO had been coupled with the NCC (the same code as in the NPSS program). They both are compressible and cell-centred codes. Usually at the interface with another application code, applications request specific flow variables, typically for a ghost/halo layer of cells or nodes. The Stanford group decided to provide numerical estimates of these flow variables through three-dimensional interpolation on the other side of the interface. This approach is the one that will be adopted in the current work. They identified some issues [88], which are typical when coupling different codes, and some of which are relevant to the current work: differing assumptions for the material properties of air (R, C_p, γ) in the two codes produce different states of the gas at the interface. Continuity of all variables of interest (density, pressure, temperature, velocity and energy) could not be achieved for any set of exchanged variables that may be chosen. Moreover differing turbulence models in the two codes required

the definition at the interface of a new set of turbulence variable to be exchanged. In more recent papers the coupled flow solvers changed. The unstructured LES flow solver CDP (developed at the Center for Turbulence Research in Stanford) was used instead of NCC [9]. And the RANS flow solver SUmb (developed at the Aerospace Computing Lab in Stanford) followed TFLO for the turbomachinery computations [96]. In the CDP solver a low Mach-number approximation is used. This introduce a further complication as primitive variables might not be conserved. This situation is common to the current work. They proposed the use of body forces to couple code, which is also exploited in the current work. Full engine (a 20^o sector of all components, with the rescaling of the turbomachinery stages to obtain sector periodicity) simulations have been achieved, performing RANS simulations in the fan/compressor domain and turbine domain coupled with LES simulation in the combustor domain. The Stanford group could not take advantage of a large amount of experimental data that was instead available in the NPSS framework. This poses a limitation on the validation of the coupled approach on real test cases, which is the same limitation we faced in the current work.

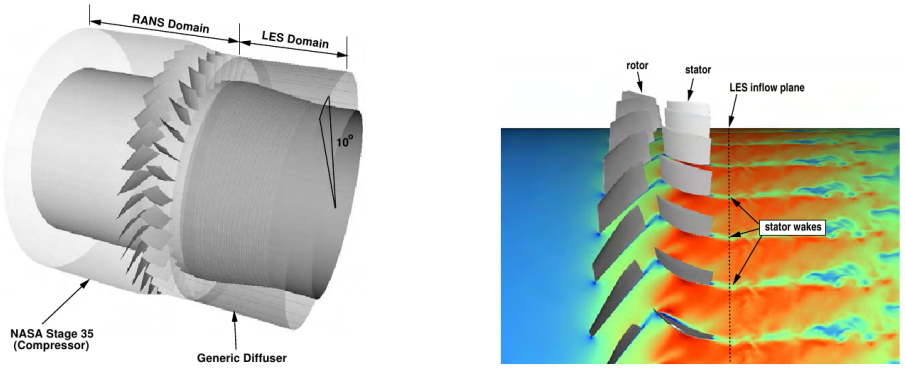

FIGURE 2.9: Integrated RANS/LES simulation of compressor/prediffuser, Stanford University [9]

University of Florence

The work of the University of Florence have been briefly reported in Sec. 2.2. They show a steady RANS coupled simulation of combustor and turbine. Both codes were compressible, the upstream solver being pressure-based while the downstream density-based, and they exchanged some boundary data at interface planes. The gas constant R was constant in the turbine, which was not reacting, and its value taken as the average from the combustor domain at the turbine inlet interface plane.

CERFACS

The initial objective of the CERFACS group was to couple an LES compressible combustion solver (AVBP) with an industrial RANS turbomachinery code (ELSA). The results of this work are published in [83]. A weak imposition is used at the RANS inlet, where all the conservative variables are interpolated from the averaged LES solution into the first two rows of mesh cells, and used by the solver scheme to update its residuals in the nearby row (imposing fluxes). A weak imposition for the downstream inlet is common with the current work, the differences lying in the computation of the fluxes and in the fact that not all the conservative variables are used in the current work.

More recently the group moved to the full LES simulation of combustor and turbomachinery components, implementing a chimera method to handle stationary and rotationary parts in the turbine [84]. This work is the first of its kind, especially considering the rarity of the use of LES for turbomachinery. The code being coupled is AVBP and it is used in all the domains. The coupling can be defined a "tight" coupling. It can still be considered a coupling as a coupling tool is used to coupled two instances of the code and different models can be used in the two domains.

The coupling procedure in CERFACS is handled by the coupler OPalm, developed by the group in collaboration with ONERA. OPalm is used in part of the current work.

2.4 Conclusions

The numerical simulation of both combustor and turbine components has reached a good level of development thanks to the many years of research experience and application in the industry. The increase in computational power and parallel computing and the introduction of new modelling techniques has allowed a continuous improvement in the field. The CFD codes that have been developed in the past reflect the differences in the flow characteristic of each component. Nowadays, simulations of both steady and unsteady flows are efficient, accurate and routinely used with good confidence. Nevertheless many years of research have also shown that the interaction between the combustor and the turbine is often significant and cannot be neglected. In particular the hot streaks generated in the combustor and migrating into the turbine are particularly important as

they influence the turbine flow features and affect the blades thermal loading. The hot streak is often observed to be partially mitigated by the stator and to migrate towards the pressure side of the rotor, overheating the blade. The clocking of the hot streak with respect to the stator blades is also known to be an important parameter and can be used to reduce the degrading effect of the streak on the rotor. In order to study both components in a single integrated simulation, few different coupling techniques have been proposed in recent years by some research groups. This is a new field and no standard practice is available. In particular the nature of the coupling is mainly related to the characteristics of the two codes being coupled. Only in one case a low Mach number code have been coupled with a compressible code, while in all the other approaches a compressible assumption was used in both components. Achieving continuity of all the variables was found to be a common problem of those cases in which different codes and different flow properties were used in the coupling.

Chapter 3

Mathematical formulation and Numerical Tools - Existing codes

In this Chapter 3 the main features of the two existing codes are detailed. They will be referred as "compressible density-based solver" (C-DBS) and "incompressible/low Mach number pressure-based solver" (ILM-PBS), reflecting the main differences of the two solvers.

3.1 Governing equations

The Navier-Stokes partial differential equations describe the conservation of mass, momentum and energy in a continuum fluid. A general representation for multispecies reacting flows is:

$$\frac{\partial \rho}{\partial t} + \frac{\partial (\rho u_j)}{\partial x_j} = 0 \tag{3.1}$$

$$\frac{\partial (\rho u_i)}{\partial t} + \frac{\partial (\rho u_j u_i)}{\partial x_j} = -\frac{\partial p}{\partial x_i} + \frac{\partial \boldsymbol{\tau}_{ij}}{\partial x_j} + \rho \sum_{k=1}^{N} Y_k f_{k,i} \tag{3.2}$$

$$\frac{\partial(\rho e_0)}{\partial t} + \frac{\partial((\rho e_0 + p)u_j)}{\partial x_j} = -\frac{\partial q_j}{\partial x_j} + \frac{\partial(\boldsymbol{\tau}_{ij} u_i)}{\partial x_j} + \rho \sum_{k=1}^{N} Y_k f_{k,j}(u_j + V_{k,j}) + \dot{\omega} + \dot{Q} \quad (3.3)$$

Conservation equations for each species read:

$$\frac{\partial(\rho Y_k)}{\partial t} + \frac{\partial(\rho(u_j + V_{k,j})Y_k)}{\partial x_j} = \dot{\omega_k} \quad (3.4)$$

N is the number of species, Y_k the mass fraction of species k and V_k the velocity diffusion of species k, f_j represents the volume forces. q_j is the heat flux due to diffusion of species with different enthalpies and to temperature gradients.

$$q_j = -\lambda \frac{\partial T}{\partial x_j} + \rho \sum_{k=1}^{N} h_k Y_k V_{k,j} \quad (3.5)$$

λ is the coefficient of thermal conductivity $\lambda = \frac{C_p \mu}{Pr}$, where Pr is the Prandtl number, μ the molecular viscosity and C_p the specific heat at constant pressure.

In Eqs. 3.4 and 3.5 the effect of diffusion velocity is usually modelled:

$$\rho V_k Y_k = -\rho D_k \frac{\partial Y_k}{\partial x_j} \quad (3.6)$$

where D_k is a diffusion coefficient for the species k with respect to the rest of the mixture.

$\dot{Q}$ is the heat due to external sources while $\dot{\omega}$ is the heat release due to the combustion process:

$$\dot{\omega} = -\sum_{k=1}^{N} \Delta h^0_{f,k} \dot{\omega_k} \quad (3.7)$$

where $\Delta h^0_{f,k}$ is the formation enthalpy of species k and $\dot{\omega_k}$ is a measure of the change of mass of the species k due to reaction

$$\dot{\omega_k} = M_k \dot{q_k} \quad (3.8)$$

M_k is the molar mass of species k and $\dot{q}_k$ is the production rate of species k.

The viscous stress tensor $\boldsymbol{\tau}_{ij}$ is calculated by:

$$\boldsymbol{\tau}_{ij} = \mu\Big(\frac{\partial u_i}{\partial x_j} + \frac{\partial u_j}{\partial x_i}\Big) + \mu^v \frac{\partial u_m}{\partial x_m}\delta_{ij} \tag{3.9}$$

where δ_{ij} is the Kronecker delta and μ^v is the bulk viscosity, defined under the Stokes hypothesis as

$$\mu^v = -\frac{2}{3}\mu \tag{3.10}$$

In Eq. 3.3, e_0 is the total specific sensible energy

$$e_0 = e + \frac{1}{2}u_i u_i \tag{3.11}$$

sum of the specific internal sensible energy e and the kinetic energy. There are multiple forms for the energy conservation equation, which can alternatively be expressed in terms of specific internal sensible energy e, specific sensible enthalpy h or total specific sensible enthalpy h_0. Even if they consist of simple rearrangements of Eq. 3.3 (and Eq. 3.2), we shall report them for completeness in the following, since the two codes solve a different version of this conservation equation. Omitting the contribution of volume forces, the conservation equation for the specific sensible energy, specific sensible enthalpy and total specific sensible enthalpy read respectively:

$$\frac{\partial(\rho e)}{\partial t} + \frac{\partial(\rho u_j e)}{\partial x_j} = -p\frac{\partial u_j}{\partial x_j} - \frac{\partial q_j}{\partial x_j} + \boldsymbol{\tau}_{ij}\frac{\partial u_i}{\partial x_j} + \dot{\omega} + \dot{Q} \tag{3.12}$$

$$\frac{\partial(\rho h)}{\partial t} + \frac{\partial(\rho u_j h)}{\partial x_j} = \frac{\partial p}{\partial t} + u_j\frac{\partial p}{\partial x_j} - \frac{\partial q_j}{\partial x_j} + \boldsymbol{\tau}_{ij}\frac{\partial u_i}{\partial x_j} + \dot{\omega} + \dot{Q} \tag{3.13}$$

$$\frac{\partial(\rho h_0)}{\partial t} + \frac{\partial(\rho u_j h_0)}{\partial x_j} = \frac{\partial p}{\partial t} - \frac{\partial q_j}{\partial x_j} + \frac{\partial(u_i\boldsymbol{\tau}_{ij})}{\partial x_j} + \dot{\omega} + \dot{Q} \tag{3.14}$$

Compressible - Density Based Solver

The code deals with compressible flows. The mass conservation Eq. 3.1 is a transport equation for the density. The pressure is specified by a thermodynamic relation (either for ideal or real gas). In case of an ideal gas:

$$p = \rho R T \tag{3.15}$$

where R is the specific gas constant and T the temperature.

The code does not model reactive flows. If the flow is assumed to behave as frozen chemistry, the term $\dot{\omega}$ in Eq. 3.3 nullify (no reaction $\dot{\omega}_k = 0$ in Eq. 3.4). Neglecting body forces and heat from external sources Eq. 3.3 becomes

$$\frac{\partial(\rho e_0)}{\partial t} + \frac{\partial((\rho e_0 + p)u_j)}{\partial x_j} = \frac{\partial}{\partial x_j}\Big(\lambda \frac{\partial T}{\partial x_j} - \rho \sum_{k=1}^{N} h_k Y_k V_{k,j}\Big) + \frac{\partial(u_i \boldsymbol{\tau}_{ij})}{\partial x_j} \tag{3.16}$$

where for thermally perfect gases the relation between temperature and specific internal sensible energy and specific sensible enthalpy is

$$e = \sum_{k=1}^{N} Y_k \int_{T_0}^{T} C_{v,k}(T)dT - RT_0 \qquad h = e + \frac{p}{\rho} = \sum_{k=1}^{N} Y_k \int_{T_0}^{T} C_{p,k}(T)dT \tag{3.17}$$

It is important to note that e and h are sensible energy and enthalpy. The contribution of the formation chemical enthalpy is not included in their definition, but it is taken into account separately in the term $\dot{\omega}$ (the heat due to reaction, null for frozen chemistry). The enthalpy diffusion due to different species is modelled.

If the flow is also assumed to behave as a single species calorically perfect gas, which is the default assumption in the code, the energy equation reads

$$\frac{\partial}{\partial t}\Big(\rho(C_v T + \frac{1}{2}u_i u_i)\Big) + \frac{\partial}{\partial x_j}\Big(\rho(C_p T + \frac{1}{2}u_i u_i)u_j\Big) = \frac{\partial}{\partial x_j}\Big(\lambda \frac{\partial T}{\partial x_j}\Big) + \frac{\partial(u_i \boldsymbol{\tau}_{ij})}{\partial x_j} \tag{3.18}$$

The equations in the density-based code are non-dimensionalised using the variables:

$$x^* = \frac{x}{L_R}, \qquad y^* = \frac{y}{L_R}, \qquad z^* = \frac{z}{L_R}, \qquad t^* = \frac{tU_R}{L_R}$$
$$u^* = \frac{u}{U_R}, \qquad , v^* = \frac{v}{U_R}, \qquad , w^* = \frac{w}{U_R}, \qquad \mu^* = \frac{\mu}{\rho_R U_R L_R}$$
$$\rho^* = \frac{\rho}{\rho_R}, \qquad p^* = \frac{p}{p_R}, \qquad T^* = \frac{T}{T_R}, \qquad h^* = \frac{h}{R_R T_R}$$

where the reference values are chosen to be $L_R = 1\ m$, $\rho_R = 1.226\ Kg/m^3$, $p_R = 101300\ Pa$, $T_R = 288\ K$, $U_R = \sqrt{\frac{p_R}{\rho_R}} = 9\ m/s$, $R_R = \frac{P_R}{\rho_R T_R} = 286.9\ \frac{kJ}{kgK}$.

Incompressible/Low Mach number - Pressure Based Solver

The code deals with incompressible and low Mach number flows. Some considerations on a low Mach number asymptotic analysis are reported in the following Sec. 4.1 and can be found in [101]. The main characteristic of these type of flows is that the pressure appearing in the momentum equations is decoupled from density and temperature fluctuations arising through the equation of state (in particular $\frac{d\rho}{dp} = \frac{\gamma}{c^2} = 0$, $c^2 \to \infty$, where c is the speed of sound). Therefore all the acoustic waves are removed from the equations. While for incompressible flows the density is constant along a pathline and consequently the velocity is required to be divergence free ($\frac{\partial u_j}{\partial x_j} = 0$), in the low Mach number approximation the density can vary (e.g. $\rho = \rho(T)$) and the divergence of velocity is a function of the heat release rate in the domain (heat conduction and heat release due to combustion and external sources) and of the time derivative of p_{therm}, the thermodynamic background pressure. $p_{therm}(t)$ can vary in time due to compression from the boundaries and to the heat release rate in the domain. If the domain is unbounded this pressure is no more a function of time but has to be defined as a known constant value ($p_{therm} = const$). In the rest of this work we will refer to it also as the "reference pressure" (as it is defined in the ILM-PBS code). The velocity divergence would be function of the heat release rate only. While in the incompressible assumption only small density variations are allowed (the velocity field is required to be divergence free and the density is constant along a streamline, or constant everywhere for homogeneous flows), the low Mach number approximation admits large density and temperature variations. These variations couple the momentum and energy equation (e.g. through density $\rho(T) = \frac{p_{therm}}{RT}$ and viscosity $\mu(T)$), while the energy equation results decoupled

from continuity and momentum equations in the case of an incompressible flow. Consequently the so called "incompressible" pressure p, the one appearing in the momentum equations for incompressible and low Mach approximations, is not specified from the density by a thermodynamic relation, but it is determined by the constraint on the divergence of velocity. Since there is no separate equation for the pressure, the typical solution to this problem is to build a new equation for the pressure from the continuity and momentum equations. The idea is to obtain a pressure field which guarantees satisfaction of the mass conservation. Taking the divergence of the momentum equation Eq. 3.2

$$\frac{\partial}{\partial x_i}\left(\frac{\partial p}{\partial x_i}\right) = -\frac{\partial}{\partial x_i}\left[\frac{\partial(\rho u_i)}{\partial t} + \frac{\partial(\rho u_j u_i)}{\partial x_j} - \frac{\partial \boldsymbol{\tau}_{ij}}{\partial x_j} - \rho\sum_{k=1}^{N} Y_k f_{k,j}\right] \tag{3.19}$$

and simplifying using the continuity equation Eq. 3.1 a Poisson equation for pressure is obtained

$$\frac{\partial}{\partial x_i}\left(\frac{\partial p}{\partial x_i}\right) = \frac{\partial^2 \rho}{\partial t^2} - \frac{\partial}{\partial x_i}\left[\frac{\partial(\rho u_j u_i)}{\partial x_j} - \frac{\partial \boldsymbol{\tau}_{ij}}{\partial x_j} - \rho\sum_{k=1}^{N} Y_k f_{k,j}\right] \tag{3.20}$$

which can be further simplified for the case of constant density and constant viscosity. The numerical implementation does often also introduce further simplifications (see the SIMPLE scheme [102]). As only gradients of pressure appear in the equations, the hydrodynamic pressure p is determined only up to a constant (gauge pressure).

The energy equation being solved in the code is the equation for the specific enthalpy (Eq. 3.13). A major difference between the ILM-PBS code and the C-DBS code stands in the form of the energy/enthalpy being considered. While in Eqs. 3.3, 3.12-3.14 and in C-DBS code (Sec. 3.1) we always dealt with sensible energy/enthalpy, the pressure-based code considers the full enthalpy, sum of the sensible and the chemical formation enthalpy. We will use a capital letter to distinguish it from its sensible part.

$$H = h + \sum_{k=1}^{N} Y_k \Delta h^0_{f,k} \qquad E = e + \sum_{k=1}^{N} Y_k \Delta h^0_{f,k} \tag{3.21}$$

$$H_0 = H + \frac{1}{2} u_i u_i \qquad E_0 = E + \frac{1}{2} u_i u_i \tag{3.22}$$

H will be the specific enthalpy, E the specific energy, H_0 and E_0 the total specific enthalpy and total specific energy. Eqs. 3.3 and 3.12-3.14 can be rewritten in function of E_0, E, H, H_0 so that the term $\dot{\omega}$ will be included in their definition, obtaining for Eq. 3.13:

$$\frac{\partial(\rho H)}{\partial t} + \frac{\partial(\rho u_j H)}{\partial x_j} = \frac{\partial p}{\partial t} + u_j \frac{\partial p}{\partial x_j} - \frac{\partial Q_j}{\partial x_j} + \boldsymbol{\tau}_{ij} \frac{\partial u_i}{\partial x_j} + \dot{Q} \tag{3.23}$$

where the heat flux Q_j has been rewritten in capital letters to account for the contribution of the formation enthalpy. Using the relation $dH = C_p dT + \sum_{k=1}^{N} H_k dY_k$ the temperature gradients can be rewritten in terms of enthalpy and species concentrations gradients, and under the assumption of single diffusion coefficient D, an expression for Q_j is obtained:

$$Q_j = -\Big[\frac{\mu}{Pr}\frac{\partial H}{\partial x_j} + \frac{\mu}{Pr}\Big(\frac{1}{Le_k} - 1\Big)\sum_{k=1}^{N} H_k \frac{\partial Y_k}{\partial x_j}\Big] \tag{3.24}$$

where $Le = \frac{\lambda}{\rho C_p D}$ is the Lewis number.

From a non-dimensional analysis of Eq. 3.23 it can be seen that for low-speed flow the terms $\frac{\partial p}{\partial t} + u_j \frac{\partial p}{\partial x_j}$ and $\boldsymbol{\tau}_{ij} \frac{\partial u_i}{\partial x_j}$ can be neglected. Moreover under the assumption of unity Lewis number and single diffusion coefficient the enthalpy equation takes the form of a scalar transport equation with a transient, convective, diffusive and source term:

$$\frac{\partial(\rho H)}{\partial t} + \frac{\partial(\rho u_j H)}{\partial x_j} - \frac{\partial}{\partial x_j}\Big(\frac{\mu}{Pr}\frac{\partial H}{\partial x_j}\Big) = \dot{Q} \tag{3.25}$$

which is the formulation solved by the ILM-PBS code when an equation for the energy is needed. The ILM-PBS code deals with dimensional variables.

3.2 Turbulent flows

Flows in turbomachinery, as most of the flows in nature, are turbulent. A turbulent flow appears as chaotic and all the variables in the flow are subject to stochastic fluctuations. The flow is characterised by turbulent structures, so called “eddies”, of different length

and time scales. For a reference on turbulence and turbulent flows see [103]. A very brief explanation on how CFD engineers approach turbulent flows has already been reported previously in this work, but we shall recall that three main strategies are possible:

[I] DNS: all the scales of turbulence are resolved. A numerical computation requires extremely fine meshes and it is unfeasible for practical real life scale engineering problems.

[II] LES: the main large scale turbulent fluctuations are captured by the computation, while only the smallest isotropic scales of turbulence need to be modelled. LES simulations are still computationally very expensive, in particular for wall resolved high Re flows, but they are becoming more and more common as they provide a much deeper insight into the flow unsteady behaviour

[III] RANS: the computationally cheapest method, the Reynolds-Averaged-Navier--Stokes approach involves a decomposition of each variable into a mean and a fluctuating component. A time average of the unsteady flow is performed, and only the mean flow is resolved, while the effect of the turbulent fluctuations is modelled. Since all the scales of turbulence are involved in the modelling, the models are highly intrusive and different models can produce quite different results. RANS is a very well known and consolidated technique, and constitute the current industrial practice. It has been extended to unsteady simulations (URANS) in which only the very big unsteady structures are captured while the majority of the turbulence is modelled using RANS approach (see Sec. 2.1.1).

Considering the last and most common approach, RANS, which is the one adopted in this work, we shall report a few implications of the averaging process involved. The Reynold time averaging of the variable ϕ reads:

$$\phi = \bar{\phi} + \phi'$$

$$\bar{\phi} = \lim_{\Delta t \to \infty} \frac{1}{\Delta t} \int_{t_0}^{t_0+\Delta t} \phi(t) dt$$

When Reynolds' time averaging is applied to variable density flows, additional terms appear in the equations which involve correlations containing density fluctuations. These term are very difficult to be modelled. A new averaging process, density weighted, has been proposed by Favre to solve this issue, for the terms involving density fluctuations [104]. The Favre-Averaging reads:

$$\phi = \tilde{\phi} + \phi''$$

$$\tilde{\phi} = \frac{1}{\bar{\rho}} \lim_{\Delta t \to \infty} \frac{1}{\Delta t} \int_{t_0}^{t_0+\Delta t} \rho(t)\phi(t)dt$$

and it is related to Reynolds' averaging by:

$$\tilde{\phi} = \frac{\overline{\rho\phi}}{\bar{\rho}}$$

Favre-Averaged Eqs. 3.1 and 3.2 become:

$$\frac{\partial \bar{\rho}}{\partial t} + \frac{\partial(\bar{\rho}\tilde{u}_j)}{\partial x_j} = 0 \tag{3.26}$$

$$\frac{\partial(\bar{\rho}\tilde{u}_i)}{\partial t} + \frac{\partial(\bar{\rho}\tilde{u}_j\tilde{u}_i)}{\partial x_j} + \frac{\partial(\overline{\rho u_j'' u_i''})}{\partial x_j} = -\frac{\partial \bar{p}}{\partial x_i} + \frac{\partial \bar{\boldsymbol{\tau}}_{ij}}{\partial x_j} + \overline{\rho \sum_{k=1}^{N} Y_k f_{k,i}} \tag{3.27}$$

Rewriting Eq. 3.3 in terms of total energy E_0 and Favre-averaging we obtain:

$$\begin{aligned}\frac{\partial(\bar{\rho}\tilde{E}_0)}{\partial t} + \frac{\partial(\bar{\rho}\tilde{H}_0\tilde{u}_j)}{\partial x_j} = &-\frac{\partial \bar{Q}_j}{\partial x_j} + \frac{\partial[\tilde{u}_i(\bar{\boldsymbol{\tau}}_{ij} - \widetilde{\bar{\rho}u_j''u_i''})]}{\partial x_j} + \\ &\overline{\frac{\partial}{\partial x_j}(-\widetilde{\bar{\rho}u_j''H''} + \overline{u_i''\boldsymbol{\tau}_{ij}} + \frac{1}{2}\widetilde{\bar{\rho}u_j''u_i''u_i''}) + \rho\sum_{k=1}^{N} Y_k f_{k,j}(u_j + V_{k,j}) + \dot{Q}}\end{aligned} \tag{3.28}$$

where $\bar{\rho}\tilde{E}_0$ and $\bar{\rho}\tilde{H}_0$ are defined such that:

$$\bar{\rho}\tilde{E}_0 = \bar{\rho}\tilde{E} + \bar{\rho}\frac{1}{2}\tilde{u}_i\tilde{u}_i + \bar{\rho}k$$

and $k = \frac{1}{2}(\widetilde{u_i'' u_i''})$ is the kinetic energy associated with the turbulence.

In $\bar{\boldsymbol{\tau}}_{ij}$ and $\bar{Q}_j$ the additional terms arising from the fluctuations of the molecular properties are in general neglected so that:

$$\overline{\mu\frac{\partial T}{\partial x_j}} = \bar{\rho}\tilde{\nu}\frac{\partial \tilde{T}}{\partial x_j} = \bar{\mu}\frac{\partial \tilde{T}}{\partial x_j}$$

$$\bar{\boldsymbol{\tau}}_{ij} = \bar{\mu}\Big(\frac{\partial \tilde{u}_i}{\partial x_j} + \frac{\partial \tilde{u}_j}{\partial x_i}\Big) - \frac{2}{3}\bar{\mu}\frac{\partial \tilde{u}_m}{\partial x_m}\delta_{ij}$$

The term $\bar{\rho}\widetilde{u_j'' u_i''} = \overline{\rho u_j'' u_i''}$ appearing in the momentum and energy equation is called the Favre-averaged turbulent stress tensor. In the most accurate and most computationally expensive approach, the Reynold Stress Modelling (RSM), a transport equation is solved for each component of the turbulent stress tensor. A simpler approach consists in defining:

$$-\bar{\rho}\widetilde{u_j'' u_i''} = \mu_T\Big[\Big(\frac{\partial \tilde{u}_i}{\partial x_j} + \frac{\partial \tilde{u}_j}{\partial x_i}\Big) - \frac{2}{3}\mu_T\frac{\partial \tilde{u}_m}{\partial x_m}\delta_{ij}\Big] - \frac{2}{3}\bar{\rho}k\delta_{ij} \tag{3.29}$$

where μ_T is an additional viscosity related to the turbulence, called turbulent viscosity. Note that the term $\frac{2}{3}\bar{\rho}k\delta_{ij}$ has been added to correctly recover the trace of the turbulent stress tensor $\bar{\rho}(\widetilde{u''u''} + \widetilde{v''v''} + \widetilde{w''w''})$. μ_T is to be modelled, and a variety of methods have been proposed. They are based on the solution of one, two or more equations and they rely on the definition of a certain number of empirical constants. The most common one-equation model is the Spalart-Allmaras model [105], where a transport equation for the turbulent viscosity is solved. Many two-equations models have been proposed. Generally a transport equation for the turbulent kinetic energy k is solved together with a transport equation for the turbulent dissipation ϵ (or the specific dissipation rate ω). The turbulent viscosity is then defined from these two quantities. The most renowned two-equations models are $k-\epsilon$ [106], $k-\omega$ [104], realizable $k-\epsilon$ [107], RNG [108] and

$k-\omega$ SST [6]. They can all give different results when applied to the same flow as they are generally best adapted to a particular flow situation or feature.

Considering the energy equation Eq. 3.28 the terms $\frac{\partial}{\partial x_j}(-\widetilde{\bar{\rho}u_j''H''} + \overline{u_i''\boldsymbol{\tau}_{ij}} + \frac{1}{2}\widetilde{\bar{\rho}u_j''u_i''u_i''})$ represent the turbulent heat flux, the turbulent viscous work and the turbulent transport of turbulent energy respectively, and they need modelling. However, the second and third terms are generally small (in particular for low-speed flows) and they are often neglected. The turbulent heat flux is generally modelled as:

$$\overline{\rho u_j'' H''} = \widetilde{\bar{\rho}u_j''H} = -\frac{\mu_T}{Pr_T}\frac{\partial \tilde{H}}{\partial x_j} = -\frac{\mu_T C_p}{Pr_T}\frac{\partial \tilde{T}}{\partial x_j}$$

where Pr_T is defined as turbulence Prandtl number and it is generally assumed to be constant.

Species conservation is given by:

$$\frac{\partial(\bar{\rho}\tilde{Y}_k)}{\partial t} + \frac{\partial(\bar{\rho}\tilde{u}_j\tilde{Y}_k)}{\partial x_j} + \frac{\partial(\overline{\rho V_{k,j}Y_k} + \overline{\rho u_j''Y_k''})}{\partial x_j} = \widetilde{\dot{\omega}_k} \tag{3.30}$$

where $\widetilde{\dot{\omega}_k}$ is the Favre-averaged reaction rate and the other terms are modelled as:

$$\overline{\rho V_{k,j}Y_k} = -\bar{\rho}D_k\Big(\frac{\partial \tilde{Y}_k}{\partial x_j} + \overline{\frac{\partial Y_k''}{\partial x_j}}\Big)$$

$$\overline{\rho u_j''Y_k''} = -\frac{\mu_T}{Sc_T}\frac{\partial \tilde{Y}_k}{\partial x_j}$$

and the turbulent Schmidt number defined as $Sc_T = Le_T Pr_T = \frac{\mu_T}{\rho D_k}$.

Compressible - Density Based Solver

With the modelling assumptions reported above, and neglecting the influence of body forces, the momentum equations read

$$\frac{\partial(\bar{\rho}\tilde{u}_i)}{\partial t} + \frac{\partial(\bar{\rho}\tilde{u}_j\tilde{u}_i)}{\partial x_j} = -\frac{\partial \bar{p}_e}{\partial x_i} + \frac{\partial}{\partial x_j}\Big[(\bar{\mu}+\mu_T)\Big(\frac{\partial \tilde{u}_i}{\partial x_j}+\frac{\partial \tilde{u}_j}{\partial x_i}\Big) - \frac{2}{3}(\bar{\mu}+\mu_T)\frac{\partial \tilde{u}_m}{\partial x_m}\delta_{ij}\Big] \tag{3.31}$$

As can be seen the C-DBS code further simplifies the equations merging the pressure $\bar{p}$ with the normal contribution from the turbulence $\frac{2}{3}\bar{\rho}k$, defining an equivalent pressure $\bar{p}_e$

$$\bar{p}_e = \bar{p} + \frac{2}{3}\bar{\rho}k$$

so that the turbulent contribution is never explicitly added to the momentum equations.

An equation for the total sensible energy e_0 in the case of a non reacting flow, neglecting body forces and external heat sources can easily be derived from Eq. 3.28

$$\frac{\partial(\bar{\rho}\tilde{e}_0)}{\partial t} + \frac{\partial(\bar{\rho}\tilde{h}_0\tilde{u}_j)}{\partial x_j} = -\frac{\partial}{\partial x_j}\Big[-\Big(\lambda+\frac{\mu_T C_p}{Pr_T}\Big)\frac{\partial \tilde{T}}{\partial x_j} + \overline{\rho\sum_{k=1}^{N} h_k Y_k V_{k,j}}\Big] + \frac{\partial}{\partial x_j}\Big[\tilde{u}_i\Big\{(\bar{\mu}+\mu_T)\Big(\frac{\partial \tilde{u}_i}{\partial x_j}+\frac{\partial \tilde{u}_j}{\partial x_i}\Big) - \frac{2}{3}(\bar{\mu}+\mu_T)\frac{\partial \tilde{u}_m}{\partial x_m}\delta_{ij}\Big]\Big\} \tag{3.32}$$

where the averaged diffusion of enthalpy due to molecular species is also modelled in case of a multi-species simulation.

Many different turbulence models are available. Among them $k-\epsilon$, $k-\omega$ SST and Spalart-Allmaras. A particular attention is spent in capturing the correct behaviour of the turbulent boundary layer for high-Re number flows, and wall functions can be used.

The turbulence parameters are non-dimensionalised as:

$$k^* = \frac{k}{U_{ref}^2}, \qquad \epsilon^* = \frac{\epsilon}{U_{ref}^3}, \qquad \omega^* = \frac{\omega}{U_{ref}}$$

Incompressible/Low Mach number - Pressure Based Solver

The Favre-averaged momentum equations read

$$\frac{\partial(\bar{\rho}\tilde{u}_i)}{\partial t} + \frac{\partial(\bar{\rho}\tilde{u}_j\tilde{u}_i)}{\partial x_j} = -\frac{\partial \bar{p}}{\partial x_i} - \frac{\partial}{\partial x_j}\Big(\frac{2}{3}\bar{\rho}k\delta_{ij}\Big) + \frac{\partial}{\partial x_j}\Big[(\bar{\mu}+\mu_T)\Big(\frac{\partial \tilde{u}_i}{\partial x_j} + \frac{\partial \tilde{u}_j}{\partial x_i}\Big) - \frac{2}{3}(\bar{\mu}+\mu_T)\frac{\partial \tilde{u}_m}{\partial x_m}\delta_{ij}\Big] + \overline{\rho\sum_{k=1}^{N} Y_k f_{k,i}} \tag{3.33}$$

The main differences with respect to the C-DBS code are:

[I] the contribution of body forces is retained, and can be modelled as $\bar{\rho}\sum_{k=1}^{N}\tilde{Y}_k f_{k,i}$

[II] the term $\frac{2}{3}\bar{\rho}k$ is explicitly retained into the momentum equations and it is not grouped with pressure

An expression for the Favre-averaged equation for the enthalpy H can be obtained directly from Eq. 3.25

$$\frac{\partial(\bar{\rho}\tilde{H})}{\partial t} + \frac{\partial(\bar{\rho}\tilde{u}_j\tilde{H})}{\partial x_j} - \frac{\partial}{\partial x_j}\Big[\Big(\frac{\bar{\mu}}{Pr} + \frac{\mu_T}{Pr_T}\Big)\frac{\partial \tilde{H}}{\partial x_j}\Big] = \overline{\dot{Q}} \tag{3.34}$$

The differences in the energy equation with respect to the C-DBS code are mainly:

[I] solving for enthalpy instead of energy

[II] different form of enthalpy being considered (chemical plus sensible)

[III] reacting case

[IV] $Le = 1$, diffusion of enthalpy due to species diffusion is neglected

[V] work done by stresses is neglected under the assumption of low Mach number flows

3.3 Multispecies and Combustion Modelling

As anticipated, resolving the averaged species conservation equations (Eq. 3.30) is complicated by the presence of the term $\widetilde{\dot{\omega}}_k$ which is difficult to be modelled and to be related to the averaged mass fractions of the species.

By combining the species conservation equations in a linear combination, and remembering that $\dot{\omega}_{OX} = s\dot{\omega}_{FU}$, where s is the stoichiometric oxidizer/fuel mass ratio, transport equations for passive scalars without source terms can be derived (under the assumption of no dissociations and equal diffusion of species). Of particular interest is the already mentioned *mixture fraction* ξ. Assuming a reaction involving two different streams, a fuel FU stream and an AIR stream, the most general definition of mixture fraction is:

$$\xi = \frac{\text{mass of material from fuel stream}}{\text{mass of mixture}} \tag{3.35}$$

An expression for it can be easily drawn as

$$\xi = \frac{[sY_{FU} - Y_{OX}] - [sY_{FU} - Y_{OX}]^{AIR}}{[sY_{FU} - Y_{OX}]^{FU} - [sY_{FU} - Y_{OX}]^{AIR}} \tag{3.36}$$

where the superscript FU and AIR denote the original fuel and air stream respectively. Both fuel and air streams may contain inert species (such as N_2). The mixture fraction is a conserved scalar and it does not depend upon the progress of reaction: ξ does not change if the fuel is fully burned or still completely unburned.

We shall make the following general assumptions:

[I] there is no fuel in the air stream

[II] there is no oxidizer in the fuel stream

The expression for the mixture fraction simplifies to:

$$\xi = \frac{sY_{FU} - Y_{OX} + Y_{OX}^{AIR}}{sY_{FU}^{FU} + Y_{OX}^{AIR}}$$

A particular value of the mixture fraction is important, and it is the stoichiometric mixture fraction (either the case $sY_{FU} = Y_{OX}$ if unburned or $Y_{FU} = Y_{OX} = 0$ if completely burned) :

$$\xi_{st} = \frac{Y_{OX}^{AIR}}{sY_{FU}^{FU} + Y_{OX}^{AIR}}$$

If $0 < \xi < \xi_{st}$ the mixture is said to be LEAN, and after combustion there will be some oxidizer left in the mixture. If $\xi_{st} < \xi < 1$ the mixture is said to be RICH, and after complete combustion some fuel will be left unburned in the mixture.

To make the expression of the mixture fraction more understandable, the mass coming from the fuel stream can always be seen as the sum of the fuel mass and the mass in products Pr that can be associated to the original fuel stream:

$$\xi = Y_{FU} + \Big(\frac{1}{1+s}\Big)Y_{Pr}$$

The idea is to solve a single convection/diffusion transport equation for the mixture fraction ξ, from which all the mass fraction of species can be eventually computed.

The mass of the inert species will always be given by

$$Y_{in} = Y_{in}^{FU}\xi + Y_{in}^{AIR}(1-\xi) \tag{3.37}$$

If the mixture is frozen (no reaction) the fuel and oxidizer are simply transported, and in each point the following holds

$$Y_{FU} = Y_{FU}^{FU}\xi$$
$$Y_{FU} = Y_{OX}^{AIR}(1-\xi)$$

If either all the fuel or the oxidizer are completely consumed, simple expressions can be derived for all the mass fractions in the two cases of lean or rich mixtures.

In a more general case, being the mixture fraction independent of the progress of the combustion process, it is necessary to solve another equation, which can be either a *progress variable* or one of the mass concentrations transport equations (e.g. Y_{FU}), to be able to reconstruct the mixture composition and its properties.

Moreover the interaction between turbulence and combustion has to be modelled, and the variance of the mixture fraction and the progress variable may be needed, depending on the model.

It is important to note that for both the codes two further assumptions are made:

[I] there is only fuel in the fuel stream $Y_{FU}^{FU} = 1$

[II] consequently there are no inert species in the fuel stream $Y_{in}^{FU} = 0$

Compressible - Density Based Solver

The C-DBS code used in this work is not reacting. Nevertheless it can handle the presence of burned fuel [3]. The variable defined in the code is the transported scalar "fuel fraction" $ffrac$, which is the mixture fraction (we recall that $Y_{FU}^{FU} = 1$ and $Y_{in}^{FU} = 0$). It is in fact defined as the mass fraction that originally came from the fuel.

If we define the local fuel to air ratio (FAR) and the air to fuel ratio (AFR) as

$$FAR = \frac{m_{FU}}{m_{AIR}} \qquad AFR = \frac{m_{AIR}}{m_{FU}}$$

where m_{FU} and m_{AIR} are the mass in the mixture that originally came from the fuel and air streams respectively, it is easy to show that:

$$ffrac = \xi = \frac{m_{FU}}{m_{FU} + m_{AIR}} = \frac{1}{1 + AFR} = \frac{FAR}{1 + FAR} \tag{3.38}$$

The local fuel/air equivalence ratio ψ can also be expressed in terms of mixture fraction:

$$\psi = \frac{FAR}{FAR_{st}} = \Big(\frac{\xi}{1-\xi}\Big)\Big(\frac{1-\xi_{st}}{\xi_{st}}\Big) \tag{3.39}$$

Thermo-fluid properties accounts for variation of temperature and mixture composition of the non reactive gaseous combustion product [3]. The gas properties are described using thermodynamic variables which depends on temperature T and fuel to air ratio FAR (e.g. $C_p(T, FAR)$, heat ratio $\gamma(T, FAR)$). It is important to highlight that the code can handle burned fuel only: the mass fraction coming from the fuel stream is considered to be fully converted into products ($Y_{FU} = 0$). This creates severe limitations on the coupling, in which a pure non reacting mixing of fuel with air can not be simulated. Moreover we shall make sure the combustion processes are completed in the combustor and there is no unburned fuel entering the turbine. Another drawback of the assumption $Y_{FU} = 0$ is to limit the range of mixture fraction to lean mixtures where $\xi \leq \xi_{st}$, and this can create localised problems and unusual behaviour if in some location $\xi > \xi_{st}$ occurs.

Incompressible/Low Mach number - Pressure Based Solver

In the pressure-based code five different combustion models are implemented, which combine different chemistry and combustion-turbulence interaction modelling. The number of species conservation equations (Eq. 3.30) to be solved depends on the model.

A brief insight into combustion modelling is given in Sec 2.1.2. We are not entering any details of the models, which can be found in literature. The list is:

[I] Eddy Break-Up (EBU) [109] model with a two-step reaction mechanism [50, 110]

[II] Flamelet Generated Manifold (FGM) [111] model with a presumed Probability Density Function (PDF) [112]

[III] Conserved Scalar Model (CSM) with a presumed PDF

[IV] Bray-Moss-Libby (BML) [113] model with FGM

[V] Transport Probability Density Function (TPDF) [114]

Soot and NOx formation modelling, as well as spray modelling are also provided. The combustion process in this work has been modelled using an EBU model. In particular it consists of a Hybrid Eddy Dissipation approach with a two step reaction mechanism,

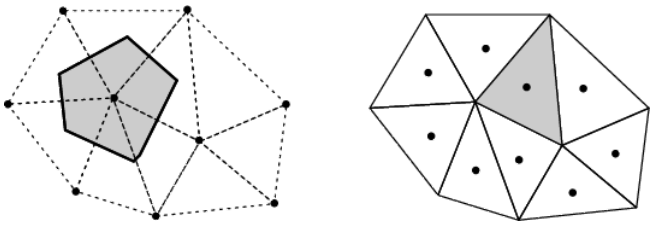

FIGURE 3.1: Comparison between vertex-centred and cell-centred approach in finite volume methods

which was deemed to be relatively simple and yet accurate enough for the purpose of this work.

3.4 Spatial discretisation

In the finite volume method the solution domain is subdivided into control volumes to which the conservation equations are applied. Both the density-based code and the pressure-based code use the finite volume method.

Finite volume methods differ between each other on the way the control volume (CV) is defined:

[I] CELL-CENTERED : the control volume is coincident with the grid cell and the variables are stored at the cell center

[II] VERTEX-CENTERED : the control volume is built around the grid vertices in correspondence of which the variables are stored

[III] CELL-VERTEX : the control volume is coincident with the grid cell but the variables are stored at the grid vertices

In Fig 3.1 the difference between the cell-centred and vertex-centred approach is shown.

In the finite volume method, the integral form of the conservation equation is considered. By using the divergence theorem a general expression for the conserved variable $\rho\phi$ is obtained:

$$\int_V \frac{\partial \rho\phi}{\partial t} dv + \int_{\partial V} [F_I(\rho\phi, \mathbf{n}) + F_V(\rho\phi, \frac{\partial \rho\phi}{\partial x_j}, \mathbf{n})] dS = \int_V S_\phi dv \tag{3.40}$$

This expression holds for both the entire domain and for each single control volume CV. The integration space V can be either seen as the domain volume or the volume of each single CV, and ∂V is the surface bounding it. F_I and F_V are the inviscid and viscous fluxes in the direction of the vector $\mathbf{n}$ normal to the surface boundary.

All the terms in Eq. 3.40 are discretised and the conservation applied to each single control volume.

Compressible - Density Based Solver

The C-DBS code was designed to work on unstructured hybrid meshes. Data are stored at the cell vertices and dual control volumes are defined around each vertex, applying a vertex-centred approach. Integration of the fluxes through the control volume surface is approximated by using pre-computed weights for each edge [115]. A second order accurate scheme is achieved by casting the flux formulation in an artificial dissipation type scheme along the edges that utilises a pseudo Laplacian operator evaluated in each median dual control volume [116]. The inviscid flux discretisation is based on a flux-differencing scheme with Jameson's eigen scaling method [117], which combines the central differencing of the nonlinear inviscid flux with a smoothing flux based on one-dimensional characteristic variables. The viscous flux is approximated half-way along each edge, where the existing edge weights are used to approximate the flow variables gradients.

Incompressible/Low Mach number - Pressure Based Solver

The ILM-PBS code uses a collocated cell-centred approach for unstructured grids [21]. The variables are stored at control volume centres. The fluxes are split into an inviscid convective term and a viscous diffusive term. To evaluate the convective term many convection schemes are available. The ones used for this work are: second-order accurate linear upwinding is used to discretise velocities, a first-order accurate upwinding for the turbulence variables and a second-order central differencing (linear interpolation) for the pressure. All the second-order accurate schemes are implemented following a deferred correction scheme [21]. The viscous dissipative term is evaluated using the method of Mathur and Murthy [118].

3.5 Solution method

Many different solution methods of the discretised form of partial differential equations have been developed in the past and applied to fluid dynamic problems. Some of them have been developed specifically for CFD problems. For an introduction on numerical methods for CFD refer to [21].

Compressible - Density Based Solver

For a steady simulation the discrete equations are iterated time-marching the solution towards steady-state using a five stage Runge-Kutta scheme [119]. A block-Jacobi preconditioner [116] combined with a multigrid method are used to damp all the error modes and accelerate the convergence [120, 121]. An implicit dual time stepping is used for the unsteady solver [122], where at each implicit time step a pseudo-unsteady term is introduced and the solution is time-marched using pseudo-timesteps towards convergence to the next physical time using the same steady multigrid solver. The code is fully parallel with high parallel performance [123].

Incompressible/Low Mach number - Pressure Based Solver

The SIMPLE [102] pressure correction approach for incompressible flows is adopted, and the method of Rhie and Chow [124] is used to avoid pressure-velocity decoupling. In case of an unsteady simulation the transient term in Eq. 3.40 is calculated combining two implicit time schemes with a blending factor [21]. The first-order Euler scheme and the second-order three level scheme are recovered when the default delimiting values for the blending factor are used.
The code is parallelised using MPI.

3.6 Rolls-Royce "In-House" Flow Solvers

The two ILM-PBS and C-DBS solvers used for this work are the in-house Rolls-Royce solvers "Hydra"(C-DBS) and "PRECISE-UNS"(ILM-PBS). Hydra is devoted to turbomachinery applications while PRECISE-UNS to combustion simulations. In Tab. 3.1

Hydra (C-DBS)	**PRECISE-UNS(ILM-PBS)**
fully compressible low Mach preconditioning	low Mach incompressible
density-based	pressure-based
Explicit Runge-Kutta 5-stage Multigrid acceleration	Implicit
(U)RANS, LES	(U)RANS, LES
vertex-centered	cell-centered
scalar transport mixture fraction variable heat ratio	combustion models: EBU, FGM, PDF BML, CSM

TABLE 3.1: Rolls-Royce in-house flow solvers

their main features are summarized. As it is shown in the table, the two solvers are very different and they reflect the considerations made in the previous Sec. 2.1.

3.7 Summary

The details of the codes reported above show that there are many differences between them. The main ones, that are particularly important for the coupling, are:

[I] different equations being solved (e.g. definition of energy as sensible (C-DBS) or sensible plus chemical (ILM-PBS)) with different modelling assumptions and simplifications applied (e.g. turbulent contribution to pressure included in the pressure term (C-DBS) or not included (ILM-PBS))

[II] compressible (C-DBS) and incompressible/low Mach number (ILM-PBS) approximations, with consequent different definition of pressure

[III] different gas properties; non-reacting (C-DBS) and reacting (ILM-PBS)

[IV] density based (C-DBS) and pressure based (ILM-PBS)

[V] vertex-centred (C-DBS) and cell-centred (ILM-PBS)

Chapter 4

Combustor-turbine interaction: methodology

In Sec.1.3 we gave a broad definition of "code coupling" and it was shown that a great variety of coupling methodologies can exist, each reflecting the characteristics of its specific application. In turbomachinery applications fluid dynamics can be coupled with heat-conduction in the solid structure, chemical kinetic and radiation in the combustor and acoustics simulations. Coupled fluid-dynamics simulations can be used to predict component interaction. The aim of this work is to pose the basis of this new type of approach for Gas Turbine simulations, and in particular for combustor-turbine interaction predictions. Understanding how the hot flow coming from the combustor can impact on efficiency, stress and life of a turbine could improve the design process to obtain lighter, more efficient and green solutions for future aeronautical propulsion or energy production.

In this Chapter 4, after some conclusions are drawn from theoretical considerations and from the past literature, the coupling methodology developed for combustor-turbine simulations is detailed.

4.1 Low Mach number/compressible solvers coupling

The necessity of coupling incompressible/low Mach number solvers with compressible ones poses a big challenge. In fact two different sets of partial differential equations are

solved in the two domains. An extended analysis of differences and analogies between the two has to be approached if a coupling process needs to be developed. Different low Mach number asymptotic analyses of the Navier-Stokes Equations have been proposed. A review may be found in the VKI Lecture [101].

4.1.1 Low Mach number asymptotic analysis

Asymptotic analyses of the Navier-Stokes equations demonstrate the possibility of obtaining the low Mach number and incompressible equations from their compressible counterpart, in the limit of zero Mach number [125]. A single time and space scale decomposition is used to obtain the low Mach number equations. Multiple time or space scale decomposition can be used to obtain intermediate equations, in which acoustic effects are retained. In such cases an additional averaging process is necessary to obtain the low Mach number equations. We shall briefly resume one of the analysis proposed in the literature.

The asymptotic analysis of Müller [126] starts from the compressible Navier-Stokes set of equations and after defining an appropriate non-dimensionalisation it proceeds with a multiple time scale and single space scale asymptotic decomposition, obtaining then intermediate equation in which acoustic effects are retained. All flow variables are expanded in power series of a non-dimensional Mach number $\tilde{M} = \frac{u_{ref}}{\sqrt{p_{therm}/\rho_{ref}}}$:

$$p(\mathbf{x}, t, \tau, \tilde{M}) = p_{(0)}(\mathbf{x}, t, \tau) + \tilde{M} p_{(1)}(\mathbf{x}, t, \tau) + \tilde{M}^2 p_{(2)}(\mathbf{x}, t, \tau) + O(\tilde{M}^3) \tag{4.1}$$

where t and τ are the flow and acoustic time scale respectively. The pressure split into a sum of a large global thermodynamic pressure $p_{(0)}$, a small acoustic pressure $\tilde{M} p_{(1)}$ and the very small pressure $\tilde{M}^2 p_{(2)}$ defined "incompressible" (determined in a similar way as in incompressible flows). By retaining the acoustic time scale explicitly in this formulation, these intermediate equations obtained in the zero Mach number limit, contrary to the traditional low Mach number equations (in which acoustic affects are removed), take into account acoustic effects.

The leading, first- and second-order continuity equations are:

$$\frac{\partial \rho_{(0)}}{\partial \tau} = 0 \tag{4.2}$$

$$\frac{\partial \rho_{(1)}}{\partial \tau} + \frac{\partial \rho_{(0)}}{\partial t} + \nabla \cdot (\rho \mathbf{u})_{(0)} = 0 \tag{4.3}$$

$$\frac{\partial \rho_{(2)}}{\partial \tau} + \frac{\partial \rho_{(1)}}{\partial t} + \nabla \cdot (\rho \mathbf{u})_{(1)} = 0 \tag{4.4}$$

The leading, first- and second-order momentum equations are:

$$\nabla p_{(0)} = 0 \tag{4.5}$$

$$\frac{\partial (\rho \mathbf{u})_{(0)}}{\partial \tau} + \nabla p_{(1)} = 0 \tag{4.6}$$

$$\frac{\partial (\rho \mathbf{u})_{(1)}}{\partial \tau} + \frac{\partial (\rho \mathbf{u})_{(0)}}{\partial t} + \nabla \cdot (\rho \mathbf{u}\mathbf{u})_{(0)} + \nabla p_{(2)} = \mathbf{G}_{(0)} \tag{4.7}$$

The leading, first- and second-order energy equations are:

$$\frac{\partial (\rho E)_{(0)}}{\partial \tau} = 0 \tag{4.8}$$

$$\frac{\partial (\rho E)_{(1)}}{\partial \tau} + \frac{\partial (\rho E)_{(0)}}{\partial t} + \nabla \cdot (\rho H \mathbf{u})_{(0)} = Q_{(0)} \tag{4.9}$$

$$\frac{\partial (\rho E)_{(2)}}{\partial \tau} + \frac{\partial (\rho E)_{(1)}}{\partial t} + \nabla \cdot (\rho H \mathbf{u})_{(1)} = Q_{(1)} \tag{4.10}$$

The analysis of Müller identifies how the heat release rate and heat conduction affect the global thermodynamic pressure $p_{(0)}$, the divergence of velocity and the material change of density. Moreover the dominant source of sound in low Mach number flows is found to be the acoustic time change of the heat release rate.

The above reported flow equations are then averaged over an acoustic wave period, and the proper low Mach number equations, in a non-dimensional form, are obtained. As previously mentioned these can be obtained directly with a single time and space asymptotic analysis of the Navier-Stokes equations. The overbar denotes acoustitc time averaging.

$$\frac{\partial \rho_{(0)}}{\partial t} + \nabla \cdot (\rho \bar{\mathbf{u}})_{(0)} = 0 \tag{4.11}$$

$$\frac{\partial \rho_{(0)} \mathbf{u}_{(0)}}{\partial t} + \nabla \cdot (\rho_{(0)} \bar{\mathbf{u}}_{(0)} \bar{\mathbf{u}}_{(0)}) + \nabla \bar{p}_{(2)} = \bar{\mathbf{G}}_{(0)} \tag{4.12}$$

$$\frac{\gamma}{\gamma - 1} \rho_{(0)} \big(\frac{\partial T_{(0)}}{\partial t} + \bar{\mathbf{u}}_{(0)} \cdot \nabla T_{(0)} \big) - \frac{dp_{(0)}}{dt} = \bar{Q}_{(0)} \tag{4.13}$$

where the subscript "(0)" stands for zeroth-order in the $\tilde{M}$ series expansion and the overbar denotes the averaging over the acoustic time period, $Q_{(0)}$ is the zeroth-order heat conduction and heat release rate and $\mathbf{G}_{(0)}$ retains viscous and buoyancy effects. In the low Mach number approximation the acoustics do not play any role. The pressure is split into a global thermodynamic pressure $p_{(0)}$, constant in space but free to vary in time, and again an "incompressible" pressure $\tilde{M}^2 p_{(2)}$ that only appears in the momentum equation. Density and temperature are not affected by the variation of the "incompressible" pressure, since they are related by the equation of state to the global thermodynamic pressure. The global thermodynamic pressure may vary in time due to nonzero volume flow and nonzero net heat conduction and heat release rate in the domain. It is shown how an evolution equation for $p_{(0)}$ may be integrated to determine the global thermodynamic pressure starting from an initial condition $p_{(0)}(0)$:

$$\frac{dp_{(0)}}{dt} \int_V dV + \gamma p_{(0)} \int_{\partial V} \mathbf{u}_{(0)} \cdot \mathbf{n} dA = (\gamma - 1) \int_V Q_{(0)} dV \tag{4.14}$$

The divergence of the velocity is in general not zero but it depends on the time change of $p_{(0)}$ and on heat conduction and heat release rate.

$$\nabla \cdot \mathbf{u}_{(0)} = \frac{\gamma - 1}{\gamma p_{(0)}} Q_{(0)} - \frac{1}{\gamma p_{(0)}} \frac{dp_{(0)}}{dt} \tag{4.15}$$

The low Mach number equations can admit large density and temperature variations, and the density couples momentum and energy equations via the equation of state:

$$p_{(0)}(t) = \rho_{(0)}(\mathbf{x}, t) T_{(0)}(\mathbf{x}, t) \tag{4.16}$$

They can be used for combustion calculations [127]. In the case of small density and temperature variation and if $p_{(0)}$ is assumed to be constant the Boussinesq equations can be derived from the low Mach number equations [128], where the momentum equation is coupled to the energy equation by the buoyancy force. Neglecting the buoyancy force means decoupling the momentum and energy equations: the incompressible equations are obtained. The divergence of velocity for Boussinesq and Incompressible flows is zero.

The second-order pressure $p_{(2)}$ is defined in the paper as "incompressible" as it is determined by the momentum equation as the pressure complying with the constraint 4.15 on the velocity-divergence, analogously to incompressible flows.

4.1.2 Review of past literature

In the literature two works are considered by the author of particular interest for the present scope of coupling incompressible/low Mach number solvers with compressible solvers, both of them coming from Stanford University. In 2008 Peet and Lele [129], on the grounds of the analysis proposed by Müller [126], reported and validated an approach to couple compressible with low Mach number/incompressible codes. The procedure is based on partially overlapping domains and on the exchange of interface conditions between the two. Their work was mainly driven by cooling applications [130]. The second work is the previously reported (Sec.2.3) full engine LES/RANS coupling from Schluter et al. [97]. The coupling procedure again relies on the presence of an overlap region between the domains and on the use either of boundary conditions or body forces.

We shall here for sake of simplicity focus only on the case of upstream incompressible/-low Mach number and downstream compressible domains, which is a representative situation for combustor/turbine simulations. The coupling conditions of interest are for the outlet of the upstream domain and the inlet of the downstream domain. In Tab. 4.1 are summarised, through their coupling conditions, the key features of the approaches proposed by the two papers. The superscript ILM and C stand for "Incompressible/Low Mach number" and "Compressible" variables respectively.

The table shows two different degrees of intimacy between the two approaches. A tight coupling is proposed in the first paper, in which direct injection of primitive variables

	Incomp/Low Mach **OUTLET**	**Compressible** **INLET**
[129]	$u^{ILM} = u^C, v^{ILM} = v^C, w^{ILM} = w^C$ $\frac{\partial p_2^{ILM}}{\partial x_n} = \frac{\partial p^C}{\partial x_n}$	$u^{ILM} = u^C, v^{ILM} = v^C, w^{ILM} = w^C$ $\rho^{ILM} = \rho^C, T^{ILM} = T^C$
[97]	Body Force in the momentum eq $\sigma(u^{ILM} - u^C)$	$(\rho u)^{ILM} = (\rho u)^C, (\rho v)^{ILM} = (\rho v)^C,$ $(\rho w)^{ILM} = (\rho w)^C, T^{ILM} = T^C$

TABLE 4.1: Coupling conditions for [129] and [97]

is used. At the upstream domain outlet a Neumann condition is used for the pressure $p_{(2)}$ while a convective outlet is used for temperature (the condition on temperature is not reported on the table). A more relaxed type of coupling is instead assessed in the latter work: proper (not over imposed) boundary conditions are used at the downstream domain inlet, letting some primitive variables to fluctuate to account for the passing of acoustic waves, or a body force is applied in the region of interest for the upstream domain outlet to kindly drive the solution to the desired values.

To the author, the degree of intimacy of the coupling proposed by Peet and Lele is susceptible to problems: with the direct injection of flow variables from incompressible/low Mach number to compressible states at the downstream domain inlet, the specification of temperature T^{ILM} and density ρ^{ILM} is equivalent to the specification of a constant pressure, equivalent to the thermodynamic pressure $p_{(0)}$, at the compressible solver inlet interface, with some possible unpleasant consequences due to waves reflections. The imposition of both velocities and normal pressure gradients at the upstream domain outlet is also too stringent to match the divergence requirements of the velocity flow field in the low Mach number domain. Their paper shows good behaviour for a vortex and a temperature disturbance crossing the low Mach number - compressible interface, and their coupling approach is proven to perform well in the test cases. We consider instead the second paper as a good example of the need for compromise, when dealing with different codes, physics and models.

Another recent paper has been recently published on the coupling of an Euler compressible solver with a Navier-Stokes incompressible solver in a nested grid approach [131], for wind turbine applications. Two different coupling strategies and both one and two ways coupling are assessed. The procedure is applied to incompressible (strictly constant density) solvers and not extended to low Mach number cases. Both methods

proposed do not ensure mass flow conservation between the two domains, and they are not considered as suitable coupling candidates.

In the literature different approaches have also been developed to couple multiphase flow with incompressible-compressible regions (e.g. [132, 133] from University of Stuttgart). In [133] a one-dimensional test case with no mass transfer between the two regions was considered. An analytical solution in the low Mach number region was coupled with the solution of an half-Riemann problem in the compressible side and different procedures on the coupling between pressures in the two regions were assessed. Those cases are less relevant for the current application.

4.1.3 Considerations on the variable "Pressure"

The value of pressure in the low Mach number domain can be defined, according to Müller, by

$$p^{ILM} = p_{(0)}(t) + \tilde{M}^2 p_{(2)}(\mathbf{x}, t) + \mathbf{O}(\tilde{M}^3) \tag{4.17}$$

which is derived from Eq. 4.1 after the removal of the acoustic components. For incompressible/low Mach number applications the Poisson equation (Eq. 3.20) for the second-order pressure $p_{(2)}$ is generally solved using Neumann boundary conditions.

When solving the Poisson equation in the low Mach number domain with a Neumann conditions, $p_{(2)}$ can be calculated only up to an additive function, constant in space, which is not part of the solution. In terms of coupling with a compressible solver the Neumann boundary condition for $p_{(2)}$, as used in [129], is particularly good since it completely avoids the necessity of matching the actual values of pressure on both sides of the coupling. When a value for pressure on the low Mach number domain is to be given, a reference has to be chosen. In many codes, such as the ILM-PBS code used in this work, when using Neumann condition at the outlet for the pressure, a reference has to be chosen at the beginning of the simulation as a point in space where $p_{(2)} = 0$. Hence for unsteady cases, the level of pressure is adapting to the null condition at the reference point at each time step. The authors of [129] instead, with the objective of being able to compare the values of pressure on both domains, they propose to reconstruct the correct pressure level in the low Mach number region given the value of pressure in the compressible solver in one single location within the interpolation region. Essentially the

one local value of pressure taken from the compressible domain fixes the level of pressure at each specific time step, while the gradients in the low Mach number domain are used to reconstruct the whole pressure field. This technique allows for the two pressures to match if needed, and it is said by the authors of [129] to be a possible approach to build interface conditions for the compressible domain based on pressure. Nevertheless, in a more weakly coupled approach as the one proposed in the current work, in which a proper boundary condition based on pressure has to be derived for the compressible domain (e.g. a typical pressure outlet or stagnation pressure inlet), reconstructing the low Mach number domain pressure, and using it in the definition of the compressible domain boundary interface pressure values, from a value taken from the interior solved domain (equivalent to impose only the two dimensional gradients on the boundary plane and extrapolate from the interior the pressure level) produces a not well posed problem.

The first one of the two coupling procedure assessed and proposed in this work (see Sec. 4.3.1.1) uses a quite uncommon Dirichlet condition for pressure at the incompressible/low Mach number domain outlet. The code works in dimensional variables and we will define the "incompressible" pressure as $p_{(2)}^{ILM-PBS}$ to distinguish it from the non dimensional $p_{(2)}$. In general $p_{(2)}^{ILM-PBS}$ is defined only up to a constant, as we previously said, because only the gradients are used in the Poisson equation for pressure. By using Dirichlet conditions at the boundary there is no need any more for any reference point to be specified (the boundary becomes the reference). No points in space in which $p_{(2)}^{ILM-PBS} = 0$ are introduced, which are instead required when usual Neumann conditions are applied. This can be a quite dangerous procedure as $p_{(2)}^{ILM-PBS}$ can take any value, according to the Dirichlet condition applied, and a gauge pressure which is not "small" (with respect to $p_{therm} = p_{(0)}^{ILM-PBS}$) would be a perfectly acceptable solution (only its gradients are required). The coupling with a compressible domain has to take into account the "relativity" of pressure in the incompressible/low Mach number domain if $p_{(2)}^{ILM-PBS}$ is to be used in the definition of boundary conditions for the compressible domain. The pressure $p_{(2)}^{ILM-PBS}$ does not in fact influence the operating condition of the upstream low Mach number domain, but only affects the flow distribution. As a consequence its absolute value should not be used to define the pressure level of the simulation, which should rely instead on $p_{therm} = p_{(0)}^{ILM-PBS}$. The coupling procedure implemented is reported in Sec. 4.3.2.1. We want in this place to remark how a Dirichlet condition for pressure allows to capture the two-dimensional pressure gradients profile at

the outlet boundary surface. No information on the gradients normal to the boundary are provided.

Other components of pressure (e.g. acoustic $p_{(1)}$) are present in the compressible domain, which are not accounted for in the definition of p^{ILM} (Eq. 4.17). Using the pressure in the construction of interface conditions between the two domains can be not only problematic but inherently error prone. Depending on the flow conditions those components of pressure can play a minor or bigger role. As an example using the pressure from the compressible domain to define a boundary condition for the outlet of the incompressible/low Mach number domain can be incorrect, as the pressure profile imposed is in general not consistent with the divergence requirements for the velocity (divergence free in case of incompressible flows). This is particularly problematic when considering unsteady turbomachinery simulations in which waves are travelling back and forth, and they cannot be correctly sustained by the incompressible flow equations, hence they should not be fed back into an "incompressible" combustor. Being said so our $ILM-PBS$ code has shown to be quite robust in handling pressure profiles. Moreover when building a coupling interface for the original existing unmodified $ILM-PBS$ code (Sec. 4.3.1), a pressure boundary condition is the only available choice to feedback information from the turbine back to the combustor. Nevertheless, being aware of the intrinsic differences in the pressure definition between the two fluid physics approximations, a coupling procedure which completely avoids relying on pressure has also been investigated in this work (Sec. 4.3.2).

4.1.4 Weak coupling and properties conservation

As reported above low Mach number and compressible codes solve two different sets of equations [126]: in the former the acoustics is completely removed and the pressure plays the role of a lagrangian multiplier to ensure continuity; the latter instead retains all the flow features while pressure is a thermodynamic variable linked to density through an equation of state. When coupling these two different physical models, attention has to be paid to ensure the interfaces do not produce unphysical behaviours. As an example acoustic waves should be allowed to freely leave the compressible domain at the interface boundary without encountering reflections. The eventual physical reflections occurring

at the combustor interface can not be correctly reproduced due to the incompressible assumption.

The objective is that each domain should have a well-posed set of boundary conditions according to the physical nature of the problem. Only the necessary number of variables should be imposed avoiding over-specification. Since some of the variables are free to adjust themselves to the flow and the solved equations are different, not all the desired quantities might be conserved at the interfaces.

A compromise has to be found in the interface region that allows for the two solutions to be consistent to a good degree, while conserving or making continuous at the interface those physical quantities we are the most interested in for engineering applications. Mass flow conservation is one of the first requirements in fluid machinery. In turbomachinery the stagnation pressure is also a key variable to describe the flow performance, but the different meanings of the pressure in the two solvers, as previously remarked, make its continuity at the interface somehow more problematic. In the end the energy of the fluid should be conserved: due to the different versions of the energy equation being solved (Sec. 3.1) and considering the variable engineers will actually be looking for, ensuring continuity at the interface of the temperature field is the most reasonable approach. In fact the conservation of energy would be really difficult to achieve between the two domains due to the completely different sensible and chemical assumptions adopted for energy, to the different energy equations being solved and to the different gas composition and thermodynamic treatment. In one of the coupling approaches developed in this work and reported later in Sec. 4.3.1 stagnation temperature is used as a coupling variable instead of static temperature as the coupling is required to rely on the original boundary conditions of the existing codes (additional comments on stagnation properties conservation are added in Sec. 4.3.1.1). When this requirement was not applying, such as in the second coupling approach developed in this work and reported in Sec. 4.3.2, we aimed instead at continuity of the static temperature across the coupling interface: typical and commonly used combustion models, such as FGM, directly provide this information through a table. Temperature is hence directly available in the combustor as the most accurate variable to be used in the coupling.

We can imagine an ideal situation, with no discretisation applied, in which at the downstream inlet interface the magnitude of momentum per unit volume $\rho|\mathbf{U}|$ is continuous

between the two domains together with the flow directions, such that the mass crossing the interface in the upstream domain enters the downstream domain without losses, ensuring mass flow conservation. If the local magnitude of momentum per unit volume $\rho|\mathbf{U}|$ is continuous at the interface a simple relation between density and velocities in the two domains can be drawn. In the low Mach number and compressible domains holds respectively

$$\rho^{ILM} = \frac{p_{therm}}{RT} \qquad \rho^{C} = \frac{p}{RT} \tag{4.18}$$

where p is the spatially and temporally variable pressure in the compressible domain and p_{therm} the uniform reference thermodynamic pressure in the low Mach number domain. From which, by imposing $\rho^{ILM}U^{ILM} = \rho^{C}U^{C}$ we obtain

$$\frac{U^{ILM}}{U^{C}} = \frac{\rho^{C}}{\rho^{ILM}} = \frac{p}{p_{therm}} \tag{4.19}$$

While conserving the mass flow, in order to minimise the differences in density and velocities, the difference between pressure in the compressible domain p and p_{therm} should be always bounded in the region close to the interface. The coupling procedure has to be built such that $\frac{|p-p_{therm}|}{p_{therm}}$ is always verified to be small (a value $< 1\%$ could ensure acceptable discontinuities) at the interface. As an example, being p_{therm} of the order of 1 to 3 MPa in a modern combustor simulation, the pressure at the compressible domain inlet should be bounded between $(p_{therm} - 10 \text{ to } 30\ kPa) < p < (p_{therm} + 10 \text{ to } 30\ kPa)$. The value of 1% is only a reference number, and may not always be strictly verified where high pressure gradients are present on the compressible inlet plane.

Mass conservation for combustor/turbine simulations

As presented in the following Sec. 4.3 two coupling procedures have been implemented in this work. To achieve mass conservation between the two domains, two different approaches have been exploited. Looking at a standard turbomachinery simulation, the mass flow is generally a result of an imposed difference in pressure between inlet and outlet boundaries. In a standard combustor simulation instead the mass flow is imposed at the domain inlet and it is not influenced by the outlet conditions. The necessity of obtaining a specific AFR in the combustor makes the massflow imposition at all inlets

a strict requirement. It is improbable to get the same mass that has been imposed at the combustor inlet out of the turbine by coupling standard simulations. In fact, as previously explained, the level of pressure in the low Mach number domain is arbitrary and it does not affect the flow. This arbitrary pressure cannot be used, as it is, to decide the level of pressure at the turbine inlet, which is in turn driving the mass flow across the turbine. As a result, a mass flow boundary condition has to be used for the turbine simulation too, if mass flow conservation has to be achieved. The coupling procedures are based either on the existing boundary conditions or on newly implemented one:

[I] Looking at the original boundary conditions of the existing C-DBS code, mass flow impositions are available to be used either at the inlet or at the exit, which simply automatically rescale the stagnation pressure or static pressure at inlets and exits respectively so as to obtain the desired mass flow. Imposing mass flow at the inlet is an option, but it requires, as explained few lines earlier, the automatically scaled level of pressure at turbine inlet to be consistent with the thermodynamic reference pressure in the combustor. If in fact the obtained static pressure at the inlet boundary is far from the reference pressure in the combustor, inconsistencies in the primitive variables can be observed. Nevertheless, this approach can be easily adopted if the operating conditions and maps of the turbine are well known. Alternatively, and this is the approach exploited in this work, the scaling of pressure at the inlet can be done not through automatic scaling of the existing mass flow boundary condition but through the coupling procedure itself such that the level of pressure at inlet is ensured to be close to p_{therm}, while mass flow is instead imposed at the turbine outlet, letting the turbine outlet pressure to adjust itself to the imposed mass flow and to the inlet stagnation properties. The assumption is that at the turbine inlet the level of pressure is very close to p_{therm}. In usual simulations p_{therm} is instead located close to the injector where combustion occurs, as all the parameter for constant pressure combustion are based on it. Nevertheless we must assume that the real small percentage pressure loss between combustion zone and turbine inlet is not affecting the simulation, or alternatively, that the combustion process is not affected by an "adjusted" p_{therm} that can be chosen to match the inlet turbine conditions. In this second approach no need of knowledge of the turbine performance is required before the coupled simulation, which is an advantage for engineers.

[II] Boundary conditions that directly impose mass flow at inlet in the form of $\rho|\mathbf{U}|$ and flow angles have been developed and used. Mass conservation between the two domains is not strictly speaking ensured by the interpolation procedure, as the case is discretised and no area weighting is performed. Nevertheless, a good level of conservation has always been observed, within the level of error generally accepted for the C-DBS code itself. In this approach the knowledge of the operating conditions and maps of the turbine is required beforehand to ensure consistency in pressure levels at turbine inlet.

By using a mass flow imposition at combustor inlet and having a low Mach number approach which implies an upstream specified constant thermodynamic reference pressure p_{therm}, it means the operating conditions of the coupled simulation are eventually fully specified by these two informations only. In fact knowing the inlet pressure (p_{therm}) and mass flow of the turbine fully specifies its operating conditions. Even in the second approach proposed, in which static pressure at the outlet of the turbine is specified instead, this outlet pressure has to be chosen such that the pressure at turbine inlet is consistent with the imposed value of p_{therm}, which is in fact the key parameter deciding the turbine operating conditions.

A limitation of the coupling approach arises when fully choked conditions for the turbine are considered. In fact knowing exactly the choking mass flow before the simulation is performed is not an easy task, as changes in stagnation pressure profiles at turbine inlet, which are not know beforehand, affect the final value of the choking mass flow. The coupling procedures are intended to perform simulation of partially choked turbine, which is a typical operating point. Fully choked simulations are not standard practice and are not considered in this work. To perform them a fully compressible approach will be preferred, or alternatively some inconsistencies in pressure levels at turbine inlet may be allowed to occur. This is outside the scope of the current work.

4.2 Boundary/Interface conditions

In this section we will list the main interface/boundary conditions treatments that have been assessed as possible candidates for the coupling procedure. In particular the inlet

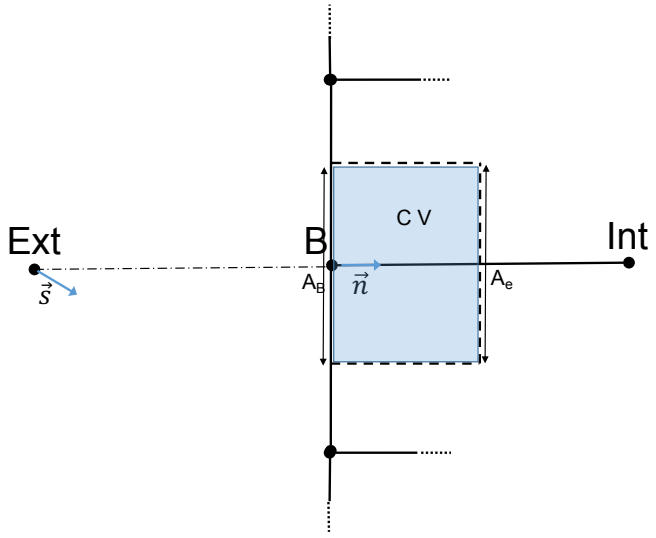

FIGURE 4.1: Schematic of a boundary node treatment, C-DBS

conditions for the downstream C-DBS code are detailed in Sec. 4.2.1 while the outlet conditions for the upstream ILM-PBS are found in Sec. 4.2.2.

4.2.1 C-DBS Inlet

All the inlet interface conditions assessed for the C-DBS inlet consist of two-dimensional profiles of variables imposed at the inlet boundary surface. The original default boundary condition in the code is based on stagnation variables p_0 and T_0, while new boundary conditions introduced for the coupling try to avoid relying on pressure impositions, for all the reasons explained in Secs. 4.1.3 and 4.1.4, and prefer a "mass flow" type of imposition.

Before proceeding with the details of the boundary conditions we shall briefly explain the general boundary treatment in the C-DBS code. As previously explained the code is vertex-centered and median dual control volumes are built around each node. We can refer to Fig. 4.1 for an easy understanding in a two-dimensional Cartesian grid. The contribution A_e of each edge connected to the node to the total surface area of the control volume is computed and used as a weight parameter on an edge based data structure. When a boundary node B is considered, the edges lying on the surface boundary provide only "half" of their usual contribution, while a weight A_B coming from the face of the control volume lying on the boundary surface is considered.

The general approach in the code is to solve the N-S equations on the boundary node too. To do so fluxes are required at the face corresponding to the area A_B. The solution is found by associating to the boundary node B an additional external node (ext) with no specific position in space, that we can imagine linked to the boundary node through an additional virtual edge, of indefinite length, normal to the boundary and associated with the area A_B. The states of the primitive variables at the boundary node and at the external node are used to compute first order convective and smoothing fluxes at the boundary face. No physical dissipation is added to the fluxes, as no real physical distance between the two nodes is specified. The states of the variables on the external node can be computed in different ways according to the type of boundary condition applied.

An alternative approach can be exploited by directly specifying (strong imposition) the boundary node values of the primitive variables avoiding the solution of the boundary node control volume. For inlet boundaries, the specification of all five primitive variables ρ, u, v, w, P is generally not recommended as it constitutes an over imposed condition, but it can be justified if the boundary is considered just as an internal interface of the coupling. Alternatively, only some of the variables might be strongly specified, while others can be computed by solving part of the N-S equations in the control volume as in the weak approach proposed above, or can be extrapolated from the interior computed domain. Extrapolation is not straightforward on general unstructured grids with the data structure implemented in the current code, so the solution of the boundary control volume with a weak formulation is preferred in this case. In the following the different inlet conditions assessed in the coupling are listed in increasing order of strength.

Original Inlet B.C.

The first condition refers to the default original inlet boundary condition implemented in the code. Stagnation pressure, stagnation temperature and flow angles are imposed in a weak approach and applying a characteristic treatment. In particular p_0, T_0 and flow angles are assumed to be imposed on the external virtual node, while the boundary node is solved. To compute the values of the primitive variables on the external virtual node to be used in the calculation of first order fluxes, a Newton-Raphson iteration is

used to evaluate p_{ext}, $\mathbf{U}_{ext}$ and T_{ext} such that p_0, T_0 and the outgoing characteristic normal to the boundary:

$$(p_{ext} - p_B) - \rho c(\mathbf{U}_{ext} - \mathbf{U}_B) \cdot \vec{n} = 0 \tag{4.20}$$

are met. $\vec{n}$ is the normal to the boundary entering the domain, c is the speed of sound and ρc is evaluated at the boundary node. In the Newton-Raphson iteration, the function for which the zero is found is the characteristic wave:

$$f = p_{ext} - \rho c \mathbf{U}_{ext} \cdot \vec{n} - (p_B - \rho c \mathbf{U}_B \cdot \vec{n})$$

in which the expression in parenthesis refers to the solved boundary node and it is known. Given the inlet flow angles the normal component of $\mathbf{U}_{ext}$ is expressed through the direction vector $\vec{s}$ as $\mathbf{U}_{ext} \cdot \vec{n} = U_{ext}(\vec{n} \cdot \vec{s})$. The Newton iteration is solved for the unknown U_{ext}: at each iteration p_{ext} and T_{ext} are recomputed given the new U_{ext}, T_0 and p_0.

As can be seen this boundary condition allows for the normal outgoing characteristic wave to leave the domain, avoiding major reflections. On the other hand the imposition is particularly weak and the profile of stagnation variables at the real boundary node can be quite different from the desired one, imposed at the external virtual node. The imposed profiles tend to be smeared out by the weak and characteristic treatment and some features can not be well represented at the inlet boundary (e.g. inlet located in the wake region of a blade).

Method A - Mass Flow, Weak Characteristics

This second boundary condition was implemented with the objective of imposing a 2D profile of mass flow in a weak formulation, being consistent with the original approach of the code for an inlet. In particular the values of the magnitude of momentum per unit volume $\rho|U|$, temperature T and flow angles α and β are imposed at the external virtual node. If the temperature is known $T_{ext} = T$, from eq. 4.20 and the equality:

$$\rho_{ext} \mathbf{U}_{ext} \cdot \vec{n} = \rho |U| \cos\theta \tag{4.21}$$

an expression can be drawn for the normal velocity $\mathbf{U}_{ext} \cdot \vec{n}$ or alternatively for the difference $(\mathbf{U}_{ext} \cdot \vec{n} - \mathbf{U}_B \cdot \vec{n})$ from which U_{ext}, p_{ext} and ρ_{ext} can be computed. θ is the angle between the unit vectors $\vec{n}$ and $\vec{s}$ and it is known at the external node. If T_0 is to be imposed instead, an iterative process is required. The boundary condition is implemented in a weak formulation and uses characteristic treatment, that it is in general the preferred approach for the turbomachinery code. Hence, it does not strongly impose the variables at the real inlet plane.

Method B - Mass Flow, Free Fluctuations

With the objective of obtaining a stronger imposition, but to still avoid an over imposed condition at the inlet boundary, a new approach in which only the continuity equation is solved at the boundary control volume was devised. The pressure (or density) is let free to fluctuate at the boundary node. The momentum per unit volume ρu, ρv and ρw (or alternatively $\rho|U|$ and flow angles) together with temperature T are strongly imposed at the inlet boundary node. The primitive variables are computed as:

$$
\begin{aligned}
p_B &\quad \textit{free to fluctuate} \\
\rho_B &= \frac{p_B}{RT} \\
u_B &= \frac{\rho u}{\rho_B} \\
v_B &= \frac{\rho v}{\rho_B} \\
w_B &= \frac{\rho w}{\rho_B}
\end{aligned}
$$

The continuity equation is solved at the control volume with the introduction of a virtual external node, as in the previous cases. No primitive variables are calculated for the external node but $\rho|U|\cos\theta$ is directly used to compute the convective flux. No smoothing is added in this case. Being the density free to fluctuate the boundary is expected to behave well in terms of reducing wave reflections.

Method C - Mass Flow, Full Interface p_{therm} and Method D - Mass Flow, Full Interface $p_{therm} + p_{(2)}^{ILMPBS}$

We grouped this two methods together as they both consist on the full strong imposition of all the primitive variables at the inlet boundary nodes. The quantities imposed at the inlet plane are, as in the previous Method A and Method B, the momentum per unit volume ρu, ρv and ρw and temperature T. But no equations are solved in the boundary control volume. To define values from the primitive variables, either pressure or density should be specified. In the coupling those values come from the incompressible/low Mach number domain too. The two methods differ from the definition of pressure adopted in the computation of density (see Tab. 4.2). The three components of velocity u_B, v_B and w_B are computed as in Method B, once ρ_B has been evaluated.

	Method C	**Method D**
p_B	$p_{therm} + p_{(2)}^{ILM-PBS}$	p_{therm}
ρ_B	$\frac{p_{therm}+p_{(2)}^{ILM-PBS}}{RT}$	$\frac{p_{therm}}{RT}$

TABLE 4.2: Method C and Method D - inlet pressure and density definition

It is clear that Method D, in the ideal case of no interpolation involved, ensure not only the continuity of ρu, ρv and ρw between ILM-PBS and C-DBS domains, but the equality of densities $\rho^{ILM-PBS} = \rho^{C-DBS}$ and all velocity components $u^{ILM-PBS} = u^{C-DBS}$. The price to be paid is the constant pressure p_{therm} value throughout the inlet boundary plane, with all the consequences about wave reflections that will arise. Method C instead is consistent with the definition of pressure between the two domains but at the price of a jump in the thermodynamic state. Both methods can be regarded as interface conditions more than as proper boundary conditions. The two methods would collapse in a single interface method if the inlet data would come from another compressible domain solution, where a unique definition of pressure and thermodynamic variables was used across the interface.

4.2.2 ILM-PBS Outlet

The most typical outlet boundary condition for incompressible/low Mach number pressure based solvers is a standard Neumann condition (zero gradient), applied under the

assumption that the boundary is located far from strong gradients and the boundary conditions applied will affect only a small portion of the domain. Alternatively many convective outlet conditions have been proposed and used and the topic of open boundary conditions is still an open field of research. In fact even though the mathematical theory does not specify any imposition at open boundaries, the numerical implementation does always require a boundary condition for all variables being solved. Body forces, sponge layers and grid stretching have been used to damp the possible numerical artefacts created by such boundaries (e.g. reflections). By definition an open boundary is not affected by what happens downstream of the flow. As a consequence it cannot be directly used as an interface condition in the coupling. Two alternative interface treatments have been assessed instead: a Dirichlet boundary condition for the second order pressure $p_{(2)}^{ILM-PBS}$ and a body force imposed in the region adjacent to the outlet boundary used in conjunction with the original open outlet condition.

Pressure Outlet Boundary

A Dirichlet condition for the pressure $p_{(2)}^{ILM-PBS}$ is used at the boundary face centre. As a consequence a zero pressure correction is imposed as well at the boundary face in the SIMPLE algorithm. In the procedure, after the solution of the momentum equations, the evaluation of mass fluxes at the pressure boundary face, to be used in the pressure correction equation, is performed using a Rhie &Chow [124] type of approach with a simplified stencil (only cell centre and face centre values are used). After the pressure correction equation is updated, being the pressure correction imposed the mass flux is corrected at the boundary face, to be used in the solution of the momentum equations at the next iteration. We recall that we are using the pressure outlet condition together with an imposed mass flow at inlets which is generally not regarded as a well posed condition, but this is less of a problem for steady state solutions as the mass flow will be conserved at convergence.

Outlet Boundary with Body Force

Before entering the details of the body force approach applied we shall briefly explain the general outlet boundary condition with no specified variables (open boundary). The treatment adopted is typical for collocated cell centred schemes. Both pressure and

pressure correction need a boundary condition to be specified. Pressure at boundaries is required in the momentum equations and it is evaluated by extrapolation from the interior to the boundary face (using the knowledge of gradients at the cell centre). The mass fluxes at the domain inlet boundaries are given when using an open outlet; velocity at the outlet is extrapolated from the interior on a zero gradient assumption and the mass flux scaled to ensure the same total mass is leaving the domain as it is entering from the inlet boundaries. The mass flux is then considered to be prescribed for the next iteration and the mass flux correction at the boundary is considered to be zero. This is equivalent to imposing a zero gradient condition for the pressure correction too. The same applies to inlet boundaries with specified mass, implying that Neumann conditions at all the domain boundaries are used for pressure, making it undefined (see Sec. 4.1.3). The approach taken in the code is to fix the pressure at one point in space so that the pressure correction is zero in that particular point and its values are in such a way uniquely defined.

With the objective of driving the solution in the last part of the combustor towards the turbomachinery solution, a body force was applied to the momentum equations, as proposed in [9]. The body force is imposed as an additional external source term of the type:

$$\mathbf{S}_{BF} = \gamma_{BF}(\mathbf{U}^{C-DBS} - \mathbf{U}^{ILM-PBS}) \tag{4.22}$$

where γ_{BF} is a constant to be specified. The body force is not prescribed at the exit plane but it is acting in a three dimensional region (which is either part of or the whole overlap region for a coupled simulation). The value of γ_{BF} is very important as it decides the strength of the body force and the degree of agreement between the obtained and desired solutions. An estimation of its value based on a one-dimensional analysis of a simplified steady incompressible Euler equation is proposed in [93].

$$\frac{\partial u}{\partial t} + u\frac{\partial u}{\partial x} = -\frac{\partial p}{\partial x} + \gamma_{BF}(u^{C-DBS} - u^{ILM-PBS})$$

To simplify the equation, they assume a zero pressure gradient and a constant convection velocity, the bulk velocity u_{Bulk}. Furthermore, the flow is stationary, which makes $u^{ILM-PBS} = u$. With $u^{C-DBS} = u_{target}$, the target velocity, the equation becomes:

$$u_{Bulk}\frac{\partial u}{\partial x} = \gamma_{BF}(u_{target} - u)$$

The analytical solution is:

$$u(x) = u_{target} + (u_0 - u_{target})\exp\Big[-(\frac{\gamma_{BF}}{u_{Bulk}})x\Big]$$

where u_0 the velocity at the beginning of the forcing region. The objective is too determine σ_{BF} so that at the end of the forcing region at $x = l_F$ (l_F the length of the body force region) the velocity difference is smaller than the relative error:

$$e = |u(l_F) - u_{target}|/u_{target}$$

Hence in the simplified one-dimensional case, the minimum value of γ_{BF} which ensure the relative error e between the target and obtained velocity at the end of the forcing region is below a desired value can be expressed as:

$$\gamma_{BF}^{MIN} = \frac{u_{Bulk}}{l_F} ln\Big(\frac{|u_0 - u_{target}|}{e u_{target}}\Big) \tag{4.23}$$

A maximum value for γ_{BF} can be instead deduced from numerical stability. The upper limit is then defined corresponding to the Courant–Friedrichs–Lewy condition:

$$\gamma_{BF}^{MAX} = \frac{u_c}{\Delta_{x_F}} \tag{4.24}$$

where Δ_{x_F} is the dimension of the smallest cell in the forcing region and u_c is the local convection velocity in that cell. For a three dimensional reacting simulation some assumptions are made. In the code the density appears in the equations and variable density flows are of interest : the approach in the choice of γ_{BF} was to make it proportional to a representative density ρ_{Bulk} in the overlap region too. The term $|u_0 - u_{target}|$ was chosen as a representative maximum velocity difference in the overlap region between the two standalone simulations, and u_{target} as a representative convective velocity in the overlap region of the forcing domain.

$$\gamma_{BF}^{MIN} = \frac{\rho_{Bulk} u_{Bulk}}{l_F} ln\Big(\frac{|u_0 - u_{target}|}{e u_{target}}\Big) \tag{4.25}$$

Above a certain value of γ_{BF} ($\approx 4-6\ \gamma_{BF}^{MIN}$) the accuracy of the obtained results with respect to the target velocity imposed were found to be satisfactory for the purpose of the coupling. Although applied to an LES solver, more details on the behaviour of the body force while varying γ_{BF} can be found in [93].

4.3 Coupling Methodologies Developed

This work is divided into two main developments, which also temporally split in half the duration of this work. Even though they both address the coupling of the same two CFD solvers (Sec. 3.6) for combustor-turbine coupled simulations and they benefited from the same knowledge gained during the coupling development, they are essentially separate works. They do not differ only from the mechanism of data exchange as the two names "File based coupling" and "Memory based coupling" may suggest, but they are two different and independent coupling tools.

[I] **FILE BASED COUPLING :** In the first part of the project a methodology based on file exchange and using existing boundary conditions for the two codes has been developed. The objective was to possibly retain the existing codes without introducing (or with very minor) modifications, and develop the coupling as a separate tool able to access flow data files and handle boundary condition files. In this way existing validated procedures within the industry will be exploited and a faster introduction of the coupling procedure into the industrial development process will be achieved. The term "file based" means that the data exchange is done through files and the coupling relies only on the existing files already produced by the two original codes. This development was dedicated to steady simulations only.

[II] **MEMORY BASED COUPLING :** The second part of the project was dedicated to the introduction of a more intimate data exchange, based on message passing between the two codes. This requires modifications in the source codes of the CFD solvers to be introduced. New boundary conditions have been developed

and assessed for the coupling together with the use of body forces (see Sec. 4.2). The data exchange is faster than in the case of file based coupling and the procedure addressed both steady and unsteady RANS simulations but mainly focused on unsteady simulations. The objective is to extend in the future this procedure to LES/URANS zonal coupling.

The coupling procedure is based on either the exchange of boundary conditions or on the application of a body force in a limited region of the domain: the domains being coupled are simulated using their specific solver while exchanging either boundary conditions data or local volume data used in the reconstruction of body forces until convergence, for steady simulations, or at each time iteration, for unsteady simulations. The coupling is essentially an outer iteration to update boundary conditions/body forces. The inner iteration is the iterative process that each solver would perform to converge or partially converge the flow field for that given boundary condition/body force. For steady state simulation the outer iteration is stopped when both solvers and boundary condition/-body force updates reach a convergence. For unsteady simulations, the outer iteration reflects the physical time stepping. Interpolation is carried out in each domain to provide new boundary condition/body force data to the other domain. Data exchange and management of the coupling are fully automated; the file based coupling is driven by a Python application which exploits the interpolation capabilities of CHIMPS [98], while the memory based coupling uses the open source coupler O-Palm [134]. The details of both developments are reported in the following sections.

4.3.1 File based coupling

The procedure is developed on the requirement that existing codes should be used, with the additional specification that each could be compiled separately on different machines using different parallelisation standards. The existing codes can communicate with the external world only through boundary conditions. This was addressed by developing an external tool capable of:

1. automatic management of the coupling procedure
2. reading flow data files of both codes

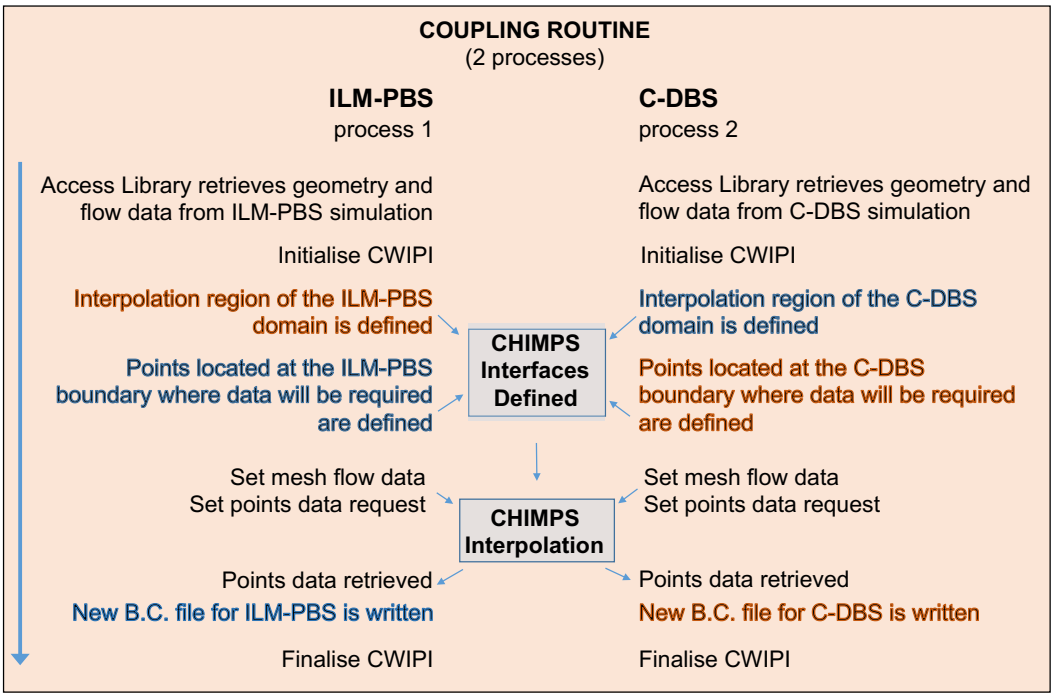

FIGURE 4.2: Schematic of the coupling routine

3. exploiting an interpolation routine

4. generating new boundary conditions for both codes

The first point is achieved by using a Python script, used for launching the executables, monitoring the coupling as well as file management. The following three points instead are embedded in a routine, defined in the following as "coupling routine", which exploits specific libraries to perform all the required data reading, interpolation and generation of new boundary condition files, and which is compiled as a standalone executable. The interpolation capabilities of CHIMPS [98], developed at Stanford University, were exploited. A common Access Library [135] for the two codes was used to retrieve the required data from the existing geometry and solution files written by each specific solver and to generate new boundary conditions. The solution files are accessed sequentially; two computing processes are used to run the main coupling routine, each devoted to the handling of one of the two domains. The interpolation in CHIMPS could be performed fully parallel but it was found to be more computationally expensive due to the necessary preliminary mesh and flow solution partitioning after the sequential access of the data files. A schematic of the main steps involved in the coupling routine is shown in Fig. 4.2. The coupling tool consists then of a Python script and one executable, in addition to the two executables of the CFD solvers. An input file is used to specify all the necessary

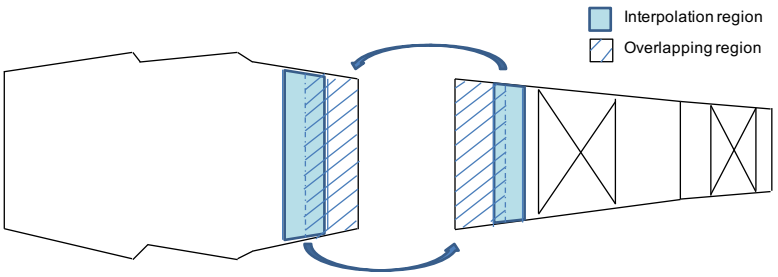

FIGURE 4.3: Coupling mechanism

informations required by the coupling procedure, which is read both by the Python script and by the coupling routine. One of the main disadvantages in using the CHIMPS library is that a hexahedral grid is required for the interpolation region of both domains, for the version of the software available in this project. This is a great limiting factor when generating the mesh, especially for the combustor domain where unstructured grids are generally required. The interpolation is performed on a small part of the domain and only that region is required to have hexahedral elements.

The coupling mechanism relies on data exchange through boundary conditions updates. Figure 4.3 shows a schematic representation of the exchange. The two domains are partially overlapping such that the inlet of the downstream domain is located in a region inside the upstream domain and the exit of the upstream domain is within the downstream domain. It should be noted that the two grids are generated independently from each other with the only requirement of having the same geometrical span in the radial direction in the overlap region. Flow field data within an interpolation region of the upstream domain are interpolated into the boundary interface plane (inlet) of the downstream domain and vice versa. The boundary data are written on files as a two-dimensional profile. As the ILM-PBS code is cell-centred, data at cell vertices are required before the CHIMPS interpolation can be performed. An additional preliminary interpolation from cell centre to cell vertices is automatically performed in the Access Library when retrieving vertex data, exploiting the knowledge of the flow gradients. The presence of an overlap between the two domains is introduced to increase the quality of the exchanged data: the boundary treatment is known in fact to degrade the solution in the region immediately adjacent. It is more accurate to extract the data to be used in the definition of the coupling interfaces from the interior of the other domain, where the influence of the boundary treatment is weakened. Moreover, the stability properties of a coupling approach have been analysed by Collado Morata [83], showing how the

overlapping region is a stability requirement in certain coupling configurations. This has not been analysed in the present work. The sequence of the data exchange process can be either sequential or simultaneous. In sequential mode the codes run one after the other while in simultaneous the codes run concurrently. This can be specified in the input file at user's choice. A schematic of the sequence of main events managed by the Python script in both sequential and simultaneous coupling is shown in Fig. 4.4. The convergence of the coupling procedure is automatically monitored by looking at the values of average pressure at combustor exit (from interpolated downstream values) and at turbine inlet (from interpolated upstream values) at each coupling iteration.

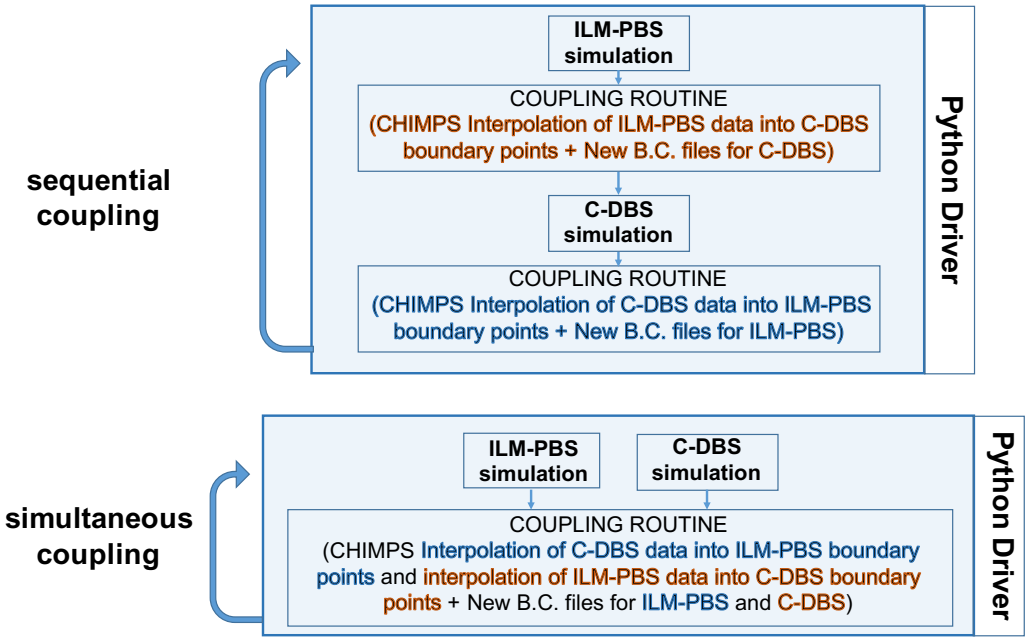

FIGURE 4.4: Schematic of sequential and simultaneous coupling

The initial core of the file based coupling was developed by Dr. Mehriar Dianat and results using a similar strategy and part of the coupling tools on a compressor-combustor realistic test case has already been shown in [135]. The main developments implemented in the current work include:

1. two-ways coupling for combustor/turbine simulations with the imposition of a two-dimensional profile at the combustor exit. The previous implementation with a constant pressure exit consisted of a one-way coupling;

2. extension of the common access library to access data of any type of combustion and low Mach number simulations and to perform area averages. Previously only cold incompressible simulations could be performed on the combustor side;

3. use of thermodynamic polynomial expressions of the C-DBS code to evaluate stagnation variables and thermodynamic states, including the presence of a fuel fraction in the exhaust gases (assumed to be burnt). Previously a simple incompressible relation was used;

4. introduction of simultaneous interpolation and coupling;

5. great simplification of the tools: one single executable can treat compressor, combustor and turbine, sequential or simultaneous coupling. Previously four different executables were used to interpolate and generate data for compressor outlet, combustor inlet, combustor outlet and turbine inlet respectively for sequential simulations only, and no simultaneous interpolation was possible;

6. introduction of a general input file, read by both the coupling executable and by the Python script, with the specification of all the necessary data regarding the coupling, used for both compressor/combustor and combustor/turbine coupling. The I/O for the coupling tool is implemented in C with Fortran wrappers to simplify its eventual future introduction in the common Access Library. The Python script is also extended and generalised to treat each possible running configuration. Previously no input file was present, and all details were hard-coded in the routines;

7. relaxed the geometry matching requirement between the two codes in the periodic direction. Previously exact matching was required for the two domains;

8. a coupling procedure for low Mach/compressible solvers based on the available boundary conditions was devised to perform reacting combustor/turbine steady coupled simulations;

9. suggestion of possible minimal desirable modifications on the source codes are pointed out: explicit addition of the turbulent contribution to pressure in the momentum equation $2/3\rho k$ in C-DBS code; modify the gas constant in the C-DBS code to make it consistent with a representative value of R at the combustor exit.

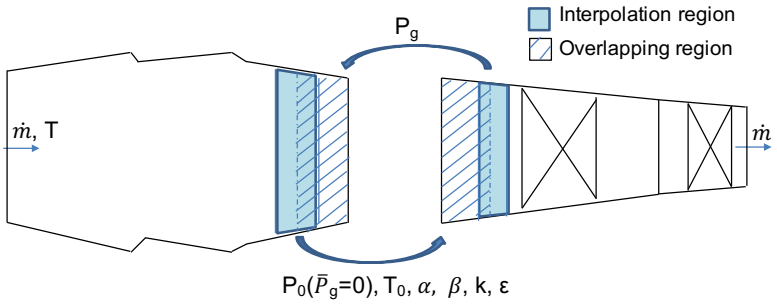

FIGURE 4.5: Schematics of the file based coupling configuration

In [135], a similar type of coupling approach has demonstrated that a coupled simulation can save computing time with respect to a standalone one, and that the time necessary to the update of boundary conditions is an acceptable part of the simulation time. Nevertheless, the time efficiency of the data exchange is reduced in the coupling routine by the time required for the Access Library to retrieve all the required informations from the geometry and flow files. In the current implementation the binary files (both geometry and flow) of the ILM-PBS code are accessed not only to retrieve the data, but also to perform the necessary interpolation from cell centres to cell vertices, slowing down the entire process.

4.3.1.1 Interface Conditions

In the low Mach number domain the mass flow is imposed at all the domain inlets together with flow angles, temperature and turbulence variables, while the gauge pressure p_g (relative to the reference thermodynamic pressure) is imposed as a two-dimensional profile at the exit coupling interface. In the compressible (turbomachinery) part, stagnation pressure p_0, stagnation temperature T_0, pitch α and radial β angles and turbulence variables are imposed at the domain inlet interface, while a mass flow imposition is used at the domain outlet. A schematic of the coupling configuration is shown in 4.5. Since the gauge incompressible pressure is only defined with respect to a reference pressure p_{therm} for low Mach number flows, in order to reconstruct the value of pressure (to be used in the evaluation of the stagnation properties) the following operation is performed at each coupling iteration:

$$p^{ILM-PBS} = p_{therm} + (p_g - \bar{p_g}) \tag{4.26}$$

where $\bar{p_g}$ is the average gauge pressure obtained by the ILM-PBS code at the turbine inlet interface plane, ensuring that the average value of pressure at the turbine inlet is consistent with the reference thermodynamic pressure p_{therm} defined for the combustion process. Mass flow conservation is ensured by its specification at both the ILM-PBS domain inlet and the C-DBS domain outlet (the pressure profile imposed is scaled to meet the desired mass flow). As a consequence the pressure level of the simulation is defined through Eqn. (4.26): the correction applied through Eqn. (4.26) keeps the level of pressure at the turbine inlet, on average, close to p_{therm} throughout the simulation. Equation (4.26) also ensure inconsistencies in density (and velocities) are small at the low Mach number/compressible interface (see Sec. 4.1.4). Attention is paid such that reflection of waves is avoided at the low Mach number/compressible interface. A weak imposition of the boundary interface conditions in used in the compressible domain which involves characteristic treatment (Original B.C.). The methodology is applied to steady simulations only: it is in fact not physical to enforce an average pressure constant in time (equal to p_{therm}) at the interface plane. We want to recall that for coupling purposes the C-DBS code has been modified to take into account the $2/3\rho k$ term in the momentum equations. Moreover a suitable gas constant R is used in the C-DBS code, consistent with a representative ILM-PBS value at the compressible domain inlet interface.

Stagnation Variables Calculation

As the original boundary condition in the C-DBS code is based on stagnation variables, a suitable way of evaluating them has to be chosen. In the incompressible assumption the stagnation pressure p_0 is the simple sum of static pressure and kinetic energy (incompressible dynamic pressure), and assuming the pressure p to be defined (summation of the thermodynamic pressure p_{therm} plus a contribution from an arbitrary defined level of the gauge component) and known, it can expressed as

$$p_0^{ILM} = p + \frac{1}{2}\rho|V|^2 \tag{4.27}$$

In the compressible assumption instead, for an ideal gas, the isentropic relations should be used:

$$p_0^C = p(1 + \frac{\gamma - 1}{2}M^2)^{\frac{\gamma}{\gamma-1}} \tag{4.28}$$

In fact, using a Taylor expansion on the Mach number this isentropic relation can be rewritten and it can be shown that additional components of dynamic pressure are appearing not considered in the incompressible simplification:

$$p_0^C = p + \frac{1}{2}\rho|V|^2(1 + \frac{M^2}{4} + \frac{(2-\gamma)}{24}M^4 + ...) \tag{4.29}$$

Stagnation enthalpy is defined as $h_0 = h + \frac{|V|^2}{2}$. The stagnation temperature can be expressed as well through isentropic relations as:

$$T_0 = T(1 + \frac{\gamma - 1}{2}M^2) \tag{4.30}$$

In case of a constant specific heat (calorically perfect gas) the relation with stagnation enthalpy becomes $T_0 = T + \frac{1}{2}\frac{|V|^2}{C_p}$.

In the C-DBS code for a calorically perfect gas the relations above are used for the calculation of stagnation values. Moreover, a more realistic gas behaviour can be used. It is implemented through a series of polynomial expressions that also take into account the presence of burnt fuel in the air. The heat ratio changes with temperature and fuel content FAR (Fuel to Air Ratio), as seen in Fig. 4.6. In such cases stagnation variables are computed using polynomial expressions [3, 136] from:

$$\log\frac{p_0}{p} = \frac{1}{R}\int_T^{T_0}\frac{C_p}{T}dT \tag{4.31}$$

In the coupling, in order to evaluate the stagnation values starting from their static counterpart, the C-DBS approach is taken, and the above mentioned expressions used to perform the calculation. This way the stagnation properties are consistent with the C-DBS code, that will be using them as its inlet boundary conditions.

Pressure and Temperature in the two domains

The discrepancy, at each coupling iteration, between the obtained average static pressure at compressible domain inlet with respect to p_{therm}, which is monitored by the coupling procedure, is a measure of the inconsistency between pressure fields in the overlap region for the two simulations. Differences in the wall region discretisation and treatment, weak boundaries as well as the evaluation of stagnation properties to define inlet interface

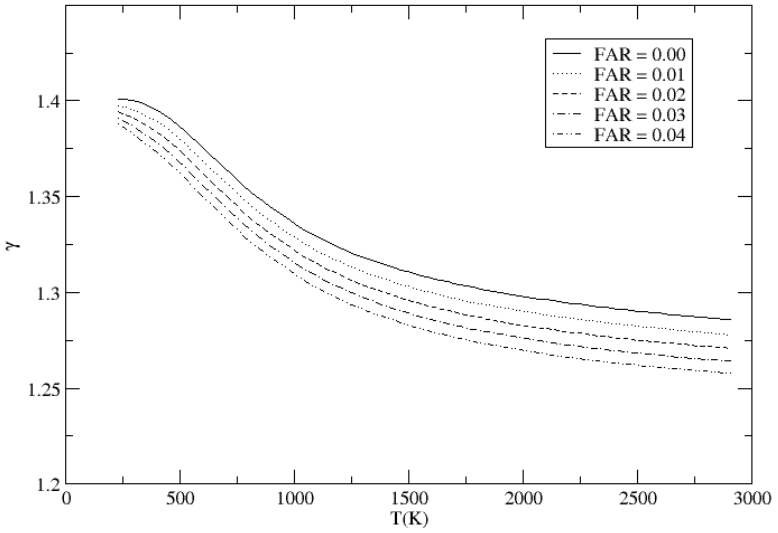

FIGURE 4.6: Variation of heat ration with temperature and FAR, C-DBS code

conditions are contributing to these inconsistencies. They can be reduced to very low values on simple test cases by having matching grids in the overlap region and consistent gas properties R in the two domains. Nevertheless, in more general and complicated test cases, the inlet static pressure profile (whose average value is p_{therm}) being used to evaluate the inlet interface stagnation properties is generally not fully recovered after the C-DBS simulation. Weak stagnation pressure inlet imposition together with mass flow exit does not ensure in the C-DBS simulation the desired inlet static pressure to be achieved. The error in average pressure at turbine inlet is found to be generally of around 0.05% of p_{therm}. Those unmatchings are considered acceptable, as inherent difficulties arise when coupling, that can be explained on a simple one-dimensional incompressible case: if we want to conserve the mass ρu flowing between the two domains and we accept the fact that unavoidable even if small differences in density and velocity can be found at the interface, due to the different definition of pressure, aiming at conservation of the dynamic component $\frac{1}{2}\rho u^2$ is not realistic and some differences will be present. The depth of the overlap region is playing a role too in the pressure consistency between the two domains, as shown in Sec. 5.1.4, and a small overlap region is preferred to a large one for pressure coupling to improve agreement of pressure in the overlap.

Similar considerations can be drawn when trying to conserve stagnation temperature

and static temperature. Specific heat can be spatially variable and differs between the two domains, and velocity is strictly speaking not enforced to be continuous. As a consequence stagnation temperature continuity does not imply temperature continuity. Generally speaking one would prefer to achieve continuity in the stagnation variables, rather than the static components. In the coupling though, as the definition of stagnation properties is somehow more problematic and different between the two domains, the ability to achieve continuity of static temperature is considered more appropriate: as explained above, the static temperature is the variable readily available and accurate from typical combustor simulation, usually computed from FGM tables. Generally speaking, conversion from static to stagnation variables is not the the same in the two codes, and also different gas properties and compositions make the values obtained by this conversion not directly comparable. Nevertheless, the existing inlet boundary condition is based on stagnation variables and static temperature cannot be imposed. The discrepancy between the two domains was always found to be very small.

4.3.2 Memory based coupling

The second part of the project was dedicated to the development of a more flexible coupling, more efficient in terms of time spent on data exchange (no Access Library and no files involved contrary to the file based coupling, use of message passing) and suitable for unsteady simulations. The assessment of new coupling methods others than the use of the original boundary conditions has been carried out in this part of the project. The overall procedure in terms of coupling methodology is generally very similar to the one used for the file based coupling, as it relies on data interpolation and boundary conditions exchange (Fig. 4.3) or it can differ from it when using application of body forces in the overlapping region (see Sec. 4.3.2.1).

As the data exchange uses message passing we define the coupling as “Memory based coupling”, to distinguish it from the file based tool previously reported. In the memory based coupling the two solvers have been modified such that the data can be directly exchanged through memory. In particular, using the coupler O-Palm [134] and its interpolator CWIPI, each code is running in parallel and sharing the same MPI communicator. The principle lays on starting the two programs since the very beginning of the application, exploiting the MPMD mode of MPI-1. This mode in not part of the

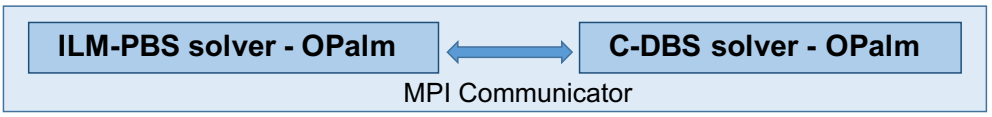

(a) Without OPalm Driver

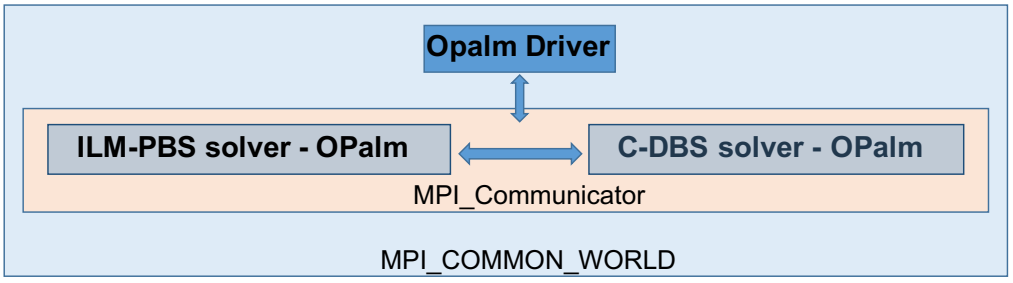

(b) With OPalm Driver

FIGURE 4.7: In the memory based coupling the two solvers are sharing the same MPI communicator

MPI-1 standard, but can be found almost everywhere on the various implementations of MPI-1. In this "extended" MPI-1 mode, many different executables can be launched at the same time, sharing the same MPI communicator.

Other options are available in the O-Palm coupler to link different codes, which do allow a less intimate way of data exchange (via sockets), but the direct introduction of a few routines in the source codes and the direct exchange through message passing was the preferred option to maximise the performance of the coupling. The original main programs of the two solvers become subroutines of the OPalm application and the ILM-PBS and C-DBS codes are now initially compiled into libraries. Simple ID cards identifying each coupled program are required, that are used in a graphical user interface PrePALM to define the coupling. PrePALM is a portable Tcl/Tk application used to entirely describe the execution scheduling, the parallel sections and the data exchange patterns. Through the GUI are produced the source code for the wrappers of the coupled programs taking care of the set-up of the communication context with no need for additional changes in the program sources, as well as the Makefile to generate the executables.

OPalm is composed of three main parts: the PALM library, the CWIPI library and the Pre-PALM GUI. For our application, most of the many capabilities of the OPalm coupler included in the PALM library are not of interest, but mainly the interpolator CWIPI is exploited. We could have retained the CWIPI library only, making direct calls

to its interpolation routines. We instead preferred to proceed in the implementation of the OPalm routines, which are wrappers of the CWIPI ones. This seemed to be the natural way as CWIPI is currently developed and released as part of the OPalm coupling tool. Moreover, in such a way many other OPalm coupling capabilities (not all of them, as some require the use of MPI-2 standard) are available, for the current or future applications. As an example, when using pressure as a coupling variable, the choice was made to work only with gauge pressures in the exchange: if the value of the reference thermodynamic pressure p_{therm} in the ILM-PBS code is required by the C-DBS code to compute the gauge pressure, an OPalm routine can be easily used to provide this value, without having to add it as an additional input of the code. In case mainly the CWIPI part of OPalm is of interest and no other OPalm communications occur between the two solvers, as for our application, only the two executables representing the two programs can be started, sharing the same MPI communicator, as seen in Fig. 4.7(a). If instead additional OPalm capabilities other than CWIPI are exploited that require communications between the two solvers, an OPalm Driver has to be launched together with the two programs: in this case all the three executables will share the MPI_COMM_WORLD communicator, while the two programs will be part of a new MPI communicator, as seen in Fig. 4.7(b).

Few calls to the coupler routines are required in the source codes of the two solvers to perform the coupling. In particular, as seen in Fig. 4.8, in the code initialisation CWIPI is initialised, the coupling characteristics are defined and both mesh and interpolation points are set. At each time step, flow data in the interpolation region is collected and the data exchange with the other solver occurs, with consequent update of the boundary conditions or the body force. We want here to notice that being the coupled application fully parallel, each process deals with its share of the mesh and interpolation points. After the final time step solution is computed CWIPI is finalised. To generate the coupling mesh for OPalm with a specific format in parallel, gather the flow data on the nodes from the two codes and apply the received data as new boundary conditions or body force it still requires quite substantial modification of the two codes, hence this coupling can not be easily introduced into the industrial process quickly.

The approach exploited is a simultaneous rather than a sequential coupling. The idea is that running both the solvers together solving concurrently their respective domains will be more computationally efficient once the space has been allocated on a cluster and

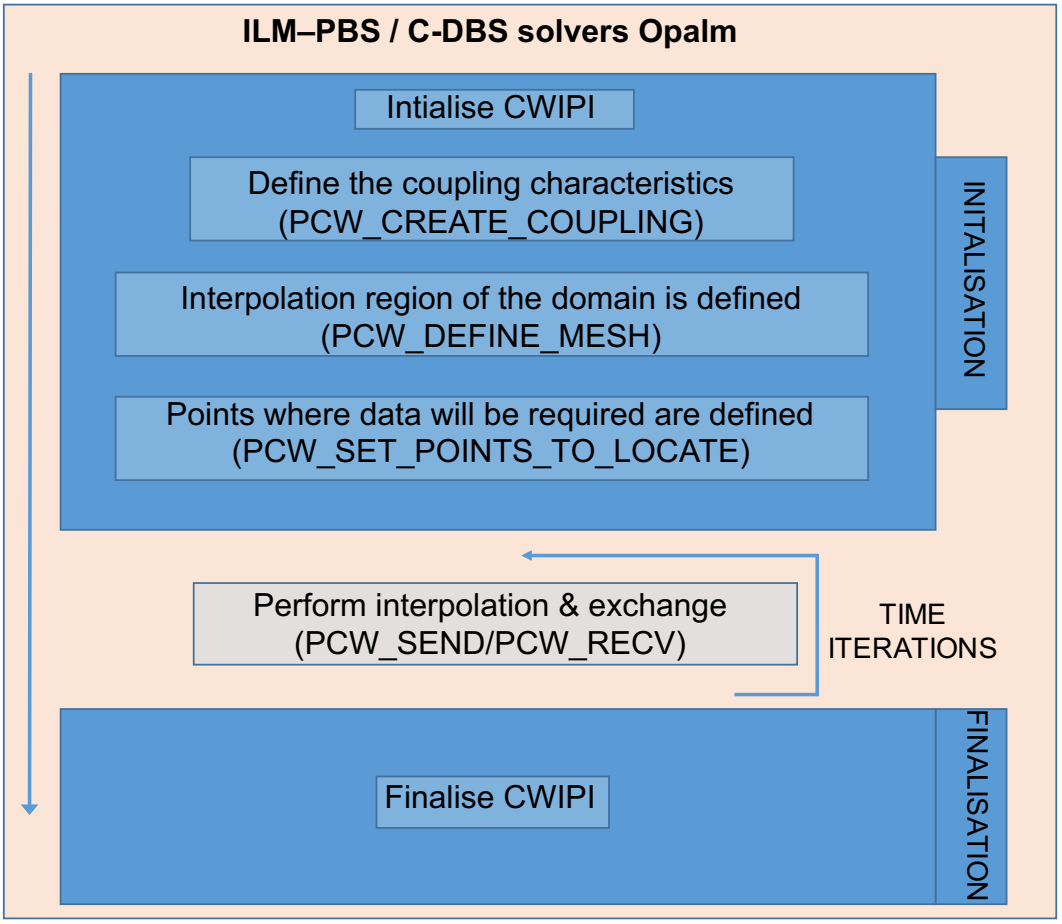

FIGURE 4.8: Schematic of OPalm coupling implementation in each code, unsteady run

a number of processes assigned to each solver. Some preliminary tests are required to ensure that the balance between the two codes is appropriate: the number of processes allocated to each solver is chosen depending on the time it takes for each solver to fully converge its time step, with the objective of obtaining an adequate share of the computing power. This way we aim at minimise the lag time in which one of the two solvers is just waiting for the next data exchange. In the case of unsteady simulation the two solvers run and solve a time step separately; at each synchronised time data exchange occurs in both directions and interface conditions are updated for the two domains (see Fig. 4.9). Sub-iterate the coupling inside each time step to converge the solution globally at each time step would be very computationally expensive. Instead, the interface conditions are kept constant by the two solvers during the time step solution. As a consequence the interface conditions will be always not matching at the end of the solution of each time step, and both solvers will result to be out of step with respect to

their interface conditions. However on overlapping grids with no coupling sub-iterations (within the time step) between the domains, even if the interface conditions are not strictly matching at the end of a time step but are merely consistent (the difference is of the same temporal accuracy as that of the overall solution method), the overall accuracy would not be lowered by the interface conditions mismatch, as seen in [137]. In their paper the authors demonstrate that using first order explicit extrapolation in time for the interface values with first or second order schemes for the time integration in the two domains, unconditionally stability is ensured. An alternative of our approach of interpolating and exchanging in two directions simultaneously is shown in Fig. 4.10: the solvers compute the same time step one after the other, the second waiting for the first to finish and receive new interface conditions. In this case the first solver running (typically the upstream solver) will see its interface conditions out of step, as in the previously reported case, but the second solver (downstream) will have its interface conditions at the correct time step. This procedure generally is expected to improve the continuity of the variables convected downstream, but at the high price of almost doubling the simulation time, which was not considered to be acceptable. The CWIPI interpolator has an in-built capability of handling cell-centred data. Nevertheless in such a case data are only localised within a specific cell rather than interpolated: at each "interpolation" point falling into a specific cell would be associated the same cell value. As a consequence a preliminary interpolation from cell-centre to vertices is performed in the ILM-PBS code before providing data to CWIPI, similarly to what is done in the Access Library for the file based coupling, and exploiting the knowledge of the flow gradients. Contrary to CHIMPS, by using CWIPI there is no limitation on the grid and any type of cell can be used. Mesh data has to be provided in a specific format to CWIPI, based on cells. This required some manipulations in the C-DBS code whose parallelisation is based on vertices and edges, rather than cells. The default interpolation in CWIPI is done via linear methods (barycentric interpolation with P1 elements).

4.3.2.1 Interface Conditions

In the memory based coupling we investigated and assessed new types of coupling interfaces treatments, not necessarily relying on existing boundary conditions. In the next Chapter 5 the process of assessment of different conditions using simple test cases is detailed.

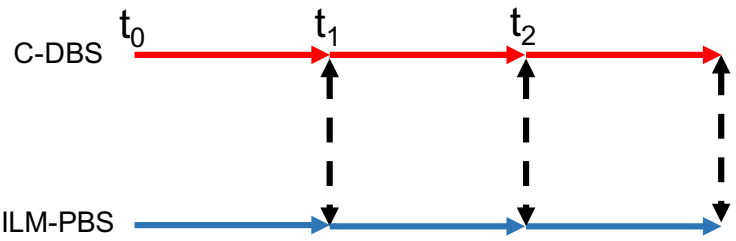

FIGURE 4.9: Data exchange occurs in both directions at each time step, solvers run concurrently

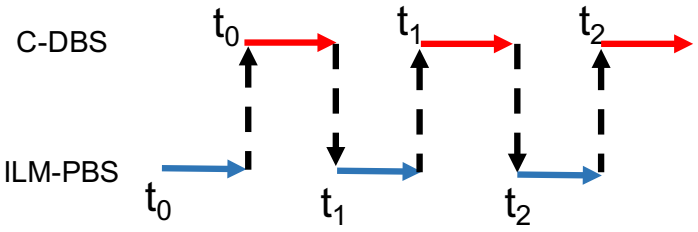

FIGURE 4.10: Data exchange occurs separately, solvers run sequentially

The interfaces of interest can be divided in two, the inlet of the downstream domain (C-DBS inlet) and the outlet of the upstream domain (ILM-PBS outlet). The schematics of the final configuration chosen for the memory based coupling is shown in Fig. 4.11. Considering the inlet condition of the downstream compressible domain a two-dimensional profile of $\rho|\mathbf{U}|$, flow angles (or equally ρU, ρV, ρW) and static temperature T is imposed using a strong imposition of a well-posed boundary condition (Method B - Free Fluctuation of Sec. 4.2.1). Considering the outlet of the low Mach number upstream domain a body force is applied in part of the overlapping region of the domain to drive the solution to the downstream values (Outlet Boundary with Body Force of Sec. 4.2.2). Due to the elliptical nature of the equations on the ILM-PBS side and the absence of acoustic pressure components, the use of a static pressure outlet (coming from a compressible domain C-DBS) is not favoured in the present work, especially for unsteady cases, and alternative approaches such as the body force are preferred for complex combustor/turbine simulations. The use of a body force weakens the coupling and allows us to completely decouple the value of pressure in the two domains. We recall that in order to minimise the interface jumps, the thermodynamic state at the turbine inlet should be as consistent as possible, on average, with the thermodynamic reference pressure in the combustor.

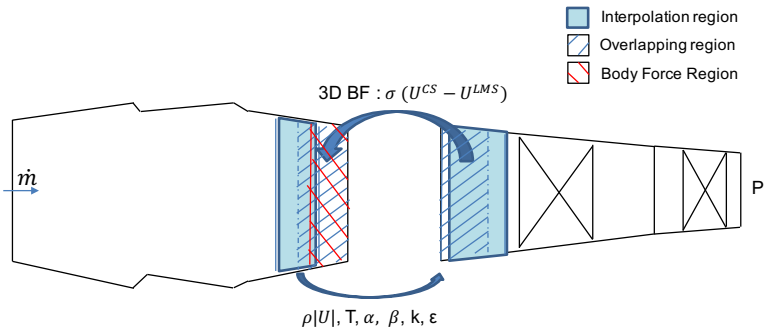

FIGURE 4.11: Schematics of the coupling configurations for memory based coupling

4.4 Closure

The objective of implementing a coupling approach of two industrial incompressible/low Mach number and compressible codes on a multi code - multi domain strategy has been achieved. The configuration involves two partially overlapping domain exchanging data through either boundary conditions or using a body force in the overlap region. Two different developments have been addressed and implemented: a "file based approach", an user friendly tool capable of coupling the original virtually unmodified codes, and devoted to steady simulations and a "memory based approach", using message passing between the two codes, which extends the coupling capabilities and allows the assessment of more coupling methodologies, mainly devoted to unsteady simulations.

After the analysis of the literature on previous low Mach number / compressible solvers coupling approaches and after some theoretical considerations on the variables pressure and on conservation properties, we opted for a weak type of coupling, in which not all the primitive variables are made continuous at the coupling interface. Mass flow conservation between the domains is the first required characteristic of the coupling. Energy is differently defined in the two codes, hence continuity of static or stagnation temperature field at the coupling interface is chosen as the second requirement. The flow angles are also continuous at the interface.

The configuration of interest is ILM-PBS solver in the upstream domain and C-DBS solver in the downstream domain. Well posed boundary conditions have been used at the inlet interface of the downstream domain: stagnation properties are used in the file based approach, while a "mass flow" type of boundary condition is used in the memory based approach. In the file based approach a boundary condition is used to provide

the feedback from the downstream C-DBS to the upstream ILM-PBS domain, which specifies the exit gauge pressure with respect to a reference thermodynamic pressure. Though, pressure is the most difficult variable to treat, for its intrinsic different meaning in the two flow physics approximation. Consequently, in order to decouple the pressure values in the two domains, a body force in the overlap region of the upstream ILM-PBS domain was used for unsteady simulations in the memory based coupling. The force, applied in the momentum equations, drives the upstream solution to the downstream values, and a pure convective condition is imposed at the outlet boundary. The objective is to further weaken the coupling, increasing its stability and robustness properties.

Chapter 5

Flow Verification Tests

The file based coupling is limited by the requirement that existing boundary conditions are to be used in the coupling procedure. Its assessment on an annular diffuser and on a backward facing step test cases is reported in Sec. 5.1.1 and Sec. 5.1.5. Nevertheless, in the memory based coupling, other configurations of possible interface treatments (see Sec. 4.2) have been assessed. In particular each treatment is assessed on a separate test case chosen to minimise the disturbances effect of other conditions and to be representative of the condition the interface is asked to deal with. We can distinguish between "Memory based coupling C-DBS Inlet" and "Memory based coupling ILM-PBS Outlet" interfaces.

Memory based coupling C-DBS Inlet: Methods A, B, C and D Different inlet conditions for the downstream C-DBS domain are investigated, keeping fixed the exit condition of the upstream ILM-PBS domain to gauge pressure boundary. Looking at the downstream domain only, the original boundary condition based on total pressure is discarded as it is not suitable for unsteady simulations and only its use together with a mass flow exit condition at the domain outlet can ensure mass conservation between the two domains. The objective is then to be able to specify a two-dimensional profile of mass flow at the domain inlet (by specifying ρU, ρV, ρW), for mass losses to be small at the interface, together with a two-dimensional profile of temperature. A static coupled gauge pressure exit (as in the file based coupling) is used at the ILM-PBS domain outlet for those tests aiming at assessing the properties of the C-DBS inlet interface only. The assumption being that strong unsteady features generated downstream of the overlap

region are not present (or only their steady component is important). Under these assumptions a gauge pressure boundary, which is stronger than a body force and can improve the quality of the coupling, is preferred for the assessment, as issues were not observed under these conditions. The methods listed in Sec. 4.2.1 as Method A, B, C and D are tested on a simple case of a vortex convected from the low Mach number to the compressible domain (Sec. 5.1.2). In all the proposed methods the variables that are object of interpolation between the two domains are ρU, ρV, ρW, T (and p_g). The case is extended to a cylinder shedding with multiple vortices crossing the ILM-PBS/C-DBS interface (Sec. 5.1.3). In order to evaluate the reflective properties of the characteristics (Method A)/over-imposed (Method D) methods a downstream obstacle case is used (Sec. 5.1.4). Finally, the ability of a strong condition (Method B) to capture the flow structures better than a weak imposition is tested on a steady backward facing step case, the same used for the validation of the file based coupling (Sec. 5.1.5).

Memory based coupling ILM-PBS Outlet - Body Force The variable "pressure" is the most difficult to retain consistency between the two domains, because of its different meanings in the low Mach number and compressible approximations. When dealing with a low Mach number domain upstream and a compressible domain downstream, the Dirichlet exit boundary condition for gauge pressure (ILM-PBS outlet) has occasionally shown instability problems when the coupling was applied to unsteady real industrial applications. Moreover it is not a well posed condition to be used together with mass flow inlet in the low Mach number domain. Furthermore we are aware acoustic perturbations are fed into the low Mach number domain where they cannot be supported by the incompressible governing equations. For these reasons we investigated the possibility of using a body force as proposed by Stanford University [93] to be applied in the overlapping region of the low Mach number domain. The body force drives the upstream solution to the downstream desired value. In this approach the pressure field is completely uncoupled between the two domains. We recall a convective outflow is used at the outlet of the ILM-PBS domain instead of pressure exit. The body force is not expected to behave strongly but instead to further weaken the coupling. In order to test the properties of the body force, and in particular to assess the ability to drive the flow to the desired values, a simple test case was devised and it is reported in Sec. 5.1.6.

In Sec. 5.1 the assessment of the file based coupling and of the boundary interface conditions for the memory based coupling is reported. In Sec. 5.2 instead the final configuration chosen for the memory based coupling through the previous analysis of Sec. 5.1 is used to perform a final assessment on the unsteady test cases.

5.1 Assessment of the Interface Conditions

5.1.1 Annular Diffuser

With the objective of an initial evaluation of the file based coupling procedure using a simple test case with main flow from upstream to downstream domains and downstream pressure disturbance, the approach described in Sec. 4.3.1 is applied to an annular diffuser case. The upstream domain consists of a straight annulus, while the downstream domain is characterised by a straight annulus followed by a divergent region. The angle of the upper wall is 10.5°. The downstream geometrical opening is located soon downstream the overlapping region between the domains. We obtain a representative situation in which the flow direction is from the upstream domain to the downstream domain with a pressure disturbance generated in the downstream field close to the coupling interface and propagating upstream. Only a 5 degree annular sector is simulated and the periodicity of the solution is exploited. The Mach number is 0.03 while the $Re = 30000$ based on the inlet annular radius. The flow is chosen to be turbulent so to assess the exchange and conservation of turbulence variables. The $k - \epsilon$ model was chosen for the test. An integral wall law is implemented in the C-DBS code to improve the solution of the standard $k - \epsilon$ model when dealing with higher wall refinement. As the wall laws implemented in the two codes differs, in order to mitigate the influence of wall modelling on the coupling we decided to refine the wall up to low values of y^+ (≈ 1). Even though this is strictly speaking incorrect to obtain meaningful physical results, we were primarily interested in the details and evaluation of the coupling procedure. The upstream mesh is composed of around $2 \cdot 10^5$ hexa elements, while the downstream part of around $3.3 \cdot 10^5$ hexahedral elements. The grids have coincident nodes in the overlap region. The coupling has been run for 70 coupling iterations, with 1300 inner iterations for the ILM-PBS code and 800 inner iterations for the C-DBS code. At each coupling iteration both codes where converged to a low level of residuals (in Fig.5.1 the residual

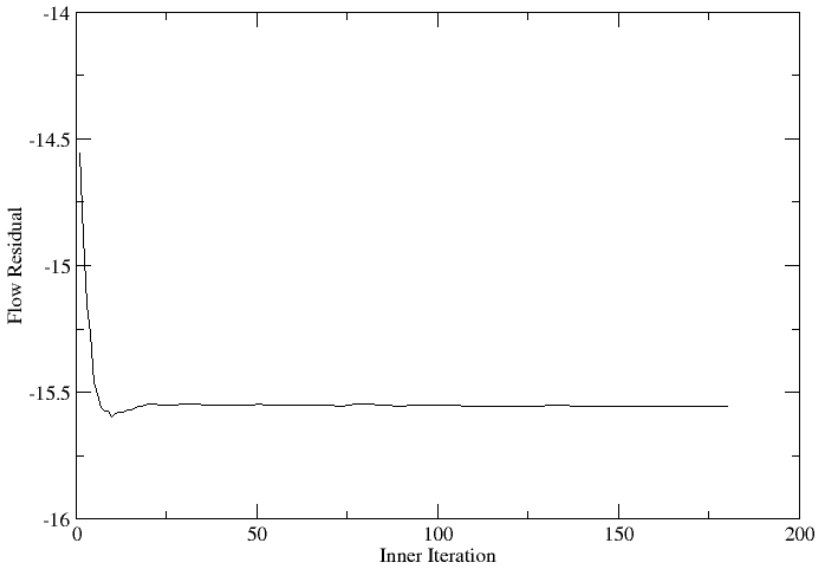

FIGURE 5.1: Residuals of the C-DBS code, convergence of a single coupling iteration, Annular diffuser case

history of the C-DBS code is shown) while for the convergence of the coupling the area averaged pressure at interface planes was monitored, and it is shown in Fig. 5.2. The results are shown on a slice along the axial direction. In the figures presenting results from coupled simulations, the two domains are overlapped. A certain degree of transparency is used in the plot so to visualise both solutions in the overlap, resulting in the darker color observed in that region (see Fig. 5.3). Contour lines are continuous in the ILM-PBS domain and dashed-dotted in the C-DBS one. In Fig. 5.3 normalised stagnation variables are shown, confirming the correct exchange of boundary informations. Stagnation variables have been computed using isentropic relations for the ILM-PBS domain and using the polynomial expressions (Sec.4.3.1.1) of the compressible code for the C-DBS domain. In the following all the variables of interest are reported in Figs. 5.4, 5.5, 5.6 5.7.

We can immediately notice from Fig. 5.6 that the density is constant throughout the ILM-PBS domain, as the inlet temperature is constant, while in the C-DBS code the density varies (the variation is very small 0.02%, due to the low Mach number). The velocity is continuous at the inlet interface and a good agreement was found between the two codes (see Figs. 5.4, 5.7). The mass flow is conserved, as it is imposed both at inlet and outlet boundaries (Fig. 4.5). Nevertheless we can observe a slight mismatch

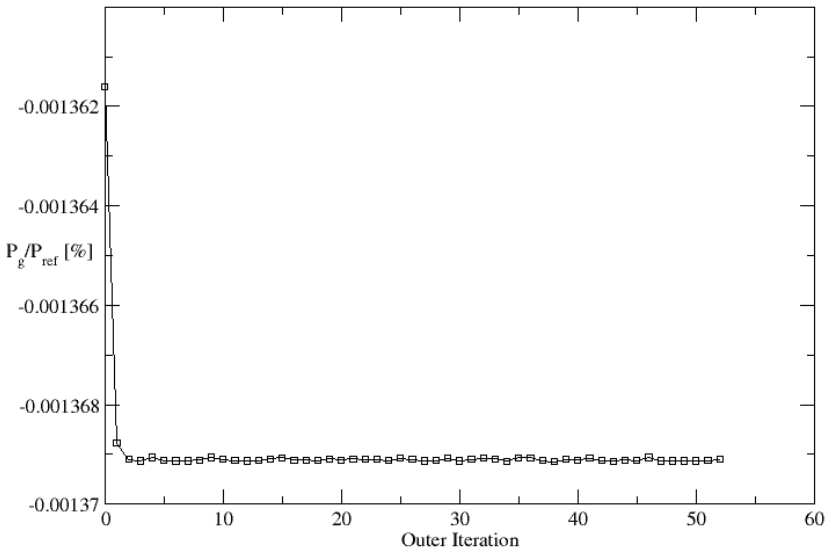

FIGURE 5.2: History of averaged pressure at annulus exit during the coupling, Annular diffuser case

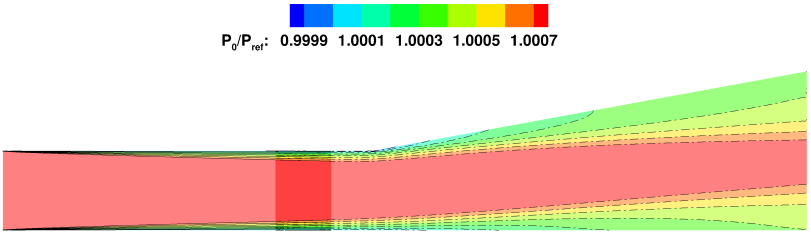

(a) Normalised Stagnation Pressure

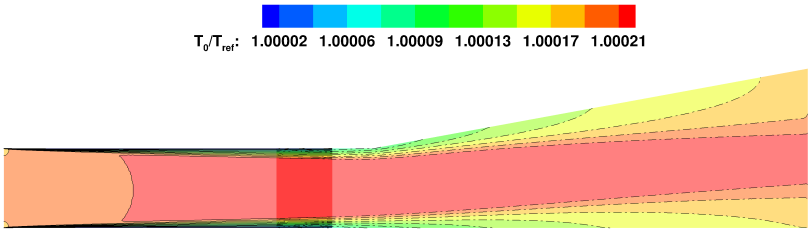

(b) Normalised Stagnation Temperature

FIGURE 5.3: Normalised Stagnation variables, file based ILM-PBS (solid line) / C-DBS (dashed-dotted line) coupling, Annular diffuser case

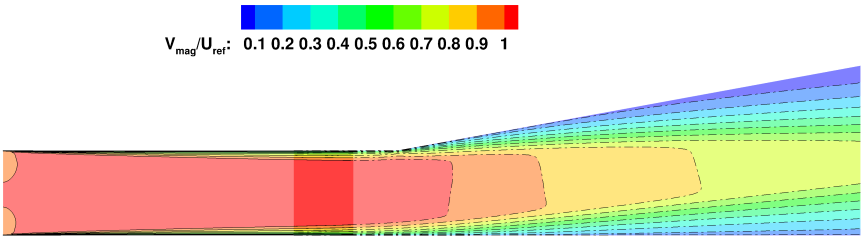

(a) Normalised Velocity Magnitude

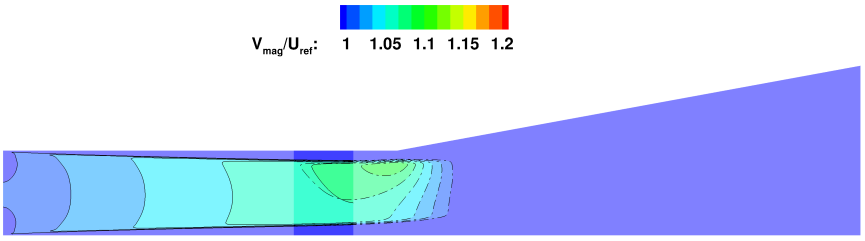

(b) Detail of Normalised Velocity Magnitude - rescaled contour levels

FIGURE 5.4: Normalised Velocity Magnitude, file based ILM-PBS (solid line) / C-DBS (dashed-dotted line) coupling, Annular diffuser case

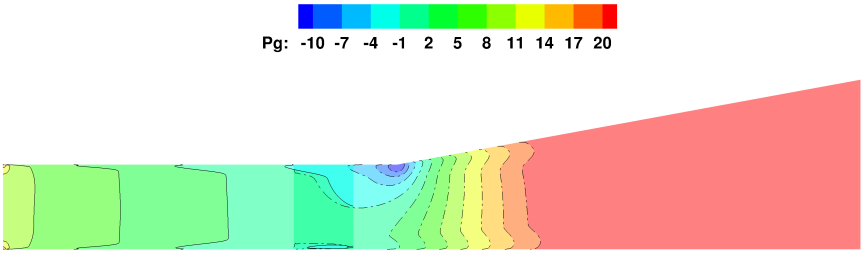

FIGURE 5.5: Gauge Pressure (Pa), file based ILM-PBS (solid line) / C-DBS (dashed-dotted line) coupling, Annular diffuser case

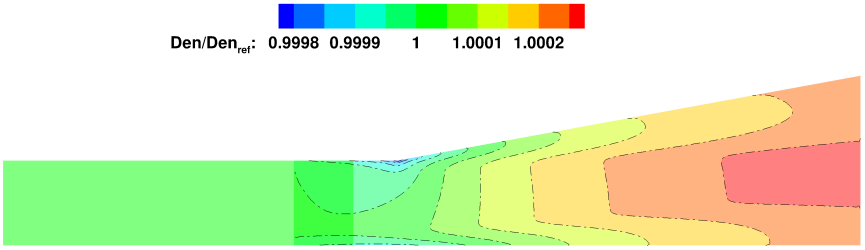

FIGURE 5.6: Normalised Density, file based ILM-PBS (solid line) / C-DBS (dashed-dotted line) coupling, Annular diffuser case

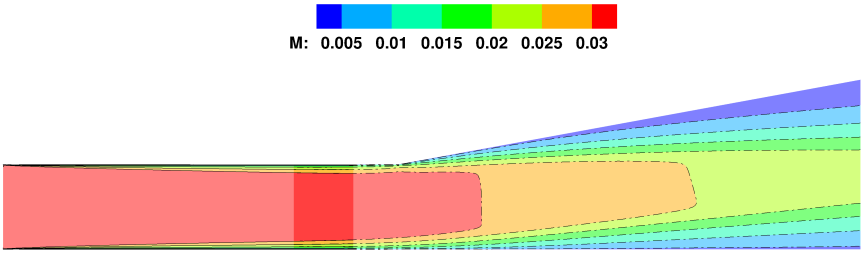

FIGURE 5.7: Mach number, file based ILM-PBS (solid line) / C-DBS (dashed-dotted line) coupling, Annular diffuser case

between the results of the two codes in the core of the overlapping region, as can be observed in Fig. 5.4(b) where the contour lines levels have been adjusted to emphasise this feature. This problem is partially due to the stagnation pressure boundary condition weakness. Nevertheless the inherent differences in the solutions of the same test case computed by the two solvers are a primary cause for this mismatch. In fact, clear differences were found in the solution of the full case (annulus and diffuser in a standalone unique simulation) between the two solvers, with relative consistent boundary conditions (see Fig. 5.8). The boundary conditions are in fact essentially coincident in the two standalone simulations, as the C-DBS code has been run first (having weak boundaries) and the obtained boundaries where then strongly applied to the ILM-PBS code (both with Open Outlet and Pressure Outlet). Massflow and temperature are imposed and consistent at the inlet. It is not of interest of this project to evaluate which solver is better in capturing the real flow physics for this test case, but to make the coupling procedure as accurate as possible. In Fig. 5.5 the gauge pressure is shown, and again good

agreement with small differences in the overlapping region was found. The exchange of turbulence variables was also assessed and it is shown in Fig. 5.9 where turbulence kinetic energy and dissipation are shown. Finally in Fig. 5.10 a comparison between standalone uncoupled and coupled simulations is reported. Dashed-dotted lines correspond to a C-DBS solution while a solid line correspond to an ILM-PBS solution. Lines in bold are from the uncoupled standalone solutions while simple lines are from the coupled ILM-PBS/C-DBS simulation. The colors of the contour are from the coupled simulation. As it can be seen the coupled simulation is closer to the ILM-PBS solution than to the C-DBS one, also in the divergent part. Nevertheless the influence of the the C-DBS solution in the divergent can be noticed in the shortening of the core velocity. The upstream domain was found to be the one that influence the most the coupled simulation, and this was found in all the test cases analysed. It can be explained with the fact that the coupling has one preferential direction, which is the one of the flow.

In conclusion, the case has shown good continuity of all variables of interest at the interface. Differences between the two standalone solutions are present, which can be responsible of the small mismatch in the overlap region observed in the coupled simulation.

5.1.2 Taylor Vortex

For a first evaluation of the memory based coupling inlet interface conditions a simple unsteady case was used. The case was proposed by Peet & Lele [129] and consists of a Taylor Vortex [138] crossing the low Mach number/compressible interface. The objective is to assess the behaviour of the four inlet interface conditions proposed in Sec. 4.2.1 for the downstream C-DBS domain. The analysis is carried out by looking at possible divergence introduced by the interface, by looking at the density field in the downstream domain (density fluctuations eventually introduced by the inlet interfaces are expected to be very small and they can be evaluated "separately" from the velocity field) and by comparing the results with the analytical solution. The overlap region between the two domains is relatively large with respect to the vortex characteristic dimension so that the exit pressure interface has little effect on the coupling. The purely tangential velocity disturbance is initialised as:

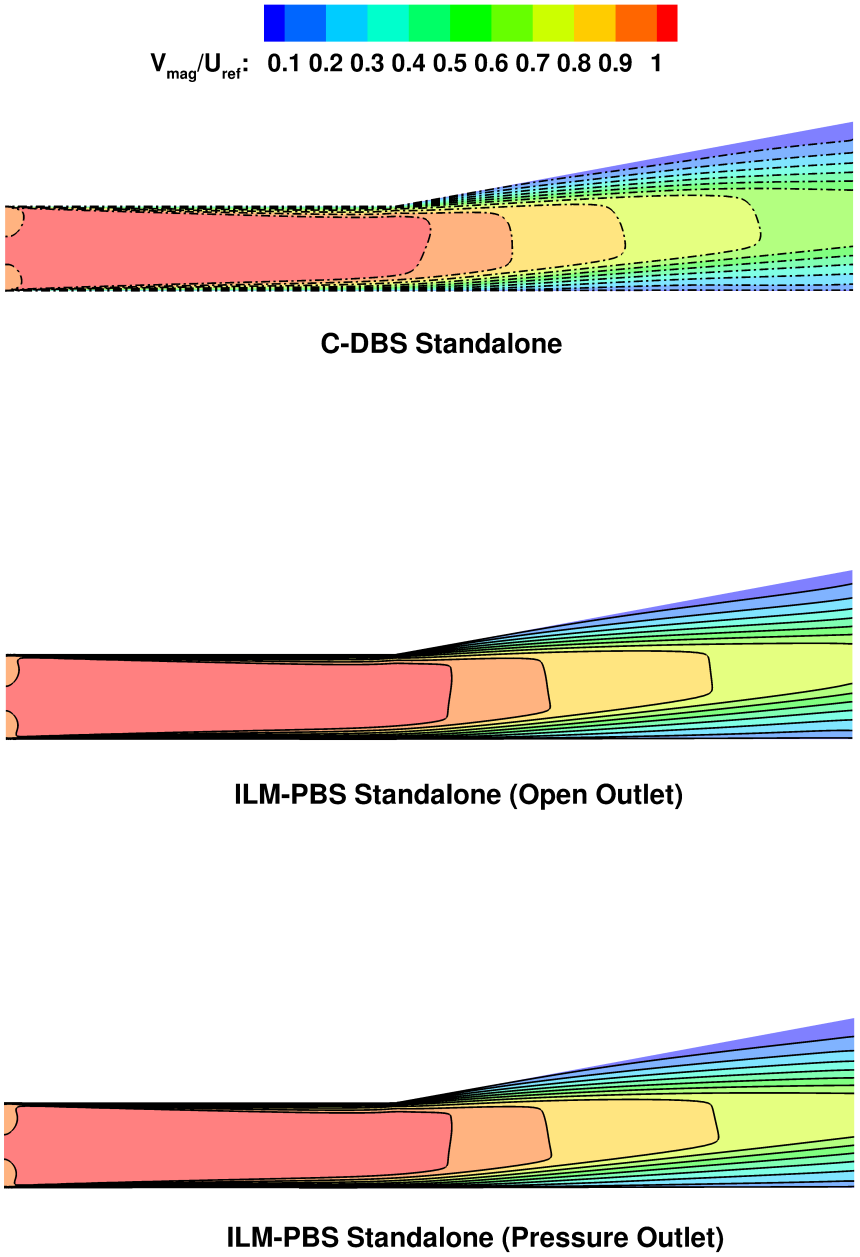

FIGURE 5.8: Standalone ILM-PBS and C-DBS solutions, Normalised Velocity Magnitude, Annular diffuser case

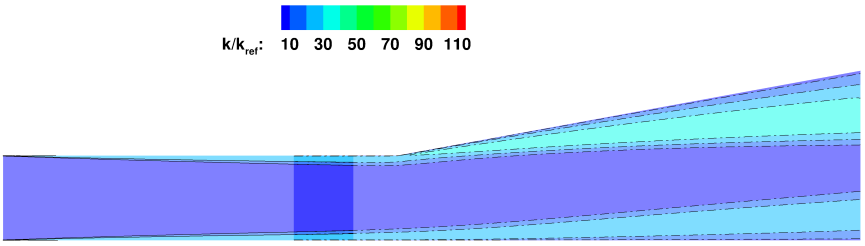

(a) Normalised Turbulence Energy

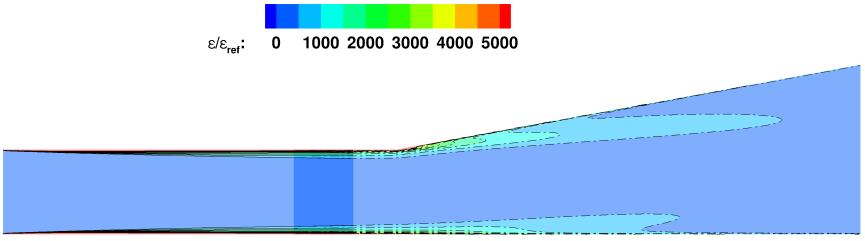

(b) Normalised Turbulence Dissipation

FIGURE 5.9: Normalised Turbulence variables,file based ILM-PBS (solid line) / C-DBS (dashed-dotted line) coupling, Annular diffuser case

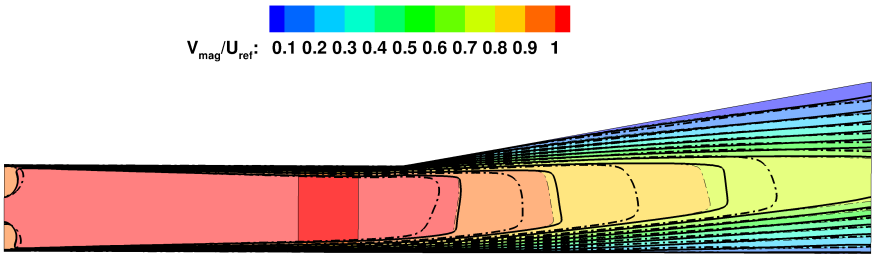

FIGURE 5.10: Comparison Standalone (ILM-PBS (-) / C-DBS (- · -)) - Coupled simulations (ILM-PBS (–) / C-DBS (– · –)), Normalised Velocity Magnitude, Annular diffuser case

$$u_t = \frac{\mathcal{M} r}{16\pi\nu^2 t^2} \exp\Big(-\frac{r^2}{4\nu t}\Big) \tag{5.1}$$

The initial time t is set so that the Reynolds number based on the initial radius of maximum velocity and the main convective velocity $\bar{U}$ is $Re = \frac{\bar{U} r_{Max}}{\nu} = 330$. The Mach number based on the convective velocity is 0.15. The angular momentum $\mathcal{M}$ is chosen to set the maximum velocity disturbance U'_{MAX} to 1% of the mean convective velocity $\bar{U}$. The grid of each domain uses a uniform spacing of 200 by 200, with 2 elements used in the normal direction together with periodic conditions to simulate a quasi two-dimensional field.

All methods have shown good agreement of velocity field in the overlapping region (the maximum error being approximately 2% of the maximum initial disturbance). The vertical velocity field is shown in Fig. 5.11 together with the vorticity magnitude at three different times during the crossing of the vortex. The tangential (vertical) velocity along the horizontal line passing through the center of the vortex, when the vortex is located inside the overlapping region, is shown in Fig. 5.12 for Method A. As can be seen the agreement of the velocity field is good. Looking at the vorticity field some inconsistencies are found in the shape of the vortex that has left the overlapping domain, possibly due to the velocity gradients not guaranteed to be continuous at the interface.

The Taylor vortex is an incompressible vortex and it is by definition divergence free. Following the analysis proposed in Peet & Lele [129], as the disturbance introduced is small compared to the convective field, the vortex should not introduce dilatation in the compressible field. The maximum value of the rate of dilatation, measured as the velocity divergence, found throughout the whole compressible domain is plotted against the axial coordinate position of the center of the vortex as it moves through the domain in Fig. 5.13.

The methods which showed best performance are Method A and Method B. In both methods, after the initial peak encountered when the vortex is crossing the interface the maximum dilatation rate returns to the initial state once the vortex has fully entered the domain. Method D has shown greater values of dilatation rate as well as higher levels remaining after the vortex has crossed. Method C instead never recovers the initial values of dilatation rate and peaks are found when the vortex has already left

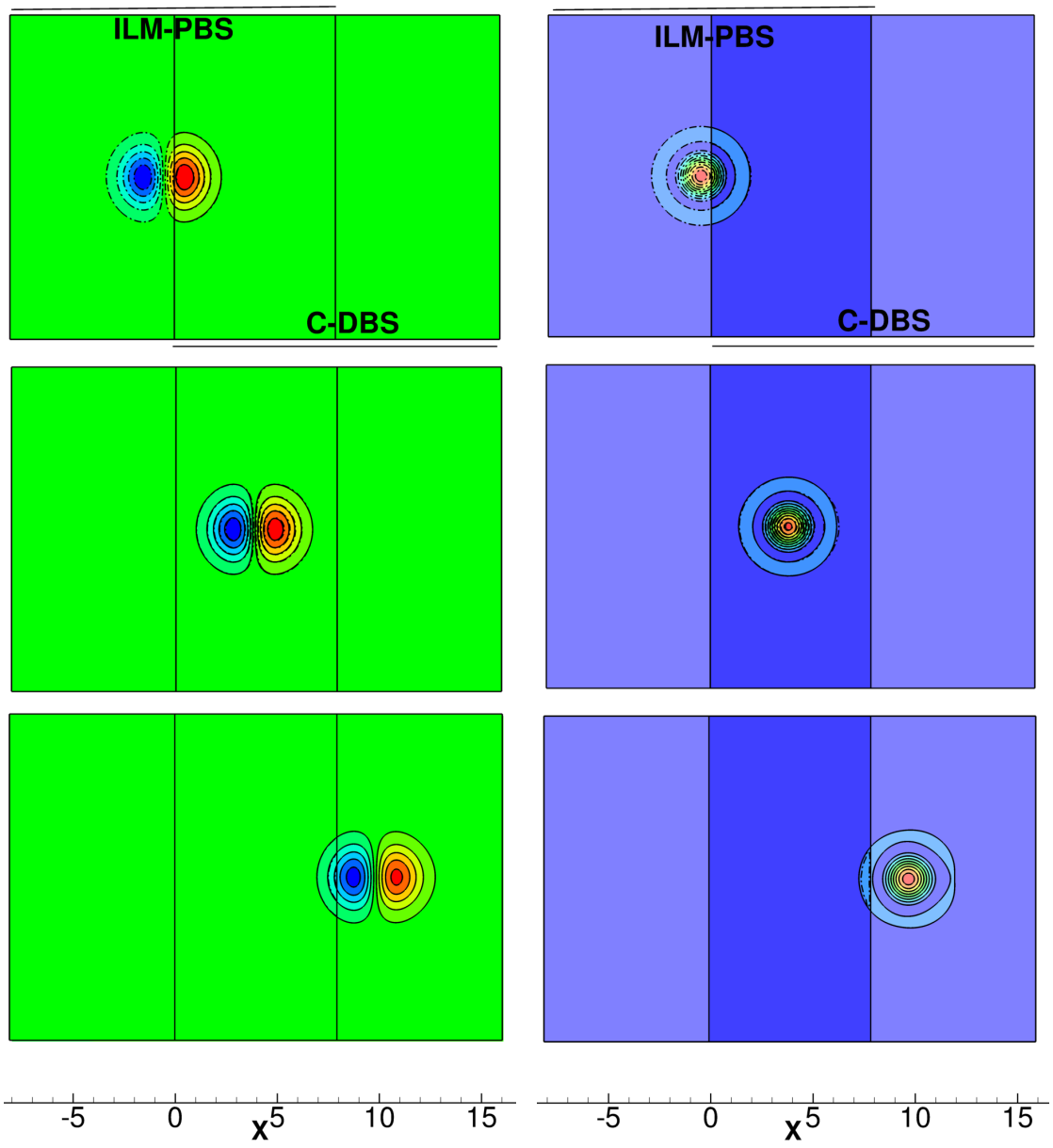

(a) (b)

FIGURE 5.11: Vertical Velocity (a) and Vorticity Magnitude (b), Taylor vortex crossing the interface from low Mach number to compressible domain

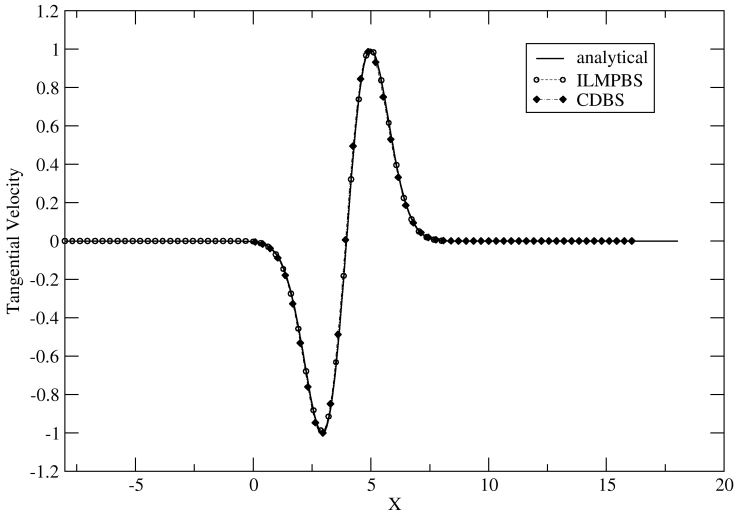

(a)

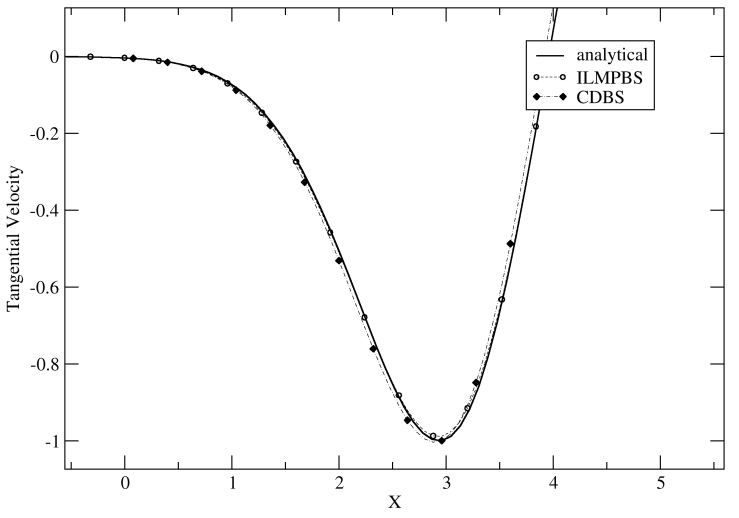

(b) detail

FIGURE 5.12: Normalised Tangential Velocity along the vortex axis, vortex located inside the overlapping region

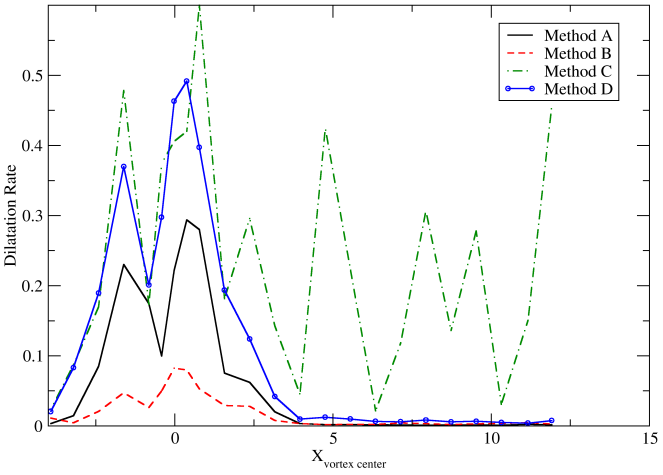

FIGURE 5.13: Maximum Rate of Dilatation obtained in the compressible domain against vortex center position with different C-DBS inlet treatments, Taylor vortex

the interface. By looking in Fig. 5.14(a) at the distribution of the dilatation rate in the compressible domain (in Fig. 5.14 is shown the downstream domain only when the vortex has almost completely left the upstream domain) we note how Method A and B show a similar wavy behaviour, Method D concentrates its peaks only in the region of the inlet interface, while Method C shows the worst behaviour. When the vortex crosses the inlet interface of the compressible domain a density fluctuation is generated, coupled to the pressure disturbance introduced. As Method D tries to keep the density constant at the inlet, this method is the one which behaves the best in terms of having a smooth rounded field of density (Fig.5.14(b)). In Method A and B pressure is more free to fluctuate and density does so as well, showing a more wavy behaviour. It should be noted that the density fluctuation introduced for this test case are very small, less than 0.001%.

A major difference with respect to the method proposed by Peet is in the low Mach number interface boundary treatment. In our approach solely the value of gauge pressure p_g is imposed at the exit boundary, while u, v, w, were imposed together with a Neumann condition for the pressure (ensuring continuity of velocities and gradients of pressure) in Peet & Lele [129]. In this work a weaker imposition of the downstream flow characteristics to the upstream flow field is used. In realistic engine test cases the imposition of velocity components at the low Mach number domain exit is not suitable

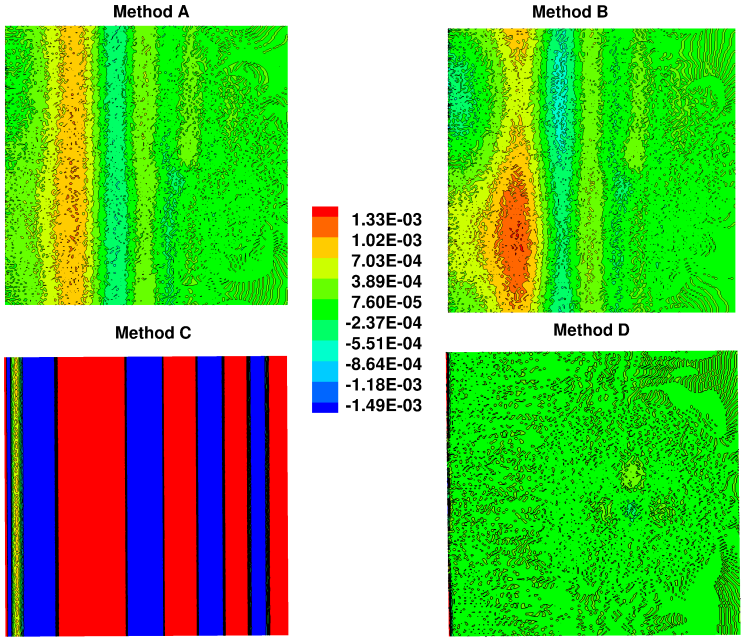

(a) Rate of dilatation

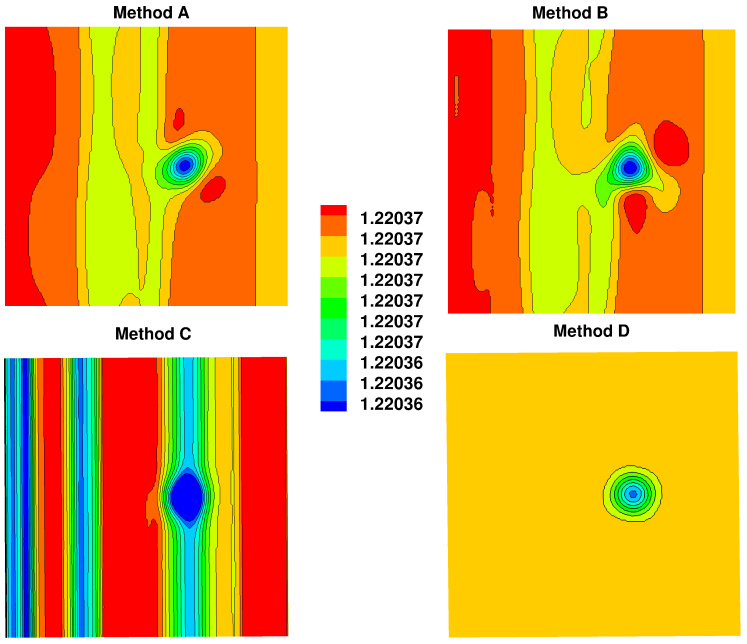

(b) Density field

FIGURE 5.14: Compressible domain when the vortex has left the low Mach number domain

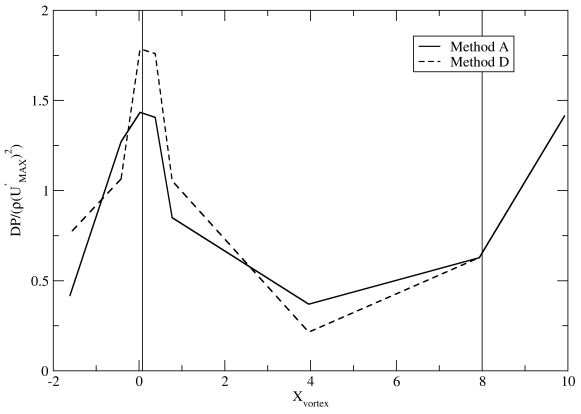

FIGURE 5.15: Difference in pressure between the two domains for Method A and D as the vortex crosses the interface region, Taylor vortex

to ensure a well behaved simulation in terms of mass conservation between inlet and outlet and in terms of requirements on the velocity field divergence characteristics. We recall that in the final coupling technique the weakening is further increased with the introduction of the body force to substitute the gauge pressure imposition. Following the asymptotic analysis of Muller [126] the gauge pressure corresponds to the second order pressure in the Mach number expansion and it is not coupled with density and temperature. The leading error term in the pressure definition scales with the square of the Mach number. The use of Dirichlet conditions for this variable allows for a direct comparison between pressures in the two domains:

$$p^{ILM-PBS} = p_{therm} + p_g \tag{5.2}$$

In Fig. 5.15 is shown the maximum value of normalised pressure difference as the vortex crosses the interface (vertical lines are showing the overlapping region limits, the abscissa is the vortex center position). As can be seen from the figure, when comparing the pressures in the two domains a difference up to 170% of the initial disturbance $(\rho(U'_{MAX})^2)$ is found, which is concentrated at the boundary interfaces. This number is within the expected errors: following Peet & Lele [129], 170% of the 1% disturbance introduced is 1.7% of the mean flow field, which is of the order of $M^2 = 0.0225$.

In conclusion, all four Methods show good conservation of the velocity field. Method A and B have shown similar behaviour, with good conservation of the divergence free

properties of the vortex. Oscillations of the divergence and density fields due to wave passing are clearly observed. Method D has shown the best conservation of the vortex shape for all the variables, but higher peaks of errors are localised only at the inlet interface. Method C is to be discarded.

5.1.3 Cylinder Shedding

To extend the vortex simulation to multiple vortices crossing the low Mach number/-compressible interface a circular cylinder has been used in the upstream domain to shed vortical structures downstream. The case is representative of a combustor-turbine coupled simulation, where the vortexes generated in the combustor are convected downstream and enter the turbine. The coupling procedures described in Method A, Method B and Method D have been applied to an unsteady case of a cylinder shedding at $Re = 100$ (based on the cylinder diameter). The Mach number of the flow is $M = 0.044$. The grid is a multi-block mesh made of a total of around 120000 hexahedral elements. The inlet is located 7 diameters upstream of the cylinder stagnation point, while the domain extends for 45 diameters downstream of the cylinder center. For the coupled simulation the inlet and exit interfaces are located respectively at 19 diameters and 20 diameters downstream of the cylinder center, generating a one diameter thick overlap region in the axial direction x. In this case the dimension of the overlap is smaller than the vortical structures crossing it, as it is expected to occur in a typical combustor-turbine application. The domain extends for 15 diameters in the transverse direction z. The case is made two-dimensional by using two cells only in the normal direction y. Symmetry conditions are used at boundaries for both the directions y and z. The time stepping has been chosen such that each shedding is resolved with 50 time steps. The analysis is carried out by looking at the continuity of the velocity magnitude for unsteady snapshots and by comparing the coupled solution with standalone ILM-PBS and C-DBS simulations.

Results are shown in Fig. 5.16 for normalised velocity magnitude. In particular an unsteady snapshot has been compared between the standalone ILM-PBS and C-DBS simulations and the coupled Method A and Method B cases. Unsteady snapshots sufficiently close in time within the period of the shedding development have been chosen between the four plots in order to make visual comparisons. It is possible to notice how

the coupled simulations are successfully compared with the standalone ILM-PBS one, which is consistent with the fact that the shedding is generated upstream in the ILM-PBS domain. The standalone C-DBS simulation instead shows some small differences in the wake as well as in the upstream potential region, due to the slightly different prediction of the shedding behaviour for the compressible code. The difference between the two Methods A and B for this test case is small, and in both cases a velocity difference of about 1.5 % is found in the overlap region between the two domains. The results obtained using Method D are shown instead in Fig. 5.17. The flow is corrupted close to the inlet interface and in particular in correspondence of the symmetric boundaries. This behaviour was not observed in the previous Taylor Vortex test case.

Looking at Fig. 5.18, which shows the density field in the coupled Method A case, it is interesting again to note that density variations are present in the compressible domain, generated at the inlet coupling interface, while density is constant throughout the low Mach number/incompressible domain (the temperature is constant). The gauge pressure for the same test case is shown in Fig. 5.19: a general agreement between the two domains is observed, but pressure oscillations at the C-DBS domain inlet interface are present, to which density oscillations are also linked. Those oscillations are generated by the inlet treatment, and they appear not to generate problems in the downstream field. Even though this does not create issues in the upstream domain too for the simple test cases investigated, it represents an additional reason why we should avoid to feed those oscillation back to the ILM-PBS domain, as they could initiate unphysical behaviours (hence the development of a weaker body force approach for real unsteady combustor-turbine applications).

In conclusion, both Method A and Method B have confirmed the observed quality of the coupling in the continuity of velocity magnitude and they have been successfully compared with standalone results. In particular the coupled simulation is comparable with the standalone ILM-PBS case, as the shedding is generated upstream in the low Mach/incompressible domain, while some differences are observed in the standalone C-DBS simulation. Density variations are introduced by the downstream compressible inlet treatment. Gauge pressure coupling has proven to be appropriate for this test case, but pressure oscillations in the downstream domain are observed, with possible eventual consequences if the condition is applied to more general and realistic industrial cases.

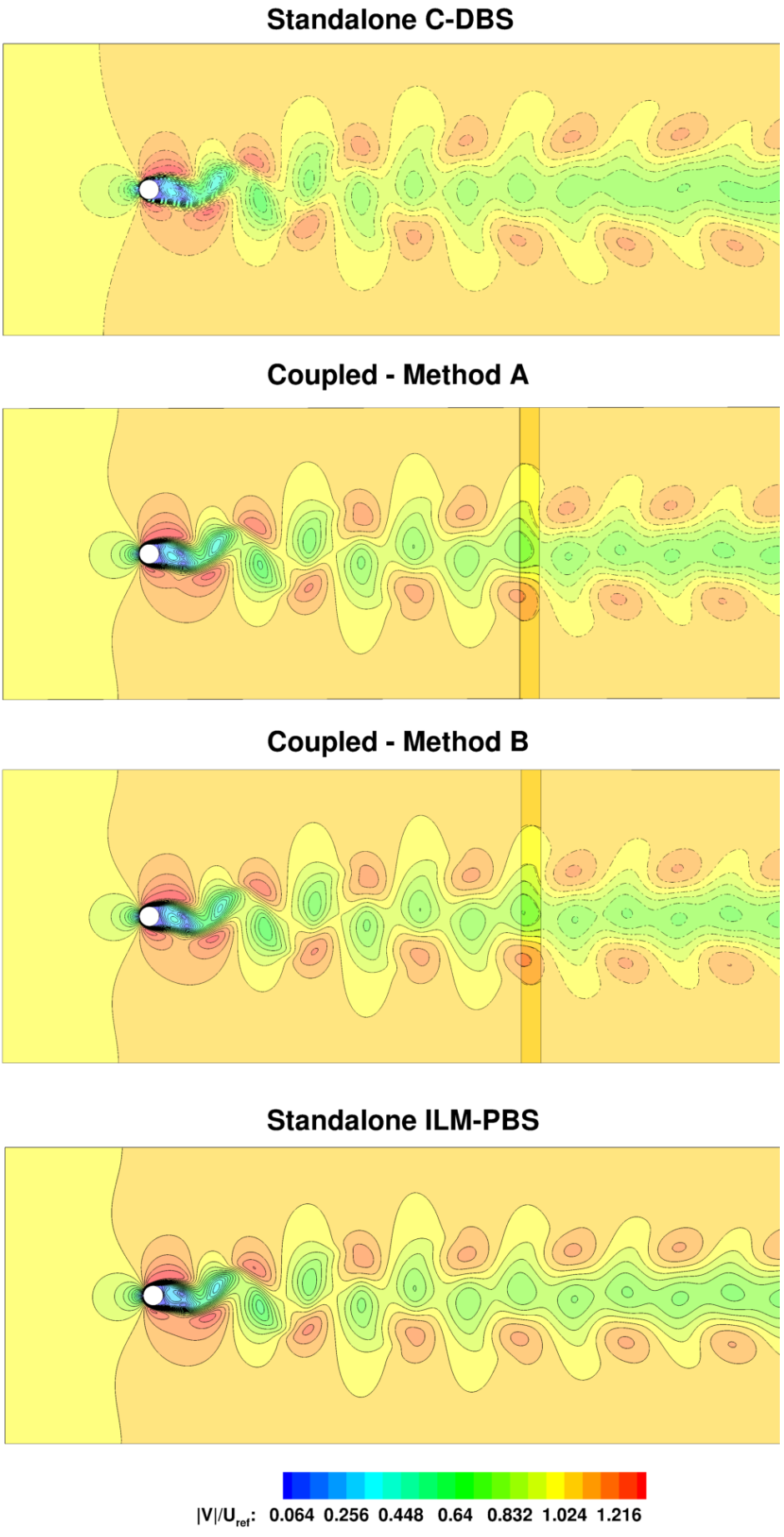

FIGURE 5.16: Normalised velocity magnitude, comparison coupled Method A and Method B ILM-PBS (solid) / C-DBS (dashed-dotted) and standalone simulations, cylinder shedding

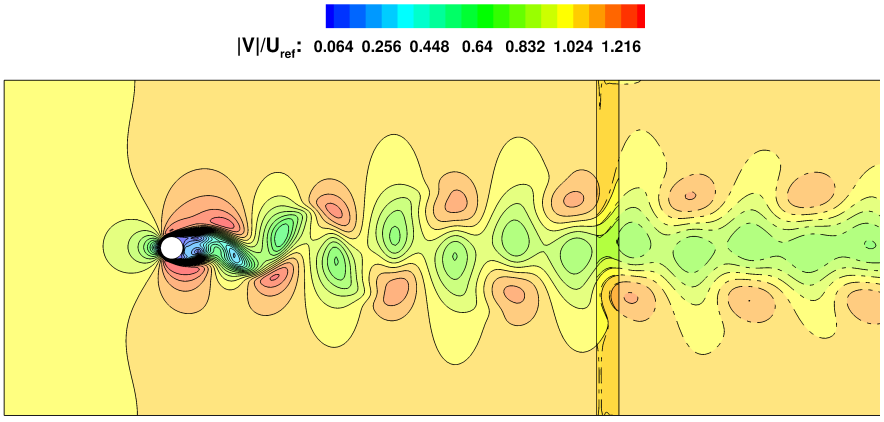

FIGURE 5.17: Normalised velocity magnitude, coupled Method D ILM-PBS (solid) / C-DBS (dashed-dotted), cylinder shedding

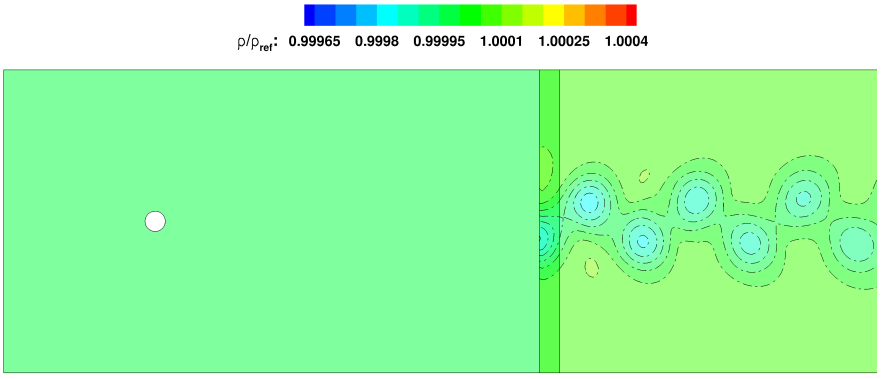

FIGURE 5.18: Normalised density, coupled Method A ILM-PBS (solid) / C-DBS (dashed-dotted), cylinder shedding

Method D has shown to corrupt the flow field in correspondence of the inlet and it will be further tested on next case.

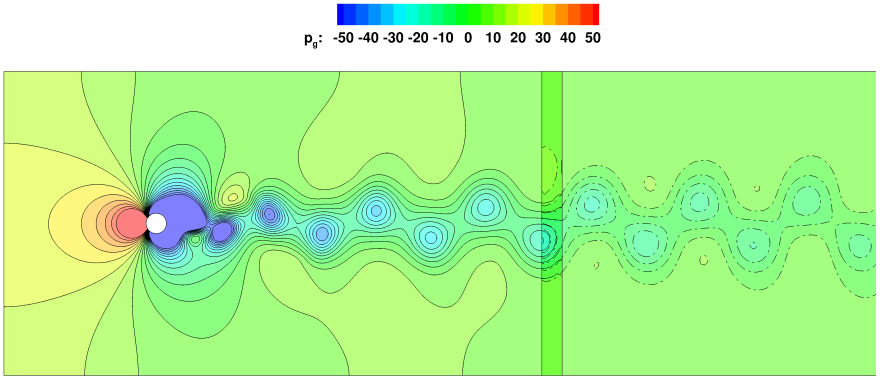

FIGURE 5.19: Gauge pressure, coupled Method A ILM-PBS (solid) / C-DBS (dashed-dotted), cylinder shedding

5.1.4 Downstream Obstacle

The vortex test case (and the circular cylinder) is characterised by a disturbance travelling from the upstream to the downstream domain. In order to assess the proposed methods in a case representative of a downstream potential field affecting the upstream flow (NGV blade potential field in a real engine) a square cylinder case was designed. In particular the main objective is the evaluation of the reflecting properties of the characteristics (Method A)/over-imposed (Method D) interface treatments. The case is also used to assess the possible influence of position and depth of the overlap region for gauge pressure exit coupling.

The obstruction square object has a side of length $L = 0.03\ m$. The total length of the case in the axial direction is $0.475\ m$, and the upstream side of the square is located $0.202\ m$ away from the inlet. The case extends for $20/3\ L$ in the vertical direction, at which periodic conditions are applied. The case is made two-dimensional by using two cells in the third normal direction where symmetry conditions are applied. The grid is uniform from the inlet boundary until the axial position of the end of the square cylinder, with a cell dimension of $1/30\ L$, and it is progressively axially unrefined downstream of it. For the coupled simulation the overlap region is located upstream of the obstacle, which is entirely resolved within the compressible domain. Two possible overlap regions with different dimensions have been assessed. In particular the downstream C-DBS domain has been left unchanged while the location of the exit of the upstream ILM-PBS

domain has been moved in the axial direction. In the first case the upstream domain has a total length in the axial direction of 20/3 L, while in the second case it has a length of 13/3 L. The first overlap has a span in the axial direction of 2.5 L and it is such that the exit of the low Mach number domain is located just two grid cells upstream of the obstacle. The second overlap region instead is only 1/6 L long. In the following they will be addressed as "Large Overlap" and "Small Overlap". The downstream domain extends for 8.1 L downstream of the obstacle. The flow is such that the Reynolds number based on L is $Re = 100$ and $M = 0.15$. In this case the mach number is chosen to be representative of a combustor exit close to the turbine. The time step of the simulation has been chosen to resolve the expected shedding period with approximately 50 time steps. The obtained CFL at inlet is 5.1.

Method A and Method D are compared in Fig. 5.20, where an instantaneous snapshot of normalised axial velocity is shown for the two Methods in the case of "Large Overlap". The results obtained with Method B are not reported in here as they are comparable to the ones obtained with Method A, and additional investigations are needed for a proper comparison between them. While for Method A a good match is observed in the overlap region between the contour lines from the ILM-PBS and C-DBS simulations, in Method D a large mismatch is found in the overlap between the contour lines, and in particular in the proximity of the inlet. A closer look at the C-DBS domain shows that the contour lines are collapsing in correspondence of the inlet interface, where they are almost parallel to the boundary. Method D has shown to be reflective: as expected the over-imposed inlet interface, conserving density and temperature from the low Mach domain, and hence keeping the value of pressure constant and equal to p_{therm}, is unphysical for compressible flows and produces reflections. Method D has to be discarded for coupling applications.

Looking at Method A, a comparison with full standalone cases was performed to assess the quality of the inlet coupling interface in the case of a downstream potential field. Results of the "Large Overlap" case are shown in Fig. 5.21 for the normalised average velocity magnitude, where solid contour lines represent the ILM-PBS solution while dashed-dotted contour lines refer to C-DBS data. Data have been averaged over 1000 time steps. Lines in bold are drawn from the standalone simulations, while simple lines are drawn from the coupled simulation. The figure is coloured with coupled simulation data. The figure shows a good general agreement between the three solutions (ILM-PBS,

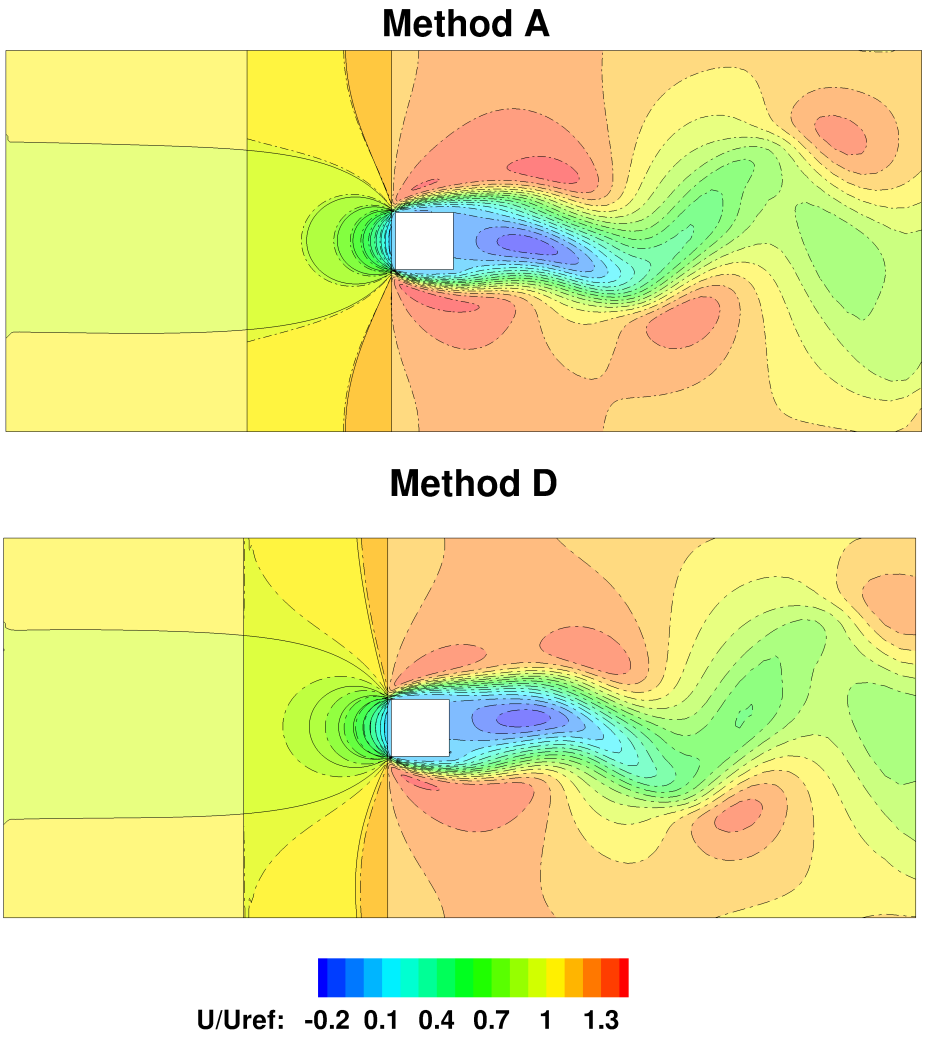

FIGURE 5.20: Assessment of Method A and D for downstream disturbance, low Mach (solid line) / compressible (dashed-dotted) coupling, downstream obstacle

C-DBS and coupled ILM-PBS/C-DBS). A zoom on the potential region of the obstacle is shown, which highlights the differences between ILM-PBS and C-DBS predictions in the extent of the potential field. It is interesting to note how the coupled simulation contour lines are localised in between the contour lines of the two standalone simulations in the potential region, where the coupling overlap is located. This is not true any more downstream of the cylinder, where the coupled simulation appears closer to the compressible standalone results and its contour lines are not always located in between the two standalone ones (e.g. see velocity in the passage between two periodic obstacles).

As a final check the influence of the location of the ILM-PBS exit boundary with respect to the obstruction and in particular of the relative axial dimension of the overlap region was assessed. In Fig.5.22 the two "Large Overlap" and "Small Overlap" cases

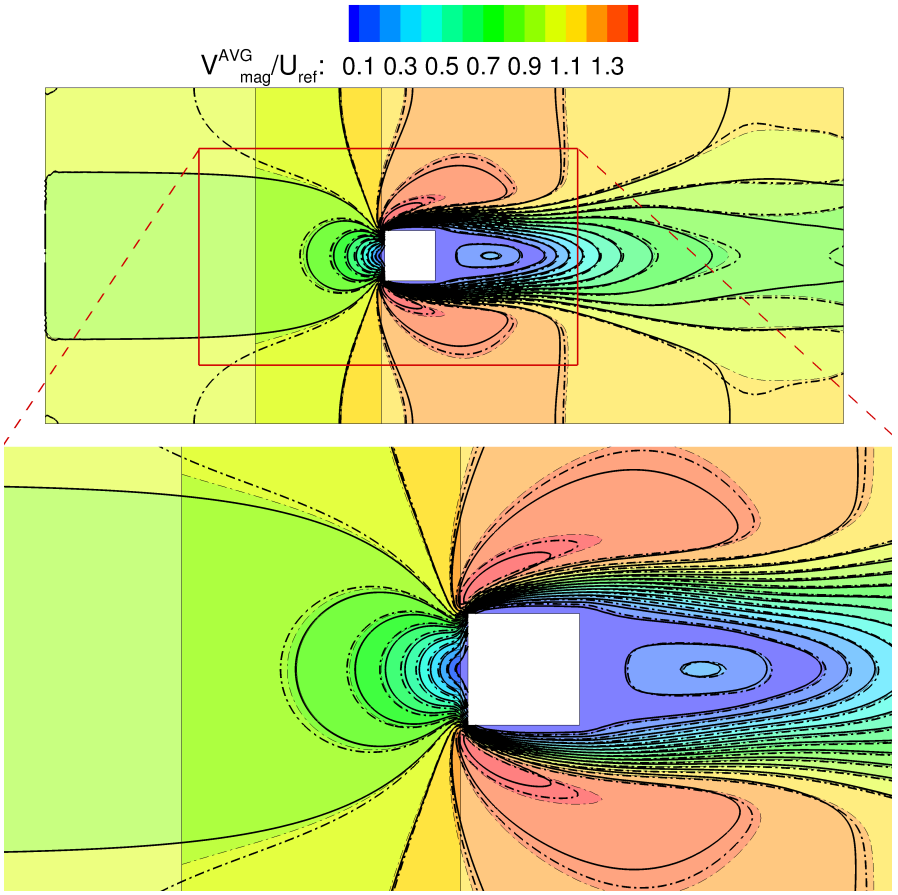

FIGURE 5.21: Normalised Average Velocity Magnitude, Comparison Standalone(ILM-PBS (-)/ C-DBS (- · -)) - Coupled simulations (ILM-PBS (–) / C-DBS (– · –)), downstream obstacle

are compared. The velocity results are almost identical, confirming the minimal influence of the dimensions and location of the overlap region. We note here that a gauge pressure imposition is being used at the ILM-PBS outlet to ensure a relatively strong coupling. The case, although being unsteady in nature, is not expected to produce very big oscillations in front of the obstacle and the results can be considered valid for steady cases, while the extension of the conclusions drawn here to unsteady cases cannot be claimed. As shown, by moving axially the location of the ILM-PBS outlet, the results in the velocity field are almost unaffected, confirming the ability of the interface to capture the downstream potential effect and its suitability to be used in the coupling. Nevertheless, looking at the gauge pressure field in Fig. 5.23 we can observe differences in the predicted pressure in the upstream ILM-PBS domain. In particular the two overlap cases are compared and contour lines are shown. A comparison with the standalone C-DBS simulation is also reported. While the results are identical for the compressible part of the domain between the three simulations (Large Overlap, Small Overlap and

Standalone C-DBS), some differences in the contour lines is observed in the ILM-PBS region between "Large Overlap" and "Small overlap" cases. A possible explanation is that in the "Large Overlap" case there is more room for inconsistencies between the two codes to appear in the overlap region, as the inlet interface is located far from the outlet one, and the region of the domain solved by both codes is bigger. As a consequence, even though the downstream field is relatively unaffected for this particular test case, the test has shown that it is advisable to have a relatively small overlap region when using a gauge pressure exit interface, to reduce the build up of inconsistencies in the overlap. Even though this conclusion has been drawn on a test case intended to evaluate the inlet interface to be used in the memory based coupling, this has to be taken into account for steady file based coupling, which inherently relies on gauge pressure exit imposition.

In conclusion, Method D has shown to be reflective at the inlet interface, as expected, and it has been discarded as a possible candidate for the coupling. Method A has shown to be capable of adjusting its inlet velocity to improve the non-reflecting properties of the interface, while ensuring that discrepancies in the velocity field in the overlap region between the two domains are small. The solution has been successfully compared with the two standalone simulations showing that the coupling is a compromise between the two solutions which often are, as in this case, different. The overlap depth has shown to have an influence on the upstream pressure field, and a small overlap has proven to be advisable with respect to a big one, to reduce inconsistencies between the two solutions.

5.1.5 Backward Facing Step

Weak interface - file based coupling and memory based coupling Method A

After the initial assessment on the Annular Diffuser case (Sec. 5.1.1), to validate the file based coupling a more demanding test case was chosen, consisting of a backward facing step, for which experimental data are readily available. The case has been experimentally and computationally investigated by Driver and Seegmiller [139]. The height of the step is here defined H and the height of the tunnel at the inlet is $Y_0 = 8H$. The case with no wall divergence is considered in our study. The Re based on the freestream velocity and hight of the step is equal to $Re = 68000$. Standard atmospheric conditions are

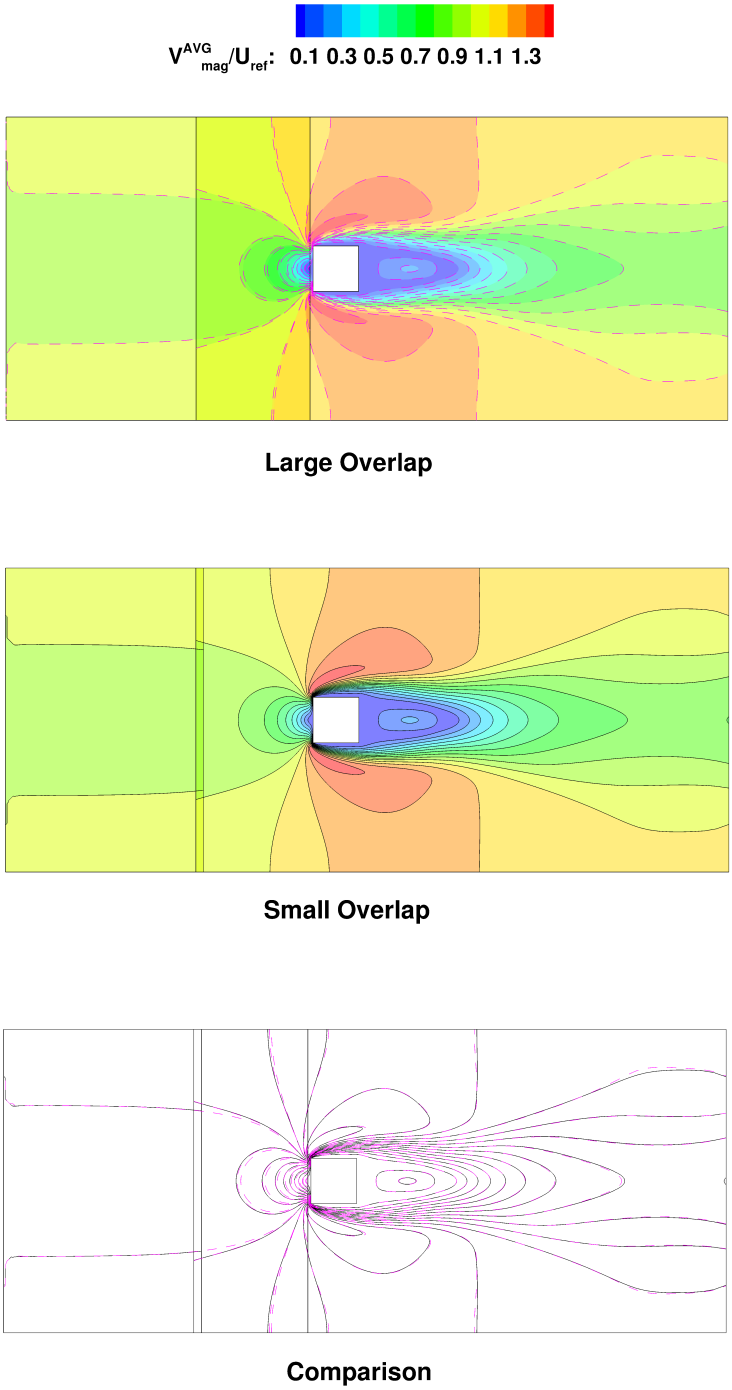

FIGURE 5.22: Normalised Average Velocity Magnitude, Comparison "Large Overlap" (lilac dotted lines) / "Small Overlap" (solid black lines), downstream obstacle

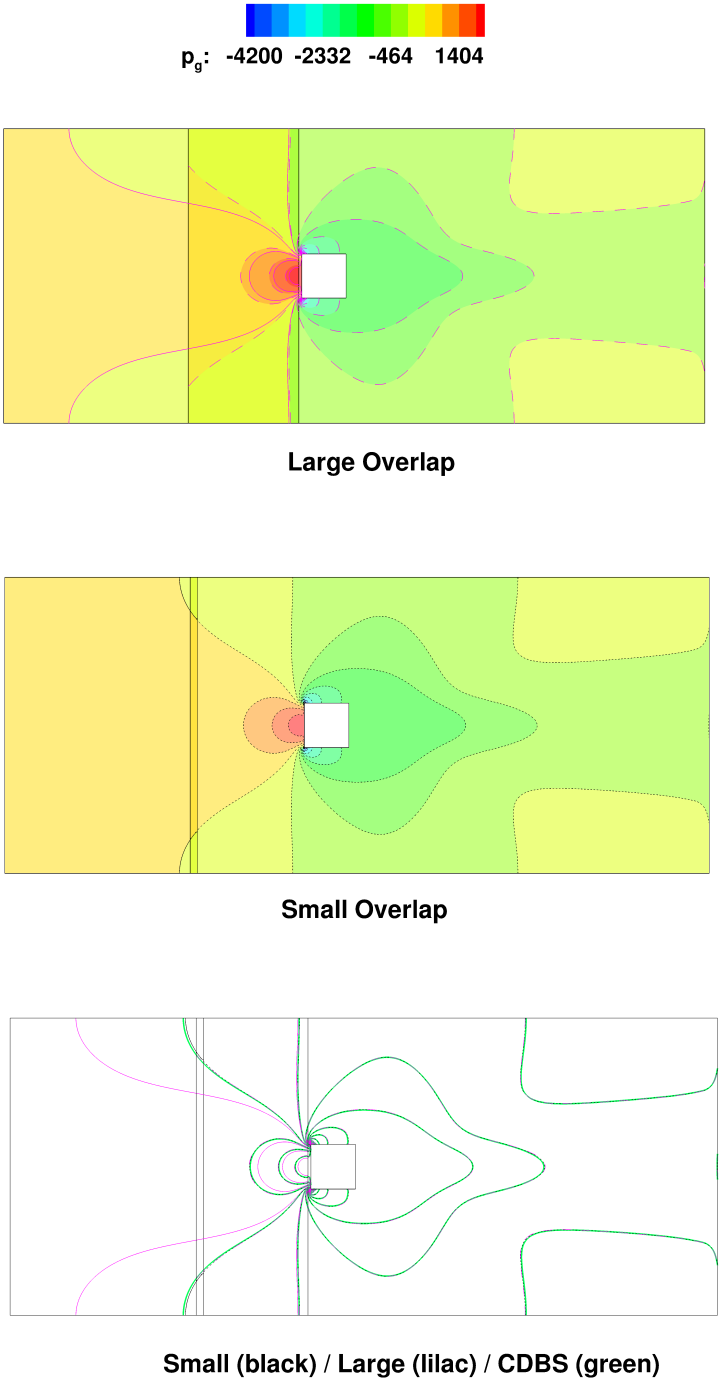

FIGURE 5.23: Gauge Pressure, Comparison "Large Overlap" (lilac) / "Small Overlap" (black) / Standalone CDBS (green), downstream obstacle

considered ($P_{therm} = 101325\ Pa$, $T = 289\ K$). The resulting Mach number of the flow is 0.129. The reference position in the flow (x) direction is taken to be the position of the step. The upstream low Mach number domain extends in the x direction from $-4H$ upstream of the step to $8H$ downstream of it. The downstream compressible domain instead extends from $7.5H$ to $50H$ downstream of the step. The overlap region is $0.5H$ long. A structured mesh has been created for both the domains, with only two cells in the spanwise (z) direction, making the case virtually two-dimensional. The grid is not coincident in the overlap region, with much more elongated cells along the flow direction in the upstream domain than in the downstream domain (with a ratio between the two of almost 7 to 1 in the x direction). This is done to test the robustness of the method as the coupling grids are independently generated and are not expected to be the same in real industrial applications. The $k - \epsilon$ turbulence model is used in both domains and a $y^+ \approx 30$ is obtained with the current near wall cell dimension. Few coupling iterations, around 20, are performed. Average pressure at the interfaces is monitored for the coupling together with the residual of each individual solver as seen in Fig. 5.24 and Fig. 5.25.

The results of the coupled simulation for the velocity magnitude normalised with respect to the bulk velocity and for the gauge pressure normalised with respect to ambient pressure are shown in Fig. 5.27. A comparison of u (x) velocity with experimental data along lines at constant x/H position is reported in Fig. 5.28. Figure 5.28 and Fig. 5.27 show that the method accurately transfer flow information between the two domains and it is capable of accurately predicting the flow behaviour.

Nevertheless, some mismatch is obtained at the interface in the vertical velocity v. In Fig. 5.29 both the axial and vertical velocities normalised with respect to the bulk velocity are reported. While the axial velocity shows perfect agreement at the interface, the vertical velocity, which is much smaller, shows clear problems. These are related to the weak imposition of the compressible inlet using characteristic treatment. Problems arise in particular in the region close to the bottom wall. The boundary treatment in fact assumes the characteristic wave to be normal to the inlet boundary, while transverse components, which can be important close to the wall, are neglected. The weak imposition, by definition, implies that different values from the ones imposed may be obtained at the boundary. This occurs in particular in regions where strong flow features are present, such as wakes etc. In order to prove the nature of the issue some more

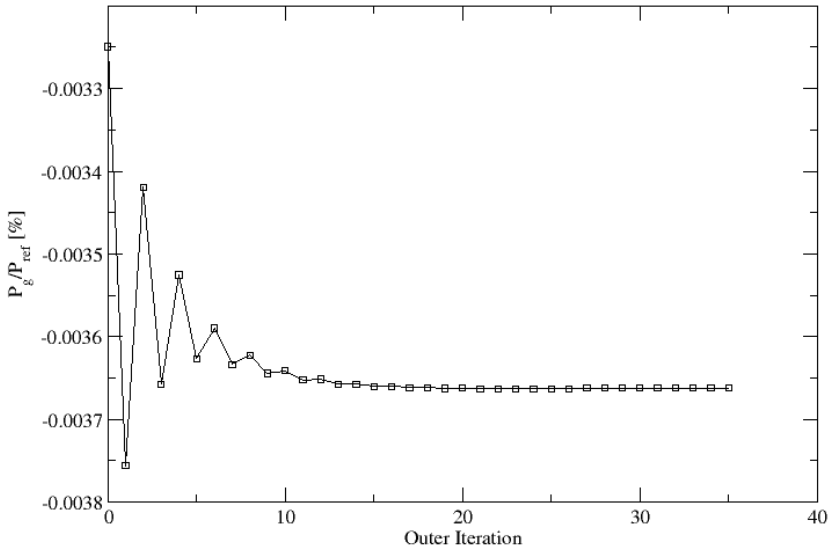

FIGURE 5.24: History if average pressure at ILM-PBS domain exit, Backward facing step

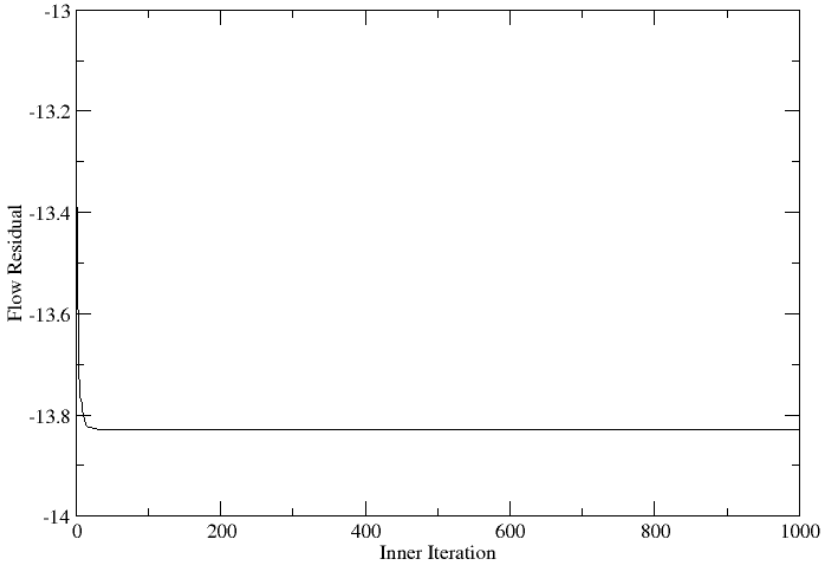

FIGURE 5.25: Residuals of the C-DBS code, convergence of a single coupling iteration, Backward facing step

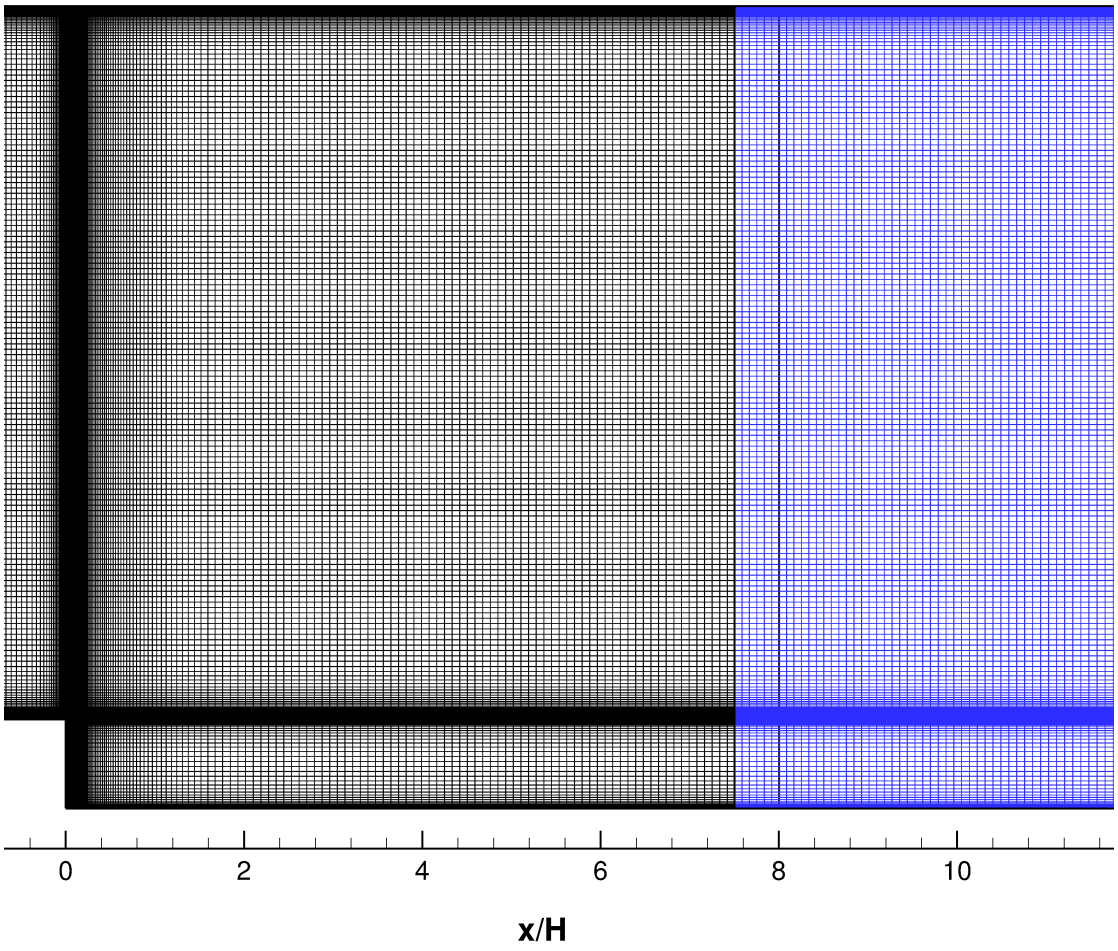

FIGURE 5.26: Detail of the refined mesh ($y+ \approx 1$) for backward facing step case - Low Mach number domain (black), compressible domain (blue)

investigations were carried out. At first the mesh was made consistent in the overlap region, and the wall was resolved up to $y^+ \approx 1$, to exclude the influence of the wall laws. Figure 5.26 shows a detail of the mesh in a region close to the overlap zone. No significant improvements were obtained. Secondly a weak mass flow boundary condition (Method A of Sec. 4.2.1) was used instead of the original stagnation variables based boundary condition. Again, only very small improvements were obtained in the v velocity at the interface. As an example of the weak behaviour shown by the characteristic boundaries, in Fig. 5.30 the pitch angle of the flow imposed at the inlet boundary and the one actually obtained in the flowfield are shown for the characteristic mass flow inlet case ($y^+ \approx 1$), with clear differences. When looking at the figure we recall the case is almost two-dimensional with only two cells in the z direction.

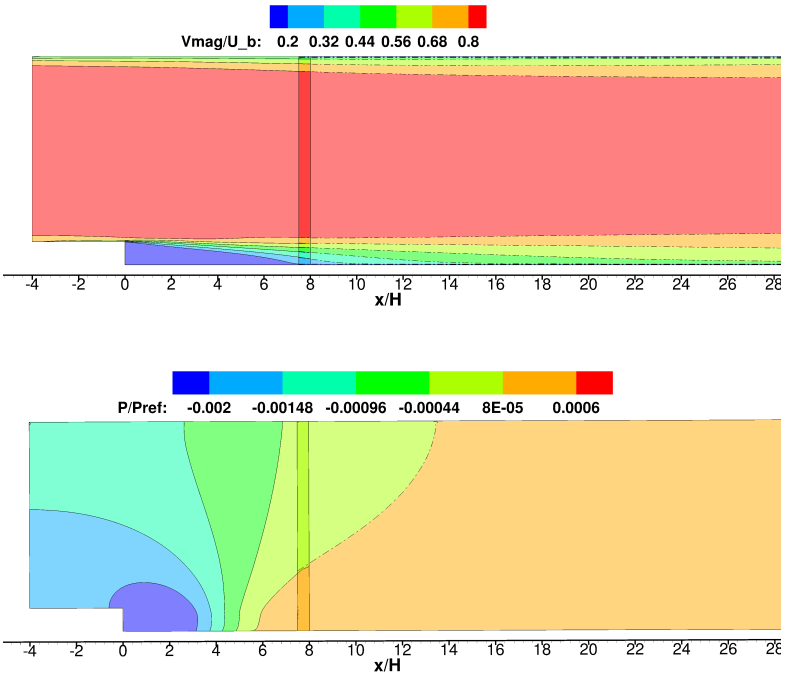

FIGURE 5.27: Normalised velocity magnitude and normalised gauge pressure for backward facing step case - Low Mach number domain (solid line), compressible domain (dashed-dotted line)

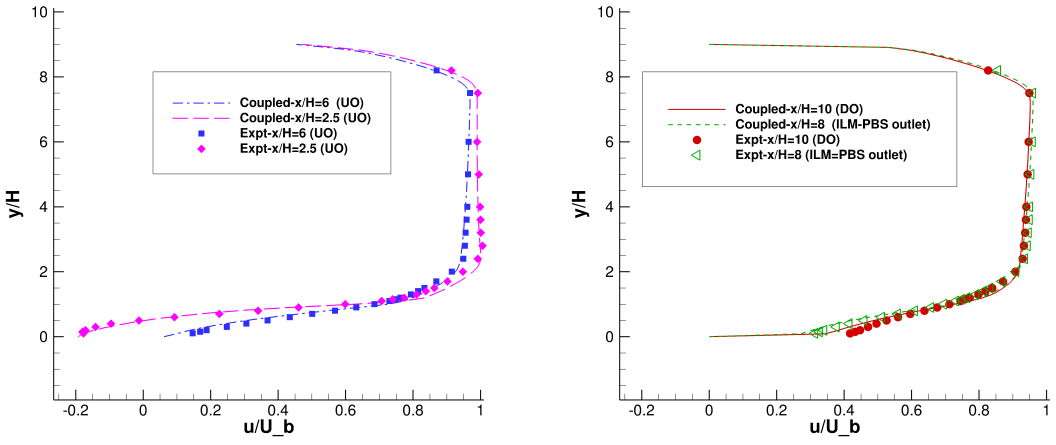

(a) Upstream of the overlap

(b) Downstream of the overlap

FIGURE 5.28: Normalised axial velocity profiles at different axial locations x/H for backward facing step case - Upstream of the overlap (UO) and downstream of the overlap (DO)

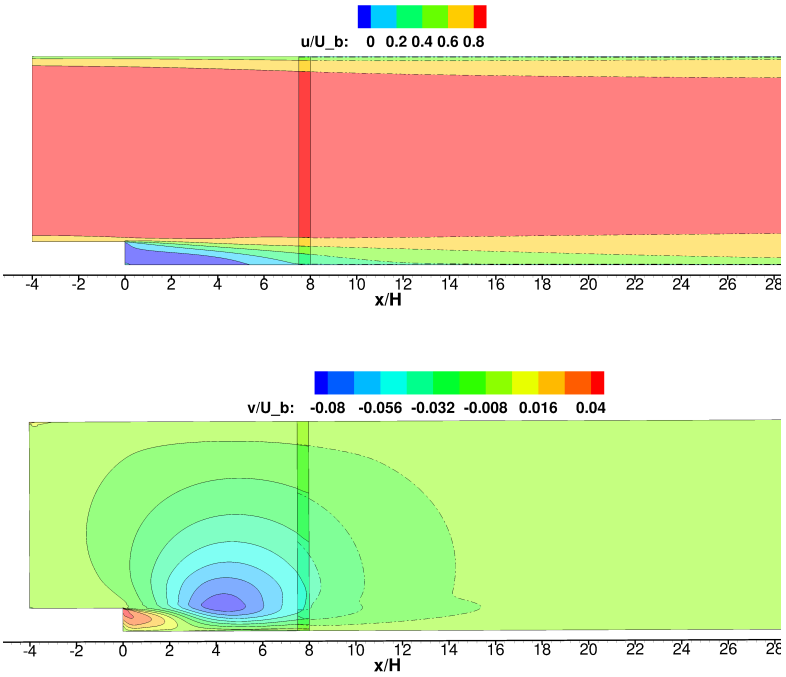

FIGURE 5.29: Normalised axial and vertical velocity for backward facing step case

In conclusion, the case, run on the file based coupling procedure, has shown good continuity of axial velocity and pressure at the interface. Very good agreement with experimental data was obtained. Some mismatches are clearly present in the vertical velocity, due to the weak imposition of the downstream inlet boundary condition. Only a strong imposition can improve the solution continuity at the interface, and it is reported in the following.

Memory based coupling Method B

The same backward facing step steady case used for the assessment of the file based coupling was adopted to investigate the improvements obtained by using a strong imposition, Method B, over a weak characteristic boundary (Original B.C. and Method A). Method C and Method D were previously discarded (see Sec. 5.1.2 and Sec 5.1.4) and they have not been tested on this case. In order to eliminate any possible wall-law difference influence on the coupling, a finer grid was used at the wall, to obtain a $y^+ \approx 1$, as already discussed above in the file based coupling section of this test case. What we are looking for is a better agreement at the inlet interface in particular for the vertical velocity v. We initialised our solution from a previous data (Method A), in which all the main structures were already developed. As can be seen from Fig. 5.31

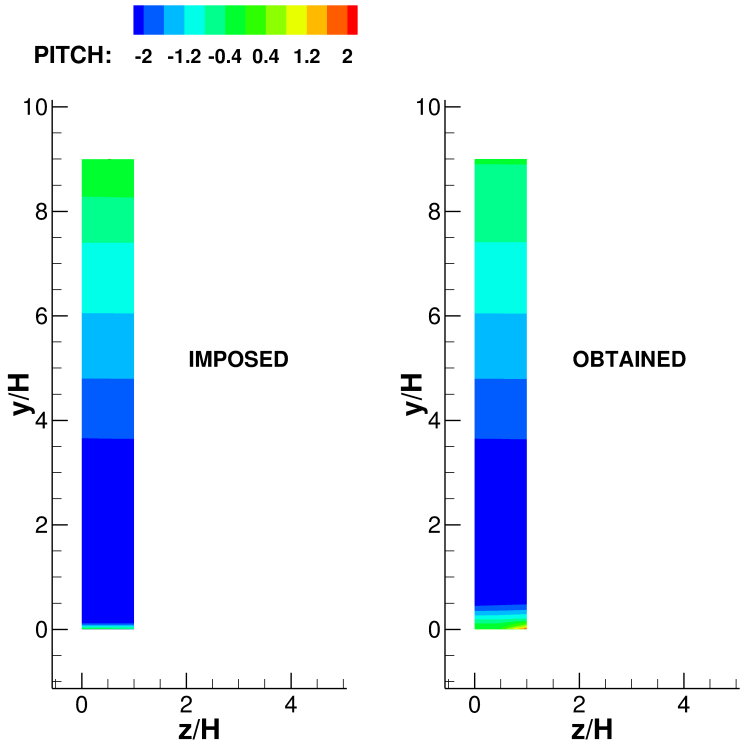

FIGURE 5.30: Normalised axial and vertical velocity for backward facing step case

using a strong imposition both velocities u and v show a very good agreement at the interface, overcoming the issue observed on using weak boundaries. The exchange of data occurs every 5 inner iterations and the convergence history of the C-DBS code is reported in Fig. 5.32. For this type of approach (memory based coupling) we did prefer not to wait for each solver to completely converge before the exchange. Whether this is helpful in speeding up the overall coupling convergence, it has not been analysed with enough details in this work. Exchanging partially converged solutions to a completely different solver is more prone to introduce errors in the coupled solution, even though in this particular case it has shown to be a perfectly working approach. We recall that in this case the data exchange occurs within the solver, so the convergence of the solver and the one of the coupling are both seen in the figure. We observe oscillating but clearly decreasing residuals of the coupled simulation. In conclusion, Method B has shown to be capable of solving the inconsistencies in velocity at the inlet interface introduced by the weak characteristic treatment. It is then chosen as the best candidate for the inlet treatment in the memory based coupling.

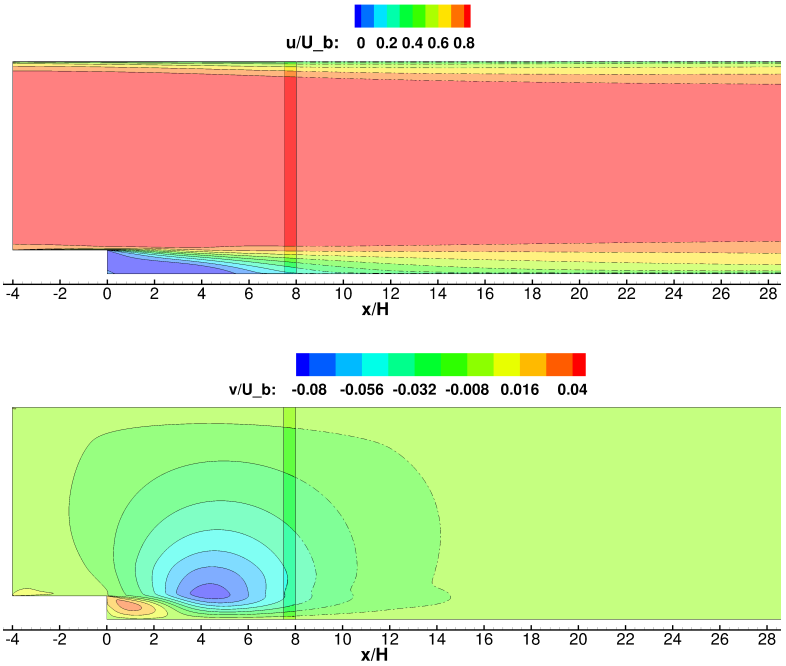

FIGURE 5.31: Normalised axial and vertical velocity for backward facing step case - Method B, Memory based coupling

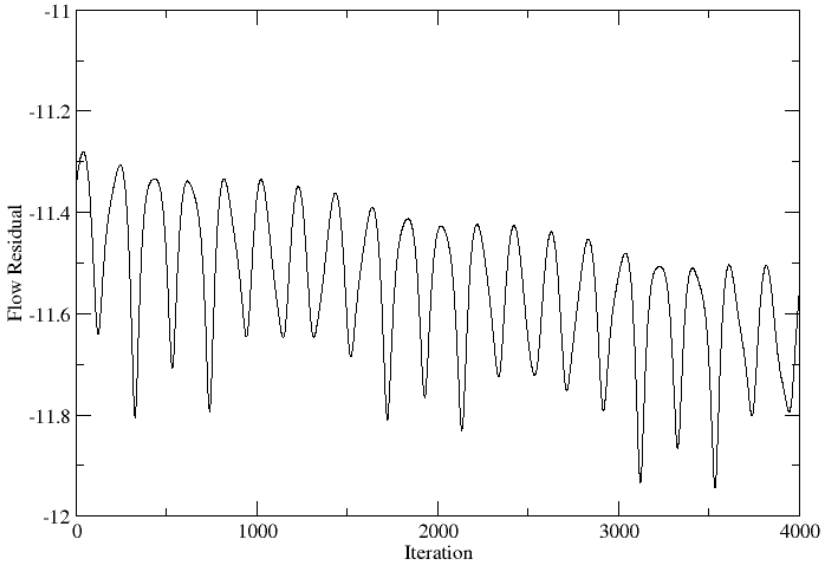

FIGURE 5.32: Residuals of the C-DBS code, convergence of a single coupling iteration, Backward facing step Method B

5.1.6 Sinusoidal disturbance

The objective of this test case is to evaluate the use of body force terms as a possible method to weakly impose a desired flow field in a region of the ILM-PBS domain. This is not a coupled case, only the ILM-PBS code will be used in a single standalone simulation, and a target velocity U_{target} of which the analytical expression is known will be forced in the ILM-PBS domain through the use of the body force approach. A rectangular domain of length $2l$ in the flow direction x was used ($0 \leq x \geq 2l$). In the direction orthogonal to the main flow direction the domain has length l and periodic conditions are applied. The case is made two-dimensional by using two cells only in the third direction with a total domain depth of $0.02l$ and symmetric conditions applied. The inlet velocity is constant u_{in} and the Re based on the inlet velocity and on the length l is 670. The body force is applied in the second half of the domain only ($x \geq l$). The target velocity imposed in the body force (see Sec. 4.2.2) has the form of:

$$U(x,y,t)_{target} = u_{in} + A(x)sin(ky - \omega t + \phi) \tag{5.3}$$

which correspond to adding a sinusoidal disturbance to the initial velocity. The frequency of the disturbance is $f = 0.16\frac{u_{in}}{l}$ while the wave length is chosen as $\lambda = \frac{1}{4}l$, from which $k = 2\pi/\lambda$ and $\omega = 2\pi f$. The speed of the wave in the vertical direction y is then $v = \lambda f$. Uniform grid spacing is used with a cell size of $\Delta x = 0.01l$. The time stepping Δt is chosen such that a mean unitary CFL is obtained with respect to the mean axial convective velocity. The amplitude of the disturbance $A(x)$ is a continuous function of the axial coordinate, chosen such that the first derivative of the U_{target} velocity component with respect to x is zero at the limits of the forcing region $x = l$ and $x = 2l$, and continuous throughout the region itself. In this way the forced velocity is inherently divergence free at the beginning of the forcing region and at the outlet boundary. $A(x)$ has the form of:

$$A(x) := \begin{cases} 0 & x < l \\ \frac{1}{(l/2)^2}(x-l)^2 & l \leq x < (l + l/2) \\ 2 - \frac{1}{(l/2)^2}(x-2l)^2 & x \geq (l + l/2) \end{cases} \tag{5.4}$$

The objective is in fact to force a divergence free velocity field both at the beginning of the forcing region and especially at the domain exit boundary, without introducing any vertical velocity component. The body force is only applied to the axial component of the momentum equations for this test case, and the velocity V is let free to adapt to the solution without any forcing. In the middle of the forced region $\frac{\partial U_{target}}{\partial x} \neq 0$ and a vertical component V different from zero is expected such that $\frac{\partial V}{\partial x} = -\frac{\partial U_{target}}{\partial x} = -sin(ky - \omega t)\frac{\partial A(x)}{\partial x}$. The constant γ_{BF} to be used in the definition of the body force, see Section 4.2.2, is chosen as $\gamma_{BF} = 2 \cdot 10^6$. This number was chosen as it is high enough to ensure very quick adaptation of the forced field to the desired values. It is also a good value as it is the same value used later for combustor-turbine interactions coupled calculations, where it is derived by the MIN-MAX considerations proposed above. The sensitivity of the flow response to its change is small. Much higher values lead to instabilities, and this value was chosen as the upper limit for stability reasons; this value is in fact already higher than the suggested $\gamma_{BF}^{MAX} = \frac{\rho u_{in}}{0.01l} = 1.22 \cdot 10^5$ obtained from the stability considerations proposed. The obtained results using $\gamma_{BF} = 2 \cdot 10^6$ represent the best we can obtain using body force for this set of grid, time step and flow conditions. $\gamma_{BF}^{MIN} = \frac{\rho u_{in}}{l} \log\left(\frac{A(x)}{0.01 * U_{target}}\right) \approx 400$ is instead very small, but we recall its meaning is the minimum value required to match forced and desired flow field at the end of the forcing region, based on their values at the beginning of it, in an ideal incompressible one-dimensional case. The minimum value is not enough for the flow field to adapt quickly to the forced values within the region itself. The case was run for 5000 time steps. The solution $U(y)$ along the vertical direction y at the final time step is shown in Fig. 5.33 and compared in Fig. 5.34 with the analytical solution at four different axial locations $x/l = 1.25$, $x/l = 1.5$, $x/l = 1.75$, $x/l = 2$. This latter figure shows that, as expected, the accuracy of the matching with the analytical solution is increasing with increasing depth in the overlap region. In particular the error on the amplitude of the disturbance is $\approx 11\%$ at $x/l = 1.25$, $\approx 6\%$ at $x/l = 1.5$, $\approx 1.7\%$ at $x/l = 1.75$ and almost zero at $x/l = 2.0$. Nevertheless, as the amplitude is increasing with the x direction, the relative error is not decreased, but it is found between $4 \cdot 10^{-4}$ and $8 \cdot 10^{-4}$ for all the four locations. The time evolution of the solution at the location $x/l = 2$ is shown in Fig. 5.35 where the normalised velocity is reported at four different time steps corresponding to $1000\Delta t$, $2000\Delta t$, $3000\Delta t$ and $4000\Delta t$. The error with respect to the analytical solution is really small at this location for all the time steps.

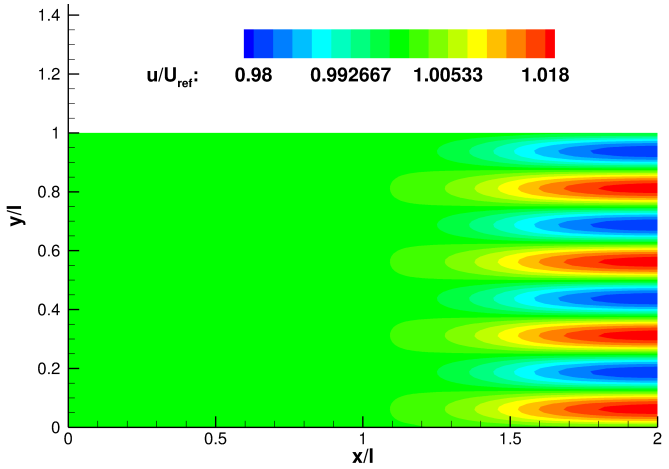

FIGURE 5.33: Normalised axial velocity, $t = 5000\Delta t$, ILM-PBS Body forced field, sinusoidal disturbance, Memory based coupling

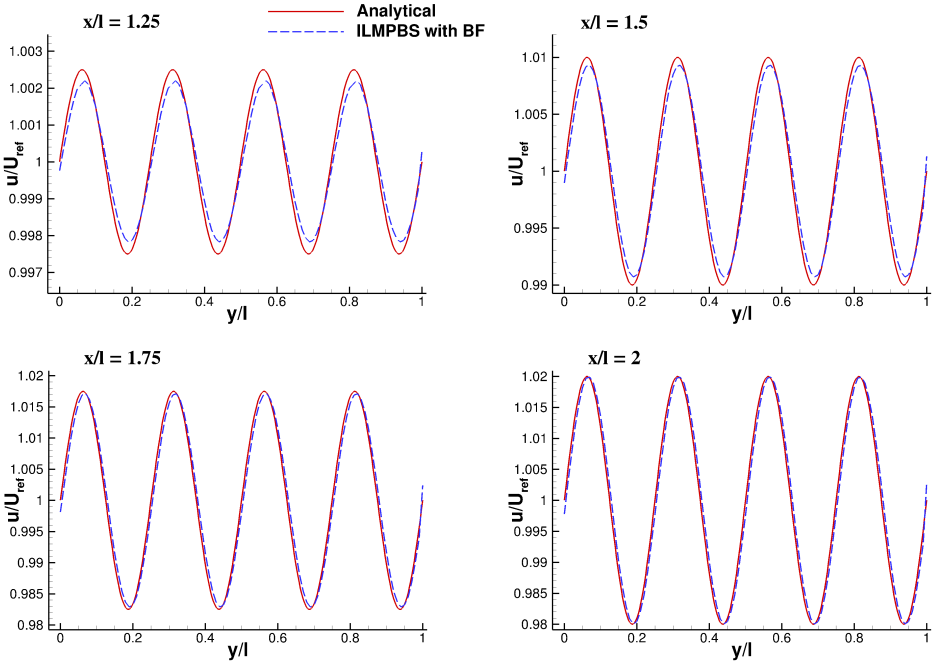

FIGURE 5.34: Normalised axial velocity, $t = 5000\Delta t$, Analytical / Body forced field comparison, sinusoidal disturbance, Memory based coupling

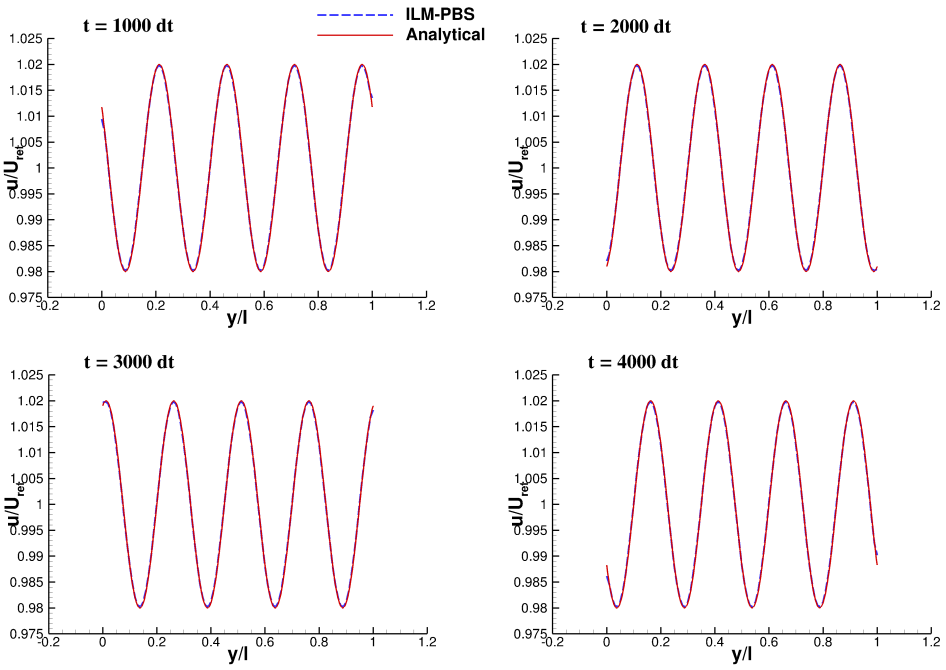

FIGURE 5.35: Normalised axial velocity, $x/l = 2$, Analytical / Body forced field comparison, sinusoidal disturbance, Memory based coupling

In conclusion, the body force is capable of weakly drive the unsteady solution to the desired analytical values. As expected the degree of agreement with the analytical solution increases as the flow penetrates into the forcing region. The error can be high at the beginning of the forcing region but it can be reduced to a very low value at the end of it.

5.2 Coupling Configuration for the Memory Based Coupling

In the previous section, for the memory based coupling, different interface treatments have been assessed for the C-DBS inlet, and the outcomes are:

1. "Method A - Mass Flow, Weak Characteristics" is a suitable method for the interface treatment, among the assessed ones, for its good performance in the vortex crossing test case (Sec. 5.1.2) and because of its intrinsic non reflective treatment (Sec. 5.1.4). Nevertheless some mismatches are present at the interfaces, due to the weak treatment applied (Sec. 5.1.5).

2. "Method B - Mass Flow, Free Fluctuations" has shown very similar behaviour to Method A, also providing some of the best results in the vortex test case (Sec. 5.1.2). It has also shown to be able to solve the inlet interface inconsistencies found when using a weak characteristic boundary (Sec. 5.1.5). It is chosen as the best candidate for the inlet treatment of the memory based coupling, to be used in realistic industrial coupled simulations.

3. "Method C - Mass Flow, Full Interface p_{therm}" has shown the worst results in the vortex test case (Sec. 5.1.2) and it is discarded as a candidate for the coupling.

4. "Method D - Mass Flow, Full Interface $p_{therm}+p_{(2)}^{ILM-PBS}$" is found to be reflective in the square cylinder test case (Sec. 5.1.4) and it is discarded as a candidate for the coupling.

The outlet treatment of the ILM-PBS domain using body force terms (Sec. 5.1.6) has demonstrated to be capable of driving a target analytical solution in the forcing region to the desired values. It is chosen as the coupling treatment in the memory based coupling, as the pressure exit condition has shown to be prone to instability in real industrial cases.

The unsteady test cases analysed in the previous section using memory based inlet interface conditions are here assessed on the chosen final memory based coupling configuration (Method B + Body Force). We do not report in here the test case definitions that can be found in the previous section, but we provide some additional results on the final configuration, which has not been shown previously as the interface conditions where separately analysed using a pressure exit interface, which is stronger and hence recommended to perform such analysis.

Taylor Vortex

The case details are reported in Sec. 5.1.2. The body force constant was imposed as $\gamma_{BF} = 3000$ and the force is imposed in most of the overlap region, with the exception of the first few cells close to the downstream inlet. The normalised vertical velocity at three different time steps during the crossing of the vortex of the overlap region is shown in Fig. 5.36. In Fig. 5.37 the tangential velocity along the vortex axis is shown

instead. The quality of the coupling configuration is confirmed and the errors in velocity are comparable with the ones obtained in Sec. 5.1.2.

Cylinder Shedding

The case details can be found in Sec. 5.1.3. The body force constant is chosen to be $\gamma_{BF} = 1000$ and the force is imposed in most of the overlap region, with the exception of the first few cells close to the downstream inlet. In Fig. 5.38 the normalised velocity magnitude is shown, to be compared with Fig. 5.16. Although a slight mismatch due to the choice of the time snapshot can be observed between all the simulations, the overall agreement is very good, confirming the final configuration of the memory based coupling is capable to properly reproduce this test case. The relative error in the velocity in the overlap region between upstream and downstream domains is of the order of 1.5% as previously found.

Downstream Obstacle

The case details can be found in Sec.5.1.4. The body force constant is chosen to be $\gamma_{BF} = 150000$ and the force is imposed in most of the overlap region, with the exception of the first few cells close to the downstream inlet. An unsteady snapshot is reported in Fig. 5.39. It confirms that the agreement between upstream and downstream domains in terms of velocity field is very good. Nevertheless, in Fig. 5.40 the time averaged results of the coupled simulation in the upstream domain are compared with the standalone ILM-PBS simulation (for clarity of visualisation only the ILM-PBS solutions are visualised and presented): a shift of the contour lines is found in the passage regions above and below the stagnation generated by the obstacle, with respect to the standalone simulation, which was not observed in the previous results of Sec. 5.1.4. This means the Body Force approach is weaker than pressure exit and less capable of reproducing the correct physics in such a demanding simulation such as the one proposed here, in which the outlet boundary is just a couple of cells upstream of an obstacle. In another way, forcing the ILM-PBS upstream domain velocity field towards the downstream C-DBS domain values in a finite region of the overlap, produces less physical results than letting the two codes compute their own "different" physical solution after the application of a simple pressure boundary condition. With this in mind, we nevertheless observe

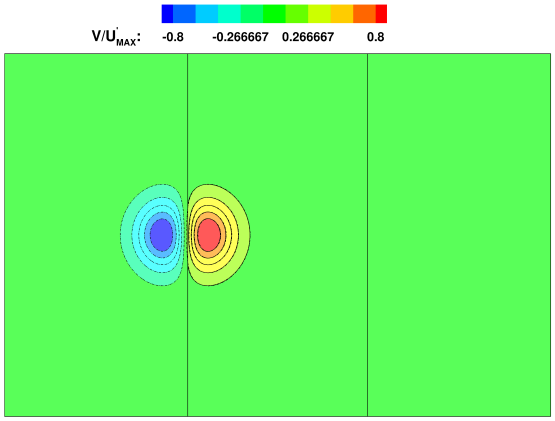

(a) vortex crossing the inlet

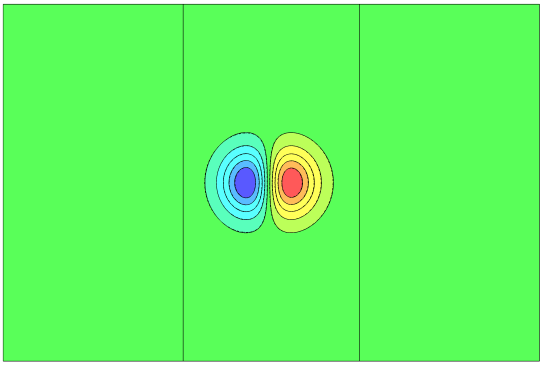

(b) vortex inside the overlap region

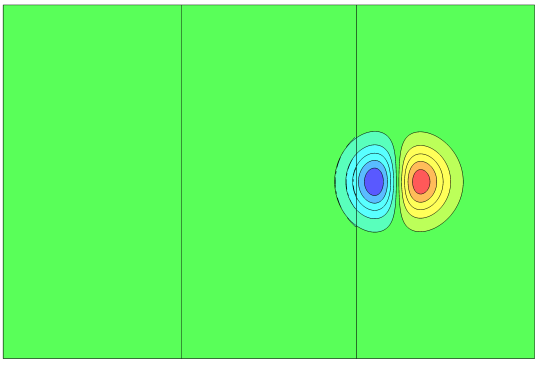

(c) vortex leaving the upstream domain

FIGURE 5.36: Normalised Vertical Velocity at three time steps, Taylor vortex crossing the interface from low Mach number to compressible domain, Method B + Body Force

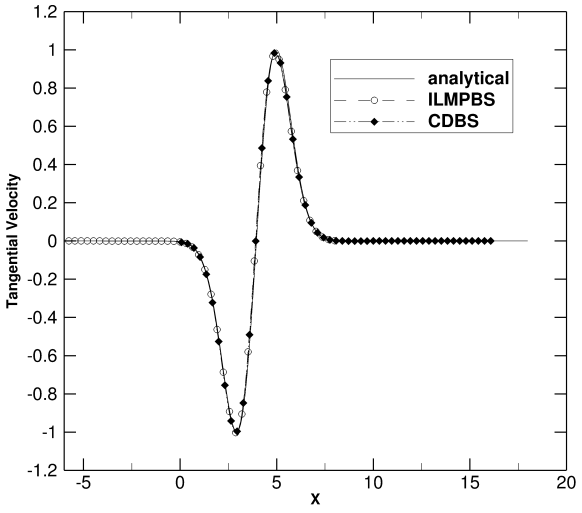

(a)

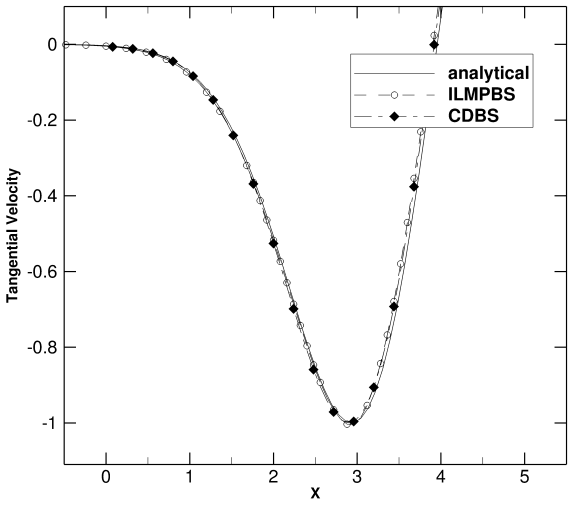

(b) detail

FIGURE 5.37: Normalised Vertical Velocity along the vortex axis, Taylor vortex located in the overlap region, Method B + Body Force

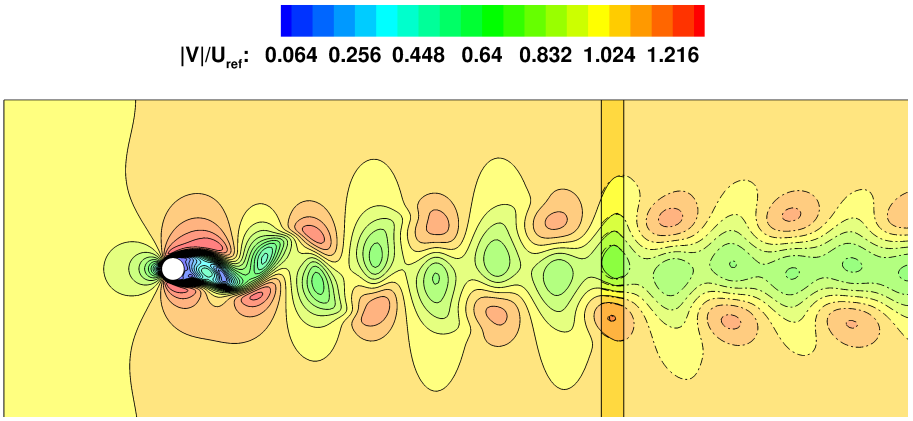

FIGURE 5.38: Normalised velocity magnitude, Method B + Body Force, cylinder shedding

a very good behaviour of the coupled simulation, it is stable and produce accurately all the main features of the flow introducing acceptable errors. The maximum velocity difference between the two (coupled and standalone) solutions is 0.3% of the reference velocity, but the relative difference $(V^{AVG}_{coupled} - V^{AVG}_{ILM-PBS})/V^{AVG}_{ILM-PBS}$ can go up to 30% or more in the very few cells close to the outlet in correspondence of the obstacle, as it can be seen in Fig. 5.41. The difference is concentrated in the very low velocity region. Taking into account that the inherent difference in the same region between standalone ILM-PBS and standalone C-DBS solutions is around 20%, this result is not surprising and totally acceptable. The pressure exit boundary is not an option for unsteady cases for all the reason explained in this work. Hence the body force is considered as a good alternative to perform two ways coupled simulations.

5.3 Closure

The file based coupling has been initially assessed on an annular diffuser case (Sec. 5.1.1) and then validated on a backward facing step case (Sec. 5.1.5), where good agreement with experimental results was obtained. Some mismatches between the solution of the two codes are observed at the interfaces, due to the weak characteristic treatment of the C-DBS inlet boundary. The procedure is ready to be applied to realistic industrial coupled simulations.

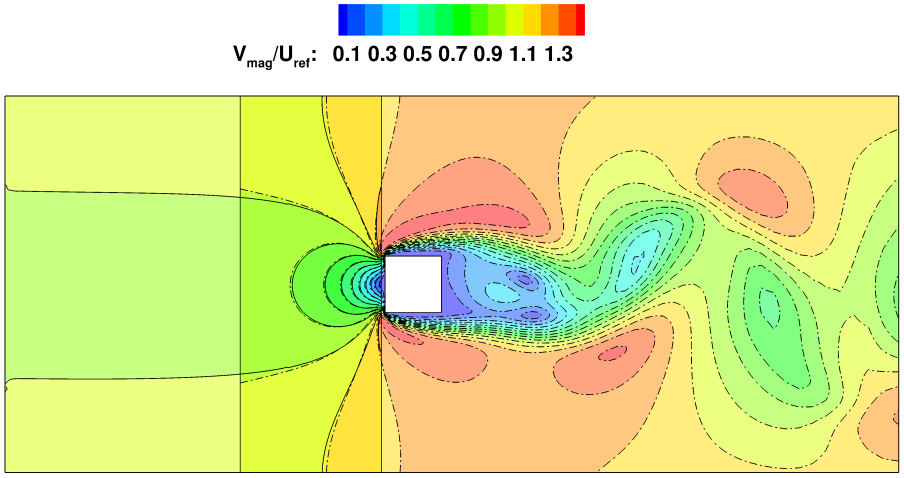

FIGURE 5.39: Normalised velocity magnitude, Method B + Body Force, downstream obstacle

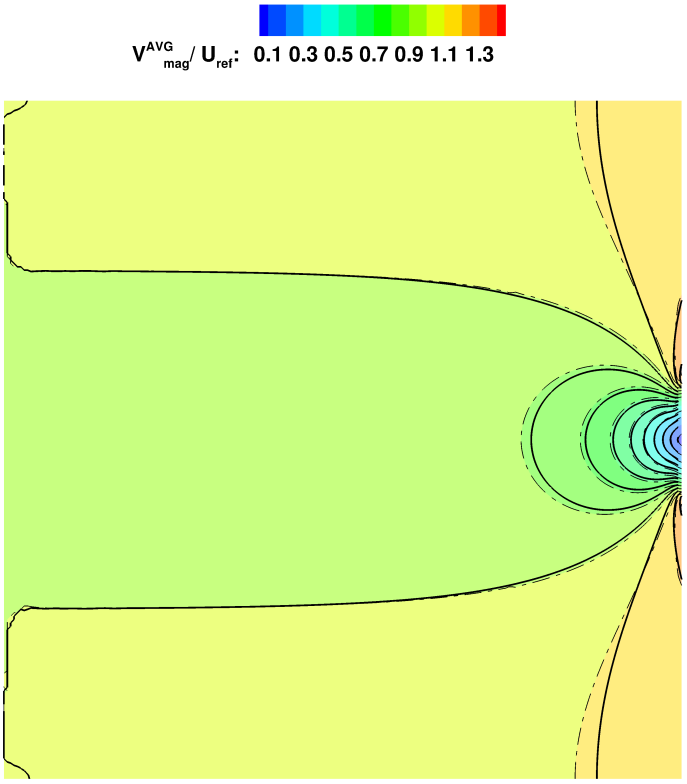

FIGURE 5.40: Normalised velocity magnitude, Comparison standalone ILM-PBS (solid) and Coupled Method B + Body Force (dashed dotted), upstream domain, downstream obstacle

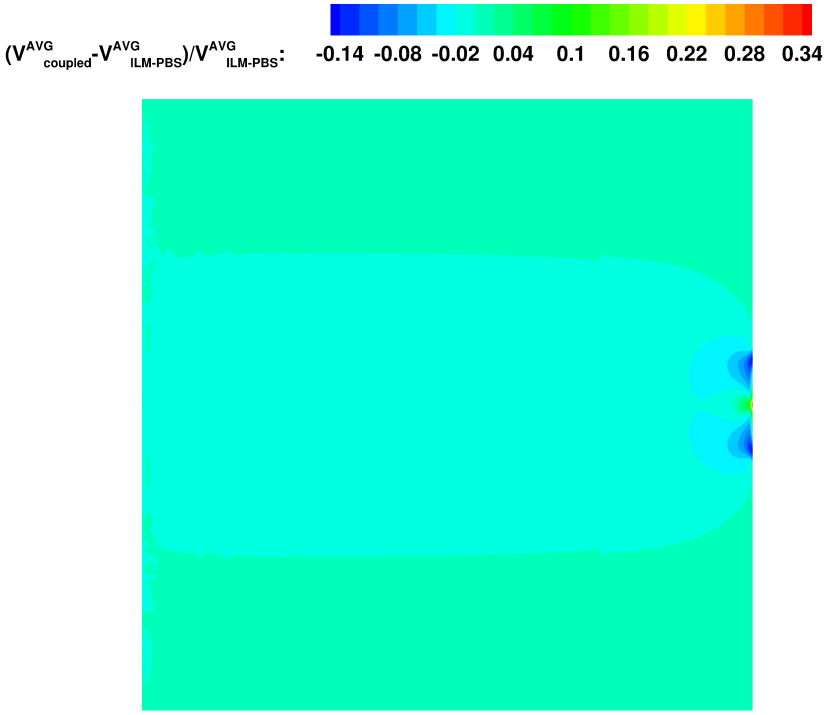

FIGURE 5.41: Relative difference in velocity magnitude between standalone ILM-PBS (solid) and Coupled Method B + Body Force (dashed dotted), upstream domain, downstream obstacle

For the memory based coupling instead, different inlet conditions for the C-DBS code have been assessed. Method B has been selected as the best candidate for the coupling. Moreover, the use of a body force in the ILM-PBS domain has been shown to be a stable and accurate procedure, whereas the pressure exit boundary had shown instability issues. The final memory based configuration has been tested and validated. Now we have a certain procedure in place to be applied to combustor-turbine interaction simulations.

Chapter 6

Combustor-turbine interaction: application

In this Chapter the application of the two coupling methodologies to a realistic industrial test case is reported. A simplified combustor-turbine configuration of a real small aero-engine was used for all the simulations. The case is presented in Sec. 6.1. Two different operating conditions were considered. In Sec. 6.2 the steady file based coupling is used and compared to a more traditional approach relying on standalone simulations, at a low velocity operating point corresponding to a ground rig test of the combustor. The boundary conditions data we were provided for the combustor reflect in fact the rig test, of which no experimental data are available. In Sec. 6.3 the memory based coupling is instead applied to an unsteady simulation and compared to the steady coupled file based solution of the same case, this time at an operating point representative of cruise conditions (the combustor boundary conditions provided were simply rescaled to obtain real cruise conditions for the turbine) .

6.1 Test Case

A simplified combustor-turbine configuration was considered. In the following the main features of the case are reported for the combustor and the HP turbine.

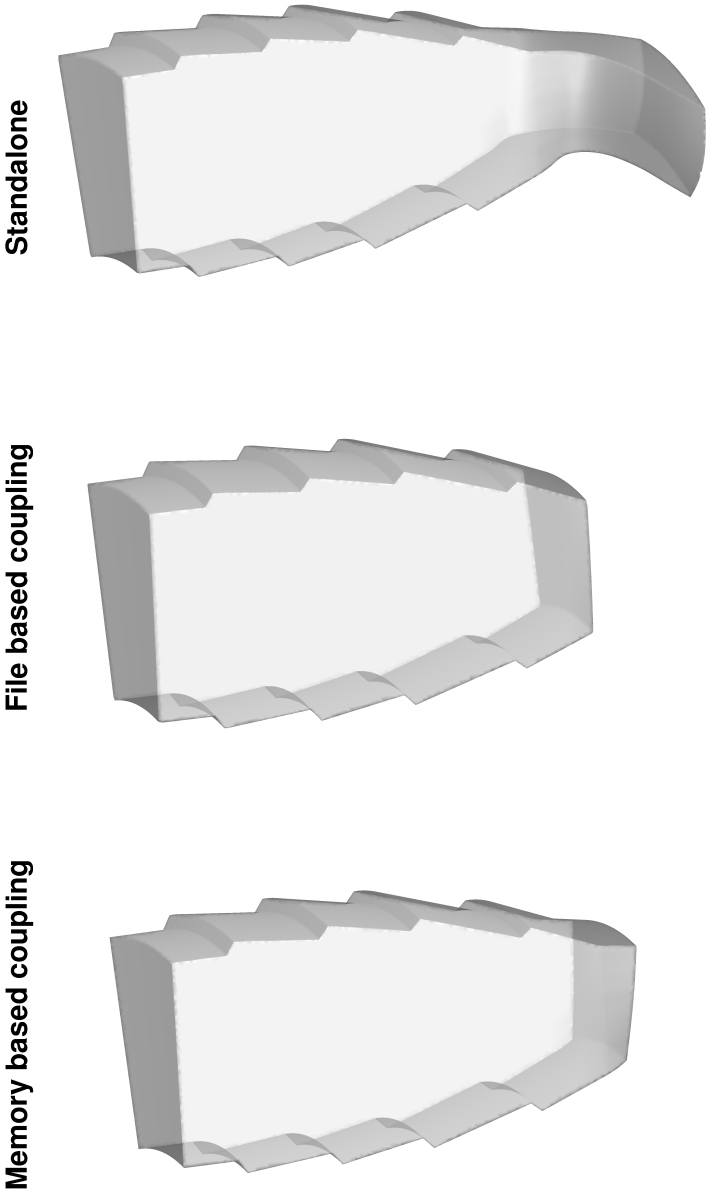

FIGURE 6.1: Combustor domain

6.1.1 Combustor

The combustor simulations details are listed in the following sections organised as: model, boundary conditions and mesh.

Model

An 18 degrees sector model of the annular combustor was used, which accounts for one fuel injector. The swirler, dilution holes and cooling slots were modelled through

TABLE 6.1: Boundary conditions for the combustor domain

	INLETS	OUTLET
Standalone	Mass flow, T, flow angles	convective outflow
File b. coupling	Mass flow, T, flow angles	gauge pressure
Memory b. coupling	Mass flow, T, flow angles	convective outflow+BF(region)

appropriate boundary conditions. The combustion process was modelled using a Hybrid Eddy Dissipation approach with a two step reaction mechanism [109], which was deemed to be relatively simple and yet accurate enough for the purpose of this work. Similarly, a simple turbulence model, the standard k-ϵ model, was chosen for the turbulence closure.

Three different configurations for the combustor exit region were considered for the standalone, file based coupling and memory based coupling simulations respectively (see Fig. 6.1). The first, adopted for the standalone simulation, represented a standard approach in which the combustor domain was extended downstream into the turbine nozzle region. In the present work the extension region corresponded exactly to the NGV domain having the blades removed. For the coupled simulations a different exit treatment was used, in which the boundary was located within a region just upstream of the NGV blades. The difference between file based and memory based coupling simulations stands in the location of the exit plane, which is much closer to the NGV leading edge for the latter case: as explained later a longer combustor, which allows a wider forcing region for the body force of the memory based coupling, from the theory gives more room at the flow to adapt to the downstream target velocity.

Boundary Conditions

In all cases mass flow imposition was used at all inlets. Temperature, flow angles and turbulence variables are also specified at those boundaries. The imposed swirl direction with respect to the NGV blades orientation and the exact mass flow split at all inlets does not necessarily represent the ones in the real machine. For the standalone combustor simulation the exit boundary is treated as a convective outflow, as this is standard practice to ensure a well behaved flow field in the last part of the combustor. For the file based coupling a pressure type of boundary condition is applied at the combustor exit. For the memory based coupling instead a convective outlet is used together with body

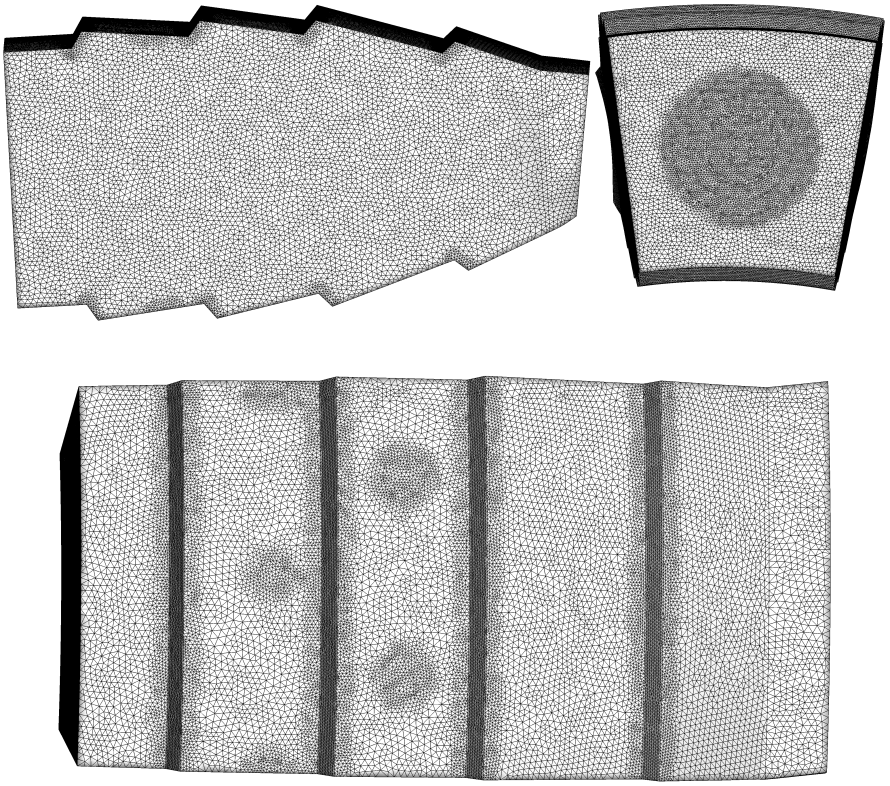

FIGURE 6.2: Combustor mesh, detail

TABLE 6.2: Mesh characteristic, combustor domain

	type	N elements	y^+
Standalone	tetra	$\approx 4.5 \cdot 10^6$	$\gg 30$
File b. coupling	tetra+hexa	$\approx 6 \cdot 10^6$	$\gg 30$
Memory b. coupling	tetra	$\approx 4 \cdot 10^6$	$\gg 30$

forces applied in a region adjacent to the exit boundary. The two coupling approaches are detailed in Sec 4.3. The main boundary conditions are reported in Tab. 6.1.

Mesh

Unstructured fully tetrahedral meshes of around 4 and 4.5 million elements were generated using the commercial software ICEMCFD for the standalone and memory based coupling configurations. A tetrahedral mesh is relatively easy to be generated and, at some cost in terms of mesh elements, is the preferred option for complicated geometries such as combustors in which a good resolution of the boundary layers is of secondary importance. For the file based configuration instead an hexahedral region is required at

the end of the combustor to perform interpolation using CHIMPS. This is a restriction present in the version of CHIMPS we are allowed to use in coupling. The mesh in this case was generated using the software Gambit and it consists of around 6 million cells. The resulting meshes were mainly uniform, with an average cell size of around 2 mm. Dilution holes and cooling slots inlet boundaries were refined with a cell size of 1 mm, while all inlets corresponding to the burner with a cell size of 0.8 mm. The value of y^+ was well above 30 for all the walls, which were treated as adiabatic. A view of the mesh (on the memory based coupled geometry) is shown in Fig. 6.2.

6.1.2 HP Turbine

As for the combustor, the turbine simulations details are listed in the following sections organised as: model, boundary conditions and mesh.

Model

The first stage of the corresponding real engine HP turbine with a shrouded rotor was considered. The geometry was simplified such that only a clean annulus gas path without film coolings were modelled. The same angular sector as for the combustor was simulated, accounting for two stator blades and the corresponding rotor. A mixing plane was used for the standalone and file based coupled steady simulations. For the unsteady memory based coupled simulation the rotor pitch was adjusted to match the periodic angle such that a 2 stator/4 rotor blade count is obtained, and a sliding plane approach is used between stationary and rotationary parts. The gas composition was assumed to be uniform throughout the simulation and no reaction processes occured. The gas constant was chosen to match the average value at the turbomachinery interface plane in the combustor domain obtained by the first coupling iteration. The value was observed not to significantly change during the coupling procedure and it was not updated. Thermodynamic properties are varying with temperature [3]. The same turbulence model used in the combustor, namely the k-ϵ model, is used to model the turbulence to limit the number of coupling parameters. The same geometrical configuration is used for both a standalone simulation and the coupled approaches, the main difference standing in the boundary treatment. For a coupled simulation the clocking of the NGV blades with respect to the combustor injector does not necessarily represent the one in the real machine.

TABLE 6.3: Boundary conditions for the turbine domain

	INLET	OUTLET
Standalone (run1)	(1-D)Mass flow, T, flow angles	static pressure (radial eq)
Standalone (run2)	(1-D)p_0, T_0, flow angles	Mass flow (radial eq)
File b. coupling	p_0, T_0, flow angles	Mass flow (radial eq)
Memory b. coupling	ρU, ρV, ρW, T	static pressure (radial eq)

TABLE 6.4: Mesh characteristic, turbine domain

	type	N elements	y^+
Standalone & File b. coupling	hexa	$\approx 1.2 \cdot 10^6$	≈ 30
Memory b. coupling	hexa	$\approx 2.4 \cdot 10^6$	≈ 30

Boundary Conditions

The boundary conditions used for the standalone and coupled simulations are listed in Tab. 6.3. Only radial inlet profiles are used for the standalone simulations, as this is standard practice. In the coupled simulations instead two-dimensional profiles of all variables are used at inlets. We distinguished between two different standalone simulations, run-1 and run-2, the reason for which will be explained in Sec. 6.2.1.2. The "Mass flow" boundary condition implies rescaling of the pressure profile (stagnation at inlet or static at exit) to match the desired specified mass flow value. We recall that, with the exception of the stronger inlet condition introduced for the memory based coupling, all the original boundary conditions of the C-DBS code exploit a weak characteristic treatment of the boundary.

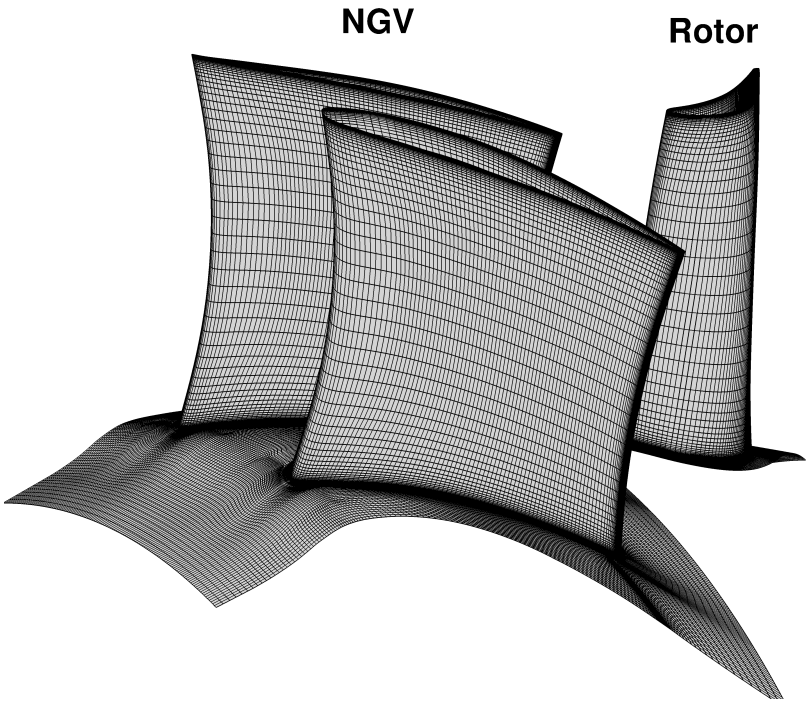

FIGURE 6.3: Turbine stage mesh view for steady simulation

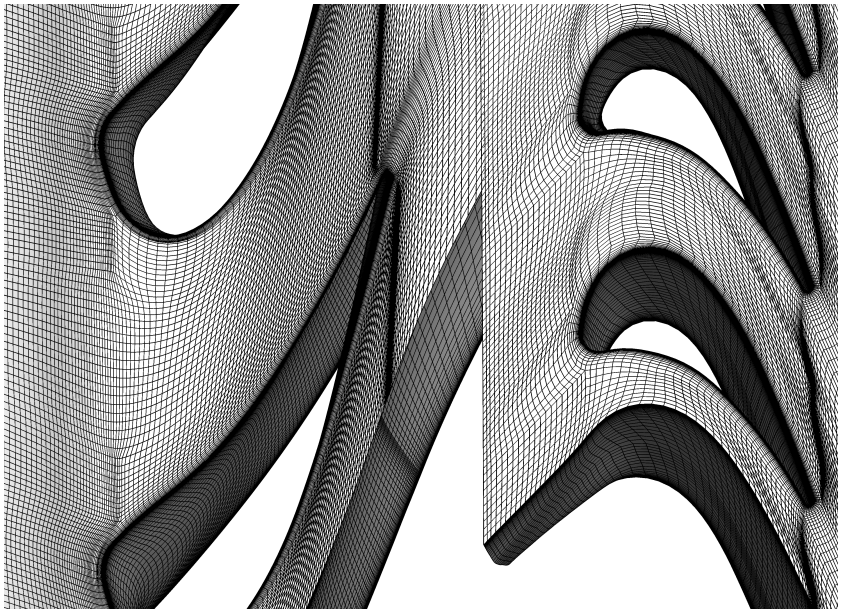

FIGURE 6.4: Turbine stage mesh view detail, reduced rotor pitch, unsteady simulations

Mesh

Multiblock structured meshes of around 1.2 million nodes were generated using a Rolls-Royce in house turbomachinery mesh generator for the NGV (2 blades) and the original rotor (See Fig. 6.3). The rotor grid with modified pitch for unsteady simulations was generated instead using the commercial software ICEMCFD (a detail is shown in Fig.6.4). Together with the original NGV the mesh in this case (2 NGV blades and 4 rotor blades)

consists of around 2.4 million nodes. To discretise the span 70 elements were used, with a typical dimension along it of around 1.5 mm, and mesh refinement was used at endwalls to better resolve the boundary layers. The same level of refinement used at endwalls was used at the blade surfaces. The wall spacing in the rotor with modified pitch was 0.012 mm. The value of y^+ was in the range of $10 - 20$ and it was smaller than for the combustor simulation, and integral wall functions were used to improve the solution in those regions as y^+ falls below the recommended minimum value of 30. Around 70 elements were used in the circumferential direction to discretise each single NGV passage and around 40 for each rotor with modified pitch. Adiabatic conditions were imposed at solid boundaries.

6.2 Combustor-HP turbine: file based steady RANS simulation

Two situations were compared: a more traditional approach in which both combustor and turbine are simulated in a standalone fashion, and the file based coupled approach (file based, see Sec. 4.3.1). In the standalone approach the turbine was simulated only after the combustor: one dimensional profile data obtained from the combustor standalone simulation were used to define inlet conditions for the turbomachinery simulation. In the coupled approach the two domains, combustor and turbine, were simulated in sequence (sequential coupling): one domain was run first and a fully converged solution was obtained to generate new boundary conditions for the other domain which run second. The fully converged solution of the second domain was used to generate new boundary conditions for the first domain. 1000 inner iterations for the convergence of each solver were used in this test case. The number of inner iterations are chosen to fully converge to a low level of residuals both the simulations. For the ILM-PBS some fluctuations in the results are still present with residuals that are already low, due to some unsteadiness of the flow, and conservations of species can be checked to ensure a good level of convergence. These four steps (solution of the first domain, boundary exchange, solution of the second domain, boundary exchange) constituted one coupling iteration. Thirty automatic coupling iterations were run, after two initial iterations were run manually as an initialisation (which is not a required procedure). In Fig. 6.5 the average pressure at combustor exit during the coupling iterations is shown. The values

do oscillate with a maximum difference of around 4 Pa which is good sign the simulation is stabilised by the special pressure boundary treatment. In fact the oscillation is a very small value with respect to the typical pressure gradients in this area and with respect to the thermodynamic pressure (of the order of the MPa).

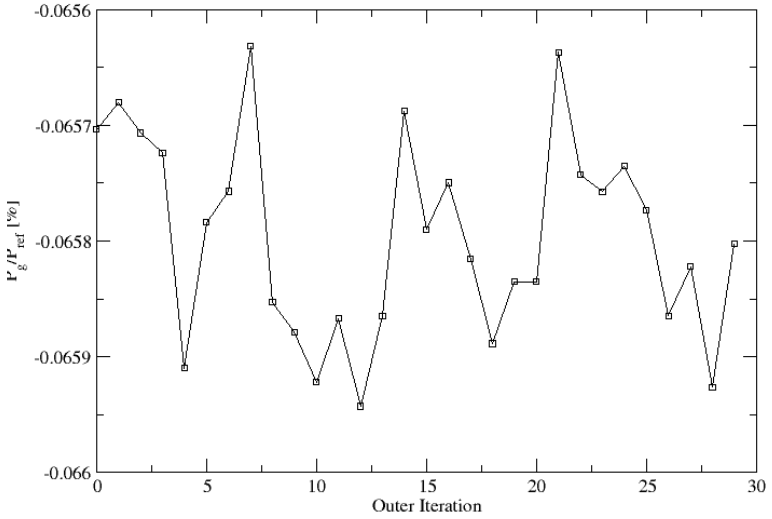

FIGURE 6.5: History of average pressure at combustor exit during the coupling iterations

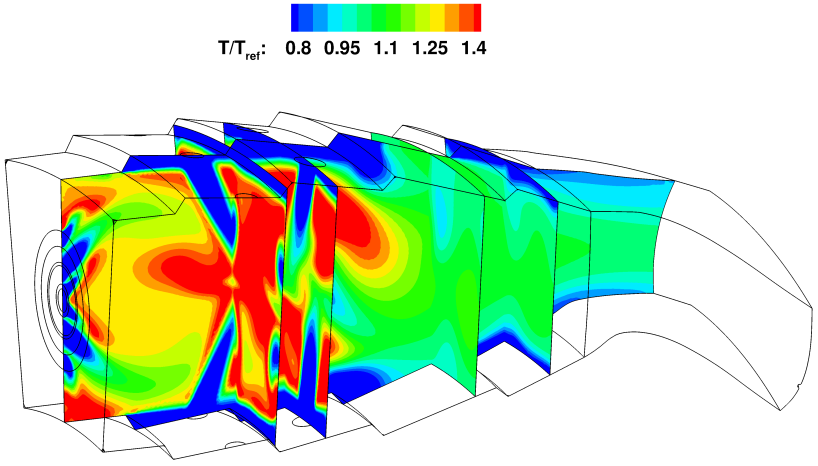

FIGURE 6.6: Combustor field, normalised temperature

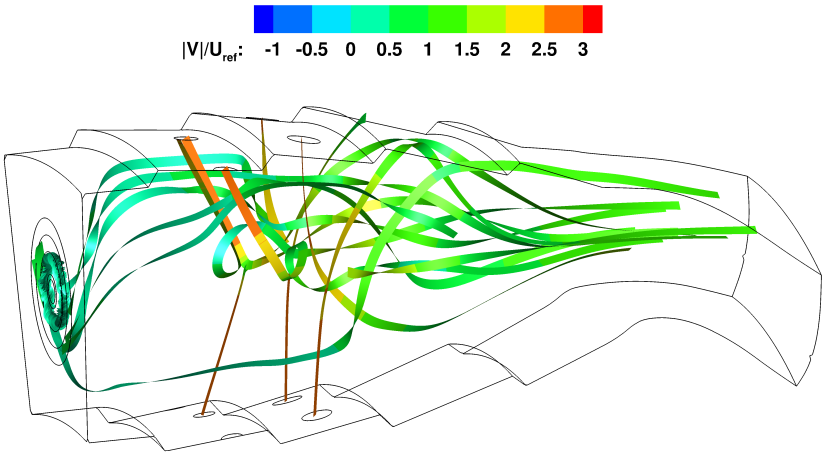

FIGURE 6.7: Combustor field, Ribbons coloured by velocity magnitude

6.2.1 Results and discussion

Before presenting the results of our investigation on the influence of the file based coupled approach, the flow development in the combustor upstream of the coupling region is briefly explained. The main flow features are shown in Fig. 6.6 and Fig. 6.7 for the standalone simulation. The configuration, typical of an RQL combustor, shows a high swirling region in the first part of the combustor where rich combustion occurs that stabilise the flame, a middle region where the injection of fresh air through primary and secondary dilution holes quenches the rich mixture and a third region towards the exit where the mixture becomes very lean and the combustion process has mainly ended. The interaction between the inlet swirler, primary and secondary jets generate distinct swirling streams at the combustor exit (Fig 6.7).

The results are focused on the impact of applying a fully coupled approach with respect to a more traditional uncoupled simulation. This section is subdivided into two parts: at first the influence of the presence of the blades on the combustor flow field is analysed, and later the influence of the fully coupled combustor on the turbomachinery field is studied. Locations close to the interface region are considered and slices at planes A, B, C, D, E, F and G (Fig. 6.8) are presented. They are located respectively at 25%, 50%, 75%, 100%, 150%, 250% and 400% of the axial chord length (ACL) upstream of the stator blade leading edge, measured from mid span of the NGV along the combustor slice plane M shown in Fig. 6.8. Plane A and B are located within the turbine domain

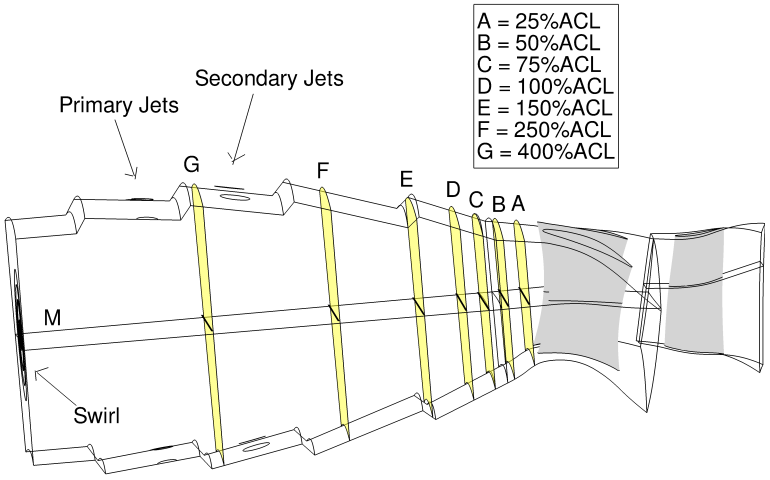

FIGURE 6.8: Slice planes configuration, file base coupling, low velocity Combustor - HP Turbine

only while D, E and F are within the combustor domain only. Plane C belongs to both domains and it also corresponds to the inlet of the turbine domain. For the coupled approach an overlapping region is present as previously stated, whose location relative to the slices can be seen in Fig. 6.8 between Planes B and C, and whose depth is 15% of the ACL. The operating point is representative of a rig test on the ground performed at low speed, hence the Mach number remains below 0.5 throughout the turbomachinery. Experimental data from the rig are not available to us. We performed this set of simulations based on the data we were provided from the industry.

6.2.1.1 Influence on combustor field

The influence of the presence of the stator blades on the combustor field is clearly visible from a mid-plane slice through the two domains. Shown in Fig. 6.9 is the axial velocity normalised with respect to the area average axial velocity at the turbine inlet. The potential field coming from the blades is projected upstream changing the flow distribution in the critical interface region. Figure 6.10 shows the axial velocity normalised with the area average axial velocity at each respective plane for both the coupled and standalone simulations. The normal to the plane entering the paper is directed towards the turbine

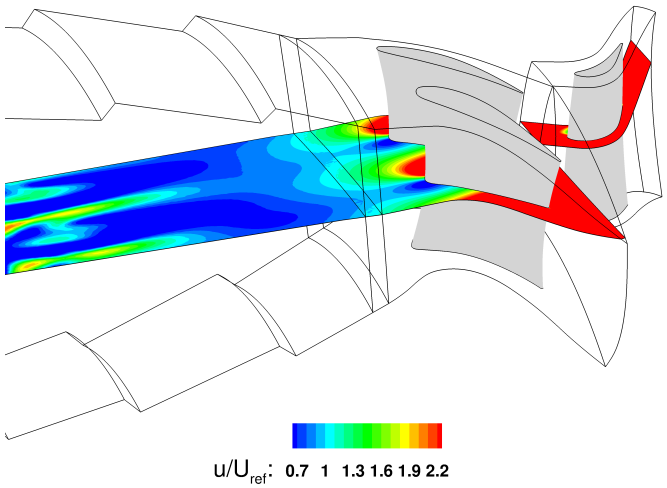

FIGURE 6.9: Normalised axial velocity, file based coupled simulation, low velocity Combustor - HP Turbine

region. The coupled simulation shows a significant influence of the NGV potential flow leading to the vane shaped low velocity regions. Streamlines drawn on the plane are also shown. On the middle left, a strong vortex can be observed both in the standalone simulation (point P) and the coupled simulation (point P'). This structure (P) appears weakened and stretched in the coupled simulation (P'). On the middle right, a vortex pair (point R and Q) can be observed. The presence of the second NGV significantly weaken this pair (R' and Q'). As a result, even if the presence of the dilution jets is still significant, the flow is adapting to the NGV passage at plane C, which is 75% axial chord length upstream of the stator blades.

A better understanding of the penetration of the NGV influence is provided by Fig. 6.11, where the axial velocity normalised with respect to the area averaged axial velocity at the turbine inlet plane (Plane C) is shown at different locations inside the combustor. The lines of data are taken from a slice plane of the combustor (Plane M) at fixed distances from the NGV leading edge (the distance is again measured in axial chord lengths). Looking at the three closest locations to the NGV (corresponding to lines extracted from Plane E, D and C) the presence of the blades is shaping the axial velocity behaviour, as it differs from the standalone case. Looking at the standalone simulation in green, it predicts some velocity peaks occurring at Plane E due to the flow field generated by the

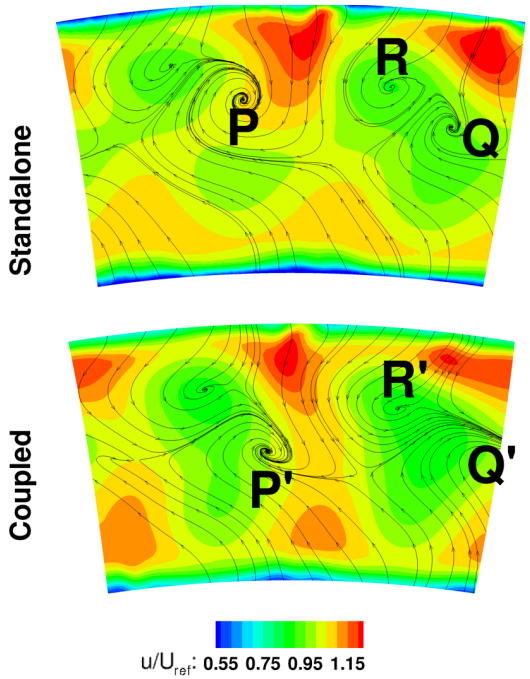

FIGURE 6.10: Normalised axial velocity at Plane C, file based coupled and standalone combustor simulations, low velocity Combustor - HP Turbine

jets; the positive peaks correspond to the secondary jets which interact and generate two separate peaks of velocity. At this plane, the interaction of the secondary jets with the modified downstream field generates a circumferential shift in the position of the higher velocity flow structures, and as a consequence of the observed peaks. In the standalone simulation, the velocity profile is flattening towards the end of the combustor as the nozzle accelerates the flow to the extent that the swirl and the jets are well mixed at this particular region (Intersection of Plane M with plane D and C). The coupled simulation of the corresponding planes (in red) sees more pronounced velocity peaks, characteristic of the presence of the NGV potential field deep inside the combustor. Further upstream (lines on Plane F and G) the axial velocity shape does not differ significantly.

The combustor is designed to provide a certain temperature distribution at the turbine inlet. During the design phase, a standalone simulation is used to predict this distribution, together with experimental results. Fig. 6.12 shows the different temperatures obtained at two planes C and D for the standalone simulation and the coupled approach. From the standalone results we observe that the dilution jets in the combustor are designed to localise the hot spots in specific locations in the plane and distribute the hot gases uniformly along the radial direction, while avoiding overheating of the endwalls. It is known [5, 140] that if the hot spots impact the NGV blade leading edge they are

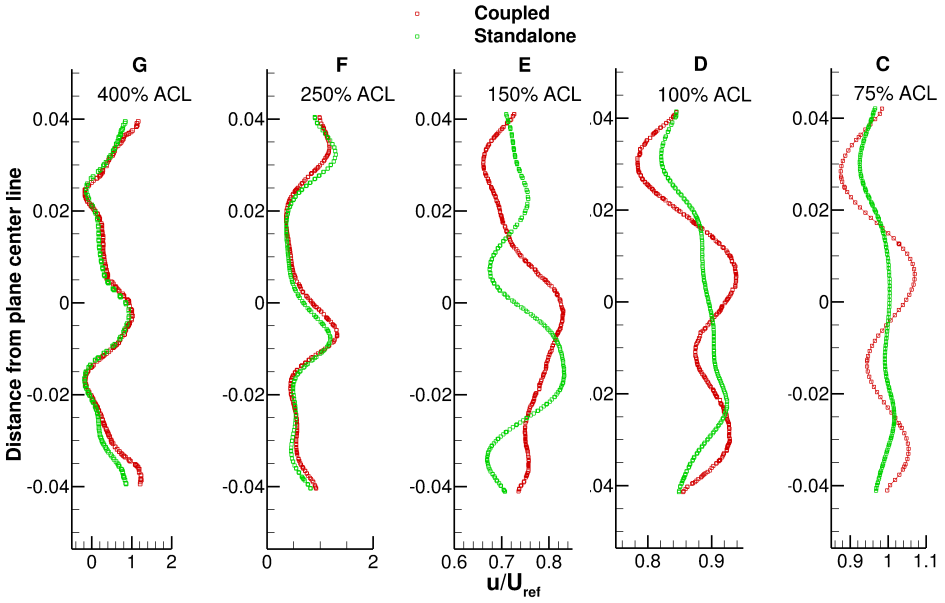

FIGURE 6.11: Normalised axial velocity along lines in the middle plane, file based coupled and standalone combustor simulations, low velocity Combustor - HP Turbine

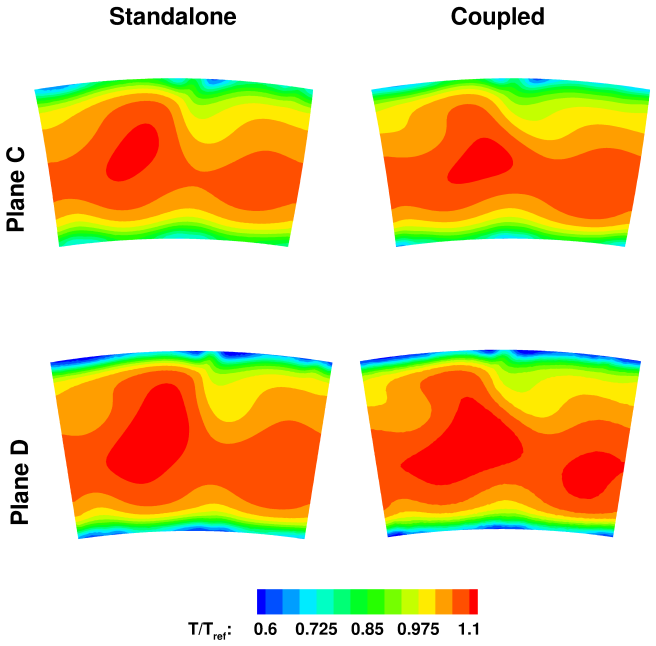

FIGURE 6.12: Normalised temperature at Plane C and Plane D, file based coupled and standalone combustor simulations, low velocity Combustor - HP Turbine

broken and mitigated during their migration towards the rotor, while if the hot spot is located in the middle of the passage it will reach the rotor with full strength. In the coupled simulation the temperature seems to be more spread in the circumferential direction but more concentrated towards the bottom half of the inlet region, which is in agreement to the distortion of the vortical structures that has been noted earlier. The consequence of this is shown in Fig. 6.13 where the RTDF at Plane C is reported. The circumferentially averaged data confirm the presence of a higher peak of temperature in the bottom half inlet region for the coupled approach with more steep radial gradients, while a more uniform profile was obtained in the standalone simulation.

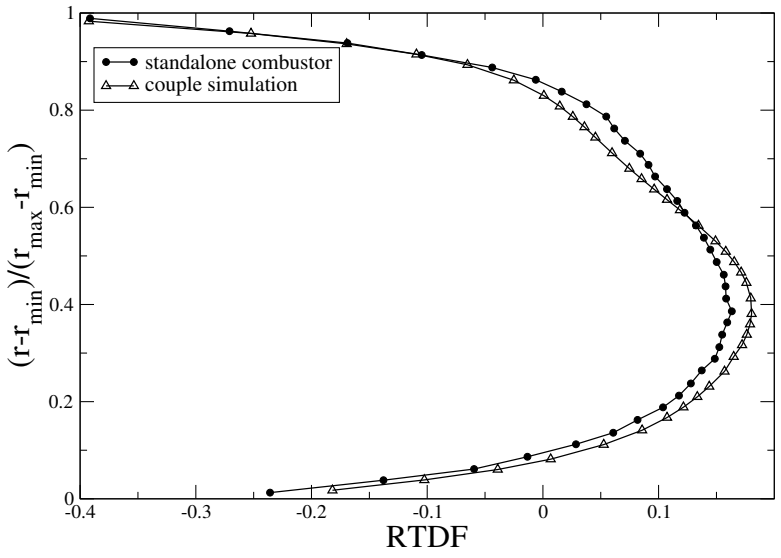

FIGURE 6.13: RTDF at Plane C, file based coupled and standalone combustor simulations, low velocity Combustor - HP Turbine

6.2.1.2 Influence on turbine field

We recall that in this work we aim to show the advantages of a coupling approach with respect to a more standard approach which uses one dimensional profiles. No assumptions on any variables are made for the generation of the profiles used in the standalone simulation. They are obtained from the standalone combustor simulation with a circumferential averaging process. Two runs of the standalone simulation have been performed. In the first (run-1) the pressure exit obtained as a result of the coupled approach (in radial equilibrium assumption) is used as a boundary condition at the outlet. The same mass flow present in the combustor is imposed at inlet, which implies automatic scaling of the stagnation pressure radial profile. All the remaining inlet profiles obtained from

the standalone combusor are used unmodified, including stagnation temperature profile. As a consequence for run-1 mass flow and pressure exit are the same as in the coupled approach. A difference in stage capacity (0.2%) is obtained due to differences (0.1%) in average stagnation values (both pressure and temperature) obtained at the inlet with respect to the coupled approach. In the second run instead (run-2) the capacity of the turbine is kept equal to the coupled approach by rescaling stagnation pressure and temperature inlet profiles. For this simulation mass flow is imposed at outlet, and the obtained level of pressure at exit differs (0.23%) from the coupled approach. The relative conditions are summarised in Table 6.6. The results shown in the following figures will be taken from the run-1 simulation, and comments will be added when providing results regarding run-2.

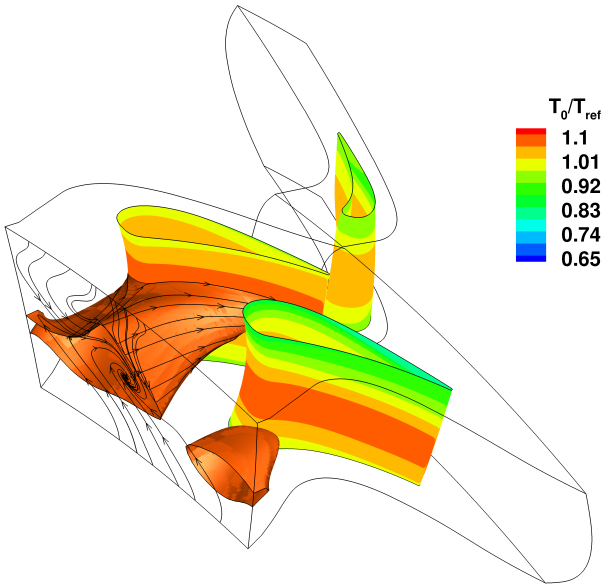

FIGURE 6.14: Hot streak impinging the stator, isosurface of normalised stagnation temperature $T_0/T_{ref} = 1.08$, low velocity Combustor - HP Turbine

The immediate drawback in using a one dimensional profile is the inability to capture non uniformities which are both radial and circumferential such as the hot streak shown in Fig. 6.14 from the coupled simulation. In the figure are shown the two streaks coming from the combustor (see Fig. 6.12), a bigger one, which corresponds to vortex P' in the earlier discussion, impinges directly on the pressure side of the top stator blade while a smaller one, which correspond to vortex Q', is directed towards the pressure side of the other blade.

TABLE 6.5: Difference (%) in OTDF between file based coupled and standalone circumferentially averaged profile (run 1), low velocity Combustor - HP Turbine

	Plane C	Plane B	Plane A
$\Delta OTDF$	37.43%	37.25%	30%

A measure of the information lost in the averaging process in shown in Table 6.5 where the difference in OTDF ($\Delta OTDF = |OTDF_{coupled} - OTDF_{radial}|/OTDF_{coupled}$), in percentage, is reported for the three planes A, B and C.

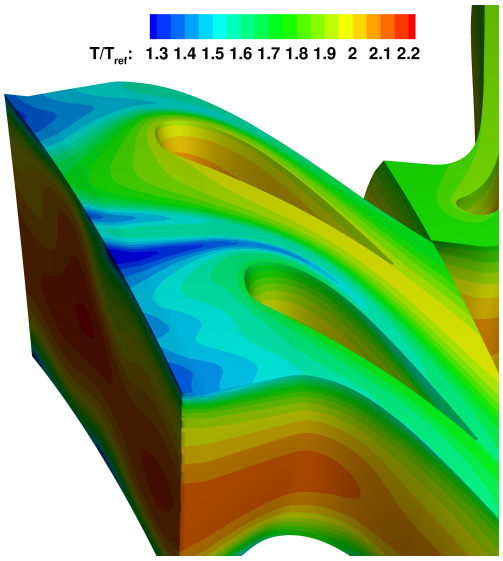

FIGURE 6.15: Detail of the external casing normalised temperature, file based coupled simulation, low velocity Combustor - HP Turbine

Endwall cooling strategies will also be certainly affected by the two-dimensional profile coming from the complex combustor flow field, as can be seen in Fig. 6.15, where the normalised temperature with respect to the average inlet temperature is shown.

An aspect which is often considered of secondary importance is the turbulence, and simple uniform and very low values of turbulence level are typically used as boundary condition for the NGV inlet. Both our simulations take into account realistic levels of turbulence; shown in Fig. 6.16 and Fig. 6.17 are the turbulence intensity $u^{'}/U$, evaluated as

$$\frac{u^{'}}{U} = \frac{\sqrt{\frac{2}{3}k}}{U} \tag{6.1}$$

and normalised length scales,

$$\frac{\ell}{H} = \frac{\frac{k^{\frac{3}{2}}}{\epsilon}}{H} \tag{6.2}$$

where H is the radial span of the considered section, at planes A and B. The turbulence intensity is found to be higher than 30% in a major zone of the inlet plane. The effect of specifying one-dimensional profiles is still visible at plane A, which is located 25% ACL upstream of the stator blades. In Fig. 6.18 is shown the viscosity ratio ν_t/ν at the turbine inlet Plane C for the coupled simulation. The value of ν_t is evaluated from the simple $k-\epsilon$ relation

$$\nu_t = C_\mu \frac{k^2}{\epsilon} \tag{6.3}$$

The value of the viscosity ratio results to be much higher than 10, a general value imposed at turbine inlet in traditional simulations, throughout the entire plane and far from being uniform. The $k-\epsilon$ model is chosen in this work to be consistent with the combustor simulation. The coupling approach will allow the user to select a more appropriate model for the turbine simulation for a more confident and accurate solution.

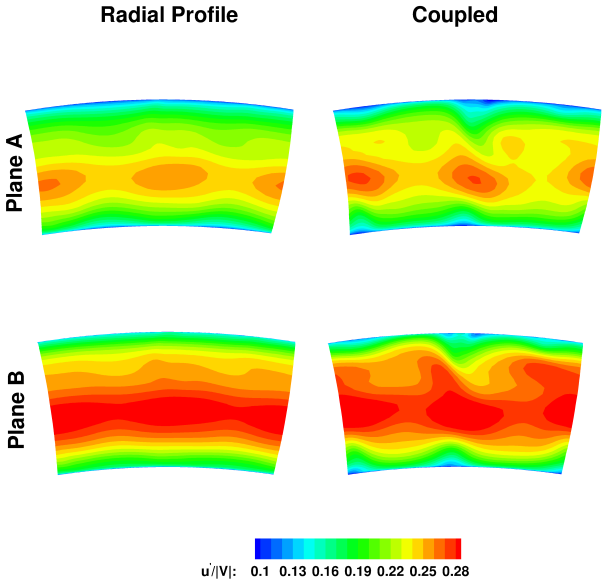

FIGURE 6.16: Turbulence intensity $u^{'}/U$ at Plane A and Plane B, file based coupled simulation, low velocity Combustor - HP Turbine

To evaluate the performance of the NGV under the two different inlet conditions the stagnation pressure losses are evaluated as $\Delta p_0 = (\bar{p}_0^{inlet} - \bar{p}_0^{NGV outlet})/\bar{p}_0^{inlet}$.

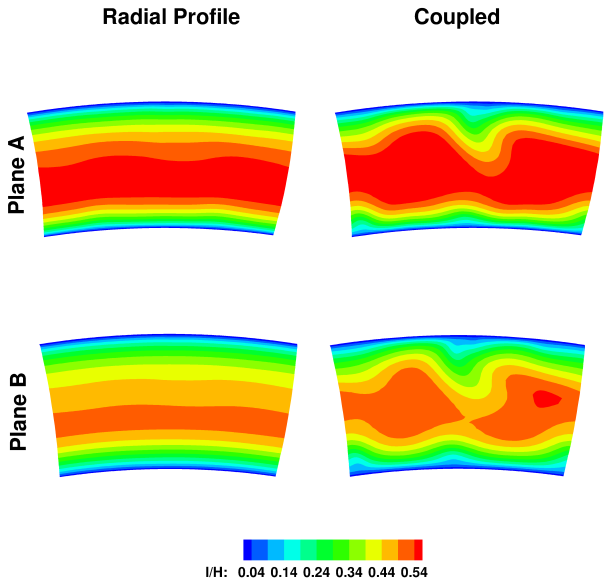

FIGURE 6.17: Normalised turbulence length scales ℓ/H at Plane A and Plane B, file based coupled simulation, low velocity Combustor - HP Turbine

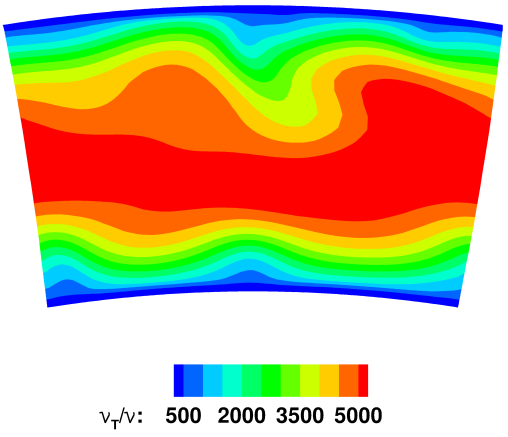

FIGURE 6.18: Viscosity ration ν_t/ν at Plane C, file based coupled simulation, low velocity Combustor - HP Turbine

They are found to be $\Delta p_{0_{COUPLED}} = 1.44\%$, $\Delta p_{0_{run1}} = 1.37\%$ and $\Delta p_{0_{run2}} = 1.32\%$ for the coupled, standalone run-1 and standalone run-2 simulations respectively, with an approximate 5% relative increase of losses in the case of the coupled simulation with respect to the standalone ones. As previously stated the simulation does not necessarily represent the operating real design condition of the turbine, and the efficiency is very low. As a consequence these numbers show a clear effect of the coupled approach, but they don't want to be representative of its application to real operating conditions.

TABLE 6.6: Relative difference between coupled and standalone turbine simulations, file base coupling, low velocity Combustor - HP Turbine

	p_0^{inlet}	T_0^{inlet}	p^{outlet}	capacity
Coup	100%	100%	100%	100%
Run-1	99.851%	100.115%	100%	100.22%
Run-2	100%	100%	100.231%	100%

With regard to the rotating part of the turbine, it has been demonstrated in the past that an unsteady simulation is necessary to properly predict the hot streak migration. Nevertheless, the addition of the rotor with a mixing plane, which implies that the rotor behaves as a perfect mixer, allows the proper prediction of the efficiency of the entire stage. The differences in pressure and temperature observed on the rotor blade between the coupled and standalone simulation are shown in Fig. 6.19. As can be seen the differences are found to be within 1%, which suggest that the rotor does respond to the peakier inlet profile, even when a perfect mixing assumption is used. The temperature contours shows that the peakier NGV inlet temperature profile of the coupled simulation leads to a generally higher rotor temperature between the root and mid span region. This differences lead to significant difference in turbine rotor reaction whereby the coupled simulation is found to be 0.05% higher than run-2. The value of reaction is computed as the enthalpy change across the rotor relative to the enthalpy change across the whole turbine stage.

TABLE 6.7: Difference in turbine performance between coupled and standalone simulations, file based coupling, low velocity Combustor-HP Turbine

	efficiency (%)	reaction (%)
Coup	0	0
Run-1	+1.06	-0.13
Run-2	+1.30	-0.05

Significant is the difference observed on the HP stage performance. The stage efficiency of the standalone turbine simulation was found to be higher than that of the coupled simulation. An increase of 1% and 1.3% in stage efficiency is found for run-1 and run-2, respectively. The value of efficiency η is calculated as the ratio between the work done by the turbine stage, produced by torque and obtained from all moving walls within the

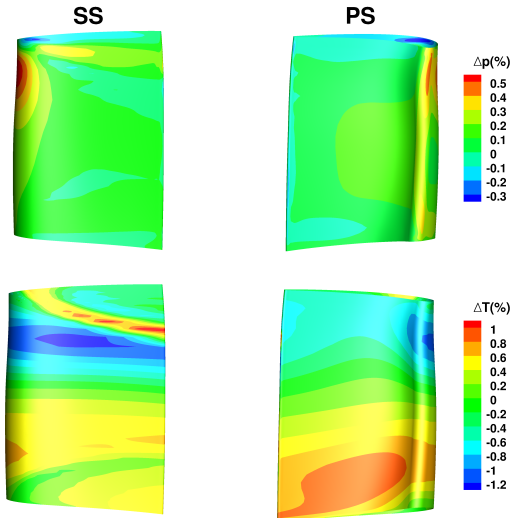

FIGURE 6.19: Percentage difference of pressure and temperature on the rotor blade between coupled and standalone turbine simulation with radial profile, file based coupling, low velocity Combustor-HP Turbine

control volume, and the ideal work that could be obtained from isentropic expansion of the working fluid entering the domain. The difference in efficiency is evaluated as:

$$\Delta\eta = \frac{(\eta_{Run} - \eta_{Coup})}{\eta_{Coup}}$$

and the same applies for the reaction.

6.3 Combustor-HP turbine: Memory based URANS simulation

The memory based coupling (Sec. 4.3.2) was developed to address unsteady RANS cases. The same geometry of combustor/turbine used for the steady file based simulation has been used for an unsteady run, with the only modification of the rotor pitch that has been adjusted so as to obtain periodic conditions with a blade count of 2 NGVs/4 rotors. A sliding plane approach is used to handle rotationaly parts. For this simulation an operating point close to the real flight cruise conditions has been chosen. In particular mass flow at all combustor inlets have been rescaled with respect to the steady case discussed above and the thermodynamic reference pressure changed so as to obtain realistic cruise conditions. The NGV blade clocking with respect to the injector location

is the same as used for steady coupling and does not necessarily represent the one in the real machine. As shown in Section 6.1, and for the reasons that will be explained shortly, the combustor domain has been extended deeper into the turbine domain, with respect to the steady case, resulting in an overlap region width of $\approx 50\%$ of the stator ACL in the axial direction. The location of the turbine inlet is unchanged, but the combustor outlet plane is located closer to the NGV blades. In particular the outlet plane is not parallel to the turbine inlet plane but instead parallel to the blades, and it is located at 25% of the ACL upstream of the blades leading edge.

At first a standalone combustor simulation and a steady file based combustor-turbine coupling (with the modified rotor pitch), have been performed on the same operating condition to allow for a comparison with the unsteady average results of the memory based coupling. As in the previous case, thirty coupling iterations were performed for the steady case. The average pressure at combustor exit is moniotred during the coupling and is reported in Fig. 6.20. The value oscillates, with a maximum difference of around 100 Pa, which as in the low velocity case is very small with respect to the pressure gradients (maximum pressure difference up to the scale of 10^4 Pa in the exit plane) and to the thermodynamic pressure (of the order of MPa). The steady coupled simulation is also helpful as it automatically defines the operating condition of the turbine, which comes as a result of the simulation. In particular the pressure at the rotor exit, obtained from the steady simulation, is used to define the boundary condition of the unsteady case. The time stepping for the unsteady case is chosen to be such that each entire periodic rotor mesh movement is resolved with 100 time steps, hence resolving each rotor blade passing with 25 steps. The same time stepping is used for both domains. The time step is such that the CFL number in the combustor is lower than unity in most of the domain. In particular, as data exchange occurs at the end of each time step only, it was found helpful for the quality of the results that the CFL number was low in the coupling region. The default temporal schemes of the two codes are used for the simulations, with a first order Euler scheme in the combustor domain and a second order backward Euler in the turbine domain. The inner iterations to converge each time step are chosen to fully converge the solution within the time step. In particular 18 inner iterations were used for the combustion solver and 15 for the turbomachinery one. To balance the load between the two solvers on the parallel machine a different number of nodes was used for the two simulations. The case was run on 32 cores, 16 for each

application. Both combustor and turbine solutions were initialised with a standalone steady solution. The turbine was later let to run standalone on unsteady mode with fixed inlet conditions (with mass flow inlet) obtained from the standalone combustor for long enough for periodic oscillations to be fully developed. The combustor was also let to run unsteady to develop the main unsteady structures before the coupling. After that the coupled simulation was run for 180° rotation of the rotor, checking again that the periodic oscillations in the turbine were fully developed after the introduction of the unsteady combustor upstream, before the start of the averaging process. Two full annular revolutions of the rotor were used to obtain the average flow field.

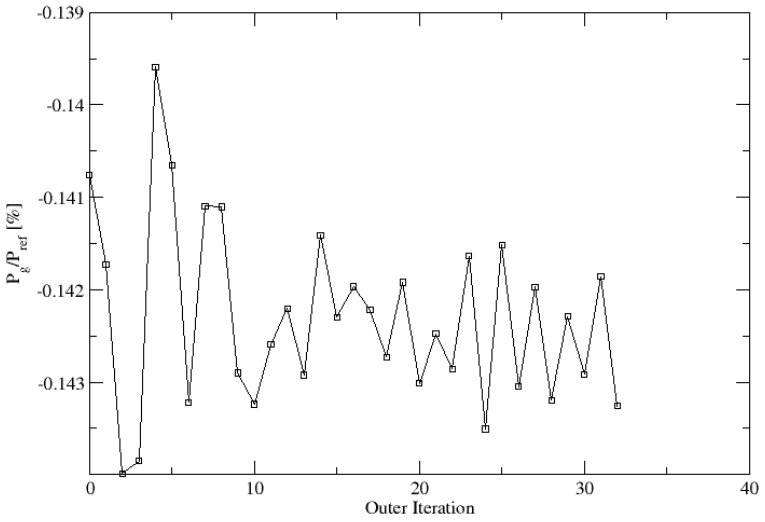

FIGURE 6.20: History of average pressure at combustor exit during the coupling iterations, steady file based cruise conditions

The ability of the body force to drive the solution in the ILM-PBS domain to a desired value in unsteady mode was assessed and proven on an uncoupled constant density case, with a single velocity component being forced (see Sec. 5.1.6). When using this technique on coupled cases, all three components of velocity are of interest and the desired values to be forced correspond to the downstream C-DBS solution and they are available in the entire overlap region, the depth of which has to be decided. From the application of the body force in the theory of steady incompressible flows, the depth of the forcing region is playing a role on the forcing method. On unsteady mode its importance may be weakened as the strength of the force has to be much bigger than on steady cases. Contrarily with respect to the steady file based coupling with pressure

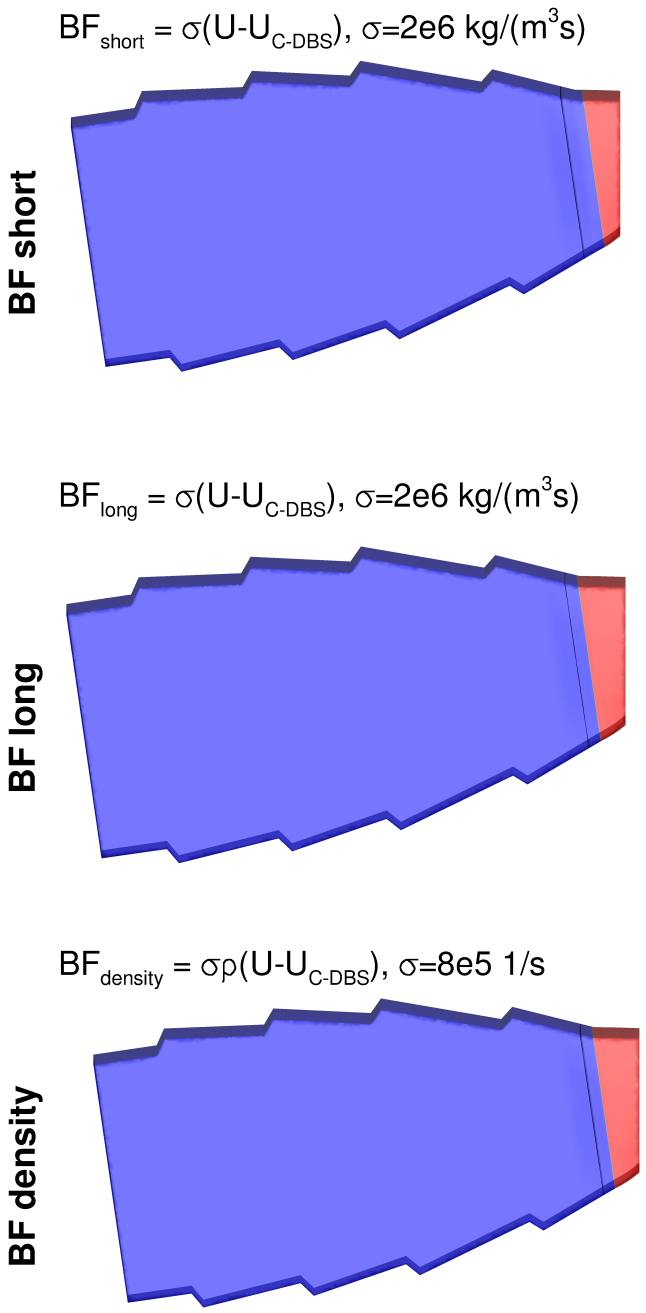

FIGURE 6.21: Forcing region (red) for body force method, "BF short", "BF long" and "BF density" runs, combustor domain, unsteady memory based coupling, cruise conditions Combustor - HP Turbine

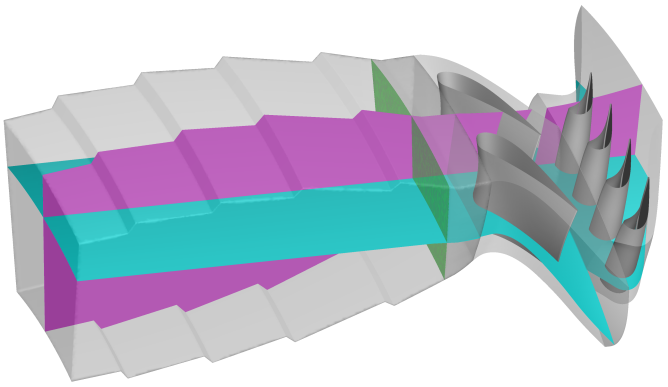

FIGURE 6.22: Post-processing slices: axial (violet), radial (cyan), turbine inlet (green), unsteady memory based coupling, cruise conditions Combustor - HP Turbine

exit profile, for which we suggested a small overlap region, a wider overlap is used in here, which increases the region of action of the body force and hence the ability of the flow to adapt to the downstream target velocity. We could not move the inlet of the turbine further upstream as the combustion process has to be fully completed. Moreover, on a more complicated geometry the turbine inlet location will be dictated by many other restrictions such as cooling holes and geometrical features. The obvious solution was to move the combustor exit further downstream with respect to the steady case, in a region close to the blades where the Mach number is still sufficiently low ($M < 0.25$) for the incompressible/low Mach number assumption to hold. The second point to consider when using the body force method on coupled cases is the depth of the forcing region, which may coincide or differ from the overlap region. We found some issues on forcing the solution in the entire overlap region, related to the bad quality of interpolation between different mesh sizes at the wall between the two domains. In particular fictitious reverse flow in the very near wall cell of the turbine inlet was observed, that needed correction and led to a closed loop between forced solution and inlet conditions, with clearly corrupted results. The consideration that forcing a region immediately adjacent to the turbine inlet may generate issues and closed loops between inlet conditions and forced solution, led to the decision of moving the beginning of the forcing region downstream with respect to the inlet interface plane. Two different depth of the forcing region were assessed, as can be seen in Fig. 6.21, that we will call "BF short" and "BF long" in the following. The region coloured in red corresponds to the

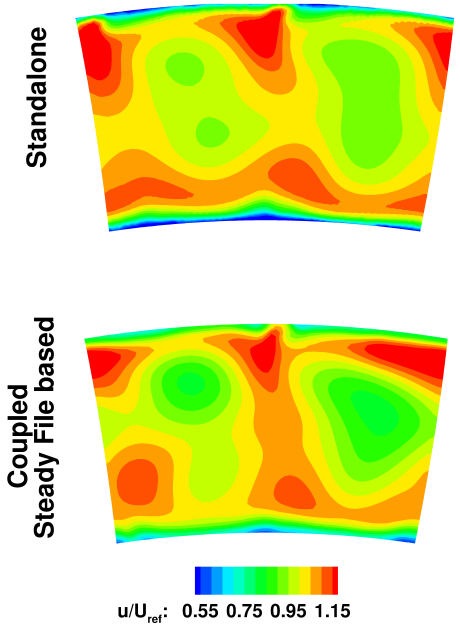

FIGURE 6.23: Normalised axial velocity at turbine inlet plane, standalone and steady file based coupled simulations, cruise conditions Combustor - HP Turbine

forcing region. In both a value of $\gamma_{BF} = 2 \cdot 10^6\ Kg/(m^3 s)$ was used. The last point to be considered is the dependence on density of the body force on variable density flows. The same depth as the "BF long" forcing region was used, and dependence on density was introduced. The constant γ_{BF} dimensionally is a frequency $1/s$ in this case, see Fig. 6.21, and its value was chosen as $\gamma_{BF} = 8 \cdot 10^5\ 1/s$. We will refer to this case as "BF density". The three "BF short", "BF long" and "BF density" approaches were assessed on the same case discussed above.

The results will be mainly presented in three slices across the domain: axial, radial and at the turbine domain inlet. The location of the slices is shown in Fig. 6.22.

6.3.1 Results and discussion

At first the velocity field results from the standalone combustor simulation and the steady file based coupled simulation have been compared for the new operating condition. In particular the flow at the turbine inlet plane is considered. Fig. 6.23 shows the axial velocity normalised with respect to the average velocity at the inlet plane for the two simulations. The flow coming from the combustor dilution jets is clearly shaping the field in both cases. Nevertheless some differences are clearly noticed between the

two. When compared to the low velocity simulation of Fig. 6.10, we can immediately see some differences in the velocity shape between the low velocity and cruise conditions simulations. The strength of the flow coming from the dilution jets appears to be increased in the cruise condition for both simulations, as a results of an increased velocity of the jets entering the domain. Nevertheless, the overall shape is in very good agreement between the two conditions for both cases, and in particular for the coupled case, confirming that the common features observed are characteristic of the presence of the downstream blades.

Looking now at the unsteady solution, the three variants "BF short", "BF long" and "BF density" in the application of the body force method have been compared. The normalised average axial velocity field is shown in Fig. 6.24 and Fig. 6.25 in which axial and radial slices are presented. A zoom over the overlap region is shown, and the contour lines are rescaled to highlight the flow features occurring in that location of interest. Solid lines correspond to the combustor solution and dashed-dotted lines to the turbine solution. Very low frequency oscillations are characteristic of the combustor, which unfortunately didn't allow the same average to be obtained in the three simulations: two full annular revolutions of the rotor are eventually not enough to obtain a complete average in the combustor domain. This is clear looking at the two slices, in which slightly different contours are observed for the three simulations, and it is further highlighted by Fig. 6.26, which shows the normalised average axial velocity at the turbine inlet plane. This last figure can be compared to the steady cases of Fig. 6.23. Many features of the standalone case can be found in the unsteady averaged solutions, confirming the approach is relatively weak with respect to the pressure exit coupling, but many shapes characteristic of the unsteady runs are also observed among the three, such as the top central velocity peak shifted to the left and much more inclined in the rotation direction with respect to the steady cases.

The objective of the three BF simulations is to evaluate the influence of the forcing region length and of the density dependence by looking at the quality of the agreement between contour lines in the two codes in the overlap region. We didn't observe any clear gain by introducing dependence on density of the body force, as while the agreement between contour lines in the two domains is very good in the radial slice of Fig. 6.25 (BF density), it is deteriorated in the axial slice of Fig. 6.24 (BF density). Moreover, even though density dependence didn't create any problem on this combustor-turbine

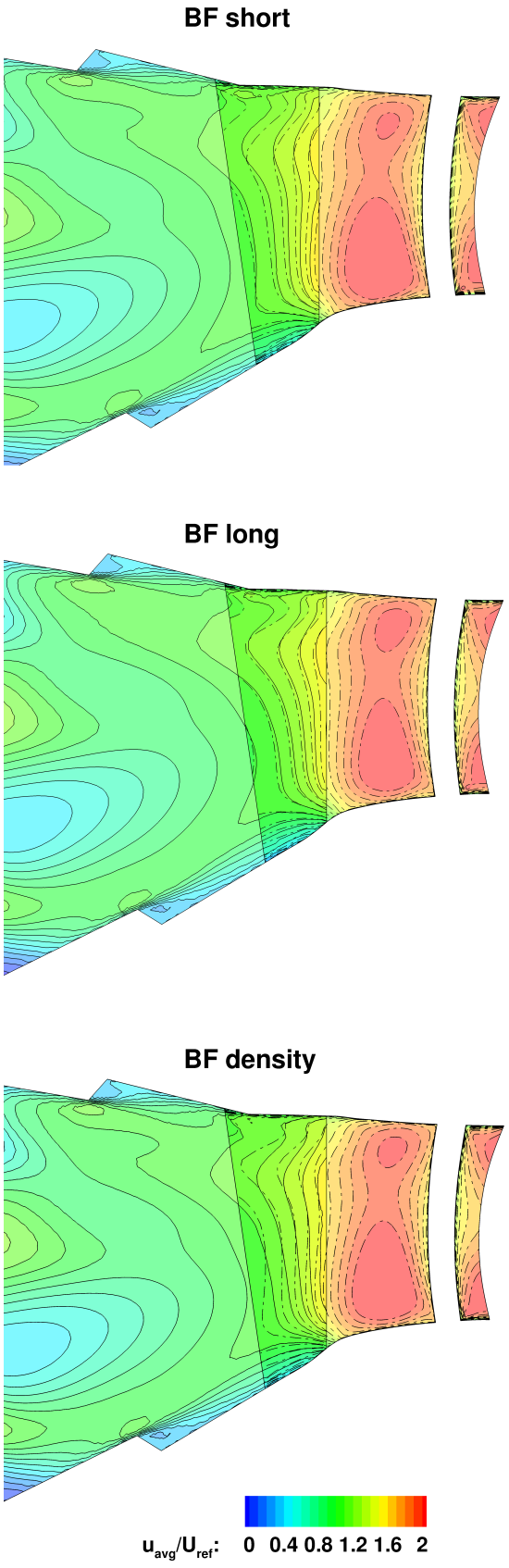

FIGURE 6.24: Normalised average axial velocity, axial slice, "BF short", "BF long" and "BF density" runs, memory based ILM-PBS (solid line) / C-DBS (dashed-dotted line) coupling, cruise conditions Combustor - HP Turbine

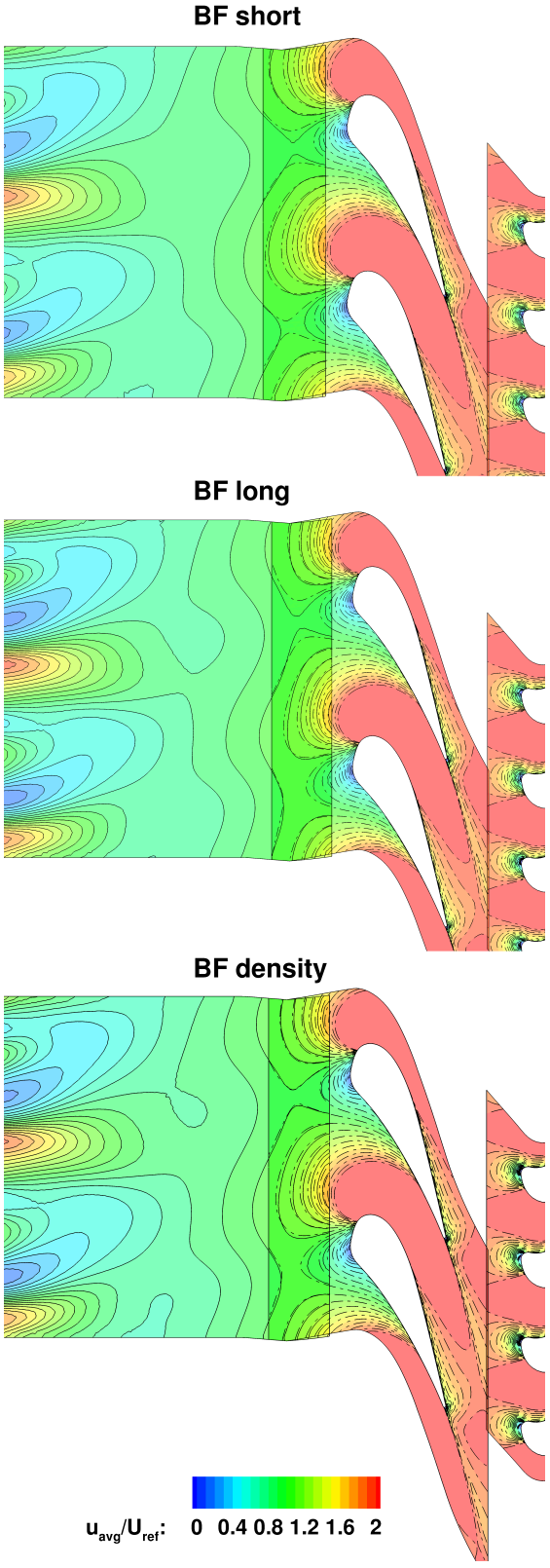

FIGURE 6.25: Normalised average axial velocity, radial slice, "BF short", "BF long" and "BF density" runs, memory based ILM-PBS (solid line) / C-DBS (dashed-dotted line) coupling, cruise conditions Combustor - HP Turbine

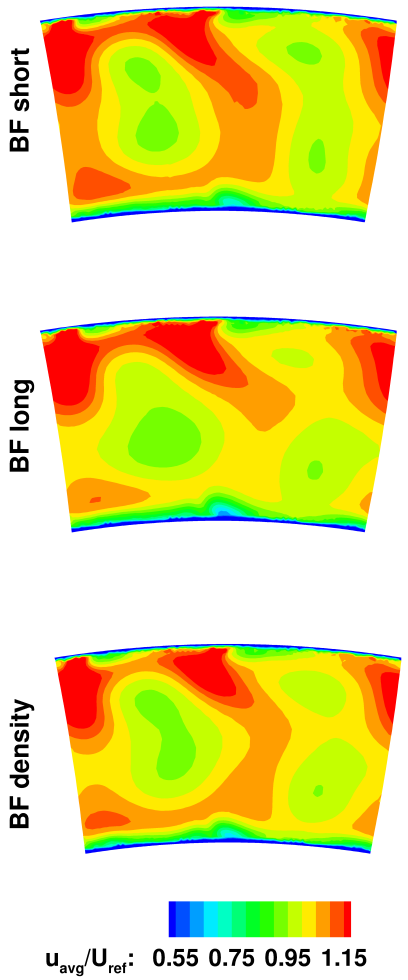

FIGURE 6.26: Normalised average axial velocity, turbine inlet plane, "BF short", "BF long" and "BF density" runs, memory based coupling, cruise conditions Combustor - HP Turbine

test case, other simpler test cases, not reported in here, have shown density dependence could reduce stability of the approach. The difference between "BF short" and "BF long" simulations is also very small, which confirms the method is robust and not very sensible to the choice of these parameters. Nevertheless for theoretical reasons the wider the region the better the solution, with equal constant γ_{BF}. The "BF long" simulation has hence been chosen as the best candidate and proposed as the reference simulation for the unsteady case. In the following we will refer to it simply as "Coupled Unsteady Memory Based" simulation.

The average of the main variables of interest for the coupled unsteady simulation are shown in the slices of Fig. 6.27, 6.28, 6.29 and 6.30. They show the obtained quality of the coupling. The presence of the downstream blades is clearly captured at the

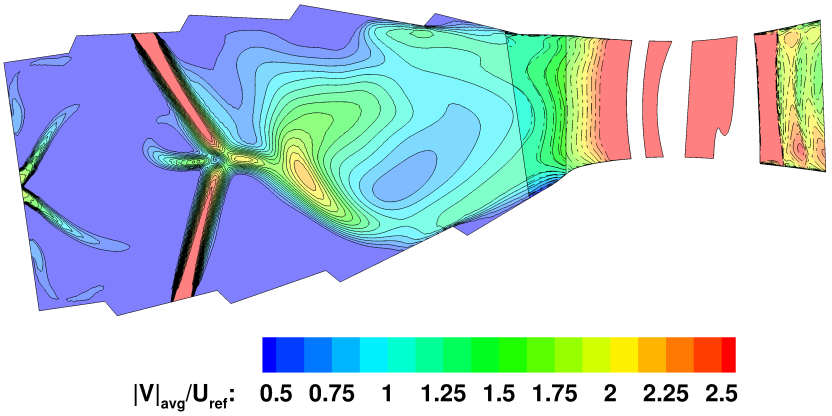

(a) Normalised average velocity magnitude, axial slice

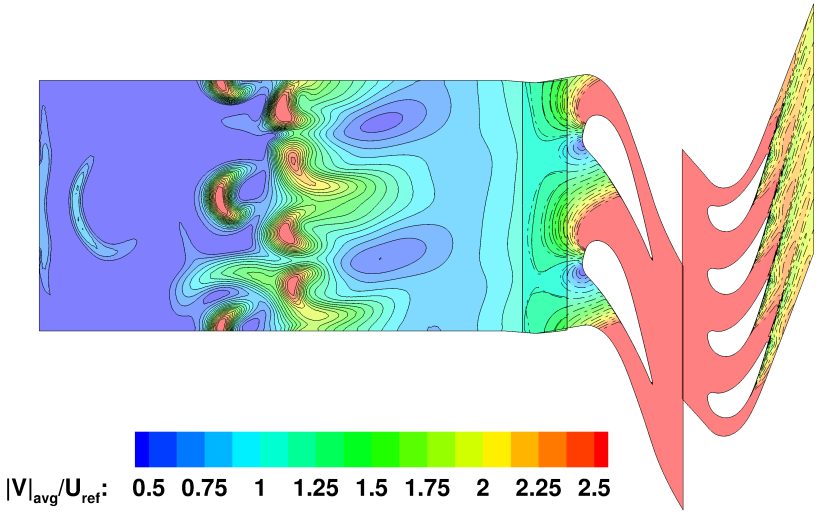

(b) Normalised average velocity magnitude, radial slice

FIGURE 6.27: Normalised average velocity magnitude, unsteady memory based coupling, cruise conditions Combustor - HP Turbine

combustor exit and flow data coming from the combustor are clearly quite smoothly entering the turbine domain. Nevertheless, the contour lines for the two simulations, which are solid lines in the combustor and dashed-dotted lines in the turbine, are not perfectly matching in the overlap region. Some degree of mismatching is present, more pronounced for some of the variables, such as temperature and density. Thermodynamics is quite different in the two domains, both because of the compressibility of the fluid and because of the different composition and fluid properties, shown in Fig. 6.31. This last point is particularly important and to be considered for future development of the coupling. The file based steady coupling is already capable of retrieving and exchanging

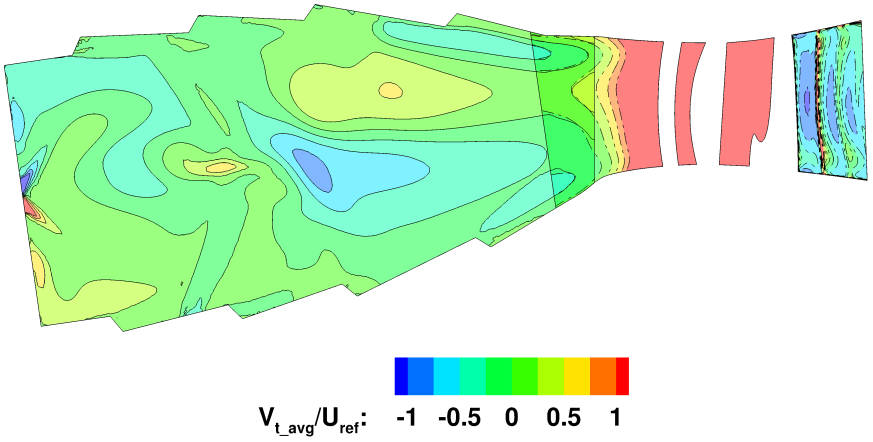

(a) Normalised tangential velocity, axial slice

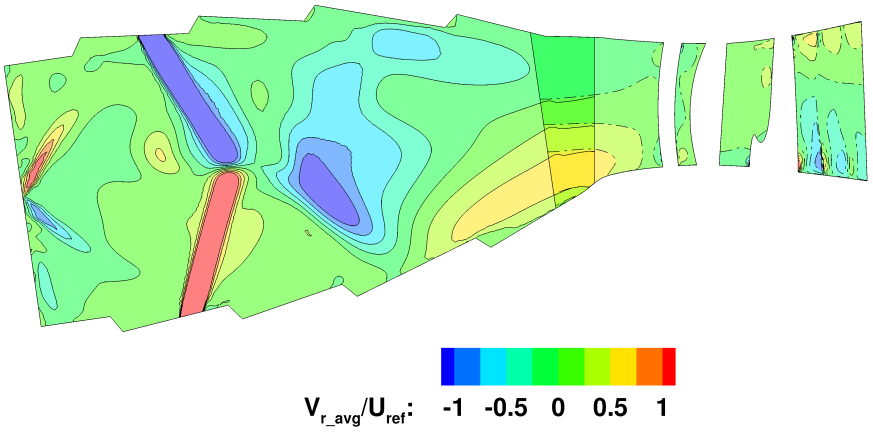

(b) Normalised radial velocity, axial slice

FIGURE 6.28: Normalised tangential and radial velocities, unsteady memory based coupling, cruise conditions Combustor - HP Turbine

flow composition data between combustor and turbine and the memory based coupling can be easily extended to do the same. Nevertheless a variable composition simulation in the turbine is very uncommon and not yet mature and it is not presented in this work. In the future this type of simulation will allow further improvement of the degree of consistency between the two domains.

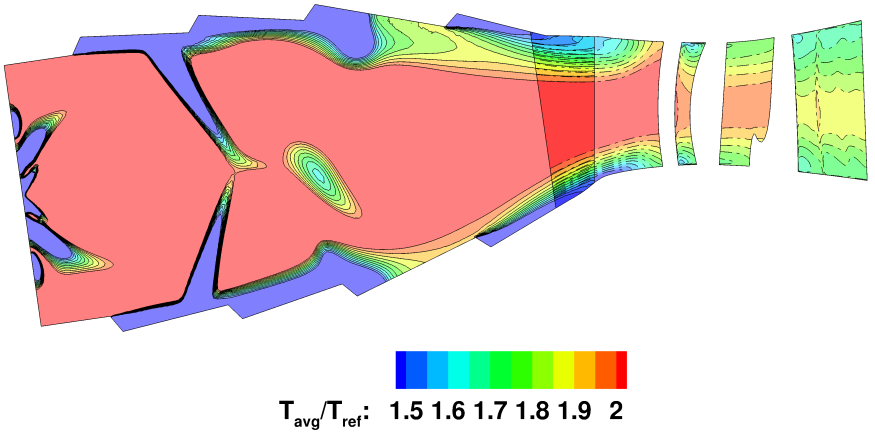

(a) Normalised average temperature, axial slice

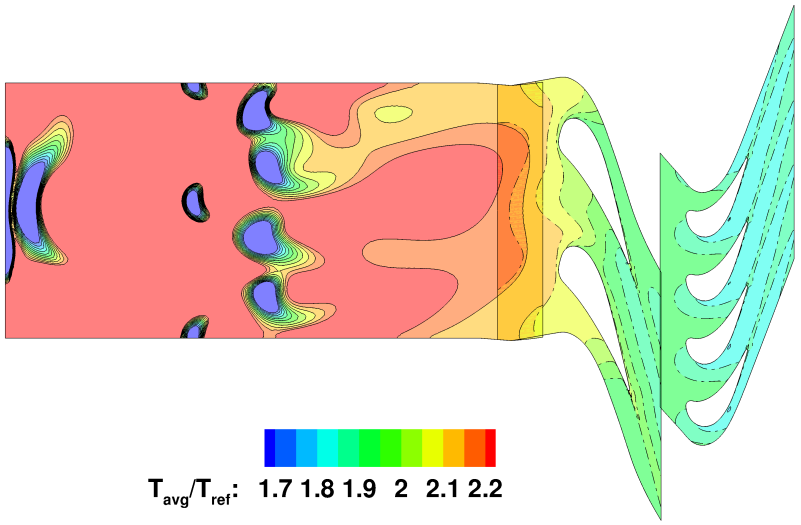

(b) Normalised average temperature, radial slice

FIGURE 6.29: Normalised average temperature, unsteady memory based coupling, cruise conditions Combustor - HP Turbine

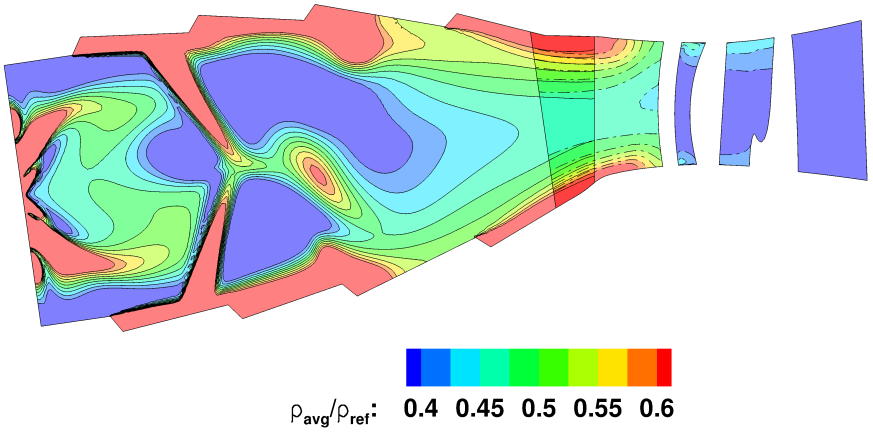

(a) Normalised average density, axial slice

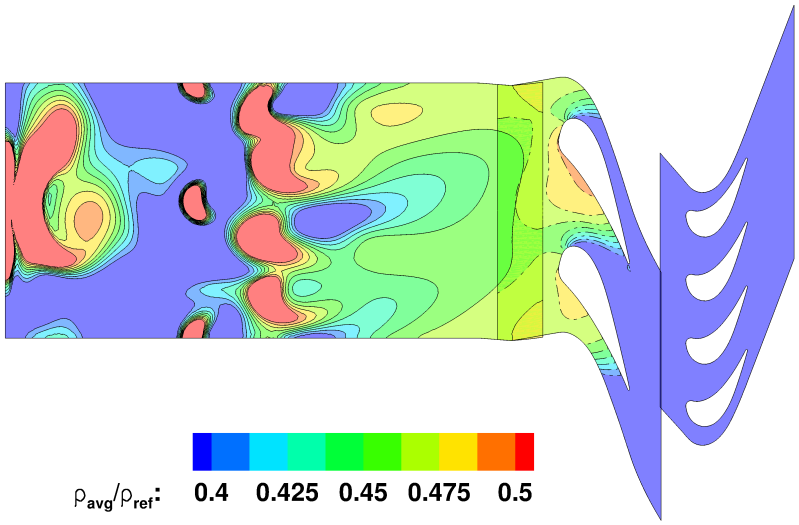

(b) Normalised average density, radial slice

FIGURE 6.30: Normalised average temperature, unsteady memory based coupling, cruise conditions Combustor - HP Turbine

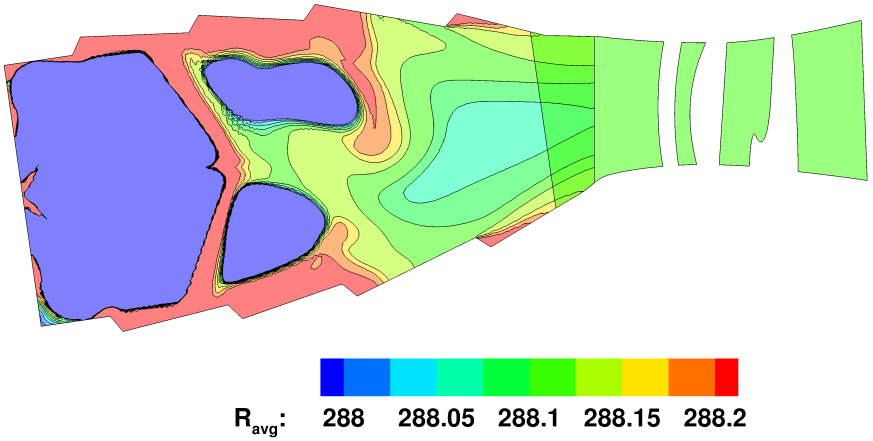

(a) Average specific gas constant, axial slice

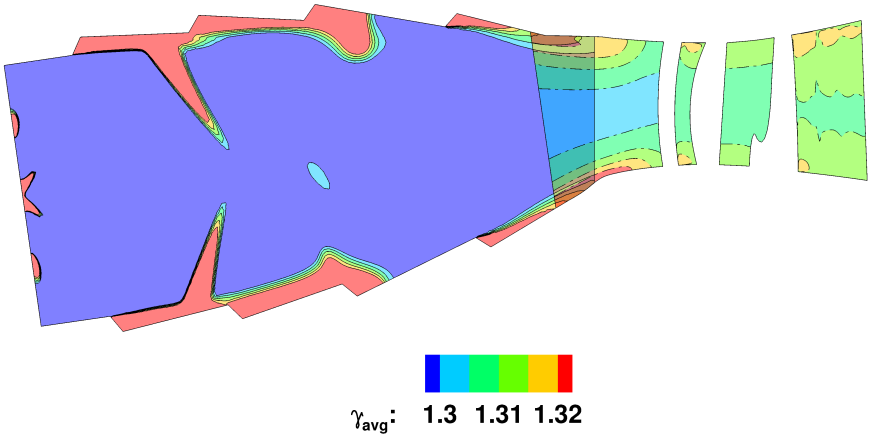

(b) Average heat ratio, axial slice

FIGURE 6.31: Average fluid properties, unsteady memory based coupling, cruise conditions Combustor - HP Turbine

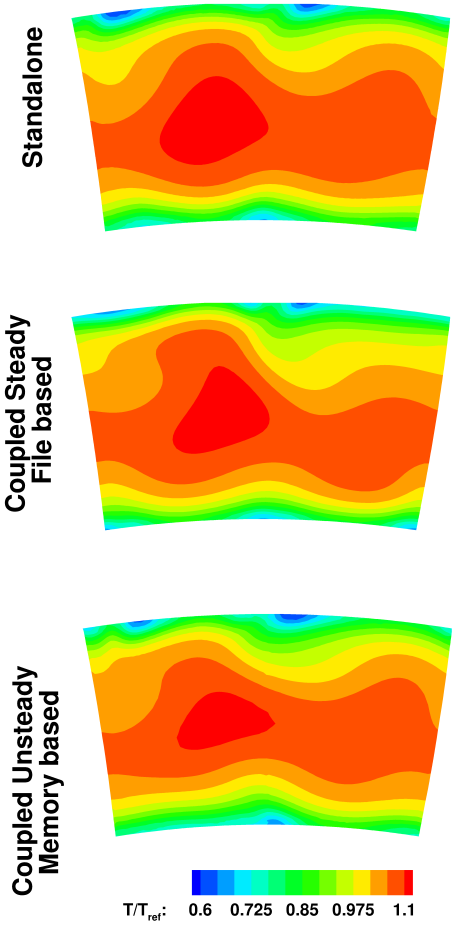

FIGURE 6.32: Normalised temperature at turbine inlet plane - standalone combustor, steady file based and unsteady memory based coupled simulations, cruise conditions Combustor - HP Turbine

Looking more in detail at the temperature field, the turbine inlet plane is considered in Fig. 6.32. We see again some differences between standalone combustor and steady coupled simulations. When compared to the low velocity case of Fig. 6.12 (Plane C) we can again find clear common features between the two low velocity and cruise conditions steady coupled simulations. The average from the unsteady run shows commonalities with both the standalone and steady coupled solutions. The RTDF on the same inlet plane is reported in Fig. 6.33. The characteristic shape of the RTDF profile for the steady coupled simulation confirms the one observed in the low velocity case of Fig. 6.13, with a peak located in the bottom part. The standalone combustor simulation for the cruise conditions (Fig. 6.32) has shown differences with respect to the low velocity case. Nevertheless the RTDF calculated is, as in the low velocity case, quite uniform and less peaky than in the steady coupled results. The RTDF from the coupled unsteady

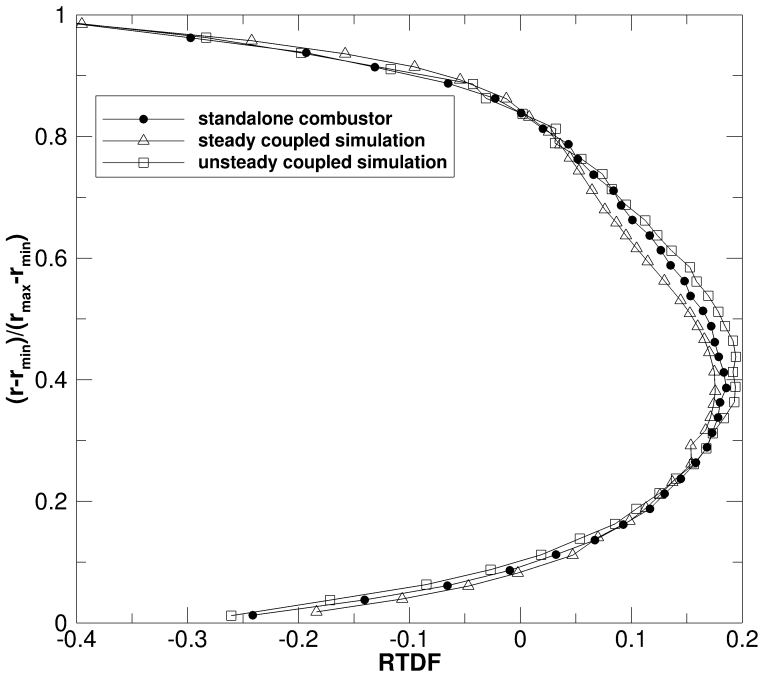

FIGURE 6.33: RTDF at turbine inlet - standalone combustor, steady file based and unsteady memory based coupled simulations, cruise conditions Combustor - HP Turbine

simulation is very similar to the standalone combustor one, but with a higher peak in the central region, confirmed by a narrower band of high velocity observed in Fig. 6.32.

One of the important benefits of an unsteady simulation is that it allows the correct prediction of the hot streaks migration through the turbine. Fig. 6.34 and Fig. 6.35 show the normalised average temperature at different stations across the NGV and the rotor respectively. As in the low velocity case (see Fig. 6.14) two hotter regions can be identified at the inlet of the turbine in Fig. 6.32, a main one and a minor one, both located at $\approx 40\%$ of the radius, the shape of which presents some differences between the two steady and unsteady coupled simulations. The hot streaks are not aligned with the stator blades leading edge but they are not located in the middle of the passage either. They are slightly clocked at a positive angle with respect to the leading edges towards the pressure sides of the stator blades, which they impinge further downstream. This is clearly visible in Fig. 6.14 and can be found again in the slices presented for the cruise condition case in Fig. 6.34. The hot streaks are only partially mitigated during their migration through the NGV and they reach the rotor. Due to the segregation effect of hot and cold gases (Sec. 2.2) the hot air migrates towards the pressure surface of the rotor, as can be clearly observed in Fig. 6.35, overheating the blades.

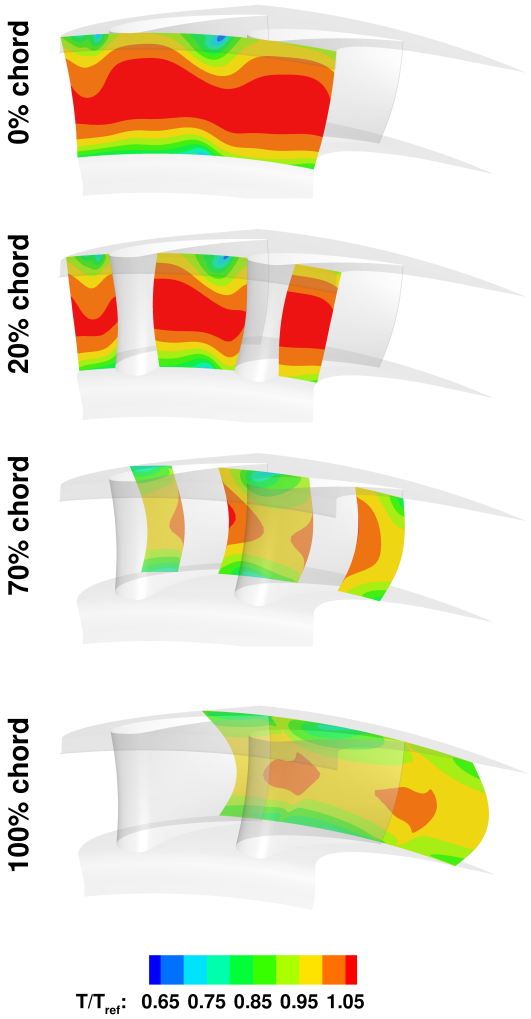

FIGURE 6.34: Normalised average temperature field through the NGV, unsteady memory based coupled simulation, cruise conditions Combustor - HP Turbine

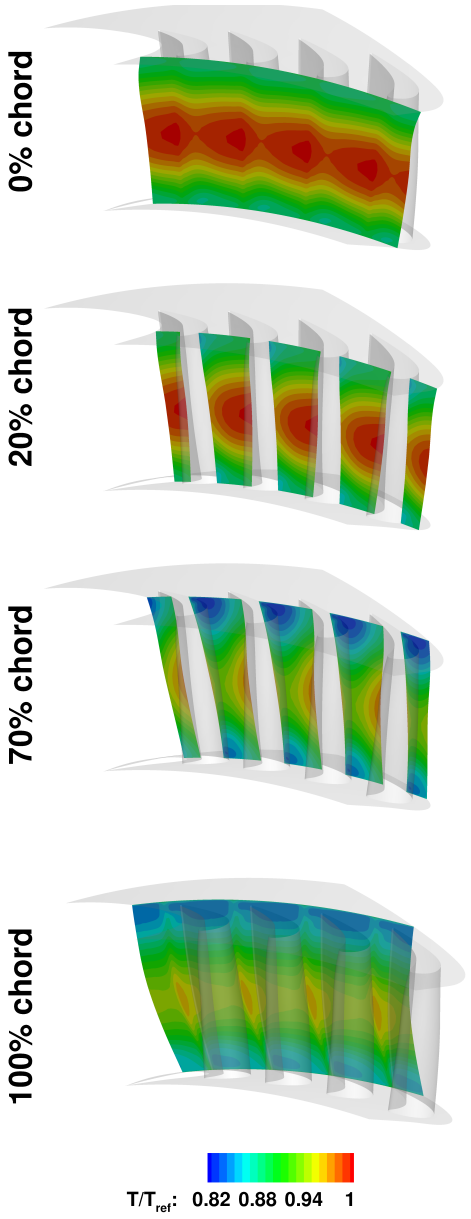

FIGURE 6.35: Normalised average temperature field through the rotor, unsteady memory based coupled simulation, cruise conditions Combustor - HP Turbine

6.4 Closure

Integrated simulations of an RQL combustor and HP turbine stage have been performed using coupled industrial CFD solvers.

Steady, low-velocity conditions

The standalone and coupled combustor simulations have shown that the combustor field is affected by the presence of the blades as far as 150% ACL upstream of the NGV leading edge, resulting in a more pronounced peak in the RTDF profile at the turbine inlet plane for the coupled simulation. In the HP turbine stage a value of OTDF up to 37% higher is present in the coupled approach (run-1) due to the circumferential averaging process applied in the standalone simulation (radial inlet profile). A decrease in turbine stage efficiency was found in the coupled simulation with respect to the standalone one, as high as 1% when matching the pressure exit and 1.3% when matching the turbine capacity. Although the conditions are not representative of a flight condition for the turbine, these changes in efficiency and OTDF seem to be quite significant of the importance of the two-dimensional profiles from a coupled approach to correctly predict performances and to capture the peak temperatures the NGV will be seeing during real operation.

Steady and Unsteady, cruise conditions

The test case has been applied to steady and unsteady simulations. The analysis of the steady file based coupling results has shown clear commonalities with the previous low velocity case, in the shape of both velocity and temperature fields at turbine inlet and in the associated RTDF profile. The unsteady memory based coupling has shown the body force approach is capable of capturing the potential effect of the stator blades at combustor exit. The average field obtained from the unsteady simulation has shown some differences from the file based steady coupled results in both velocity and temperature fields at turbine inlet. Looking at the contour lines in the overlap region of the two domains an overall very good agreement was observed between the average fields, but for some discrepancies seen in temperature and density, related to different fluid physics approximations and fluid properties involved. The analysis from unsteady average of the hot streaks coming from the combustor and entering the turbine has shown that the hot air is only partially mitigated during its movement though the stator and due to segregation effects is migrating towards the pressure side of the rotor.

Chapter 7

Conclusions and perspectives

In this work two simple, robust and reliable coupling techniques have been developed and applied to realistic combustor-turbine interaction problems. In particular an industrial incompressible/low Mach number combustion solver has been coupled with a turbomachinery code, on a zonal type of coupling. The configuration of interest is of an upstream low Mach number reacting domain and a downstream non-reacting compressible domain. The first approach does not require any modification of the source codes and the original unmodified executables can be retained (even if small adjustments are suggested). Data exchange occurs through file and via update of boundary conditions. The methodology is devoted to steady RANS simulations only. The second approach instead is mainly developed to address unsteady problems. Data exchange is done through message passing and modifications of the original source code are required to perform the data exchange. The coupling is based on boundary conditions update and on the application of body forces. Both approaches have been assessed on simple test cases and later applied to a realistic industrial case. The following conclusions have been drawn:

[I] due to the different set of governing equations in the two codes (low Mach number and compressible) not all the primitive variables can be conserved at the interface. Mass flow conservation, continuity of momentum per unit volume and temperature fields at the interface are chosen to be the main desired requirements for the coupling to achieve.

(a) In the first coupling approach, in which only existing boundary conditions can be exploited for the coupling, an appropriate definition of stagnation

pressure, together with stagnation temperature are used as inlet interface conditions of the downstream domain, while gauge pressure is provided as a feedback to the upstream domain exit plane.

(b) In the second coupling approach the momentum per unit volume with static temperature are used at the downstream inlet interface. A body force is used to drive the upstream low Mach number solution to the downstream one in the last part of the upstream domain.

[II] To minimise inconsistencies in the primitive variables at the inlet coupling interface the average value of pressure at the downstream domain inlet plane has to be "consistent" with the global reference thermodynamic pressure defined in the low Mach number domain.

[III] Pressure is the most problematic variable to deal with in the coupling. Its absolute value is undefined in a low Mach number approximation and it cannot be used, as it is, to define interface conditions for the downstream domain. Assumptions are necessary to make it uniquely defined. Moreover this pressure carries no acoustic components and it has to comply with the velocity divergence requirements, with possible problems when used as an outlet condition for the low Mach number domain. A coupling which avoids to rely on the variable pressure, where possible, is to be preferred.

[IV] The use of weak boundary conditions with characteristic treatment is a limiting factor in the quality of the coupling interface. A strong imposition of boundary conditions is preferred to improve the continuity of variables across the two domains.

[V] Because of the big differences between the two codes a weak type of coupling, in which only well posed boundary conditions are used, is found to provide accurate results without introducing reflections or unphysical behaviours, which are instead observed when stronger interfaces are assessed.

[VI] The analysis of a steady, low velocity coupled combustor-turbine realistic configuration has shown the influence of the presence of the NGV blades on the combustor field far upstream of the blades leading edge inside the last part of the combustor. On the other hand the turbine performance is changed in a coupled simulation

with respect to a more standard uncoupled simulation that typically relies on one-dimensional inlet radial profiles, confirming the necessity of taking into account in the development phase all the non-uniformities occurring at the combustor-turbine interface.

[VII] An unsteady simulation has shown that body forces can be successfully used for low Mach number/compressible zonal coupling. The analysis of a cruise condition combustor-HP turbine simulation has shown the hot streaks behaviour across the turbine: they are only partially mitigated by the stator blades and, due to segregation effect of hot and cold gases (Sec. 2.2), migrate towards the pressure side of the rotor blades.

[VIII] Future extension of the implemented unsteady coupling to LES/RANS simulations is planned

[IX] Further improving the consistency of the gas properties between the two domains is an additional possible area of work for future developments. The first coupling implemented is already capable of handling flow compositions data and when a variable composition simulation will be possible for the turbine domain, the coupling method will allow additional accuracy in coupled solutions.

This work has shown the necessity of an integrated simulation of the HP section of the engine and presented an easy and effective way of pursuing it using coupled existing specialised solvers.

Bibliography

[1] Flightpath 2050 europe's vision for aviation. http://www.acare4europe.com/sites/acare4europe.org/files/document/Flightpath2050_Final.pdf, 2011.

[2] M. S. Anand, R. Eggels, M. Staufer, M. Zedda, and J. Zhu. An advanced unstructured-grid finite-volume design system for gas turbine combustion analysis. In *Proc. ASME 2013 Gas Turbine India Conference*, Bangalore, India, 2013.

[3] I. H. Tristanto, L. Lapworth, and J. D. Northall. A Simulation Method for Turbomachinery Flows with Variable Gas Properties, Part1. In *Proc. 2nd CEAS Air And Space Conf.*, 2009.

[4] L. Lapworth. HYDRA CFD: A Framework for Collaborative CFD development. In *Proc. 2nd International Conference on Scientific and Engineering Computation*, Singapore, 2004.

[5] D J Dorney and K L Gundy-Burlet. A Survey Of Hot Streak Experiments And Simualtions. *International Journal of Turbo and Jet Engines*, 16:1–15, 1999.

[6] F R Menter. Two-Equation Eddy-Viscosity Turbulence Models for Engineering Applications. *AIAA Journal*, 32, 1994.

[7] J G E Cleak and D G Gregory-Smith. Turbulence Modeling for Secondary Flow Prediction in a Turbine Cascade. *Journal of Turbomachinery*, 114:590 – 598, 1992.

[8] Bradshaw P. Turbulence Modelling with Application to Turbomachinery. *Prog. Aerospace Sci*, 32:575–624, 1996.

[9] J. U. Schluter, X. Wu, S. Kim, S. Shankaran, J. J. Alonso, and H. Pitsch. A Framework for Coupling Reynolds-Averaged With Large-Eddy Simulations for Gas Turbine Applications. *Journal of Fluids Engineering*, 127(4):806, 2005.

[10] M G Turner, A Norris, and Joseph P Veres. High-Fidelity Three-Dimensional Simulation of the GE90. In *33rd AIAA Fluid Dynamics Conference and Exhibit*, Orlando, FL, 23-26 July 2003.

[11] M Insinna, S Salvadori, and F Martelli. Simulation of Combustor/NGV interaction using coupled RANS solvers: validation and application to a realistic test case. In *ASME Turbo Expo 2014: Turbine Technical Conference and Exposition*, Dusseldorf, Germany, 16-20 June 2014.

[12] E. V. Klapdor. *Simulation of Combustor-Turbine Interaction in a Jet Engine*. PhD Thesis, Fachbereich Machinenbau, Darmstadt Technical University, Darmstadt, 2011.

[13] M. D. Turrell and P. J. Stopford. Cfd simulation of the flow within and downstream of a high-swirl lean premixed gas turbine combustor. In *ASME Turbo Expo, Power for Land, Sea and Air*, Vienna, Austria, 2004.

[14] S. Roux, M. Cazalens, and T. Poinsot. Outlet-boundary-condition influence for large eddy simulation of combustion instabilities in gas turbines. volume 24, 2008.

[15] F. Haselbach and R. Parker. Hot end technology for advanced, low emission large civil aircraft engines. In *Proceedings of the 28th International Congress of the Aeronautical Sciences*, 2012.

[16] J. E. Temme, P. M. Allison, and J. F. Driscoll. Combustion Instability of a Lean Premixed Prevaporized Gas Turbine Combustor studied using Phase-averaged PIV. *Combustion and Flame*, 161:958–970, 2014.

[17] Ying Huang and Vigor Yang. Dynamics and Stability of Lean-Premixed Swirl-Stabilized Combustion. *Progress in Energy and Combustion Science*, 35(4):293–364, August 2009.

[18] Rql combustor configuration. http://powerturbines.blogspot.it/2015_04_01_archive.html.

[19] Lean combustor configuration. ICAO Emission workshop, 2012.

[20] Malalasekera W Versteeg H K. *An Introduction to Computational Fluid Dynamics*. Pearson, second edition, 2007.

[21] Peric M Ferziger J H. *Computational Methods for Fluid Dynamics*. Springer, third edition, 2002.

[22] Anderson J D J. *Computational Fluid Dynamics - the Basics with Applications*. MacGraw Hill, 1995.

[23] J. D. Denton and W. N. Dawes. Computational Fluid Dynamics for Turbomachinery Design. *Proceedings of the Institution of Mechanical Engineers, Part C: Journal of Mechanical Engineering Science*, 213(2):107–124, February 1998.

[24] C. H. Wu. A Genereal Through Flow Theory of Fluid Flow with subsonic or supersonic Velocities in Turbomachinery of arbitrary Hub and Casing Shapes. *NACA paper*, TN2302, 1951.

[25] C. H. Wu. *A General Theory of Three Dimensional Flow in subsonic and supersonic Turbomachines of Axial-, Radial-, and Mixed-flow Types*. Number May 1994. Lewis Flight Propulsion Laboratory, Cleveland Ohio, 1952. NACA.

[26] M. Kuerner, G. A. Reichstein, D. Schrack, M. G. Rose, S. Staudacher, J. Gier, and K. Engel. Low Pressure Turbine Secondary Vortices: Reynolds Lapse. *Journal of Turbomachinery*, 134(6):061022 –1, 7, 2012.

[27] Piotr Lampart. Investigation of Endwall Flows and Losses in Axial Turbines. Part I. Formation of Endwall Flows and Losses. *Journal of theoretical and applied mechanics*, 47(2):321–342, 2009.

[28] Budimir Rosic, John D. Denton, and Graham Pullan. The Importance of Shroud Leakage Modeling in Multistage Turbine Flow Calculations. *Journal of Turbomachinery*, 128(4):699, 2006.

[29] Chao Zhou and Howard Hodson. The Tip Leakage Flow of an Unshrouded High Pressure Turbine Blade With Tip Cooling. *Journal of Turbomachinery*, 133(4): 041028, 2011.

[30] J. Denton and U. Singh. *Time Marching Methods for Turbomachinery Flow Calculations*. Number 1979-7. von Karman Institute, 1979. VKI Lecture Series.

[31] J J Adamczyk. Model Equation for simulating Flows in Multistage Turbomachinery. *ASME paper*, 85-GT-226, 1985.

[32] John D Denton. Some Limitations of Turbomachinery CFD. GT2010-22540:1–11, 2010.

[33] P.G. Tucker. Computation of Unsteady Turbomachinery Flows: Part 1—Progress and Challenges. *Progress in Aerospace Sciences*, 47(7):522–545, October 2011.

[34] P.G. Tucker. Computation of Unsteady Turbomachinery Flows: Part 2—LES and Hybrids. *Progress in Aerospace Sciences*, 47(7):546–569, October 2011.

[35] R Haimes. Validation of a Numerical Method for Unsteady Flow Calculations. *Journal of Turbomachinery*, 115:110–117, January 1993.

[36] A H Epstein and M B Giles. Comparison of Time-Resolwed Turbine Rotor Blade Heat Transfer Measurements and Numerical Calculations. *Journal of Turbomachinery*, 114:818–827, October 1992.

[37] M M Rai. Unsteady three-dimensional Navier-Stokes simulations of turbine rotor-stator interaction. In *23rd Joint Propulsion Conference, Joint Propulsion Conferences*, San Diego, California, 29 June 1987.

[38] F. Montomoli, H. P. Hodson, and L. Lapworth. RANS-URANS in axial compressors, a design methodology. *Journal of Power and Energy*, 225:363–374, 2011.

[39] Michael B. Giles. Stator/Rotor Interaction in a Transonic Turbine. *Journal of Propulsion and Power*, 6(5):621–627, September 1990.

[40] L. He, T. Chen, R. G. Wells, Y. S. Li, and W. Ning. Analysis of Rotor-Rotor and Stator-Stator Interferences in Multi-Stage Turbomachines. *Journal of Turbomachinery*, 124:564–571, 2002.

[41] Van Zante D, Hathaway M, Cheng J, and Randall C. The Influence of Compressor Blade Row Interaction Modeling on Performance Estimates from Time-accurate, Multi-stage, Navier-Stokes Simulations. *ASME Turbo Expo 2005*, (GT2005-68463):1–13, 2005.

[42] J P Lewis, R A Delaney, and E J Hall. Numerical Prediction of Turbine Vane-Blade Aerodynamic Interaction. *Journal of Turbomachinery*, 111:387–393, 1989.

[43] K C Hall and E F Crawley. Calculation of Unsteady Flows in Turbomachinery using the Linearized Euler Equations. *AIAA Journal*, 27(6):777, 1989.

[44] M S Campobasso and M B Giles. Computing Linear Harmonic Unsteady Flows in Turbomachines with Complex Iterative Solvers. In *17th AIAA CFD Conference*, Toronto, Canada, 6-9 June 2005.

[45] Arathi K Gopinath, Edwin Van Der Weide, Juan J Alonso, Antony Jameson, Kivanc Ekici, and Kenneth C Hall. Three-Dimensional Unsteady Multi-stage Turbomachinery Simulations using the Harmonic Balance Technique. pages 1–20.

[46] M. Sergio Campobasso and Mohammad H. Baba-Ahmadi. Analysis of Unsteady Flows Past Horizontal Axis Wind Turbine Airfoils Based on Harmonic Balance Compressible Navier-Stokes Equations With Low-Speed Preconditioning. *Journal of Turbomachinery*, 134(6), 2012.

[47] W. A. McMullan and G. J. Page. Towards Large Eddy Simulation of Gas Turbine Compressors. *Progress in Aerospace Sciences*, 52:30–47, July 2012.

[48] Kuo K K. *Principles of Combustion.* John Wiley and sons, second edition, 2005.

[49] Veynante D Poinsot T. *Theoretical and Numerical Combustion.* Aquaprint by the authors, third edition, XXXX.

[50] B. Franzelli, E. Riber, M. Sanjosé, and T. Poinsot. A Two-Step Chemical Scheme for Kerosene–Air Premixed Flames. *Combustion and Flame*, 157(7):1364–1373, July 2010.

[51] S James, M S Anand, and S B Pope. The Lagrangian PDF Transport Method for Simulations of Gas Turbine Combustor Flows. In *38 th AIAA / ASME / SAE / ASEE Joint Propulsion Conference and Exhibit*, number AIAA 2002-4017, Indianapolis , Indiana, 7-10 July 2002.

[52] D B Spalding. Development of the Eddy-Break-Up Model of Turbulent Combustion. In *International Simposium on Combustion*, pages 1657–1663, 1977.

[53] W J S Ramaekers, B A Albrecht, J A Van Oijen, L P H De Goey, and R G L M Eggels. The application of Flamelet Generated Manifolds in Modelling of Turbulent Partially-Premixed Flames.

[54] Marcus Herrmann, Frank Ham, Edwin Van Der Weide, and Gianluca Iaccarino. Large-eddy Simulation Analysis of Turbulent Combustion in a Gas Turbine Engine Combustor. *Center for Turbulence Research Annual Research Briefs*, 2008.

[55] Av Coriolis and Toulouse Cedex. Dynamically Thickened Flame LES Model for Premixed and Non-Premixed Turbulent Combustion. *Proceedings of the Summer Program 2000, Center for Turbulence Research*, pages 157–168, 2000.

[56] A J Chorin. A Numerical Method for solving Incompressible Viscous Flow Problems, 1997.

[57] The avbp code. http://www.cerfacs.fr/avbp7x/.

[58] L.Y.M. Gicquel, G. Staffelbach, and T. Poinsot. Large Eddy Simulations of Gaseous Flames in Gas Turbine Combustion Chambers. *Progress in Energy and Combustion Science*, 38(6):782–817, December 2012.

[59] W J Whitney, R G Stabe, and T P Mof?tt. Description of the warm core turbine facility and the warm annular cascade facility recently installed at NASA Lewis Research Center. NASA TM 81562, NASA, 1980.

[60] R G Stabe, W J Whitney, and T P Mof?tt. Performance of a High-Work, Low-Aspect-Ratio Turbine Stator Tested With a Realistic Inlet Radial Temparature Gradient. NASA TM 103738, NASA, 1991.

[61] D J Dorney and J R Schwab. Unsteady Numerical Simulations of Radial Temperature Profile Redistribution in a Single-Stage Turbine. *Journal of Turbomachinery*, 118:783–791, 1996.

[62] T L Butler, O P Sharma, H D Joslyn, and R P Dring. Redistribution of an inlet temperature distortion in an axial flow turbine stage. *AIAA J. Propulsion and Power*, 5:64–71, 1989.

[63] D J Dorney, R L Davis, and Sharma O P. Two-dimensional inlet temperature profile attenuation in a turbine stage. In *ASME International Gas Turbine and Aeroengine Congress and Exposition*, number 91-GT-406, Orlando, FL, 3-6 June 1991.

[64] D J Dorney, R L Davis, D E Edwards, and N K Madavan. Unsteady analysis of hot streak migration in a turbine stage. *AIAA J. Propulsion and Power*, 8(2): 520–529, 1992.

[65] T Shang, G R Guenette, A H Epstein, and A P Saxer. The influence of inlet temperature distortion on rotor heat transfer in a transonic turbine. In *AIAA*, number 95-3042, 1995.

[66] K S Hermanson and K A Thole. Effect of Inlet Conditions on Endwall Secondarty Flows. In *37th AIAA Aerospace Sciences Meeting and Exhibit*, Reno, NV, 11-14 January 1999.

[67] R W Radomsky and K A Thole. High Free-Stream Turbulence Effects on Endwall Heat Transfer for a Gas Turbine Stator Vane. *Journal of Turbomachinery*, 122: 699–708, 2000.

[68] M D Barringer, O T Richard, J P Walter, S M Stitzel, and K A Thole. Flow Field Simulations of a Gas Turbine Combustor. *Transactions of the ASME*, 124: 508–516, 2002.

[69] R W Radomsky and K A Thole. Flowfield Measurements for a Highly Turbulent Flow in a Stator Vane Passage. *Transactions of the ASME*, 122:255–262, 2000.

[70] W F Colban, K A Thole, and Zess G. Combustor-Turbine Interface Studies-Part1: Endwall Effectiveness Measurements. *Journal of Turbomachinery*, 125:193–202, 2003.

[71] W F Colban, A T Lethander, and K A Thole. Combustor-Turbine Interface Studies-Part1: Flow and Thermal Field Measurements. *Journal of Turbomachinery*, 125:203–209, 2003.

[72] S Stitzel and K A Thole. Flow Field Computations of Combustor-Turbine Interactions Relevant to a Gas Turbine Engine. *Transactions of the ASME*, 126:122–129, 2004.

[73] I. Qureschi, A. Beretta, and T. Povey. Effect of simulated combustor nonuniformity on hp vane and end wall heat transfer: An experimental and computational investigation. *ASME Journal of Engineering for Gas Turbines and Power*, 133, 2011.

[74] I. Qureschi, A. Beretta, K. Chana, and T. Povey. Effect of aggressive inlet swirl on heat transfer and aerodynamics in an unshrouded transonic hp turbine. In *ASME Turbo Expo*, Vancouver, British Columbia, Canada, 2011.

[75] M. Insinna, D. Griffini, S. Salvadori, and Martelli M. Conjugate heat transfer analysis of a film cooled high-pressure turbine vane under realistic combustor exit flow conditions. In *ASME Turbo Expo, Turbine Technical Conference and Exposition*, Dusseldorf, Germany, 2014.

[76] S. Salvadori, G. Riccio, M. Insinna, and Martelli M. Analysis of combustor/turbine interaction with decoupled and loosely coupled approaches. In *ASME Turbo Expo*, VCopenhagen, Denmark, 2012.

[77] S. Salvadori, F. Montomoli, F. Martelli, P. Adami, K. S. Chana, and L. Castillon. Aerothermal study of the unsteady flow field in a transonic gas turbine with inlet tempertaure distortion. *ASME J. Turbomachinery*, 133, 2011.

[78] S. Salvadori, F. Montomoli, F. Martelli, Chana K. S., I. Qureschi, and T. Povey. Analysis on the effect of a nonuniform inlet profile on heat transfer and fluid flow in turbine stages. *ASME J. Turbomachinery*, 134, 2012.

[79] C. M. Cha, S. Hong, P. T. Ireland, P. Denmann, and V. Savarianandam. Experimental and numerical investigation of combustor-turbine interaction using and isothermal, nonreaction tracer. *ASME J. Engg. Gas Turbines and Power*, 134, 2012.

[80] X Wu, S Hahn, M Herrmann, J J Alonso, and H Pitsch. A python approach to multi-code simulations. 2005.

[81] R Lynn, J Heidegger, J Hall, A Delaney, Dale Hubler, and Scott Townsend. Energy Efficient Flow Engine Analysis Low Pressure Subsystem. NASA/CR 206597, NASA, 1998.

[82] Russell W Claus, Scott Townsend, and Nasa Glenn. A review of high fidelity gas turbine engine simulations.

[83] E Collado Morata. *Impact of unsteady aerothermal environment on the turbine blades temperature*. PhD thesis, Universite de Toulouse, Oct 2012.

[84] M. D. Papadogiannis. *Coupled Large Eddy Simulations of Combustion Chamber-Turbine Interactions*. PhD Thesis, Universite de Toulouse, INP Toulouse, 2015.

[85] J J Adamczyk, R A Mulac, and M L Celestina. A Model for Closing the Inviscid Form of the Average-Passage Equation System. *ASME Journal of Turbomachinery*, 108(2):180–186, October 1986.

[86] M G Turner, A Norris, and Joseph P Veres. Multi-Fidelity Simulation of a Turbofan Engine With Results Zoomed Into Mini-Maps for a Zero-D Cycle Simulation. In *ASME Turbo Expo*, Vienna, Austria, 14-17 Jun 2004.

[87] M G Turner, A Norris, and Joseph P Veres. Lessons Learned from the GE90 3D Full Engine Simulations. In *48th AIAA Aerospace Sciences Meeting*, Orlando, FL, 4-27 Jan 2010.

[88] Juan J Alonso, May-fun Liou, Roger Davis, Nan-Suey Liu, and Sriram Shankaran. A Multi-Code-Coupling Interface for Combustor / Turbomachinery Simulations. In *39th Aerospace Sciences Meeting and Exhibit, Aerospace Sciences Meetings*, Reno, NV, 2001.

[89] J J Alonso. Integration of RANS and LES Flow Solvers : Interface Validation. *Center for Turbulence Research, Annual Research Briefs*, 2002.

[90] J U Schluter, J J Alonso, H Pitsch, and S Kim. Integrated RANS-LES Computations of Turbomachinery Components : Generic Compressor / Diffuser. *Center for Turbulence Research, Annual Research Briefs*, 2003.

[91] J. U. Schluter, H. Pitsch, and P. Moin. Large-Eddy Simulation Inflow Conditions for Coupling with Reynolds-Averaged Flow Solvers. *AIAA Journal*, 42(3):478–484, March 2004.

[92] J U Schluter, X Wu, S Kim, J J Alonso, and H Pitsch. Coupled RANS-LES Computation of a Compressor and Combustor in a Gas Turbine Engine. In *40th AIAA/ASME/SAE/ASEE Joint Propulsion Conference and Exhibit*, Lauderdale, FL, 11-13 July 2004.

[93] H Pitsch and P Moin. Outflow Conditions for Intregrated Large Eddy Simulation / Reynolds-Averaged NavierStokes Simulations. *AIAA Journal*, 43(1):156–164, 2005.

[94] J U Schluter, X Wu, S Kim, J J Alonso, and H Pitsch. Integrated Simulations for Multi-Component Analysis of Gas Turbines : RANS Boundary Conditions. In *40th*

AIAA/ASME/SAE/ASEE Joint Propulsion Conference and Exhibit, Lauderdale, FL, 11-13 July 2004.

[95] G Medic, G Kalitzin, D You, M Herrmann, F Ham, and E Van Der Weide. Integrated RANS / LES Computations of Turbulent Flow Through a Turbofan Jet Engine. *Center for Turbulence Research, Annual Research Briefs*, pages 275–285, 2006.

[96] G Medic, G Kalitzin, D You, E van Der Weide, J J Alonso, and H Pitsch. Integrated Simulations for Multi-Component Analysis of Gas Turbines : RANS Boundary Conditions. In *45th AIAA Aerospace Sciences Meeting and Exhibit, Aerospace Sciences Meetings*, Reno, Nevada, 8-11 January 2007.

[97] Jorg Schluter, Xiaohua Wu, Edwin van der Weide, Seonghyeon Hahn, Juan Alonso, and Heinz Pitsch. Multi-Code Simulations: A Generalized Coupling Approach. *17th AIAA Computational Fluid Dynamics Conference*, pages 1–12, June 2005.

[98] JJ Alonso, S Hahn, and F Ham. CHIMPS: A High-Performance Scalable Module for Multi-Physics Simulations. In *42nd AIAA/ASME/SAE/ASEE Joint Propulsion Conference & Exhibit, Joint Propulsion Conferences*, Sacramento, California, 9-12 July 2006.

[99] T.J. Poinsot. Boundary Conditions for Direct Simulations of Compressible Viscous Flows. *Journal of Computational Physics*, 99(2):352, April 1992.

[100] Guido Lodato, Pascale Domingo, and Luc Vervisch. Three-Dimensional Boundary Conditions for Direct and Large-Eddy Simulation of Compressible Viscous Flows. *Journal of Computational Physics*, 227(10):5105–5143, May 2008.

[101] B Muller. Low Mach Number Asymptotic of the Navier-Stokes Equations and Numerica Implications. *VKI Lecture Serie 1999-03*, March 1999.

[102] S V Patankar. *Numerical Heat Tranfer and Fluid Flow.* McGraw-Hill, New York, 1980.

[103] S B Pope. *Turbulent Flows.* Cambridge University Press, 2000.

[104] D C Wilcox. *Turbulence Modeling for CFD.* DCW Industries, Inc., La Canada, California, 1994.

[105] P R Spalart and S R Allmaras. A One-Equation Turbulence Model for Aerodynamic Flows. In *AIAA, 30th Aerospace Sciences Meeting and Exhibit*, 1992.

[106] B E Launder and B I Sharma. Application of the Energy Dissipation Model of Turbulence to the Calculation of Flow Near a Spinning Disc. *International Journal of Heat and Mass Transfer*, 15:301–314, 1974.

[107] T H Shih, W W Liou, A Shabbir, Z Yang, and J Zhu. A New k - Eddy-Viscosity Model for High Reynolds Number Turbulent Flows. *Computers and Fluids*, 24: 227–238, 1995.

[108]] V Yakhot, S A Orszag, S Thangham, T B Gatski, and C G Speziale. Development of Turbulence Models for Shear Flows by a Double Expansion Technique. *Physics of Fluids A*, 4:1510–1520, 1992.

[109] B.F. Magnussen and B.H. Hjertager. On mathematical modeling of turbulent combustion with special emphasis on soot formation and combustion. In *Symp. (Int.) on Combustion*, volume 16, pages 719–729, 1977.

[110] C K Westbrook and F L Dryer. Simplified Reaction for the Oxidation of Hydrocarbon. *Combustion Science and Technology*, 27:31–43, 1981.

[111] J A van Oijen and L P H de Goey. Modelling of Premixed Laminar Flames Using Flamelet-Generated Manifold. *Combustion Science and Technology*, 161:113–137, 2000.

[112] R L G M Eggels. Modelling of NOx Formation of a Premixed DLE Gas Turbine Combustor. ASME 2001-GT-0069.

[113] B Hakberg. A Critical Study of the Bary-Moss-Libby Model. *Combustion Science and Technology*, 125:1-6:25–45, 2007.

[114] A Gupta, J Zhu, M S Anand, and R Eggels. A Flame-Generated-Manifold Chemistry Based Transport PDF Model for Gas-Turbine Combustor Simulations. *AIAA SciTech 2014*, 2014.

[115] P I Crumpton, P Moinier, and M B Giles. An Unstructured Algorithm for High Reynolds Number Flows on Highly-Stretched Grids. In *10th Int. Conf. Num. Meth. for Laminar and Turbulent Flows*, Swansea, England, July 25-27 1998.

[116] P. Moinier. *Algorithm Developments for an Unstructured Viscous Flow Solver*. PhD Thesis, University of Oxford, UK, 1999.

[117] Jameson. Analysis and Deisgn of Numerical Schemes for Gas Dynamics: 1 and 2. *Int. J. Comp. Fluid Dynamics*, 1 and 2, 1995.

[118] S R Mathur and J Y Murthy. A Pressure-Based Method for Unstructured Meshes. *Numerical Heat Transfer*, 31:195–215, 1997.

[119] L Martinelli. Calculations of Viscous Flows with a Multigrid Method. *PhD thesis, Dept of Mech and Aerospace Eng, Princeton University, USA*, 1987.

[120] Pierre Moinier and M B Giles. Preconditioned Euler and Navier-Stokes Calculations on Unstructured Meshes. *6th ICFD Conference on Numerical Methods for Fluid Dynamics, Oxford, UK*, 1998.

[121] Pierre Moinier, Jens-Dominik Muller, and Michael B Giles. Edge-based Multigrid and Preconditioning for Hybrid Grids. *AIAA,14th Computational Fluid Dynamics Conference, Norfolk, VA*, 99-3339, 1999.

[122] P I Crumpton and M B Giles. Implicit Time Accurate Solutions on Unstructured Dynamic Grids. *AIAA*, (95-1671), 1995.

[123] N Hills. Achieving High Parallel Performance for an Unstructured Unsteady Turbomachinery CFD Code. *The Aeronautical Journal*, (3100):185–193, March 2007.

[124] C M Rhie and W L Chow. A numerical Study of the Turbulent Flow Past an Isolated Airfoil with Trailing Edge Separation. *AIAA Journal*, 21(11):1523–1532, 1983.

[125] S Klainerman and A Majda. Compressible and Incompressible Fluids. *Communications on Pure and Applied Mathematics*, 35:629–653, 1982.

[126] B Muller. Low-Mach-Number Asymptotics of the Navier-Stokes Equations. *Journal of Engineering Mathematics*, pages 97–109, 1998.

[127] A Majda and J Sethian. The Derivation and Numerical Solution of the Equations for Zero Mach Number Combustion. *Combustion Science and Technology*, 42: 185–205, July 1985.

[128] Ronald G Rehm and Howard R Baumt. The Equations of Motion for Thermally Driven Buoyant Flows. 8(3), 1978.

[129] Y. V. Peet and S. K. Lele. Computational Framework for Coupling Compressible and Low Mach Number Codes. *AIAA Journal*, 46(8):1990–2001, August 2008.

[130] *Near Field of Film Cooling Jet Issued into a Flat Plate Boundary Layer: LES Study*, Germany, 2008.

[131] M. A. Sprague and I Satkauskas. Nesting an Incompressible-Flow Code within a Compressible-Flow Code: A Two-Dimensional Study. *Computers and Fluids*, 115: 75–85, 2015.

[132] Veronika Schleper. On the Coupling of Compressible and Incompressible Fluids. pages 201–208, November 2012.

[133] Markus Boger, Felix Jaegle, Rupert Klein, and Claus-dieter Munz. On the Coupling of Compressible and Incompressible Regions. 528:527–528, 2012.

[134] A. Piacentini, T. Morel, A. Thevenin, and F. Duchaine. O-palm: an open source dynamic parallel coupler. In *V International Conference on Computational Methods for Coupled Problems in Science and Engineering*, 2011.

[135] Kannan K V. *Coupling of Compressible Turbomachinery and Incompressible Combustor Flow Solvers for Gas Turbine Applications*. PhD Thesis, AAE, Loughborough University, Loughborough, 2015.

[136] I. H. Tristanto. personal communication.

[137] Y Peet and P F Fischer. Stability Analysis of Interface Temporal Discretisation in Grid Overlapping Methods. *SIAM J. Numer Anal*, 50(6):3375–3401, 2012.

[138] G I Taylor. On the Dissipation of Eddies. Reports and Memorandum 598, Aeronautical Research Council, 1918.

[139] D. M. Driver and H. L. Seegmiller. Features of a reattaching turbulent shear layer in divergent channel flow. *AIAA Journal*, 23(2), 1985.

[140] L. He and V. Menshikova. Effect of hot-streak count on turbine blade heat load and forcing. *J. Propulsion and Power*, 23(6), 2007.